Dada, Tewodros Kassa (2023) ***Investigation of novel mono- and bimetallic catalysts for high quality bio-oil production using biomass co-pyrolysis.*** **PhD Thesis, James Cook University.**

https://doi.org/10.25903/p631%2Ds341

Investigation of Novel Mono- and Bimetallic Catalysts for High Quality Bio-oil Production Using Biomass Co-pyrolysis

PhD Thesis

Tewodros Kassa Dada (MSc)

in March 2023

For the degree of Doctor of Philosophy
in the College of Science and Engineering
James Cook University
Townsville

Advisors: Dr Elsa Antunes, A/Prof Madoc Sheehan

Declaration

I declare that this thesis is my own work and has not been submitted to elsewhere in whole or in part to obtain other degree award. The content of this thesis is the result of the author work, and the contribution of others has been acknowledged in the statement of contribution of others.

____

Tewodros Kassa Dada

March 2023

Statement of Access to this Thesis

I, the under-signed, the author of this research work, understand that James Cook University will make this thesis available for use within the University Library and via the Australian Digital Thesis Network, for use elsewhere.

I understand that an unpublished work, a thesis has significant protection under the Copyright Act. I do not wish to place any restriction on access to this thesis, but any use of its content must be acknowledged.

Tewodros Kassa Dada

March 2023

Acknowledgement

During my Ph.D. journey, many people assisted and supported me in various ways. I am grateful to all of them. Here, I would like to distinguish and express my special thanks.

First and foremost, I sincerely express my deepest gratitude to my primary supervisor, Dr Elsa Antunes, for the patient guidance, encouragement, and advice she has provided me. I always knew I could count on a wide array of balanced feedback and counsel whenever we met, and I am so glad I could benefit and learn from all your experience and wisdom. I also would like to express my gratitude to my secondary supervisor, A/Prof Madoc Sheehan, for his guidance and great support during my research.

I am also profoundly grateful to Dr Alex Xiaofei Duan, The University of Melbourne for helping me with the Py-GC/MS experiments. I also owe special thanks to A/Prof Jason Scott, The University of New South Wales for helping me with the TPD analysis.

I am very grateful to A/Prof George Vamvounis for allowing me to use his laboratory for thermogravimetric analysis.

Special thanks to Dr Kevin Blake, Dr Shane Askew, and Brendan Jones, Advanced Analytical Centre at James Cook University, for providing me access to the surface area analyser, X-ray diffraction, scanning electron microscopy, and inductively coupled plasma characterizations facilities. I sincerely thank Dean Frendon, Mechanical workshop, for helping me with the fabrication of accessories for my experimental setup.

I would also like to express my profound gratitude to my research group members at James Cook University for their continuous motivation and inspiration. Especially, I would like to acknowledge Dr Ravinder Kumar, Dr Arun Vuppaladiyam, Tejas Koushik, Md Anwarul Islam, and Dr Ateeq Rehman for their support and encouragement throughout my Ph.D. journey.

I am grateful to the Graduate Research School, James Cook University, for granting me the James Cook University Postgraduate Research Scholarship (JCUPRS). Besides, I would also greatly acknowledge the College of Science and Engineering, James Cook University, for providing me financial support that was essential for the successful completion of this research.

This Ph.D. thesis would not be possible without my family and friends never-ending support, continuous cooperation, and unlimited encouragement and love. They have cared the most about my feelings and supported my education from the very beginning. They may be miles away from me, but I felt their short-distance support and encouragement.

Abstract

In recent times, biofuels have gained significant importance as an alternative fuel source for the world economy and environmental conservation. Bio-oil is a type of biofuel that can be produced from different types of feedstocks such as biomass, polymeric, and triglycerides wastes. However, the quality of bio-oil depends mainly on the feedstock types and pyrolysis parameters. Pyrolysis of a single feedstock produces bio-oil with low yield of aromatic hydrocarbons, hence co-pyrolysis of biomass with hydrogen-rich wastes has been used to enhance the bio-oil quality. However, conventional co-pyrolysis still fails to produce bio-oil with acceptable properties to replace standard fossil fuels. Therefore, catalytic co-pyrolysis using both acidic and alkaline catalysts is a potential approach to producing bio-oil as per gasoline, diesel, and jet fuel grade standards.

This research work investigated the synthesis of hierarchical Y-zeolites loaded with SrO for catalytic co-pyrolysis of ironbark (IB) and waste cooking oil (WCO). The catalyst was produced and optimised using dealumination and desilication processes, and wet and dry impregnation methods were used to load strontium on the hierarchical Y-zeolite. The catalyst characterisation confirmed the successful loading of strontium on the hierarchical Y-zeolite. The kinetic parameters of the catalytic co-pyrolysis were also studied, and the addition of the catalyst reduced the activation energy.

After optimising the catalyst preparation, the effect of reaction temperature, IB:WCO ratio, and SrO loading on product distribution and bio-oil quality was examined. The results showed that a reaction temperature of 550°C, SrO loading of 10 wt. %, and IB:WCO ratio of 1:1 produced bio-oil with the highest aromatic yield C-H (28.6%). The presence of SrO created new basic active sites on the hierarchical Y-zeolite and enhanced the aromatic carbon yield. It was demonstrated that SrO/Y-zeolite is a potential catalyst to produce high-quality bio-oil from co-pyrolysis of IB and WCO.

Furthermore, this thesis examined the effect of loading a second metal (Ni, Cu, Zn, Ag, and Fe) on SrO/Y-zeolite for catalytic co-pyrolysis of IB and WCO. Among the bimetallic catalysts, Cu-SrO/Y-zeolite produced the highest aromatic yield of 65.43% at a temperature of 750°C with a catalyst to feedstock ratio of 1:1. The effect of mono- (SrO) and bimetallic (Cu-SrO) catalysts over different catalyst supports on pyrolysis by-products, aromatic selectivity, and carbon yield was also assessed. The results showed Cu-SrO/ZSM-5 significantly increased the amount of C8-C14 compounds to 87.28% and produced low acid content of 4.43%. Overall, this research demonstrates the potential of biomass and waste cooking oil as feedstock for renewable energy production and introduces a new SrO/Y-zeolite catalyst for bio-oil upgradation and to produce high–quality bio-oil.

Table of Contents

List of Figures

List of Tables

List of Publications

1. Journal publications included in this thesis

- **Tewodros Kassa Dada**, Madoc Sheehan, S. Murugavelh, Elsa Antunes. A review on catalytic pyrolysis for high-quality bio-oil production from biomass. Biomass Conversion and Biorefinery, 2021.

- **Tewodros Kassa Dada**, Md Anwarul Islam, Arun K. Vuppaladadiyam, Elsa Antunes, Thermo-catalytic co-pyrolysis of ironbark sawdust and plastic waste over strontium loaded hierarchical Y-zeolite, Journal of Environmental Management, Volume 299, 2021, 113610.

- **Tewodros Kassa Dada**, Anwarul Islam, Ravinder Kumar, Jason Scott, Elsa Antunes, Catalytic co-pyrolysis of ironbark and waste cooking oil using strontium oxide-modified Y-zeolite for high-quality bio-oil production, Chemical Engineering Journal, 2022, 138448.

- **Tewodros Kassa Dada**, Md Anwarul Islam, Alex Xiaofei Duan, Elsa Antunes, Catalytic co-pyrolysis of ironbark and waste cooking oil using X-strontium /Y-zeolite (X= Ni, Cu, Zn, Ag, and Fe), Journal of the Energy Institute, Volume 104, 2022.

- **Tewodros Kassa Dada**, Arun Vuppaladadiyam, Alex Xiaofei Duan, Ravinder Kumar, Elsa Antunes, Probing the effect of Cu-SrO loading on catalyst supports (ZSM-5, Y-zeolite, activated carbon, Al_2O_3, and ZrO_2) for aromatics production during catalytic co-pyrolysis of biomass and waste cooking oil, Bioresource Technology, Volume 360, 2022, 127515.

2. Other publications

- Md Anwarul Islam, **Tewodros Kassa Dada**, Mst Irin Parvin, Arun K Vuppaladadiyam, Ravinder Kumar, Elsa Antunes, Silver ions and silver nanoparticles removal by coffee derived biochar using a continuous fixed-bed adsorption column, Journal of Water Process Engineering, Volume 48, 2022, 102935.

- Elsa Antunes, Arun K Vuppaladadiyam, Ravinder Kumar, Varsha SS Vuppaladadiyam, Ajit Sarmah, Md Anwarul Islam, **Tewodros Kassa Dada**, A circular economy approach for phosphorus removal using algae biochar, Cleaner and Circular Bioeconomy, Volume 1, 2022, 100005.

3. Conference publications

- **Tewodros Kassa Dada**, Elsa Antunes, Catalytic co-pyrolysis of biomass and waste cooking oil over Cu-SrO/Y-zeolite catalysts. Oral presentation at the ACS Fall 2022, Chicago, IL & Hybrid, August 21 - 25, 2022.

1 Introduction

1.1 Problem statement

Decarbonisation is the next approach towards a zero-carbon economy by providing clean and renewable energy alternatives. Lignocellulosic biomass is a key and alternative renewable energy source to replace fossil fuels, ensuring a zero-carbon economy [1]. Thermochemical processes such as pyrolysis predominantly convert biomass into high-quality bio-oil [2]. Pyrolysis of biomass can selectively produce desired products such as jet fuel, diesel, gasoline, and heavy oil [3]. The target product yield and selectivity mainly depend upon feedstock types (biomass, polymeric, and triglycerides wastes) and pyrolysis process conditions [4]. The common bio-oil obtained from the biomass pyrolysis process is not suitable for fossil fuel substitution due to the high content of oxygenated compounds (i.e., phenols, ketones, hydrocarbons, sugars, and alcohols), high viscosity, high acidity, and high moisture content. Therefore, it is necessary to upgrade bio-oil properties by converting the oxygenated compounds into aromatic hydrocarbons for better utilisation of bio-oil as a renewable energy source.

Co-feeding biomass with a hydrogen-rich feedstock is a viable solution to increase the H/C ratio and upgrade the bio-oil quality. Among hydrogen-rich feedstocks, polymeric wastes such as polystyrene (PS), polypropylene (PP), and polyethylene (PE) increase the aromatic yield and selectivity contributing to an improvement of the bio-oil quality. The addition of plastic waste would increase hydrocarbon yield and reduce coke formation by suppressing the formation of long-chain hydrocarbons. On the other hand, triglyceride feedstock such as waste cooking oil shows high potential as a hydrogen co-feed during co-pyrolysis, subsequently producing bio-oil rich in aromatic and aliphatic hydrocarbons. Waste cooking oil (WCO) is mainly utilised to produce biodiesel, which generates large amounts of by-products (glycerol) and requires additional pre-treatment [5, 6]. However, conventional co-pyrolysis process still failed to produce bio-oil with suitable properties for fossil fuel replacement.

Catalysts have also been investigated to upgrade bio-oil, but more research is required to combine all desired properties in a single catalyst. According to literature, the research gaps identified are: (1) most catalytic upgradation of bio-oil has been carried out via a mono-catalytic system (acidic or alkaline catalysts), which is unable to address all oxygenated compounds available in the bio-oil mixture. (2) Application of basic catalysts during catalytic co-pyrolysis (CCP) process enables ketonisation reaction to upgrade pyrolytic vapour. The presence of strong basic sites in the catalyst favours high conversion of carboxylic acids via ketonisation reaction [7]. However, the use of basic catalysts is not enough to convert the oxygenated fraction in bio-oil into aromatic compounds. Therefore, synthesis of catalysts with both acidic and alkaline sites is required to enhance the bio-oil quality. (3) Also, low mesoporous surface area, catalyst deactivation over coke deposition and sintering are responsible for low catalytic activity. In this research work, three research questions were formulated based on the identified knowledge gaps, which were addressed in the different data chapters of this thesis.

1. Can new catalysts be developed to reduce high oxygenated compounds in the bio-oil?
2. Can a bifunctional (acidic - basic) catalyst enhance the quality and yield of bio-oil?
3. What is the effect of catalyst support on bio-oil quality?

1.2 Research Objectives

The main objective of this research was to investigate the impact of different catalyst preparation methods on catalyst properties and how they affect the pyrolysis process and bio-oil yield and quality. Further, investigation the effect of the pyrolysis processing variables, feedstock to catalyst ratio on the production of high-quality bio-oil using mono-catalysts and bifunctional catalysts. Finally, probe the effect of catalyst support on bio-oil quality.

The specific objectives of this research thesis are:

1. To investigate the catalyst preparation methods and variables to obtain catalysts with high mesoporous surface area and volume.
2. To produce high-quality bio-oil and study the impact of catalytic co-pyrolysis conditions (SrO loading, IB:WCO ratio, and catalytic) on bio-oil quality and yield.
3. To investigate the effect of bimetallic catalysts on bio-oil quality and yield.
4. To investigate the effect of catalyst supports on bio-oil quality.

1.3 Thesis organization

This thesis contains seven chapters; introduction, literature review, four data chapters and conclusions. This thesis is a compilation of five published journal articles, each containing a clearly described materials and methods section, thus this thesis does not have a stand-alone methodology chapter.

Chapter 1 – Introduction – includes the main motivations for this research and its potential applications and beneficial outcomes. This chapter also outlines the research objectives.

Chapter 2 – Literature Review

This chapter reviews the basic features of catalytic pyrolysis for producing high-quality bio-oil and recommends different types of catalysts for specific products/chemicals. This chapter also explains in detail the physicochemical properties of bio-oil, bio-oil upgrading by catalytic pyrolysis, and its reaction mechanisms to produce high-quality bio-oil. In the last section, advanced analytical techniques used for bio-oil characterisation are also discussed. This chapter identifies the knowledge gaps that were later used to formulate the research hypothesis for this work.

This work has been published as: Tewodros Kassa Dada, Madoc Sheehan, S. Murugavelh, Elsa Antunes. A review on catalytic pyrolysis for high-quality bio-oil production from biomass, Biomass Conversion and Biorefinery, 2021.

Chapter 3 – Probing the impact of catalyst synthesis conditions on the preparation of catalyst with high mesoporous surface and volume catalyst

This chapter investigates the process conditions to prepare catalyst with high surface area and mesoporosity. Parent Y-zeolite was used as a precursor to create a hierarchical structure. During the synthesis of hierarchical Y-zeolite, sequential dealumination and desilication using citric acid (0.05 M and 0.1 M) and NaOH (0.2 M, 0.4 M and 0.8 M) were used, respectively. Moreover, loading of strontium on hierarchical Y-zeolite was performed using two different methods: wet and dry impregnation methods. The prepared catalysts were characterised by N_2 adsorption-desorption isotherms, field emission scanning electron microscopy (FESEM) combined with energy dispersive x-ray spectroscopy (EDS), X-ray diffraction (XRD), Fourier-transform infrared spectroscopy (FTIR), and thermogravimetric analyser (TGA). This chapter also contains a small section about the application of the prepared catalyst for bio-oil production. The best catalyst with high mesoporous surface area and low activation energy was tested for the production of high-quality bio-oil in the chapter 4.

This work has been published as: Tewodros Kassa Dada, Md Anwarul Islam, Arun K. Vuppaladadiyam, Elsa Antunes. Thermo-catalytic co-pyrolysis of ironbark sawdust and plastic waste over strontium loaded hierarchical Y-zeolite, Journal of Environmental Management, Volume 299, 2021, 113610.

Chapter 4 – High quality bio-oil production and optimisation of process parameters

This chapter examines the application of SrO-loaded hierarchical Y-zeolite catalyst for bio-oil upgrading via in-situ co-pyrolysis of biomass (ironbark) and waste cooking oil (WCO). The effect of reaction temperature (450°C, 550°C, 650°C), IB:WCO ratio (1:1, 1:2, and 1:4) and SrO loading (5%,10%, and 15%) on product distribution and quality was examined. This chapter also proposed a reaction mechanism for catalytic co-pyrolysis of IB:WCO mixture in the presence of SrO/Y-zeolite catalyst. Among the parameters, IB:WCO (1:1) mixture with a 10 % SrO loading Y-zeolite at 550°C produced the highest aromatic yield of 28.6 %.

This work has been published as: Tewodros Kassa Dada, Anwarul Islam, Ravinder Kumar, Jason Scott, Elsa Antunes. Catalytic co-pyrolysis of ironbark and waste cooking oil using strontium oxide-modified Y-zeolite for high-quality bio-oil production, Chemical Engineering Journal, 2022, 138448.

Chapter 5 – Examining the effect of bimetallic catalyst on bio-oil product distribution

This chapter discusses the impact of loading a second metal (Ni, Cu, Zn, Ag, and Fe) on SrO/Y-zeolite to enhance bio-oil quality. The pyrolysis kinetic parameters and product distribution in pyrolytic vapour were investigated using both TGA and Py-GC/MS techniques, respectively. The bimetallic catalysts were prepared via wet impregnation and characterised using N2 adsorption-desorption, SEM, XPS and FTIR. The results showed that Cu-SrO/Y-zeolite produced bio-oil with a high aromatic content of 65.43 % at 750°C and the lowest acid content. In addition, Cu-SrO/Y-zeolite catalyst showed a higher yield of C17-C20 (jet fuel range) than the mono-metallic SrO/Y-zeolite catalyst. The high mesoporous area and strong interaction between Cu-SrO helped in the conversion of higher molecular weight compounds into aromatic hydrocarbons.

This work has been published as: Tewodros Kassa Dada, Md Anwarul Islam, Alex Xiaofei Duan, Elsa Antunes. Catalytic co-pyrolysis of ironbark and waste cooking oil using X-strontium /Y-zeolite (X= Ni, Cu, Zn, Ag, and Fe), Journal of the Energy Institute, 2022.

Chapter 6 - Effect of catalyst supports on bio-oil product distribution

This chapter examines the effect of mono- (SrO) and bimetallic (Cu-SrO) catalysts prepared with different catalyst supports (ZSM-5, Y-zeolite, AC, Al_2O_3, and ZrO_2) on bio-oil properties and yield. The catalysts were analysed using N_2 physisorption isotherms, XRD, and XPS. The catalytic co-pyrolysis products were analysed based on the relative area of the peaks obtained via Py-GC/MS. The chapter also discusses the effect of catalyst support on product distribution, aromatic selectivity, and carbon yield. Among the catalysts Cu-SrO/ZSM-5 significantly increased the content of gasoline-grade compounds (C8-C14) to 87.28% while reducing compounds over the range of C20 to 1.19%.

This work has been published as: Tewodros Kassa Dada, Arun Vuppaladadiyam, Alex Xiaofei Duan, Ravinder Kumar, Elsa Antunes. Probing the effect of Cu-SrO loading on catalyst supports (ZSM-5, Y-zeolite, activated carbon, Al_2O_3, and ZrO_2) for aromatics production during catalytic co-pyrolysis of biomass and waste cooking oil, Bioresource Technology, Volume 360, 2022, 127515

Chapter 7 – Conclusions and recommendations – presents the overall conclusions of this research and recommendations for future research and development.

2 Literature Review

Abstract

Biomass is a renewable source and potentially sustainable fossil fuel replacement due to its availability, lower processing cost, high conversion, and lower life cycle carbon emissions. Pyrolysis can be used to convert biomass into bio-oil, but the quality of bio-oil is usually poor exhibiting high viscosity, thermal instability, and corrosiveness. This review article has focused on the application of catalytic pyrolysis to toward getting high-quality bio-oil and its advanced techniques to characterisation. Structural arrangement (i.e mesoporous, microporous), number of acid site (Lewis and Brønsted acid sites), and amount of metal loading are considered as a key factor for deoxygenation reactions and selective production of aromatic hydrocarbons. Nobel metal loading on hierarchical zeolite favours hydrogenation of C–O, C=O, or C=O and reduce coke deposition to produce polycyclic aromatics. Overall reaction mechanism, aromatic yield and selectivity, the effect of Si/Al ratio, and process challenges of metal loaded zeolite are summarized. The advantage and disadvantage of different types of advanced analytical techniques for bio-oil characterization are also discussed. The results showed that two-dimensional gas chromatography (2D GC) technique can identify 70% of chromatograph from bio-oil analysis. However, there is need to combine analytical techniques to accurately quantify bio-oil components.

Keywords: Biomass; Bio-oil; Catalyst; Organic compounds; Pyrolysis

This work has been published as: Tewodros Kassa Dada, Madoc Sheehan, S. Murugavelh, Elsa Antunes. A review on catalytic pyrolysis for high-quality bio-oil production from biomass, Biomass Conversion and Biorefinery, 2021.

2.1 Introduction

Biomass is widely used as a renewable source for substitution of fossil fuel and a precursor for the production of chemicals [8]. For example, the conversion of lignocellulosic biomass (i.e., sugarcane, corn) into bioethanol has been extensively investigated [9, 10]. Biomass is a carbon-rich biological mate- rial widely used due to its availability, lower processing cost, and higher conversion [11]. In the course of biomass conversion, there is no overall increase in carbon footprint, making biomass a potential sustainable renewable energy source, and having a critical role in environmental mitigation and energy supply. Biomass can be grouped into four subgroups: (1) agricultural and forestry residues, (2) municipal and industrial solid waste, (3) herbaceous crops: Napier grass and weeds, and (4) aquatic and marine biomass [12]. Biomass is converted into bioenergy and chemicals via biological and thermochemical processes [13]. The thermochemical processes are carried out at high temperatures, between 300 and 1400°C [14, 15] Amongst the thermochemical processes, pyrolysis is widely used, with biomass conversion by high heat energy (207–434 kJ/kg) in the absence of oxygen [16, 17].

Pyrolysis enhances the energy density of biomass with the flexibility to be carried out at a small scale or remote location setups [18]. Pyrolysis is a flexible and attractive process to converting biomass into bio-oil, chemicals, and heating energy. Slow pyrolysis is usually performed in batch mode for long periods of residence time (5–30 min) at low temperatures and heating rates [19]. The decomposition of biomass gives rise to three main products: biogas, bio-oil, and biochar. Bio-oil is the main product of pyrolysis, with a higher heating value than the raw material, which can be converted into different chemicals [20]. Catalysts have been used to improve the efficiency of pyrolysis process and to upgrade the bio-oil quality [21].

Catalytic pyrolysis operates in in-situ and ex-situ modes [22]. In the case of the ex-situ catalytic pyrolysis process, the biomass is separated from the catalyst, and pyrolytic vapour from the pyrolysis process reacts with the catalyst in a secondary reactor [22]. Nevertheless, there are not many comparative studies in the literature to understand the catalytic mechanisms and kinetic pathways of in-situ and ex-situ catalytic pyrolysis. The most important catalyst groups used in catalytic pyrolysis are zeolites, mesoporous catalysts, and biomass-derived catalysts.

Zeolites with distinctive pore structure and acidity (Lewis and Brønsted acid sites), are used in bio-oil upgrading [23, 24]. The zeolites predominantly used in pyrolysis are ZSM- 5, Beta-zeolites, and Y-zeolites [25-27]. ZSM-5 has demonstrated excellent efficiency in deoxygenation reactions for aromatic compounds, producing bio-oil with low oxygen content and high calorific value [28]. Metals have been loaded into zeolites to enhance bio-oil quality due to their high resistance to coke deposition and high acidity [29]. However, mass transfer limitations, catalyst deactivation over coke deposition, and sintering should be optimised for zeolite catalytic pyrolysis. Mesoporous catalysts, with a pore size range of 20–30 Å, are used in catalytic pyrolysis due to their unique porosity and high surface area (900–1100 m^2/g) [30, 31]. Mesoporous silica catalysts, such as SBA-15, MCM-41, and MUS-S, are widely used in catalytic pyrolysis of biomass due to their supramolecular structure, and their propensity to synthesize different crystalline structures [32]. Biochar produced during biomass pyrolysis is also utilized as biomass-derived catalyst for bio-oil upgrading [33].

In this chapter, the impact of biomass composition on the quality and yield of bio-oil produced via pyrolysis has been discussed. Different types of pyrolysis, product distribution, and key factors on the process performance are also discussed in the subsequent sections. In the review article more stress has being laid on bio-oil physicochemical properties and its upgrading by catalytic pyrolysis. The reaction mechanisms and application of heterogeneous catalysts to produce high quality bio-oil are explained in detail. In the last section, advanced analytical techniques used for bio-oil characterisation are also reviewed. The main objectives of this review article are to (1) summarise the basic features of catalytic pyrolysis to produce high quality bio-oil, (2) recommend different types of catalysts for specific products/chemicals production, and (3) summarise bio-oil advanced characterisation techniques.

2.2 Biomass composition

Biomass comprises hemicellulose, cellulose, lignin, and a small number of other extractives [34]. Agricultural and forestry residues have a high energy content, which mainly consists of cellulose [35]. However, herbaceous plants are generally continuous, with loosely bonded fibres, which showed a smaller percentage of lignin that connects the cellulose fibres [36]. Lignin has a higher resistance to heat and chemical degradation than cellulose and hemicellulose [34].

As shown in Figure 2.1, different biomass feedstocks comprise different amounts of hemicellulose, cellulose, and lignin. The total amount of lignin and cellulose is one of the determinant factors for subsequent energy and chemical conversion processing. Numerous herbaceous crop families, such as elephant grass, Bermuda grass, esparto grass, alfalfa-full flower, contain 10–25% hemicellulose, 20–40% cellulose and 10–30% lignin [36-38]. Typical switch grasses contain 32% cellulose, 19.2% hemicellulose, and 15-30% lignin [39]. Generally, biomass with lower lignin content and higher cellulose/hemicellulose content is desired for activated carbon production [40]. High lignin content gives the lowest aromatic yield and the highest coke yield while high hemicellulose content contributes to low coke yield and high non-condensable gas production [41].

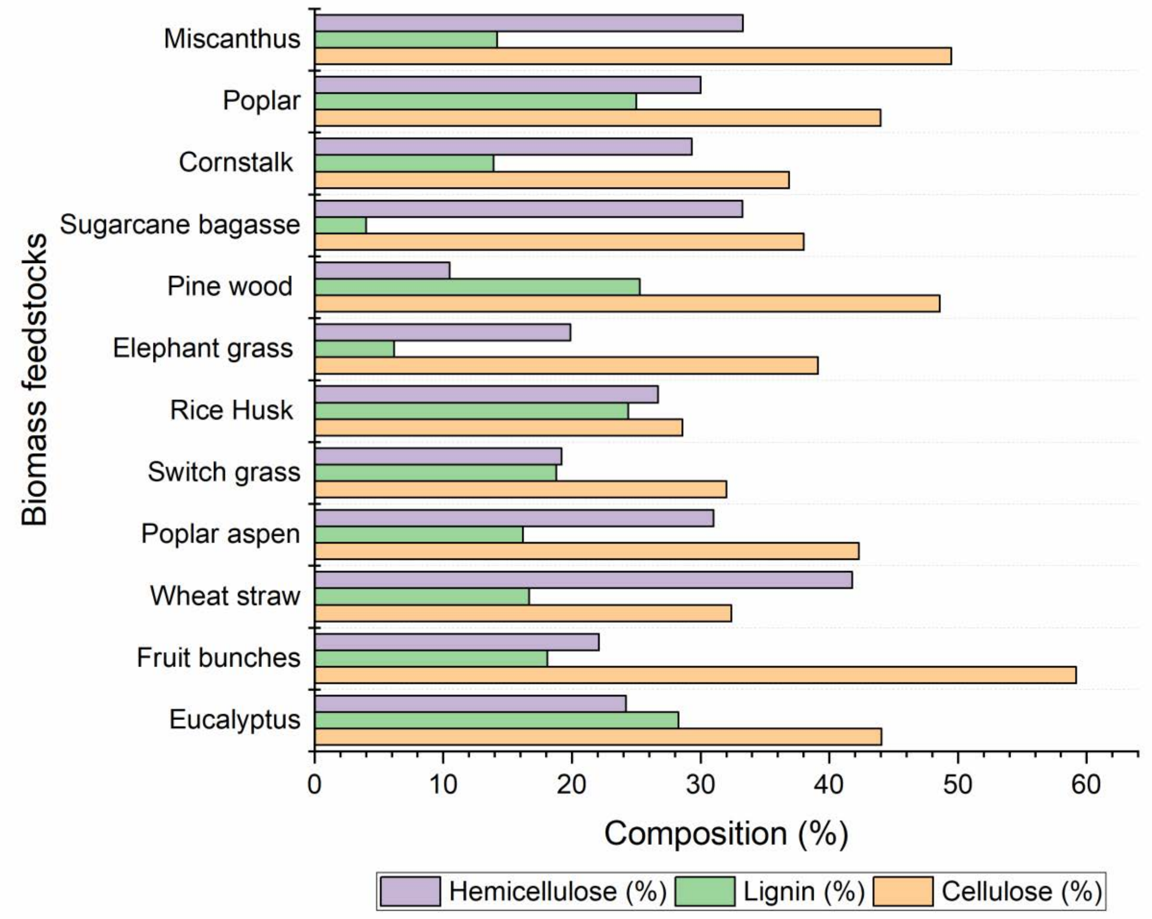

Figure 2.1. Composition of different biomass [39, 42-47].

The elemental composition of different biomass groups, pyrolysis conditions, bio-oil yield and composition obtained by conventional pyrolysis are summarized in Table 2.1. Herbaceous crop biomass has an overall elemental composition of 41-49% carbon, 44-47% oxygen, with bio-yield in the range of 44-60%. The energy per unit mass increases with decreasing oxygen content in the feedstock. For example, agricultural residues have a high amount of oxygen (38-47%), which reduces the calorific value of the bio-oil [48]. Municipal and industrial wastes are primary sources of nitrogenous compounds, having a nitrogen content of 3-8% [49].

The quality and yield of bio-oil produced by thermochemical conversion is strongly affected by the elemental composition of biomass. The bio-oil constituents typically depending on the carbon and hydrogen content of biomass. As shown in Table 2.1, spruce wood contains a high carbon and hydrogen content, 49.11% and 6.14 %, respectively, which enhance the bio-oil phenolic content [50]. The hydrogen amount seems to increase the heating value and aromatic compounds of bio-oil, but slightly varies over biomass types. Amongst the agricultural and forestry residues, oak showed the highest aromatic content due to its high hydrogen content (7.16%).

Similarly, municipal and industrial wastes have a high conversion into bio-oil with a yield in the range of 30.1–65%. The coffee husk showed higher conversion into phenolic and aromatic compounds due to high carbon to hydrogen ratio (7.33) [51]. The average C, O, and H percentages of the aquatic and marine biomass are 41.62, 5.90, and 44.26%, respectively. The variation in the elemental composition of biomass results in a high variation in the bio-oil yield and composition. The high carbon to hydrogen ratio (8.2) of P. indicus results in a high aromatic yield in the bio-oil [52]. In contrast, Nannochloropsis showed a lower aromatic yield due to lower carbon to hydrogen ratio of 6.3, but the pyrolysis conditions were different which makes this comparison difficult. Understanding the degree of biomass composition variation helps to design an effective thermochemical process for bio- mass conversion [53]. The bio-oil properties such as viscosity, pH, and chemical composition depend on the feedstock biomass type, pyrolysis conditions and reactor design. The effect of pyrolysis process parameters on bio-oil quality is discussed in detail in section 2.3.2.2.

Table 2.1. Elemental composition of different biomass groups and bio-oil yield obtained by conventional pyrolysis.

Biomass groups	Biomass	C (%)	O (%)	H (%)	N (%)	Bio-oil yield (%)	Pyrolysis conditions			Bio-oil composition percentage (wt. %)								
							Temperature (°C)	Heating Rate (°C/ min)	Gas flow rate (ml/min)	Phenols	Acids	Esters	Ketones	Alcohols	Aldehydes	Furans	Aromatics	Ref.
Agricultural and Forestry Residues	Rice husks	42.36	39.79	5.13	0.72	42	500	ND	100	6.9	18.5	3.1	5.7	9.1	3.9	5.1	ND	[54]
	Sweet sorghum	43.6	45.1	5.7	1.0	44	600	100	100	2.51	2.7	0.68	2.3	0.35	ND	0.17	1.1	[55]
	Birch wood	48.45	45.46	5.58	0.20	ND	800	50	150	ND	ND	ND	ND	ND	ND	ND	ND	[56]
	Eucalyptus bark	38.7	54.9	4.5	0.3	60	500	ND	3000	ND	ND	ND	ND	ND	ND	ND	ND	[57]
	Oak	42.5	49.74	7.16	0.12	54	400	10	200	15.38	11.89	ND	12.8	22.6	9.27	3.28	4.22	[58]
	Pine wood	45.92	48.24	5.27	0.22	36	500	40	300	ND	ND	ND	ND	ND	ND	ND	ND	[59]
	Spruce wood	49.11	44.62	6.14	0.08	ND	580	ND	180	28.14	5.68	ND	5.8	ND	2.57	2.23	ND	[50]
Herbaceous Crops	Switch grass	41.41	46.27	6.63	0.5	60	480	ND	70	3.5	ND	ND	ND	2.7	17.4	ND	ND	[60]
	Arundo donax	49.2	37.3	11.2	2.3	ND	490	ND	ND	29.1	107	ND	20.2	ND	11.2	11	16.3	[61]
	Bamboo whole	52.0	42.5	5.1	0.4	42	700	30	50	20.56	8.14	ND	0.84	0.44	ND	4.83	ND	[62]
	Alfalfa-full flower	45.97	40.58	5.52	1.6	53	500	ND	1050	4.2	3.49	ND	ND	ND	1.05	0.2	ND	[37]
	Achnatherum splendens	48.09	44.22	7.69	ND	44.85	450	30	ND	ND	ND	ND	ND	ND	ND	ND	ND	[63]

	Para grass	33.1	60.6	5.33	0.9	38.8	500	10	40	38.4	ND	ND	17.1	3.9	ND	12.5	18.6	[64]
	Kenaf grass	44.6	47.7	5.7	0.1	ND	590	4	ND	18.53	9.87	ND	ND	2.0	1.81	2.73	ND	[65]
Municipal and Industrial waste	Sewage sludge	48.6	34	7.7	8.2	45.2	500	ND	35	5.3	1.6	0.5	3	4.6	ND	ND	6..2	[66]
	Waste furniture Sawdust	49.1	41.7	6.2	3	65	450	10	5000	9.9	15.9	1.9	1.5	ND	ND	2.2	ND	[67]
	Pig compost	50.9	36.6	6.8	5.2	44.4	500	ND	35	11.1	11	1.3	8.5	8	ND	ND	6.3	[66]
	Chicken Litter	46.9	42	5.5	5.38	39	500	10	5	ND	ND	ND	ND	ND	ND	ND	ND	[68]
	Coffee husk	46.41	44.51	6.33	2.66	30.1	450	10	ND	28.4	0.98	24.42	0.55	ND	ND	ND	12.07	[51]
Aquatic and marine biomass	Spirulina Sp.	39.26	47.41	6.11	6.65	45.7	550	8	30	2.61	ND	ND	ND	ND	6.43	ND	1.94	[69]
	P. indicus	49.10	42.3	5.98	1.02	55.7	550	ND	ND	2.55	1.8	ND	ND	2.71	6.73	9.06	3.8	[52]
	Nannochloropsis	42.90	11.6	6.80	6.7	40	600	20	50	0.97	ND	ND	0.71	0.52	0.48	0.70	0.77	[70]
	Enteromorpha clathrata	35.20	32.98	5.20	2.10	33.7	550	ND	200	14.74	32.36	1.13	4.08	ND	ND	ND	0.82	[71]

ND: No Data

2.3 Biomass Processing Methods

2.3.1 General overview

Biomass consists of various precursors to produce green chemicals and fuels [72]. In general, biomass conversion is undertaken by two types of processes: biological and thermochemical processes [73]. Thermochemical methods are preferred over the biological processes due to the short reaction times and high degradation efficiency [74-77].

The product distribution and bio-oil quality from thermo- chemical processes depend on the residence time, heating rate, temperature, degree of oxidation, the feedstock particle size, and moisture content. The thermochemical processes can be classified into three primary processes: pyrolysis, gasification, and liquefaction [74, 78]. The main products of pyrolysis and gasification are biogas, bio-oil, and biochar, whereas bio- crude and sugars are the main products of the liquefaction process. The intermediate products obtained from thermochemical process such as sugar, bio-crude, and bio-gas can be further converted into bioenergy and chemicals via catalytic pyrolysis, steam reforming, fermentation, water-gas shift reaction, and hydro-processing [79, 80].

Liquefaction is an alternative thermochemical process, primarily designed for producing liquid fuel from biomass [81]. The process is carried out in an aqueous medium at a pressure of between 5 and 20 MPa, and temperatures between 250 and 370°C. These are subcritical conditions in which complex biomass structures decompose by hydrolysis and repolymerize into smaller molecules such as levoglucosan, hydroxyacetaldehyde, hydroxyacetone, pyruvic aldehyde, glyceraldehyde, and furfural [82].

Gasification is a thermochemical process to converting biomass into gaseous fuel with the presence of a gasifying agent [83]. The gasification process is carried out at high temperatures, between 500 and 1400°C, and at a range of pressures, from atmospheric pressure to 33 bar [14]. The gaseous products during gasification are CO_2, H_2, CH_4, CO, and N_2 [84]. Biomass moisture content varies between 30 and 60% while gasification process requires biomass with a moisture content between 10 and 15%. Therefore, drying biomass is a fundamental pre-treatment process to meet the moisture content criteria for gasification, which significantly increases the overall processing costs [85]. Complex operation, high energy costs because of low moisture content requirement for the biomass and relatively high processing temperature make gasification process unsuitable for biomass conversion [86]. On the other hand, pyrolysis is a versatile process to efficiently convert biomass into bio-oil, which is suitable for all types of biomass [87].

2.3.2 Pyrolysis

Pyrolysis is a thermochemical degradation of biomass by high heat energy (207–434 kJ/kg) in the absence of oxygen [16, 17]. The pyrolysis process is ascribed as the sum of three main routes: char formation, depolymerization, and fragmentation [88]. The char formation pathway results in producing solid residue with a high amount of polycyclic aromatic hydrocarbons [89]. The primary steps in this path are the production and incorporation of benzene rings in a polycyclic structure [90, 91]. Depolymerization consists of degradation of polymeric structures and at low temperatures the degraded monomers condense into a liquid fraction [92]. Fragmentation results in incondensable gas formation and a variety of organic compounds that are condensable at ambient temperature [90, 93].

2.3.2.1 Types of pyrolysis processes

Based on processing pyrolysis parameters, the conversion of biomass is divided into three classes: slow, fast, and flash. Operation conditions for various types of pyrolysis are summarised in Table 2.2. Slow pyrolysis is mainly applicable for charcoal production and chemicals like acetic acid, furfural, and phenols. Most slow pyrolysis literature is primarily focused on biochar production and its applications [36, 94]. Of the slow processes, carbonization, with a low heating rate of 0.1–0.4°C/s, is a widely applicable process carried out without condensation of the pyrolysis products [95]. Carbonization is a biomass conversion technique for charcoal production and performed when biochar is the desired product. The ideal feedstock moisture content for slow pyrolysis is between 15 and 20% [96].

Flash pyrolysis produces high bio-oil yield (70%) and low gas and tar amounts in comparison with slow pyrolysis [97]. Flash pyrolysis takes place at high temperatures (650– 000°C) and requires short residence time (max. 2 s). During the process, the feedstock is heated rapidly to be vaporized and then condensed into bio-oil [98, 99]. On the other hand, fast pyrolysis takes place at moderately low temperature (500–800°C) and short residence vapour time (5 s) [100]. During fast pyrolysis, approximately 60–75% of the biomass is converted into bio-oil [101]. However, fast pyrolysis temperatures higher than 650°C favour biogas production. Fast pyrolysis is a flexible and desired process to trans- form biomass into a liquid that is easily stored and transported for biofuel and chemical production [102, 103].

Vacuum pyrolysis is the decomposition of biomass in a pyrolysis reactor under vacuum to reduce vapours residence time [45]. Vacuum pyrolysis is characterised by a slow heating rate and takes place at temperature between 350 and 520°C resulting in low bio-oil yield (35–50 wt.%) [104]. Hydropyrolysis is the decomposition of biomass in the presence of hydrogen gas [105]. During hydropyrolysis hydrogen gas is reduced to form hydrogen radical, which reacts with pyrolytic vapour [103, 106]. The amount of aromatic hydrocarbons produced via catalytic pyrolysis is much lower than via catalytic hydropyrolysis [107].

Table 2.2. Operation conditions for bio-oil production via pyrolysis.

Pyrolysis type	Residential time	Heating rate (°C/s)	Temperature (°C)	Bio-oil yield (wt. %)	Ref.
Slow	5-30 min	< 0.8	600	30-40	[108]
Fast	< 5sec	> 10^4	500-800	50-60	[109]
Flash	< 2 sec	10^3-10^4	650-1000	65-70	[109, 110]
Vacuum	5-35 sec	10-20	350-520	35-50	[111]
Hydropyrolysis	< 10 sec	10-50	< 500	70	[107]

2.3.2.2 Pyrolysis process parameters

The pyrolysis processing parameters affect the composition and yield of the desirable products. The main processing parameters include the heating rate, temperature, gas flow rate, reactor design, and particle size [112]. Any of the three pyrolysis products, such as bio-oil, biogas, or biochar can be improved by optimizing pyrolysis conditions [113-117]. The impact of operational conditions on the quality and yield of the pyrolysis products is summarized in the next paragraphs.

Temperature plays a predominant role in the degradation of high molecular weight components of biomass into smaller molecular fragments. Partial degradation of the biomass structure at the molecular level occurs at a temperature below 300°C that produces heavy residual tar. In contrast, large molecular weight biomass degradation occurs at a temperature higher than 550°C, enhancing the composition of bio-oil [118]. Some studies suggest that the temperature to achieve the highest bio-oil yield is 450–550°C. However, optimum processing temperature to maximise bio-oil yield depends on biomass composition and pyrolysis conditions such as heating rate and gas flow rate [114, 119, 120]. Ji-lu et al. [121] con- ducted rice husk pyrolysis in a fluidized bed at a temperature between 420 and 540°C, and obtained a maximum bio-oil yield of 56 wt.% at 465°C. This study demonstrated that a further increase of the pyrolysis temperature decreased bio-oil yield to 45 wt.%.

Biomass particle size affects mass and heat transfer rates during pyrolysis, which have an impact on bio-oil yield. The bio-oil yield is usually higher for biomass particles with a size lower than 2 mm [122]. Small biomass particles enhance the biomass decomposition rate due to a better and faster mass and heat transfer rates [123]. The fast decomposition of small particles favours high bio-oil yields, however the larger particles cause slow decomposition and favour the production of char [124]. Biomass particles lower than 0.6 mm reduce bio-oil yield due to quick decomposition and participation in secondary reactions leading to an increase in biogas yield [125]. The mass and heat transfer rates are also depending on the types of reactors used in the pyrolysis process.

Many reactor types such as, fixed bed, fluidized bed, rotative, vacuum, plasma, and microwave have been used for pyrolysis. Fluidized bed reactor (bubbling) is frequently used to achieve high heating transfer rates (uniform temperature distribution) resulting in a high bio-oil yield of 70–75% [108]. However, it requires small biomass particles and is difficult to remove the biochar. Microwave reactor is another option that is mainly used due to high heating rates, high temperatures and short residence times resulting in a bio-oil yield of 60–70% [126]. However, the high processing costs, high power consumption and the need to use microwave absorbers limit its application. Several researchers used plasma reactor for biomass pyrolysis, but despite of its high operating costs, high energy and small biomass particles requirements, the bio-oil yield was still low between 30 and 40% [127].

Pyrolysis process produces a significant amount of vapour during biomass conversion, which can promote side reactions, giving rise to thermal cracking, repolymerization, and recondensation into biochar, resulting in a reduction of bio-oil production [99, 128]. Nitrogen gas is preferably used to remove vapours from the pyrolysis reactor because is chemically stable, inexpensive, and abundant. Increasing the nitrogen gas flow rate reduces the residence time of vapour in the pyrolysis reactor [124]. Choi.et.al. [129] showed that an increase in nitrogen flow rate increased the non-condensable gas percentage, from 22.2 to 31.9%. The increased nitrogen flow rate enhanced the vigorous bubbling motion and improved both mixing and heat transfer rates. For example, Mohamed. A.R. et al. [130] showed that an increase of nitrogen gas flow rate from 150 ml/min to 500 ml/min, in empty fruit bunch pyrolysis fluidized the bed reactor decreased bio-oil yield from 45.7 to 37.8%. However, the non-condensable gas percentage increased from 28.4 to 35.1%.

Heating rate is also another key pyrolysis variable that influences the extent of degradation during pyrolysis. The abundance of volatile matter during the degradation process increases with an increase of the heating rate due to the endothermic decomposition of feedstock [131]. An increase of the heating rate also impacts on the optimal pyrolysis for bio-oil production. For example, Debdoubi et al. [132] conducted pyrolysis of esparto by varying the pyrolysis temperatures from 400 to 700°C and using different heating rates of 50°C/min, 150°C/min, and 250°C/min. The researchers found the optimum heating rate for 57% of bio-oil yield was 150°C/min at 500°C. However, higher bio-oil yield was achieved for a heating rate of 250°C/min at 550°C. In general, a comprehensive ANOVA analysis of all parameters is necessary to optimize the pyrolysis process to obtain high bio-oil quality and yield.

2.3.3 Bio-oil from pyrolysis: composition and properties

Bio-oil is a dark brown colour liquid that can be used for power generation or extraction of various chemicals. Huber et al. [133] stated that typical pyrolysis bio-oil contains acids (propionic and acetic), alcohols (ethanol, methanol and ethylene glycol), phenols, aldehydes (acetaldehyde, formaldehyde and ethanediol), ketones, aromatics and furans, regardless of the type of feedstock. Table 2.1 presents the major chemical groups present in bio-oil for different biomass feedstock processed via pyrolysis.

Biomass with higher lignin content gives a higher bio-oil yield. Coffee husk pyrolysis at higher temperatures produces bio-oil with low molecular weight compounds of ketones, acids, and aromatic hydrocarbons [134]. Bio-oil obtained from herbaceous crops, for example Para grass and Arundo donax, contains a high amount of phenolic and high molecular weight aromatic compounds, making this feedstock desirable for phenol extraction. However, bio-oil produced from the pyrolysis process exhibits high viscosity, is corrosive, and thermally unstable. These properties make bio-oil undesirable for the synthesis of fuel and chemicals [135].

Table 2.3. Physical characteristics of bio-oil and crude oil [139-142].

Physical property	Bio-oil	Crude oil
Moisture content (wt %)	15-30	0.1
Ash (wt %)	0-0.2	0.1
C (wt %)	54-58	83-87
O (wt %)	35-40	<1
H (wt %)	5.5-7.0	11-14
N (wt %)	0-0.2	0.1
S (wt %)	0.05	4
HHV (MJ/Kg)	17-20	40-44

Different physicochemical properties of bio-oil produced via biomass pyrolysis and typical crude oil properties are summarized in Table 2.3. The concentration of elemental oxygen and moisture content in bio-oil are much higher than in crude oil which explain the low heating value of bio-oil. Several studies have reported that the quality of bio-oil is affected by physicochemical properties, such as pH, elemental composition, oxygen content, char, suspended solid, and ash content [136-138].

Kinematic viscosity of bio-oil ranges from 35 to 100 cP, which depends on the types of biomass and pyrolysis processing parameters. Bio-oil viscosity tends to increase over time during storage due to further chemical reactions between the bio-oil components [36]. Boucher et al. [143] reported the effect of adding a stabilizing agent (alcohol) on the viscosity of bio-oil. When bio-oil was stored in 10% methanol, the viscosity only increased from 20 to 22 cP over four months at 20°C. Similarly, 20% of ethanol showed a marginal increment, from 13 cP to 15 cP, on the viscosity of bio-oil at 40°C [144]. High viscosity of bio-oil causes incomplete combustion and poor atomisation during applications; however, adding organic solvents could enhance physicochemical properties and storage stability of bio-oil [145].

The presence of acetic and formic acids in the bio-oil increases acidity (pH <3). Reactive oxygenated compounds in bio-oil causes a change in viscosity, which alters thermal and storage stability [146]. Thereby these acids make the bio-oil corrosive and unsuitable for handling storage vessels and equipment [147]. Ash content in bio-oil arises from the different inorganic compounds such as sodium, magnesium, and potassium (predominantly) in the feedstock. Thangalazhy-Gopakumar et al. [148] reported that bio-oil synthesis from wood biomass showed 0.09 to 0.2% ash content. Moisture content in bio-oil results from dehydration reactions during pyrolysis and moisture in the feedstock [67]. In general, bio-oil can have 15–30% moisture content depending on the type of biomass [149]. Heo et al. [67] reported bio-oil with moisture content ranging from 40 to 60% obtained by pyrolysis of sawdust with 9.1% moisture content. The rise in bio-oil moisture content is due to esterification reactions taking place between bio-oil constituents.

The complexity of bio-oil composition limits its application as an alternative energy source. The separation of bio-oil fractions has been employed to improve the calorific value and recover valuable chemicals from bio-oil. Several methods such as solvent extraction, distillation, centrifugation, and column chromatography have been employed to recover and separate of bio-oil fractions [150, 151]. Amongst the bio-oil fractions, phenolic compounds are most suitable for various applications including pharmaceuticals, resin manufacturing, fine chemicals, and food processing [152]. Solvent extraction of phenolic compounds from bio-oil is mainly performed by hexane, chloroform dichloromethane, and toluene [151]. However, the requirement of large volumes of solvent makes the solvent extraction undesirable.

Direct application of bio-oil without upgrading is giving undesired results due to high oxygen content, high viscosity, thermal instability, and low calorific value. Bio-oil can be upgraded via different techniques such as hydrotreating, steam reforming, emulsification, and catalytic pyrolysis [153, 154]. Catalytic pyrolysis is a promising method for producing high-quality bio-oil, as it requires lower decomposition temperature, amount of energy and hydrogen cracking [155, 156]. By eliminating oxygenated compounds through the form of CO, CO2, and H2O, catalytic pyrolysis can improve the quality of bio-oil [157]. Thus, catalytic pyrolysis is a potential technique for producing bio-oil of superior quality.

2.4 Biomass catalytic pyrolysis and reaction mechanism

2.4.1 Catalytic pyrolysis

Catalysts play a critical role in promoting process efficiency, targeting specific reactions and reducing processing temperature and time. Catalysts affect chemical composition and distribution of pyrolysis products. Catalytic pyrolysis has shown potential for converting oxygenated compounds in bio-oil mixture and consequently enhancing bio-oil quality.

Catalysts have been used in the bio-oil upgrading process through various approaches [158, 159]. The process configuration of catalytic pyrolysis are grouped into in-situ and ex-situ modes, based on how pyrolytic vapour contacts with catalyst [160].

In-situ catalytic pyrolysis consists of mixing catalyst with biomass directly in the pyrolysis reactor [161]. For ex-situ, catalytic reaction occurs in a secondary independent reactor instead of the pyrolysis reactor [162]. Nevertheless, it is possible to convert oxygenated compounds effectively into hydrocarbons by either mode. However, during the in-situ process, the pyrolytic vapours could not react with substantial quantities of catalyst, which requires a higher biomass to catalyst ratio (i.e., 2:1) for adequate reaction [163]. Also, the optimum pyrolysis temperature is insufficient for in-situ upgrading, requiring a separate ex-situ reactor. Char formed during the in-situ catalytic pyrolysis can also lead to deactivation of the catalyst due to pores blockage [164]. The secondary reactor in ex-situ mode gives an advantage over in-situ mode such as, easy recovery of biochar without catalyst contamination and versatile temperature controls [165].

Synthesis of catalyst can be tailored to the final product requirements. Understanding the reaction mechanisms in the catalytic pyrolysis of bio-oil upgrading is fundamental. The mechanisms of catalyst pyrolysis depend on the reaction path- ways of the catalytic system and specific compositions of biomass. The complexity of biomass matrix, inadequate mass transfer phenomena, and immobilisation of catalysts challenge the understanding of the catalyst pyrolysis mechanisms [166].

The major reaction pathways during catalytic pyrolysis are deoxygenation, ketonisation, cracking, aldol condensation, and aromatization as present in equation (2.1-2.5) [167, 168]. Hydrodeoxygenation (HDO) is a promising route to enhance the quality of bio-oil by removing oxygenated compounds in the form of CO, CO_2, and H_2O in the presence of H_2 and catalyst [157]. The primary renewable fuel products from HDO include gasoline and diesel hydrocarbons. Various catalysts have been used during HDO including, noble metals, metal oxides, microporous (zeolites), and mesoporous.

$$\text{Hydrodeoxygenation}: \mathrm{R-OH+H_2 \rightarrow R-H+H_2O} \tag{2.1}$$

$$\text{Hydrocracking}: \mathrm{R_1-CH_2CH_2-R_2+H_2 \rightarrow R_1-CH_3+R_2-CH_3} \tag{2.2}$$

$$\text{Ketonization}: \mathrm{R_1-CO-OH+R_2-CO-OH \rightarrow R_1COR_2+CO2+H_2O} \tag{2.3}$$

$$\text{Aldol condensation}: \mathrm{R_1-CO-R_2 \rightarrow R_1-C_2H_2-CO-R_2+H_2O} \tag{2.4}$$

$$\text{Decarboxylation} : \mathrm{R - CO - OH \rightarrow R - H + CO_2} \qquad (2.5)$$

HDO has significant benefits, such as high effectiveness on removing oxygen atoms, low reaction temperatures, and pre- serves the number of carbons in the products [169]. Various types of reactions are taking place during the hydrodeoxygenation process, including hydrogenation, decarboxylation, hydrogenolysis, dehydration, and hydrocracking [170]. Apart from phenolic molecules, aromatic compounds like guaiacols and syringol are also hydrogenated into a wide range of products, including cycloketones, cycloalcohols, arenes, methanol, and cycloalkanes [171, 172].

Conversion of phenols via HDO, as shown in Figure 2.2, can be carried out through three different reaction paths: the first is the removal of oxygen by the cleavage of the C=O bond from the aromatic compound. Then cyclohexane and cyclohexene are formed after forming benzene in the presence of hydrogen. The second path is hydrogenation of phenol into cyclohexanol, followed by the removal of oxygen to produce cyclohexene and cyclohexane. The third path is the combination of both hydrodeoxygenation and hydrogenation to con- vert phenol compounds into cyclohexanone, which is immediately followed by hydrogenation to form cyclohexene, cyclohexanol, and cyclohexane [173, 174]. Eventually, all three paths lead to cyclohexane formation, which can also isomerize into methyl cyclopentane. The selection of one of the three paths to convert phenol into methyl cyclopentane depends on different parameters of catalysts such as metal composition, surface properties, reaction temperature, and required intermediate products.

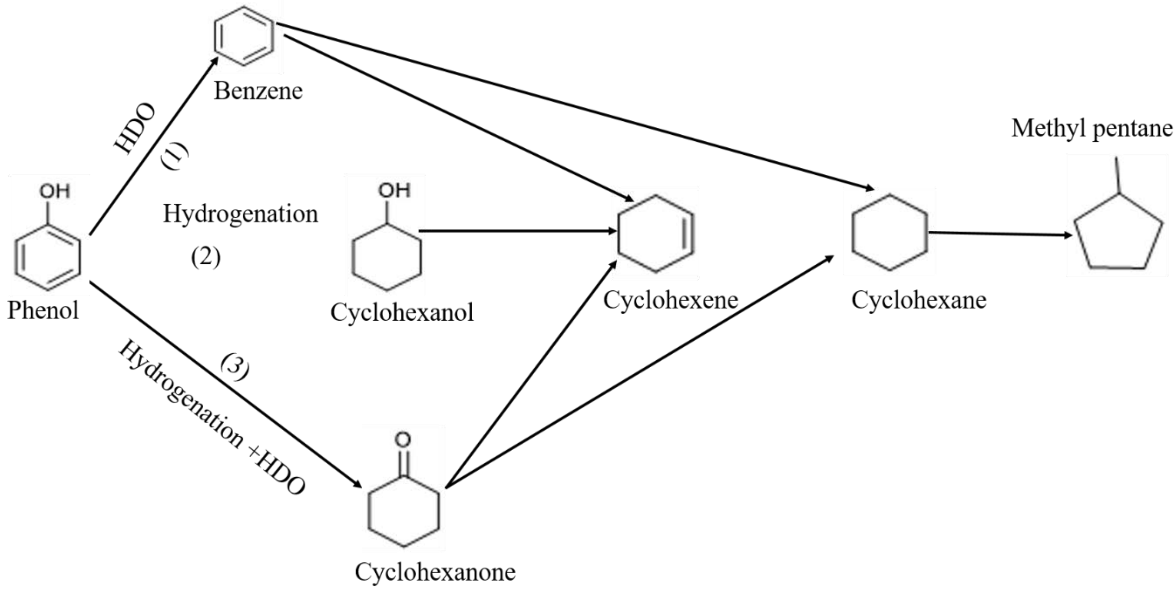

Figure 2.2. Reaction mechanism for phenols, adapted from [175].

2.4.2 Bio-oil quality: catalytic reactions and mechanisms

Zeolite catalysts have received much attention due to its relatively low cost, availability, and its potential to yield high quality bio-oil. Amongst zeolite catalysts, ZSM-5 (exhibiting high acidity and pore size) demonstrated excellent efficiency for bio-oil upgrading, producing less viscous, less acid, and high energy value bio-oil [176]. ZSM-5 also increased the concentration of aromatic hydrocarbons, organics, and gaseous compounds in bio-oil caused by aromatization, decarbonization, and cracking reactions [177, 178]. Zhang et al. [179] utilized ZSM-5 for ex-situ mode catalytic pyrolysis of corncobs using a fluidized bed reactor. The bio-oil obtained from the reactor showed a reduction of oxygenated compounds by 25% with a high heating value (HHV) of 34.6 MJ/kg, which is similar to heavy fuel oil and diesel values.

Many transition metals, such as cobalt, nickel, iron, cerium, and gallium, have been used to fine-tune ZSM-5 acidity to enhance bio-oil yields and decrease coke formation on catalysts [178, 180, 181]. Zeolite supports are frequently used to support metal-based catalysts because of the need to have metals and acidic sites to support the H_2 and O-containing compounds activations. Zeolite supports with high Lewis and Brønsted acid site density favour high dehydration reaction. Kumar et.al. [114] prepared metal-based catalysts over zeolite support catalysts (Cu/zeolite, Ni/zeolite, and Cu–Ni/ zeolite) to investigate their synergy effect on the deoxygenation reaction of pinewood. The authors found Cu–Ni/zeolite catalyst produced 34% of aliphatic hydrocarbons; however, monometallic combination favoured the production of aromatic hydrocarbons, Cu/zeolite: Ni/zeolite (1:1) generated 18.87% of aromatic hydrocarbons. Also, Cu/zeolite: Ni/zeolite (1:3) significantly reduced in comparison to noncatalytic pyrolysis, with 1.81% of acids, 6.42% of phenols, and 0.4% of ketones in the oxygenated compounds of bio-oil. Table 2.4 the key findings from modification of zeolites using transition metals and pyrolysis conditions. Selectivity and yield of catalysts depend on the catalyst to feedstock ratio, types, and percentage of metals. For example, incorporation of metals in the zeolite framework increases the production and composition of polycyclic aromatics while decreases bio-oil yield.

Table 2.4. Analysis of the impact of metal-ZSM-5 catalysts and pyrolysis condition on bio-oil production.

Catalyst	Pyrolysis conditions	Key findings	Ref.
Fe/ZSM-5	Feedstock: sawdust Catalyst / feedstock ratio = 1:3 Pyrolysis temperature = 400-800°C	Fe/ZSM-5 produces more monocyclic aromatic hydrocarbons than ZSM-5. The increase of Fe loading increased hydrocarbon content but reduced the bio-oil yield.	[182]
Ga-, Zn-, Co-, Ni/ZSM-5	Feedstock: Yunnan pine Catalyst / feedstock ratio = 1:2 Pyrolysis temperature = 450°C	M-ZSM-5 content reduces bio-oil yields and enhances the non-condensable gas amount. Zn/ZSM-5 contributes to the formation of single-ring aromatics, such as xylenes and toluene. Ga/ZSM-5 produced the maximum oil yields and the lowest amount of coke. However, Ni/ZSM-5 produce more polycyclic aromatic hydrocarbons and Co/ ZSM-5 shows high selectivity for indene production.	[183]
Co- and Ni/ZSM-5	Feedstock: Beech wood Catalyst / feedstock ratio = 3/2.85 Pyrolysis temperature = 500°C	Reduced metallic Ni and Co formed during pyrolysis, which favoured hydrogen transfer reactions. The bio-oil was rich in phenols and aromatic compounds. NiO/ZSM-5 was more reactive than Co_3O_4/ZSM-5 in increasing the gaseous products and reducing the organic phase.	[184]

Zn-,Co,- Ni-, Fe/ZSM-5	Feedstock: Wheat straw and polystyrene Catalyst / feedstock ratio = 1:1 Pyrolysis temperature = 500-650°C	Maximum bio-oil yield obtained by Co-ZSM-5(39.0%) followed by Zn-ZSM-5 (38.2%), Fe-ZSM-5 (37.7%) and Ni-ZSM-5 (36.1%). Fe-ZSM-5 show much better performance with monocyclic aromatic hydrocarbons (83.3%) and organochlorines (0.5%).	[185]

*All catalysts were prepared by the wet impregnation method.

Metal catalyst activates hydrogenation of C–O, or C=O to produce polycyclic aromatic hydrocarbons. Noble metal catalysts show better hydrogenation performance due to its stability and selectivity [186]. Metal electronic configuration and band structure also contribute to high hydrogenation performance. The binding capacity of substrate to metal catalyst surface depends on the availability of d orbital in *spd* hybrid bonding orbit. Therefore the higher d orbital percentage of noble metal the stronger interaction between substrate and catalyst [187]. The overall reaction pathways, advantages, and disadvantages of the use of metal-based catalysts in bio-oil production are summarized in Table 2.5.

The addition of electron donor groups, such as metal oxides, can enhance the abundance of redox sites leading to an increase in catalytic activity. Of the various metal oxides, strontium oxide is particularly remarkable for its ability to enhance the Lewis alkaline sites in the zeolite framework, imparting basicity. Strontium oxide catalysts have been employed in various reactions, including oxidative coupling of methane, nitroaldol reactions, ketonisation, and aldol condensation. These reactions facilitate the deoxygenation of bio-oil and foster the production of aromatic compounds. Strontium oxide-based catalysts exhibit several chemical properties that make them effective in catalytic reactions. One of the key properties of these catalysts is their basicity, which allows them to act as a base in various chemical reactions. The basicity of these catalysts facilitates the breaking of chemical bonds and accelerates the reaction rates. In addition to basicity, strontium oxide-based catalysts can also exhibit Lewis acidity, which helps in the activation of reactant molecules by accepting electron pairs. The Lewis acidity of these catalysts can also promote selectivity in certain reactions. Strontium oxide-based catalysts can participate in redox reactions, which involve the transfer of electrons between reactants. The redox properties of these catalysts can facilitate the formation of desired products while reducing the formation of unwanted by-products. Finally, the stability of strontium oxide-based catalysts is an important chemical property that determines their lifespan and effectiveness in catalytic reactions. These catalysts have good thermal stability, thus maintaining their catalytic activity even at high temperatures. In summary, strontium oxide-based catalysts exhibit basicity, Lewis acidity, redox properties, and thermal stability. These properties make them effective in facilitating various chemical reactions and promoting the formation of desired products. The chemical properties of these catalysts can be tailored to suit specific catalytic reactions and improve their effectiveness.

Metal oxides are also viable for deoxygenation of the pyrolysis vapour to form aromatic hydrocarbons. Metal oxides are widely used in biomass pyrolysis because of their higher degree of active sites during reaction [29]. Additionally, they are highly temperature-stable and resistant against relatively nonpolar compounds under different pH conditions [121, 188]. Kaewpengkrow, et. al [189] upgraded fast pyrolysis vapours from Jatropha curcas waste residue produced at 600°C using metal oxide/activated carbon catalysts prepared by wet impregnation. These metal oxide/activated carbon catalysts promoted aromatics formation and produced 86.56% hydrocarbon yield, considerably higher than 11.32% yield without catalysts.

The small size of micropores in the zeolite structure hinders the mass transfer of reactant and formation of polycyclic aromatic hydrocarbons [190]. Therefore to overcome this problem, hierarchically structured zeolites have been developed [191]. Hierarchical zeolites are vastly utilized in biomass catalysis because of their high surface area, better mass transfer, high selectivity, and yield [192]. As shown in Table 2.6 hierarchical structure of zeolites can be achieved by creating zeolite materials with multiple porosity levels, i.e., mesoporous and microporous structures. Mesoporosity on zeolite materials is obtained by alkaline treatment (to remove Si atom) and acid treatment (to remove Al atom). The dealumination process increases the Si/Al ratio and enhances the formation of mesoporosity in the zeolite framework [193, 194]. Desilication of zeolites provides a well-controlled mesoporous formation with an optimal Si/Al ratio between 25 and 50 [195].

Table 2.5. Summary of reaction mechanisms and main process challenges for metal-based catalysts.

Metal	Reaction mechanisms	Process challenge	Ref.
Pt	Hydrodeoxygenation, dehydration, and hydrogenation are predominant reaction pathways. High hydrogenation activity for converting oxygenated compounds in the bio-oil into aromatic ring compounds. Interims of hydrogenation reactions: Pt > Pd > Ni > Cu>Zn.	Catalytic deactivation of a catalyst via fouling and coke formation. Expensive and requires extensive optimisation of metal to acid sites ratio.	[196, 197]
Cu	Hydrodeoxygenation, hydrogenolysis, decarbonylation, decarboxylation, dehydrogenation, and hydrogenation are the dominant reaction pathways. Loading of porous catalysts with copper enhances micropores formation. Increase in copper crystalline size decreases hydrogenation activity.	The high concentration of Cu (10 wt. % Cu) causes aggregation on the surface of the catalyst support.	[198, 199]
Zn	Favours C-H bond cleavage rather than C-C bond, which increases the selectivity of a partially deoxygenated product. Inexpensive and has excellent reducing properties for homogeneous organic synthesis.	High probability of catalyst sintering at high temperatures.	[200, 201]
Ni	Decarboxylation, hydrodeoxygenation decarbonylation, dehydrogenation, and hydrogenation are reaction pathways. Favours the production of short-chain hydrocarbon at elevated temperatures and high hydrogenation activity.	Lower electrophilicity, which makes difficult to degrade C-O and C-C bonds.	[202, 203]
Fe	Hydrodeoxygenation is the reaction pathway.	Inactive for hydrogenation of the aromatic ring. Prone to catalyst poisoning due to its oxidation tendency.	[204]

Table 2.6. Properties of hierarchical zeolites used on catalytic pyrolysis.

Biomass	Zeolite	Si/Al ratio	Metal loading %	Mesoscale template	S_{BET} (m^2/g)	V_{total} (cm^3/g)	V_{micro} (cm^3/g)	V_{meso} (cm^3/g)	Aromatic conversion %	Ref.
Beechwood	ZSM-5	25.5	-	-	406	0.222	0.164	0.164	23.7	[205]
	ZSM-5	25.5	-	0.1M NaOH	400	0.222	0.158	0.158	26.9	
	ZSM-5	21.6	-	0.4M NaOH	285	0.293	0.126	0.167	28.6	
Waste cardboard	HZSM-5	50	-	-	332	0.153	0.132	0.021	24.43	[206]
	HZSM-5		-	0.3M NaOH	308	0.188	0.127	0.061	28.48	
	HZSM-5		-	0.7M NaOH	274	0.193	0.120	0.073	30.54	
Pinewood	ZSM-5	15	-	-	438	0.29	0.16	0.13	13.1	[207]
	ZSM-5	25	-	-	421	0.27	0.15	0.12	17.4	
	ZSM-5	40	-	-	481	0.28	0.18	0.1	14.8	
	ZSM-5-04M	15	-	0.4 NaOH	418	0.42	0.15	0.27	15	
	ZSM-5-0.2M	25	-	0.2 NaOH	480	0.52	0.13	0.39	20.5	
	ZSM-5-0.2M	40	-	0.2 NaOH	506	0.66	0.11	0.50	22.3	
	HZSM-5	56	-	-	325	0.21	0.104	0.101	49.8 [a]	[208]

Palm kernel shell (PKS	Meso-HZSM-5	40.3	-	NaOH	321	0.25	0.098	0.152	32.6 [a]	
	Ga(1)/meso-HZSM-5	40.8	0.95	NaOH	317	0.23	0.083	0.132	35.8 [a]	
	Ga(5)/meso-HZSM-5	40.5	4.55	NaOH	300	0.21	0.079	0.127	39.2 [a]	
Oak Wood	H-ZSM-5				384	0.237	0.117	0.12		[195]
	Co/H-ZSM-5		4.3		377	0.225	0.114	0.111		
	Ds-HZSM-5			NaOH	405	0.253	0.115	0.138		
	Co/Ds-HZSM-5		4.1		397	0.243	0.116	0.127		

a: Bio-oil yield %

A wide variety of mesoporous silica has also been used for bio-oil upgrading such as MCM-41 (Mesoporous molecular sieve) and SBA (Santa Barbara Amorphous). MCM-14 exhibits a high surface area (1000 m^2/g), narrow pore size distribution (20–30 Å), and a hexagonal arrangement [209]. However, due to weak acidity compared to aluminosilicate, MCM-14 is only applicable to a narrow range of processes. Acidic properties of mesoporous silica were enhanced by loading metals into the silica structure [30, 31]. Aluminium is the principal metal-doped into the structure of mesoporous silica to enhance catalytic cracking [210]. For instance, by optimizing the Al/Si ratio, the new mesoporous alumina–silica catalyst is created with high acid properties and high surface area. Similarly, different metals including Co, Sn, and Zr are used to prepare high-performing mesoporous silica catalysts [211].

Jeon et.al. [212] studied the application of mesoporous Pt and Al within SBA-15 support catalysts for catalytic pyrolysis of cellulose, hemicellulose, and lignin. AlSBA-15 and Pt/AlSBA-15 showed better catalytic performance than SBA- 15 and Pt/SBA-15. In particular, Pt/AlSBA-15 showed a high yield (65 wt. %) for aromatic and furans. The presence of both acid sites and Pt are responsible for the conversion of levoglucosan into aromatics and furans during catalytic upgrading. Pd/SBA-15 revealed a better selectivity for the production of phenol from lignin-derived oligomers [213]. As show in Figure 2.3, the lignin depolymerized into monomeric phenols that were further converted to phenols without the side chain and unsaturated C-C bond [214, 215]. The incorporation of acidity or alkalinity in the structure of mesoporous silica is likewise a promising methodology to duplicate its applications in catalysis [216]. The pore volume of mesoporous silica gives sufficient space to accommodate these species [217]. Table 2.7 presents a concise conclusion for the advantages and disadvantages of using mesoporous catalysts for bio-oil synthesis.

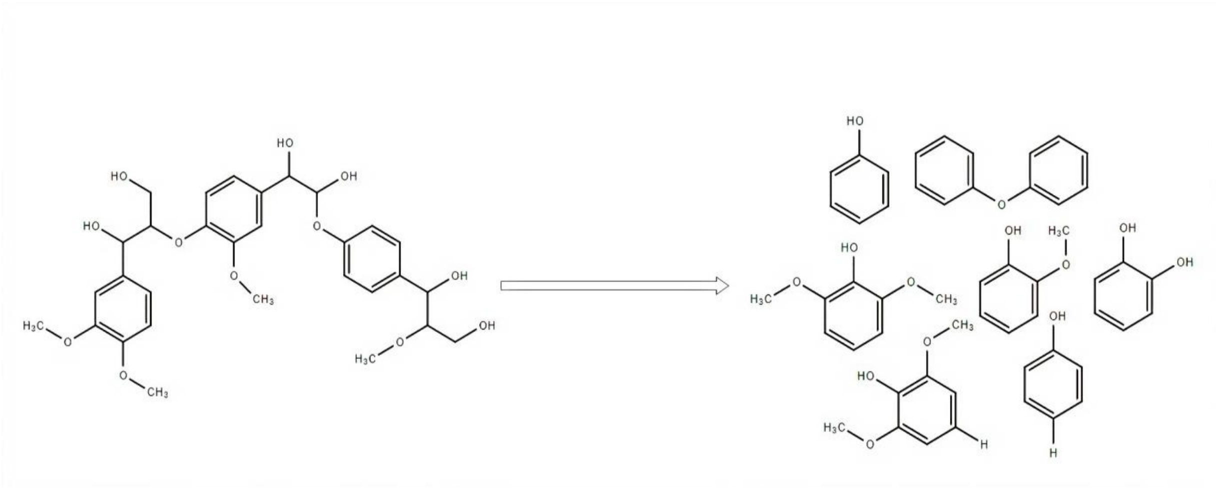

Figure 2.3. Reaction mechanism of lignin depolymerization for phenolic monomers production.

Table 2.7. Main advantages and disadvantages of using mesoporous catalysts for bio-oil production.

Catalyst	Advantages	Disadvantages	Ref.
SBA-15	High thermal and hydrothermal stability.	Limited mesoporous formation.	[213, 218]
Pt/SBA-15	High yields for aromatic and furans compounds synthesis.	Lower dispersion of Pt inside SBA-15.	[219, 220]
MCM-41	Better mass transfer for large molecules.	Low catalytic degradation. Low thermal stability and acidity.	[216]
Al/MCM-41	Higher Al content leads to high aromatic compound yields. Conversion of poly-aromatic hydrocarbon (PAHs) into phenol.	High coke formation.	[221]
Al/MCM-48	High selectivity towards phenol production and higher stability than Al/MCM-41.	Low acid strength.	[222]
MSU-S	Strong acid sites and high selectivity towards high fraction and poly-aromatic hydrocarbon.	High coke formation and a low organic phase. No production of alcohols, acids, and carbonyl compounds.	[223]

Biomass waste (sawdust) was also used to produce a highly efficient magnetic solid-acid catalyst through fast pyrolysis-sulphonation process [224]. First, the Fe^{3+} ions were adsorbed into the biomass waste to achieve Fe-loaded biomass, then pyrolysis to produce biochar. Finally, solid-acid magnetic porous catalyst was prepared via sulfonation method from the biochar. The fast pyrolysis method induced reduction of Fe^{3+} to Fe_3O_4 and incorporated magnetism into the material, which was kept after sulfonation. The catalyst exhibits a surface area of 296.4 m^2/g and acidity of 2.57 mmol/g. The catalyst had notable catalytic activity, including dehydration, esterification, and hydrolysis for distinct acid catalytic reactions. A furfural yield of 6% in dimethyl sulfoxide (DMSO) was obtained at 150°C with a xylose conversion of 96%. The sulfonated catalyst was less active, producing only 45% furfural under the same conditions, due to its lower acidity of 1.26 mmol/g than the iron catalyst. The catalyst was also extremely efficient in producing 94% glucose and fructose [224].

2.5 Advanced analytical technique for bio-oil characterization

Evaluating bio-oil chemical and physical characteristics is a significant process to decide future applications as well as upgrading techniques to improve the composition. Bio-oil physical characteristics, such as viscosity, pH, ash content, moisture content, cetane index, refractive index, heating values, and elemental composition, can be performed accurately by the existing standards procedure. However, qualitative and quantitative analysis of chemical properties remains challenging. The complexity and number of compounds in bio-oil require multiple analytical methods for its chemical characterisation. Therefore, the spectroscopic and chromatographic techniques are implemented and interpreted as complementary. Nuclear magnetic resonance (NMR), thermogravimetric analysis (TGA), gel permeation chromatography (GPC), gas chromatography (GC), and Fourier-transform infrared spectroscopy (FTIR) have been used to elucidate the chemical characteristics of bio-oils at distinct levels [225]. Amongst the analytical technique, NMR spectroscopy and GC are the most comprehensive techniques to characterise bio-oil components. The next section will discuss the application of NMR, GC, and TGA for bio-oil chemical analysis.

2.5.1 Gas chromatography

Gas chromatography (GC) is a widely used separation method to identify thermally stable volatile compounds. The flame ionisation detector (FID) and thermal conductivity detector (TCD) have been used for GC detector because of highly sensitive, rapid response, and a wide range of linear dynamics. GC-FID can be used for bio-oil composition characterisation such as phenols, aldehydes, alcohols, organic acids, sugars, and ketones [226]. Additionally, GC-FID has been used for estimation of the concentrations of compounds in biochar from the non-condensate stream during pyrolysis [227]. Bio-oil samples are usually separated by a conventional 1-D GC with a non-polar column or a weak-polar column depending on the boiling point or vapour pressure [228-230].

2.5.1.1 Conventional gas chromatography (1-D GC)

Conventional 1-D GC techniques employed in bio-oil characterization are based on bio-oil compounds boiling point and volatility [231, 232]. Also, the type of detector, polarity difference between the molecules and their interaction with column material are an important consideration. Types of solvent used during sample preparation should not affect the early eluting of bio-oil fractions. However, most solvents except acetone hinder separation, such as chloroform, tetrahydrofuran, and ethyl acetate elute along with low molecular weight fraction of bio-oil [233]. Co-elutions of solvent and bio-oil fractions hinder absolute quantification while using FID and TCD. Therefore, combining GC with mass spectrometry (GC- MS) will help to accurately identify peaks, which are not detected by FID such as alkanes, C5–C15 hydrocarbon, 2- methoxy and phenols [234].

1-D GC mostly used non-polar or slightly polar column for boil-oil characterization, which oversight polar fraction [229, 230]. Therefore, it is required additional GC columns to quantify both nonpolar and polar compounds. 1-D GC identifies a small portion of high molecular weight or non-volatile polar fractions of bio-oil due to the low volatility nature of the components [235, 236]. Derivatization enhances the detectability of non-volatile polar fractions by converting into volatile low polarity derivatives using derivatization reagent [237]. Siylation and *N*-methyl *N*-(trimethylsilyl) trifluoroacetamide are among mostly used derivatization agent for quantification of hydroxyl and carboxyl groups compounds [238].

2.5.1.2 Two-dimensional gas chromatography (2-D GC)

2-D GC (GC x GC) analytical technique employs two independent columns with different polarity for GC separation, superior peak detection and resolution [239]. Bio-oil analysis conducted by 2-D GC identified 70% of chromatograph; however, 1-D GC only identified about 47 % [233]. Quantification of bio-oil components with 2-D GC depends on the type of columns and the modulator. Typically, the first column is nonpolar or slightly polar, while the second column is polar [240]. Bio-oil fractions are separated by their volatility in the first column, while the second column separates via hydrogen-bonding, π–π interactions, and steric effects [241]. The chromatographic resolution of 2-D GC technique can be improved by increasing resolution in the first column and optimise split-flow [242]. Analysing all bio-oil fractions using a single analytical is almost impossible, therefore there is a need to combine GC with other technique such as NMR to better understand the chemical and molecular weight properties of bio-oil samples. Gas chromatography is an effective technique to analysis volatile components in bio-oil; however, analysing higher molecular weight molecules of bio-oil is still a challenge.

2.5.2 Nuclear magnetic resonance (NMR) spectroscopy

NMR spectroscopy provides structural information of high molecular weight compounds in bio-oil. NMR is a powerful technique to analyse bio-oil functional groups such as aromatic, carbonyl, olefin, aliphatic, and methoxy/hydroxyl from the integration of appropriate chemical shift regions [243, 244]. The advantage of NMR over other spectroscopy are its simplicity, short analysis time and able to acquire information about bio-oil composition from a single spectrum [245]. Hydrogen (^{1}H) and carbon (^{13}C) NMR techniques are widely used to analysis the hydrogen-carbon framework of bio-oil. Accuracy and repeatability of NMR analysis depend on solvent, baseline compensation, selection of chemical-shift regions, and longitudinal relaxation [246]. Polar solvents are mainly used for analysis of bio-oil components such as furan, ketones, phenols, and organic acids. During sample preparation dried bio-oil is dissolved in polar deuterated solvents such as dimethylsulfoxide (DMSO-d_6), deuterated dichloromethane (DCM-d_2), deuterium oxide (D_2O), and ethanol-d_2. The hydrogen bond strength of polar solvent affects NMR analysis of bio-oil, solvents such as ethanol, dichloromethane, and water exhibit strong hydrogen bonding but DMSO-d_6 exhibits much less hydrogen proton shifts. Also, solvent signals such as $CDCl_3$ (^{13}C NMR 77.00 ppm and ^{1}H NMR 7.25 ppm) overlap with aromatic group chemical shift region and interfere with quantification of bio-oil fractions. Therefore, the use of DMSO-d_6 as solvent allows the collection of chemical structure information from both ^{13}C and ^{1}H NMR [229]. In the following section, the application of ^{1}H and ^{13}C NMR for bio-oil analysis with chemical shift assignments will be discussed.

2.5.2.1 ^{1}H NMR

^{1}H NMR is the most extensively and convenient spectrometric technique used to quantify the oxygenated compounds in bio-oil [247]. The abundance of hydrogen atom (major isotope^{1}H) in an organic compound makes ^{1}H NMR spectroscopy analysis sensitive to identifying bio-oil constituents. This technique is characterized by fast analysis and high sensitivity [248]. Table 2.8 summarizes the major chemical shifts of bio-oil components and the hydrogen percentage of bio-oil obtained from non-catalytic and ZSM-5 catalytic pyrolysis of pinewood. Bio-oil produced with ZSM-5 catalyst contained more hydrogen from ethers (3.0–4.2 ppm) than the non-catalyst pyrolysis bio-oil. The chemical shift range of 9.5–11.0 ppm is assigned to aldehydes and phenols while carboxylic acid proton is assigned to the range of 11.0–12.5 ppm. The spectral overlap of aldehydes and phenols in the region from 9.5 to 11.0 ppm made the quantification of phenols difficult because of low resolution and chemical shift overlaps of ^{1}H

NMR. Therefore, it is required to use several characterisation techniques simultaneously to obtain a full insight into bio-oil composition. However, the chemical shift of the hydrogen atom on alkanes and aromatic groups shows clear signals making ^{1}H NMR spectroscopy suitable for the analysis of aromatic ring rich bio-oil.

Table 2.8. ^{1}H NMR chemical shifts for common compounds presented in bio-oil and hydrogen percentage obtained from pine wood pyrolysis [229, 244, 249, 250].

Bio-oil component	Chemical Shift (ppm)	Hydrogen percentage	
		Conventional pyrolysis	Catalytic pyrolysis
Aliphatic hydrocarbon, alkane CH_2, CHβ	0.5-1.6	25.5	21.2
Acetic acid CH_3, CHα	1.8-3.0	28.6	32.6
Alcohol, ethers, water	3.0-4.2	13.7	14.9
Aliphatic-OH,	4.2-6.0	7.8	7.6
Aromatics-H, HC=C-	6.4-7.6	18.2	20.1
Formic acid, HCOOH	8.10	-	-
Glycolaldehyde	9.5	-	-
Aldehydes, phenols, -CHO, aromatic-OH	9.5-11.0	5.8	3.6
Carboxylic acid, COOH	11.0-12.5	0.2	0.1

H: Type of proton

^{1}H NMR spectroscopy can also explain the effect of biomass types in the overall chemical composition of bio-oil. Mullen et al. [244] used ^{1}H NMR to characterise bio-oil from different energy crops and categorised bio-oil composition based on the hydrogen atom percentage. ^{1}H NMR is an essential and sensitive technique for determining hydrogen distributions in bio-oil; however, chemical shift ranges are not well-known because of several overlaps. Therefore, to obtain distinguished chemical shift range, the ^{1}H NMR spectrum should complement additional NMR techniques such as ^{13}C NMR spectroscopy.

2.5.2.2 ^{13}C NMR

^{13}C provides a quantitative analysis of carbon atoms in the different functional groups, which can be used as complementary information for bio-oil characterisation [251]. The low natural abundance of ^{13}C atom makes ^{13}C NMR spectroscopy less sensitive, therefore it provides a better signal to noise ratio by accumulating large numbers of transient [252]. The ^{13}C NMR chemical shift of carbon atom from various compounds in bio-oil is summarized in Table 2.9. The region between 1-60 ppm corresponds to alkyl hydrocarbon, which enhance the energy content of bio-oil [242]. The region between 50 and 65 ppm provides information about hydroxyl or methoxy functional groups in bio-oil while the region from 65 to 105 ppm explains carbohydrate (levoglucosan) in bio-oil. ^{13}C NMR spectra between 150 and 215 ppm resonates with the presence of acid, ketones, esters, and aldehydes. ^{13}C NMR spectroscopy techniques provide valuable qualitative analysis; however, spectra overlap occur due to bio-oil complexity, limiting its application. Therefore, it is required to correlate both ^{13}C NMR and ^{1}H NMR spectra information to obtain a better insight into the overlapping regions.

Table 2.9. ^{13}C NMR chemical shift of bio-oil [229, 253].

Bio-oil component	Chemical shift (ppm)
Paraffinic, aliphatic hydrocarbon	1-38
Primary alkyl carbons	6-24
OCH3 groups, amino acids, sterols	41–60
Hydroxyl/methoxy	50-65
Carbohydrates (syringyl or guaiacyl carbons), aliphatic	65–105
Aromatic, sterols, N-heterocyclic	106–150
Phenols	151–170
Amide, CO2H, ester groups	171–190
Aldehyde, ketone	180-215

2.5.3 Thermal analysis

Thermal properties of bio-oil are studied using thermogravimetry (TGA) and its derivatives (DTG). TGA measures weight losses based on the volatility of molar fractions against the temperature or time at a specific heating rate. Thermal degradation takes place in three stages: the first stage corresponds to carbon dioxide, carbon monoxide, and water removal from the feedstock at a temperature less than 200°C; the primary degradation occurs in the second stage at a temperature between 460°C and 680°C; and the final stage of decomposition occurs at slow reaction rate at a temperature higher than 680°C [254].

TGA analysis helps on the characterisation of evaporation, combustion, and thermal degradation of bio-oil. Also, TGA analysis of biomass generates information about carbon, water, ash, cellulose, hemicellulose, and lignin content that can be used to enhance the quality and composition of bio-oil. The percentage of weight loss in a region during the thermal analysis of biomass provides information about the reactivity; for example, biomass containing high lignin content showed low reactivity resulting in high biochar production. TGA data is also used to optimize bio-oil yield by analysing the ash content in different biomass, where higher ash content corresponds to lower bio-oil yield [255]. TGA has further been used to determine the amount of coke deposited in porous catalysts such as zeolites. The formation of coke on internal and external surfaces of catalysts causes catalyst deactivation and reduces catalyst activity for bio-oil upgrading [256].

TGA analysis has frequently been used to determine chemical kinetic parameters such as a pre-exponential factor (A) and activation energy (E) using different modelling methods [257]. Modelling of chemical kinetics uses TGA analysis conducted via non-isothermal and isothermal with multiple and single heating rates [258, 259]. However, more than one reaction pathway is considered to study kinetic parameters of thermal decomposition of biomass [260, 261].

2.6 Conclusions

Biomass is a renewable source and potential fossil fuel replacement due to its availability, lower processing cost, higher conversion, and lower carbon emissions. Pyrolysis is an attractive and flexible process of converting biomass into bio-oil, which can be utilized for the production of energy and chemicals. However, bio-oil obtained from biomass pyrolysis process is not suitable for fossil fuel substitution due to the high amount of oxygenate compounds (i.e., phenols, ketones, aromatic hydrocarbons, sugars, alcohols). Therefore, there is a need to upgrade bio-oil properties by converting the oxygenated compounds into aromatic hydrocarbons. Catalysts have been used to upgrade bio-oil properties, but not all the desired properties of a fuel have been achieved yet. According to our literature review, most catalytic upgrading of bio-oil has been carried out via a mono-catalytic system (acid or base catalysts), which is unable to address all oxygenated compounds available in the bio-oil. Also, catalyst deactivation over coke deposition and sintering promotes lower catalytic activity. Future research should focus on synthesising robust bifunctional catalysts to address both acidic and alkaline bio-oil fractions.

In addition, hierarchical zeolites have been used to enhance the bio-oil quality. The sequential dealumination–desilication process is used to create additional mesoporosity in the zeolite framework. However, the optimum amount of mesoporosity for high-quality bio-oil is still unknown, so we recommend that future research should be focused on studying the effect of both mesoporosity and loading of metal oxides on bio-oil quality and yield. Analysing chemical composition of bio-oil is fundamental for the optimisation of the pyrolysis process and its application as alternative energy source. NMR spectroscopy and GC techniques are mainly used to obtain structural and molecular weight information. To obtain a comprehensive understanding of bio-oil molecular fractions, combining both analytical techniques is required. Further work should be carried out to better understand the impact of pyrolysis processing parameters on bio-oil composition using statistical techniques.

3 Probing the impact of catalyst synthesis conditions on the preparation of catalyst with high mesoporous surface and volume catalyst

Abstract

The objective of this research is to synthesise hierarchical strontium loaded Y-zeolite and study its application for ironbark (IB) and plastic waste (PW) co-pyrolysis. Commercial parent Y-zeolite (Si/Al=2.48) was modified via sequential dealumination-desilication using citric acid and NaOH. Further, strontium (8 wt. %) was loaded into the modified Y-zeolite via wet and dry impregnation methods. The prepared catalyst was characterized by N_2 adsorption-desorption isothermal, field emission scanning electron microscopy (FESEM) combined with energy dispersive x-ray spectroscopy (EDS), X-ray diffraction (XRD), Fourier-transform infrared spectroscopy (FTIR), and Thermogravimetric analyser (TGA). After dealumination (treatment using 0.1 M of citric acid), the external surface area and Si/Al ratio increased from 53.5 to 147.4 m^2/g and 2.48 to 5.36, respectively. However, the sequential desilication treatment reduced Si/Al ratio from 5.36 to 2.57. In addition, Y-zeolite enhanced the total aromatic percentage and reduced the acidic group in co-pyrolysis oil.

Keywords: Catalyst; Co-pyrolysis; Hierarchal zeolite; Plastic waste; Strontium; Wood biomass

This work has been published as: Tewodros Kassa Dada, Md Anwarul Islam, Arun K. Vuppaladadiyam, Elsa Antunes, Thermo-catalytic co-pyrolysis of ironbark sawdust and plastic waste over strontium loaded hierarchical Y-zeolite, Journal of Environmental Management, Volume 299, 2021,113610.

3.1 Introduction

Continuous increase in energy demand and growing environmental concerns mandated the global research community to identify an alternative energy resource to replace petroleum fuel resources [262]. Biomass is widely recognized as a renewable resource and energy production from biomass could alleviate the burden on fossil-based energy sources [263]. Different types of biomass such as agricultural residues, herbaceous crops, solid waste biomass and aquatic have been used as a renewable energy source to replace fossil fuel. Pyrolysis, liquefaction, and gasification have been widely used to convert biomass into fuel and chemicals [16, 17, 264]. Among the available thermochemical conversion pathways, pyrolysis is the most promising way to convert biomass into value added fuel. However, bio-oil obtained via pyrolysis exhibits undesirable properties such as low calorific value, high oxygen content, and thermal instability [265]. The quality of the bio-oil needs to be upgraded in order to make it suitable for engine applications [181], and co-pyrolysis of biomass with hydrogen enriched feedstocks can be considered as an approach to improve aromatic yield and selectivity in bio-oil [266, 267]. Several studies revealed that co-pyrolysis of plastics (e.g., polystyrene (PS), polypropylene (PP), and polyethylene (PE)) with biomass can improve the aromatic yield and selectivity [268, 269]. Considering plastic waste as a co-feedstock not only improves the quality of bio-oil, but at the same time could levy the burden on landfills. During co-pyrolysis process, the addition of plastics would increase hydrocarbon yield and reduce coke formation by suppressing the formation of long-chain hydrocarbons [270]. However, bio-oil produced via conventional co-pyrolysis is still not accepted as a replacement for fossil fuel due to the high nitrogen-containing compounds [271].

Catalytic co-pyrolysis of plastic and biomass has been extensively investigated with a primary focus on acid- and base-catalysts [272, 273]. Co-pyrolysis of biomass with plastic waste improves the calorific value of bio-oil [274]. Zhou et al. [275], stated that plastics with a high hydrogen content, greater than 14%, could donate hydrogen during co-pyrolysis with biomass, enhancing bio-oil yield and quality. By removing oxygenated fractions via decarboxylation, dehydration, and decarbonylation reactions, catalytic co-pyrolysis can result in an upgraded version of bio-oil [177, 178]. Catalytic co-pyrolysis using acid catalysts can enhance bio-oil quality via Diels–Alder reaction, which is expected to occur between biomass-derived furans and plastic-originated olefins [276]. The oxygenated compounds from biomass, such as acetic acids, levoglucosan, xylose, absorb hydrogen from olefins to facilitate aromatic formation [277]. Among those catalysts, zeolites have received much attention due to their relatively low cost and availability, and ease in tuning to suit different pore architecture [278-281]. Zeolites with strong Brønsted acidity sites promote aromatization reaction during co-pyrolysis and yield monocyclic aromatics hydrocarbon resulting in high-quality bio-oil [282, 283].

Zeolites consist of aluminosilicates and exhibit unique properties such as high surface area (i.e., Y-zeolite 970 m^2/g), acid-base properties, uniform microporosity, crystalline framework, and hydrothermal stability [284-286]. During catalytic pyrolysis, pyrolytic vapor reacts with the acid sites of zeolites to produce aromatic compounds and gas (CO_2 and CO) [287]. The hierarchical zeolites minimize steric and diffusion limitations during biomass conversion and allow bulky compounds to get converted into aromatic compounds. The hierarchical structure of zeolites can be achieved by creating zeolite materials with multiple porosity levels, i.e., mesoporous, and microporous. Mesoporous zeolites are usually regarded as hierarchical zeolites because of two-pore size distributions [288]. The hierarchy factor (HF) is used to quantify the extent of mesoporosity formation at the expense of microporous volume (Brønsted acidity) [289]. The hierarchy factor implies an increase in mesoporous area (S_{meso}) and a decrease in the microporous volume (V_{micro}) for hierarchical zeolites [290]. Therefore, zeolite materials with a high hierarchy factor ($HF > 0.1$) are expected to have beneficial catalytic properties [291].

Generally, mesoporosity is introduced into the zeolite framework through top-down (post-treatment) or bottom-up (direct synthesis) approaches [193, 194]. Bottom-up approaches use mesoporous-directing agents and processes such as exfoliation, templating (soft or hard templates), pillaring, and solid zeolitization to impart hierarchical structure [292]. Bottom-up approaches have the disadvantage of lacking control on mesoporosity formation leading to structural damage. However, post-synthesis modification mainly uses demetallation such as dealumination and desilication [293]. Post-synthetic modification has been widely applied due to its simplicity, less processing time and economic feasibility. Post-synthetic modification is generally employed to develop a hierarchical structure in lower Si/Al ratio zeolites (i.e., Y-zeolites) [294]. Chemical dealumination and desilication methods using acid and alkaline solutions, respectively, have been used to develop hierarchical structure in Y-zeolites (Si/Al=2.5-3.2). Verboekend et al. [295] performed sequential dealumination (ethylenediaminetetraacetic acid) and desilication (NaOH) on Y-zeolites (Si/Al=2.6) and obtained a high mesoporous surface area of 330 m^2/g with well-developed mesoporosity. However, the proposed process requires 72 h at 100°C. In addition, it is to be noted that post-treatment of Y-zeolites could decrease Lewis acidity and increase Brønsted acidity as compared to the parent zeolite [296, 297], which can lead to poor catalytic performance during biomass pyrolysis [298]. Incorporating electron donor groups such as metal oxides will enhance the presence of redox sites that could increase the catalytic activity. Among the metal oxides, strontium oxide imparts basicity to the zeolite framework by enhancing the Lewis alkaline sites [299]. Strontium oxide catalyst supports the oxidative coupling of methane, nitroaldol reactions, ketonisation and aldol condensation, which contribute to the deoxygenation of bio-oil and promote the formation of aromatic compounds [300, 301].

The presence of strong alkaline sites in catalysts favours high conversion of carboxylic acid via ketonisation reaction [7]. The basicity in catalysts can be associated with the adsorption energy: SrO (2.85 eV), > CaO (-2.05 eV) > MgO (-1.35 eV). Therefore, it is expected that the strong alkalinity of SrO can enhance bio-oil quality by converting low molecular weight acid fractions [302]. However, using alkaline catalyst (SrO) is not enough to convert the oxygenated fraction of bio-oil into aromatic compounds. Therefore, this study put forward a new idea by combining hierarchical Y-zeolites (acidic sites as support) loaded with SrO (alkaline sites). The new SrO/Y-zeolite catalyst showed lower activation energy for co-pyrolysis of ironbark (IB) and plastic waste (PW), and a higher aromatic percentage in the bio-oil. Optimisation of dealumination and desilication of Y-zeolite has been carried out using citric acid (0.05 M and 0.1 M) and NaOH (0.2 M, 0.4 M and 0.8 M), respectively. Moreover, wet and dry impregnation methods have been used to load strontium on the hierarchical Y-zeolite. The kinetic parameters were also studied using a thermogravimetric analyser. The catalyst with the lowest activation energy was further tested for bio-oil production and compared with non-catalytic co-pyrolysis of IB and PW. This current work can be considered as a baseline to select the optimised conditions for catalyst preparation in view of bio-oil upgradation using strontium loaded hierarchical Y-zeolites.

3.2 Materials and methods

3.2.1 Materials

Commercial Y-zeolite (Si/Al=2.65) was purchased from Sigma Aldrich (Ref.334413). Citric acid (99.5%) was used for acid treatment. Cetyl-trimethylammonium bromide (CTAB) and sodium hydroxide (NaOH) were used for the desilication process to induce substantial mesoporosity. Strontium nitrate ($Sr(NO_3)_2$) was also used to load strontium into the modified Y-zeolite.

3.2.2 Modification of Y-zeolite

Parent Y-zeolite was subjected to a sequential dealumination and desilication process to create a hierarchical structure. The modification of this method has been explained in the literature elsewhere [303]. Dealumination process (acid treatment) was conducted with two different concentrations of citric acid, 0.05 M (ATl) and 0.1 M (AT2), with a solution/zeolite ratio of 30 ml/g. The mixture was magnetically stirred at 400 rpm while kept at 100ºC for 6 hours. After dealumination treatment, the resultant mixture was separated by centrifugation (7500 rpm,1 min at room temperature), washed with distilled water until reaching a pH between 7-8. The mixture was later dried for 12 h at 100ºC. All dried samples after dealumination were subsequently subjected to the desilication process (Figure 3.1).

The desilication process was carried out with different NaOH concentrations (0.2 M, 0.4 M, and 0.8 M) in the presence of CTAB. Firstly, 10 g of acid-treated Y-zeolite and 0.05 M CTAB were dissolved in 250 ml water and stirred at 400 rpm. Then NaOH was added and heated at 70ºC for 30 min. The solid modified Y-zeolite was recovered from the centrifuge (7500 rpm, 1 min) and washed with distilled water until reaching a pH of 7-8. The mixture was then dried overnight at 100ºC. The final product was calcined at 550ºC for 6 hours under atmospheric air with a heating rate of 10ºC/min.

3.2.3 Catalyst preparation

After sequential dealumination and desilication, strontium was loaded to the modified Y–zeolite via wet and dry impregnation methods (Figure 3.1). These two methods were used to examine the dispersion and loading percentage of strontium on the zeolite framework. For the wet impregnation method, strontium nitrate (8 wt. % Sr) was mixed with 5 g of modified Y-zeolite, then dissolved in 100 ml water at 400 rpm and heated at 80°C for 2 hours. Then the product was filtered and dried at 100ºC overnight, followed by calcination at 700°C for 6 hours under atmospheric air with a heating rate of 10°C/min. The calcination temperature was obtained from TGA/DSC analysis of $Sr(NO_3)_2$. During the dry impregnation method, strontium nitrate (8 wt. % Sr) and 5 g of modified Y- zeolite were dissolved in 30 ml water. The mixture was then placed in an ultrasonic bath (FinnSonic M3, Kemet) at 40 kHz for 2 h. The resultant mixture was left at room temperature for 22 h and subsequently dried at 100°C overnight. After drying, the material was calcined at 700°C for 6 h under atmospheric air with a heating rate of 10ºC/min. The prepared samples were labelled as SrD/W-ATn-mM, where D/W represents dry or wet impregnation, respectively, m represents NaOH concentration, and AT1 and AT2 are 0.05 M and 0.1 M concentrations of citric acid, respectively.

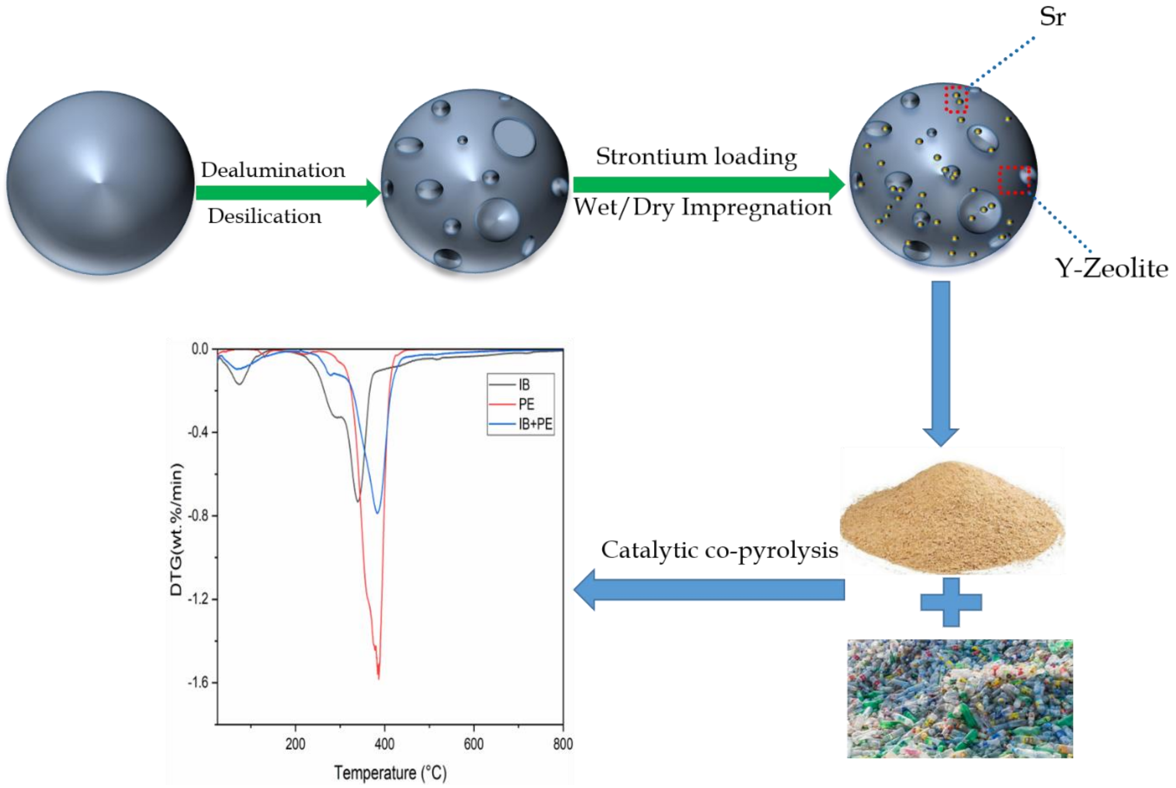

Figure 3.1. Schematic diagram of the main experimental steps used in this study, including catalyst preparation steps, co-pyrolysis and analysis of bio-oil.

3.2.4 Catalyst characterization

The N_2 adsorption-desorption was conducted at 77 K using an Autosorb iQ station 2 instruments. Before the adsorption, the catalysts were degassed at 200 °C for 19 h. The total surface area was obtained using the Brunauer-Emmett-Teller (BET) model. Moreover, the average mesoporous area and volume were determined using the adsorption Barrett-Joyner-Halenda (BJH) model. The mesoporous and microporous volume was calculated using the t-plot method. As shown in equation (3.1), the hierarchical factor (HF) was calculated as the ratio of volume fraction of microporous and the surface fraction of mesoporous [304].

$$\mathbf{HF} = \frac{\mathbf{V_{micro}}}{\mathbf{V_{total}}} \times \frac{\mathbf{S_{meso}}}{\mathbf{S_{total}}} \tag{3.1}$$

The catalyst thermal degradation and calcination temperature for catalyst preparation were examined using a thermogravimetric analyser (TA instrument, SD 600) under a nitrogen atmosphere. The samples were placed in an alumina crucible and heated from room temperature to 800°C at 10°C/min. During the thermal degradation studies, nitrogen gas at a flow rate of 50 ml/min was used to maintain an inert atmosphere within the system. Also, to determine the calcination temperature of $SrNO_3$, TGA analysis was conducted from room temperature to 800°C with 10°C/min under atmospheric air.

The morphology and chemical composition of parent and modified Y-zeolite were analysed using Field Emission Scanning Electron Microscopy (FESEM, SU5000, Hitachi) supported with Energy Dispersive X-ray Spectroscopy (EDS, X-Max, Oxford instrument). Before EDS mapping and monograph, all samples were coated with carbon and measured at Vac = 3.0 kV, EC = 115 K nA, WD = 7.5 mm. The amount of Si, Al, and Sr in the Y-zeolite was determined using the EDS mapping feature.

The crystalline phases in the catalysts were analysed using X-ray diffraction (XRD) with an X-ray diffractometer with a CU Kα source operated at 40 kV and 200 mA. Phases were identified using search-matching software (Eva 4.00) with 2-theta ranging from 20 to 70° with 0.05° steps and 1°/min speed.

The FTIR spectra of parent and strontium modified Y-zeolite were recorded by an IR 2 spectrometer supported with attenuated total reflection mode (ATR). The band range of 400–4000 cm^{-1} was used to record the spectra at a resolution of 8 cm^{-1} using a combined 64 scans.

3.2.5 Kinetics Study

The apparent kinetic parameters for the co-pyrolysis of ironbark (IB) and plastic waste (PW) with strontium loaded Y–zeolite were studied using TGA data. Before each run, ironbark and plastic waste powder were mixed with a mass ratio of 4:1. During the catalytic co-pyrolysis, the catalyst to feedstock ratio was set to be 1:4 based on previous literature [305]. The Coats-Redfern integral method is widely used as a single heating rate approach to estimate the non-isothermal kinetics parameters. Therefore, in this work, Coats-Redfern integral method was used to study the kinetics parameters. In general, the thermal decomposition of co-pyrolysis of IB and PW is expressed in equation (3.2).

$$\mathbf{\frac{dx}{dt} = Aexp\left(\frac{E}{RT}\right)(1 - x)} \tag{3.2}$$

Where *E* is the activation energy (kJ/mol), *A* is the pre-exponential factor (1/s), T is temperature (K), R represents universal gas constant (kJ/mol K), t represents time (s), and *x* is the weight loss fraction.

$$\mathbf{x} = \frac{\mathbf{W_o} - \mathbf{W_t}}{\mathbf{W_o} - \mathbf{W_f}} \tag{3.3}$$

Where W_0, W_t *and* W_f refer to the initial mass of the sample, the mass at time *t,* and final mass, respectively. Rearranging equations (3.2) and (3.3), we obtain equation (3.4).

$$\mathbf{ln}\left(\frac{\mathbf{g(x)}}{\mathbf{T^2}}\right) = \mathbf{ln}\left(\frac{\mathbf{AR}}{\boldsymbol{\beta}\mathbf{E}}\left(\mathbf{1} - \frac{\mathbf{2RT}}{\mathbf{E}}\right)\right) - \frac{\mathbf{E}}{\mathbf{RT}} \tag{3.4}$$

Where β is a heating rate, and $g(x)$ is a function for the reaction mechanism models. As shown in **Error! Reference source not found.**, eight reaction models were taken to express the reaction mechanism. The reaction models expression were adopted from previous work [306]. Considering $Y = \ln\left(\frac{g(x)}{T^2}\right)$ and $X = \frac{1}{\mathrm{T}}$ then equation (3.4) can be rewritten as follow.

$$\mathbf{Y} = \mathbf{ln}\left(\frac{\mathbf{AR}}{\boldsymbol{\beta}\mathbf{E}}\left(\mathbf{1} - \frac{\mathbf{2RT}}{\mathbf{E}}\right)\right) - \frac{\mathbf{E}}{\mathbf{R}}\mathbf{X} \tag{3.5}$$

Table 3.1. Reaction models and its functions.

S.No	Model name	Reaction mechanism	f(x)
1	Parabolic law	One-dimensional diffusion, 1D	x^2
2	Va lensi equation	Two-dimensional diffusion, 2D	x+(1-x)ln(1-x)
3	Avrami-Erofeev equation	Nucleation and growth (n = 1)	-ln(1-x)
4	Avrami-Erofeev equation	Nucleation and growth (n = 2)	$[-\ln(1-x)]^{1/2}$
5	Avrami-Erofeev equation	Nucleation and growth (n = 3)	$[-\ln(1-x)]^{1/3}$
6	Chemical reaction	n = 1	$(1-x)^{-1}$
7	Chemical reaction	n = 2	$(1-x)^{-1}-1$
8	Chemical reaction	n = 3	$([(1-x)^{-2}-1]/2)$

3.2.6 Bio-oil collection and characterization

A fixed bed reactor equipped with two condensation systems was used to collect bio-oil obtained during the co-pyrolysis process. IB is a typical Australian hardwood and the sawdust used in this study was collected from a local furniture shop. PW sample was collected from the James Cook University mechanical workshop, basically the plastic waste sample used in this study is a residue from plastic machining activities. In-situ catalytic upgrading reactions are expected to occur as the feedstock and catalyst were mixed before the experiments at a ratio of 4:1. For bio-oil collection, the catalyst that improved the co-pyrolysis kinetics was considered. The IB and PW were mixed at a ratio of 4:1 before the co-pyrolysis process. A biomass sample, *ca.* 15 g weight, was heated from room temperature to 550ºC in an inert atmosphere using a heating rate of 10ºC/min. For all the experiments, nitrogen was used as carrier gas and the flow rate was maintained at 1000 ml/min. A graham condenser (8 mm I.D., 40 mm length) was used to condense the pyrolytic vapor into bio-oil.

^{13}C NMR AVANCE III HD 600 MHz NMR spectrometer (Bruker Inc) was used to characterize the composition of the collected bio-oil. Bio-oil samples (100 mg) were dissolved in 450 μL dimethyl sulfoxide-d6 (DMSO-d6). All NMR spectra were recorded at room temperature, at 90° pulse angle, inverse gated decoupling pulse sequence, pulse delay of 8 s, and 8000 scans.

3.3 Result and Discussion.

3.3.1 Catalyst characterization

3.3.1.1 N_2 adsorption-desorption

N_2 adsorption-desorption isothermal and textural properties of parent and Sr loaded Y-zeolite catalysts were investigated and are presented in

Table 3.2. The microporous parent Y-zeolite has low mesoporous surface area (53 m^2/g) and mesoporous volume (0.066 cm^3/g), and consequently limited Brønsted acidic sites for large hydrocarbon molecules [307]. The parent Y-zeolite shows type-I adsorption-desorption isotherms with a total surface area of 577 m^2/g and a microporous volume of 0.267 cm^3/g, indicating that parent zeolite is a microporous material [308]. However, after sequential dealumination and desilication treatments, all samples show a type-IV isotherm curve with a hysteresis loop for P/P_0 greater than 0.4, which confirms the existence of mesoporous in the zeolite framework.

Dealumination process was carried out with citric acid due to its ability to form organic ligands, low corrosiveness, and excellent pore formation [309]. High concentrations of citric acid (> 0.15 M) will remove higher amounts of aluminium, but the pores will plug in the zeolite leading to the formation of large pores [310]. Therefore, in this study, low concentrations of citric acid (0.05 M and 0.1 M) were used to optimise the dealumination process. Y-zeolite treated with 0.05 M of citric acid (AT1) is characterized by high mesoporous surface area and mesoporous volume as 113 m^2/g and 0.118 cm^3/g, respectively. Further increasing citric acid concentration to 0.1 M (AT2) increased the mesoporous surface area (147 m^2/g) and mesoporous volume (0.147 cm^3/g), which is in-line with literature [311]. According to Xing et al. [312], during dealumination process, citric acid can act as chelating agent to selectively remove extra-framework aluminium and contribute to the formation of mesoporosity in the zeolite framework. The Si/Al ratio results also support the increase in mesoporosity (

Table 3.2) due to the reduction of aluminium concentration in the zeolite.

Samples AT1 and AT2, were subsequently subjected to a desilication process with different NaOH concentrations in the presence of CTAB. Increasing NaOH concentration during the desilication process can cause a large hysteresis loop, which confirms the formation of mesoporosity and in-line with literature [313]. After the desilication process with 0.2 M NaOH, the mesoporous volume increased to 0.192 cm^3/g and 0.314 cm^3/g, for AT1 and AT2, respectively. According to Zhang et al. [303], sequential desilication process can enhance mesoporosity by removing the debris remaining in the zeolite framework resulted from dealumination treatment. The use of CTAB in desilication process provided stability to the zeolite framework by removing silicon atoms and restoring the microporosity [314]. However, it is to be noted that increasing NaOH concentration for sample AT1 (0.2 M-0.8 M) shows a decrease in mesoporous surface area from 219 m^2/g to 87 m^2/g and mesoporous volume from 0.192 cm^3/g to 0.134 cm^3/g. Similar trends were also observed for sample AT2 (0.2 M-0.8 M), with the highest mesoporous surface area (395 m^2/g) and mesoporous volume (0.314 cm^3/g) for sample AT2-0.2M. Correspondingly, microporous volume increased from 0.227 cm^3/g to 0.284 cm^3/g (AT1) and 0.147 cm^3/g to 0.271 cm^3/g (AT2). According to these results, further increasing NaOH concentration restored the microporosity at the expense of mesoporous volume.

Table 3.2. Physicochemical properties of parent and strontium modified Y-zeolite.

Sample	S_{BET} [a] (m^2/g)	S_{Meso} [b] (m^2/g)	V_{total} [c] (cm^3/g)	V_{micro} [b] (cm^3/g)	V_{meso} [d] (cm^3/g)	H-Index[e]
Y-Zeolite	577.20	53.50	0.333	0.267	0.066	0.0743
AT1	657.24	113.73	0.392	0.274	0.118	0.1209
AT2	639.78	147.36	0.402	0.255	0.147	0.1461
AT1-0.2M	685.07	219.21	0.419	0.227	0.192	0.1733
AT1-0.4M	649.90	87.27	0.434	0.291	0.143	0.0900
AT1-0.8M	646.97	87.84	0.418	0.284	0.134	0.0923
AT2-0.2M	680.75	395.70	0.461	0.147	0.314	0.1853
AT2-0.4M	661.41	358.02	0.495	0.134	0.361	0.1465
AT2-0.8M	627.17	103.40	0.498	0.271	0.227	0.0897
SrD-AT1-0.2M	603.40	183.66	0.383	0.205	0.178	0.1629
SrD-AT1-0.4M	581.45	74.96	0.411	0.262	0.149	0.0821
SrD-AT1-0.8M	602.92	74.03	0.393	0.269	0.124	0.0840
SrW-AT1-0.2M	619.34	156.41	0.409	0.240	0.169	0.1481
SrW-AT1-0.4M	584.56	89.05	0.401	0.251	0.15	0.0953
SrW-AT1-0.8M	598.25	63.16	0.391	0.278	0.113	0.0750
SrW-AT2-0.2M	573.64	379.70	0.401	0.074	0.327	0.1221
SrW-AT2-0.4M	524.63	225.60	0.434	0.155	0.279	0.1535
SrW-AT2-0.8M	547.02	88.56	0.453	0.231	0.222	0.0825
SrD-AT2-0.2M	549.97	275.82	0.407	0.142	0.265	0.1749

SrD-AT2-0.4M	502.37	247.65	0.419	0.115	0.304	0.1353
SrD-AT2-0.8M	534.72	67.642	0.459	0.242	0.217	0.0666

a: BET method; b: t-plot method; c: single point at P/P^o=0.99; d: V_{meso}= V_{total} -Vmicro; e: HF=V_{micro}/V_{total} *S_{meso}/S_{total}

Verboekend et al. [315] stated that realumination could occur during the desilication of Al-rich zeolites leading to an increase in the aluminium content in the external surface of Y-zeolite. These results agree with the Si/Al ratio analyses; the aluminium concentration increased from 8.7 % to 11.4% as the NaOH concentration increased from 0.2 to 0.8 M. The increase of aluminium concentration can be attributed to a simultaneous increase in microporous volume and a decrease in mesoporous volume for both AT1 and AT2, which hinders the availability of active sites during catalytic pyrolysis.

Wet and dry impregnation methods were used to load strontium in the Y-zeolite, and both methods showed similar results with alkaline treated samples. Both methods showed a decrease in mesoporous volume and mesoporous area with the loading of Sr ion into zeolite framework. Among all samples, wet impregnation samples, SrW-AT2-0.2M displayed a high external surface area (379.70 m^2/g) with HF of 0.1221, while dry impregnation samples, SrD-AT2-0.2M showed a better S_{meso} of 275.82 m^2/g and higher HF (0.1749). These results confirm that irrespective of strontium loading, a high concentration of citric acid (AT2) increased mesoporous area by increasing aluminium removal. Comparatively, strontium loading via dry impregnation caused less reduction in mesoporous volume than the conventional wet impregnation method, which might be due to a comparatively less amount of strontium dispersed into the zeolite. Based on the relative crystallinity results in

Table 3.2, the strontium loading via dry impregnation did not cause major destruction in the zeolite framework [303].

3.3.1.2 Chemical analysis

The Si/Al ratio and strontium (Sr) quantities were obtained from EDS analysis and are summarized in Table 3.3. Parent Y-zeolite shows a typical NaY-Zeolite Si/Al ratio of 2.48. However, during dealumination, H^+ ions from citric acid removed Al from the zeolite framework by forming a chelating compound, resulting in an increase in the Si/Al ratio to 4.38 and 5.36 for AT1 and AT2, respectively. An increase in the citric acid concentration reduced the amount of Al in the framework of Y-zeolite and increased the Si/Al ratio. During the desilication process, the Si/Al ratio decreased as the concentration of NaOH increased. The high concentration of NaOH for both samples AT1-0.8M and AT2-0.8M resulted in the low Si/Al ratio, which are 2.62 and 2.57, respectively. The reduction in Si/Al ratio indicates that the extraction of Si from the zeolite framework was effective with an increase of NaOH concentration. The removal of Si from the zeolite framework would enhance the availability of active sites for catalytic co-pyrolysis.

Moreover, strontium loading did not cause a significant change in the Si/Al ratio, following the same trend as in the case of desilicated samples. The strontium loading increased with the decrease in Si/Al ratio during wet and dry impregnation methods. The increase in Sr dispersion is possibly due to the higher basicity of desilicated Y-zeolites, which caused a drop in Si/Al ratio [316]. The interaction between the Sr^{2+} species and $[AlO_4]^-$ tetrahedra sites (the negatively charged oxygen sites) would be minimal with the decrease in Si/Al ratio during calcination. However, the actual loading (8 wt.%) was not achieved due to the large atomic radius of strontium to interact with zeolite framework and less active sites during impregnation. In general, wet impregnation method resulted in higher strontium loading with an average of 6.78%, while the dry impregnation method resulted in an average strontium loading of 5.33%.

Table 3.3. Relative crystallinity and Si/Al ratio of parent and strontium modified Y-zeolite.

Samples	Relative Crystallinity [a] (%)	Si/Al [b]	Sr %	
			Nominal loading	Actual loading
Y-Zeolite	100	2.48	-	-
AT1	78	4.38	-	-
AT2	75	5.36	-	-
AT1-0.2M	88	3.04	-	-
AT1-0.4M	88	2.74	-	-
AT1-0.8M	86	2.62	-	-
AT2-0.2M	78	3.67	-	-
AT2-0.4M	81	3.38	-	-
AT2-0.8M	84	2.57	-	-
SrD-AT1-0.2M	83	3.14	4.59	8

SrD-AT1-0.4M	85	2.75	5.82	8
SrD-AT1-0.8M	86	2.71	6.19	8
SrW-AT1-0.2M	84	2.89	8.11	8
SrW-AT1-0.4M	86	2.85	6.56	8
SrW-AT1-0.8M	86	2.71	7.08	8
SrW-AT2-0.2M	77	3.82	4.53	8
SrW-AT2-0.4M	79	3.12	6.25	8
SrW-AT2-0.8M	82	2.65	7.22	8
SrD-AT2-0.2M	78	3.58	5.14	8
SrD-AT2-0.4M	80	3.32	6.27	8
SrD-AT2-0.8M	83	2.57	7.10	8

a: Calculated based on XRD analysis; b: EDS analysis used to calculate Si/Al

3.3.1.3 XRD analysis

The XRD pattern of the parent, hierarchical, and strontium modified Y-zeolites displayed characteristic peaks of NaY-zeolite (JCPDS = 01-077-1551) at 2-Theta of 6.3°, 10.25°, 12.2°, 16°, 19.1°, 20.7°, 23.3°, 27.6°, 31.4°, 32°, and 34.8°. As shown in Figure 3.2 and Figure 3.3, the intensity of diffraction peaks decreased after sequential dealumination, desilication, and strontium loading. The relative crystallinity of all samples is summarized in Table 3.3. The relative crystallinity of parent Y-zeolite was 100%. However, AT1 and AT2 exhibited the lowest relative crystallinity of 78% and 75% after the dealumination process, respectively. This indicates that citric acid caused partial damage to the Y-zeolite crystalline framework [315]. The high concentration of citric acid (AT2) displayed slightly lower relative crystallinity than AT1 due to the higher removal of aluminium from the zeolite framework. The extraction of aluminium is also confirmed by Si/Al analyses in Table 3.3. However, unlike other mineral acids, citric acid dealumination does not cause significant destruction of the zeolite structure [309].

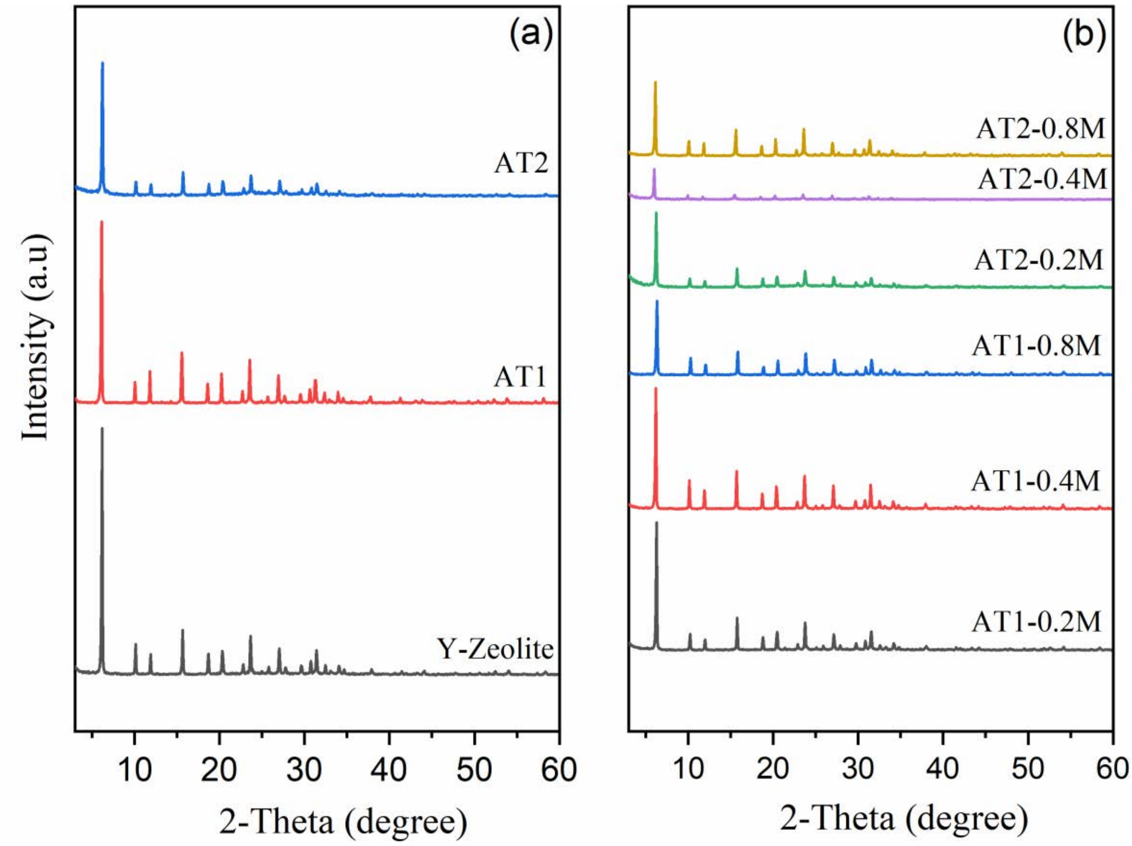

Figure 3.2. XRD characterization of modified Y-zeolite (a) dealumination treatment with acid 0.05M citric acid (AT1), 0.1M citric acid (AT2); (b) desilication treatment, using NaOH concentration of 0.2M, 0.4M and 0.8M.

After the sequential desilication process in the presence of CTAB, the relative crystallinity of Y-zeolite increased significantly compared to the dealumination samples, which can be explained by the removal of amorphous silicon and realumination process, causing alkaline-induced recrystallization [295]. The removal of non-framework silicon is confirmed with a decrease in Si/Al ratio. The relative crystallinity was not significantly impacted by increasing the concentration of NaOH during desilication of AT1 (0.2M-0.8M); which can be attributed to the low concentration of citric acid to chelate the aluminium. However, desilication of AT2 showed an increase in relative crystallinity during treatment with high concentrations of NaOH, showing a decrease in S_{meso} for treatments with high concentrations of NaOH. Creating mesoporosity on zeolite framework may cause a slight damage to the zeolite structure, resulting in a reduction in relative crystallinity.

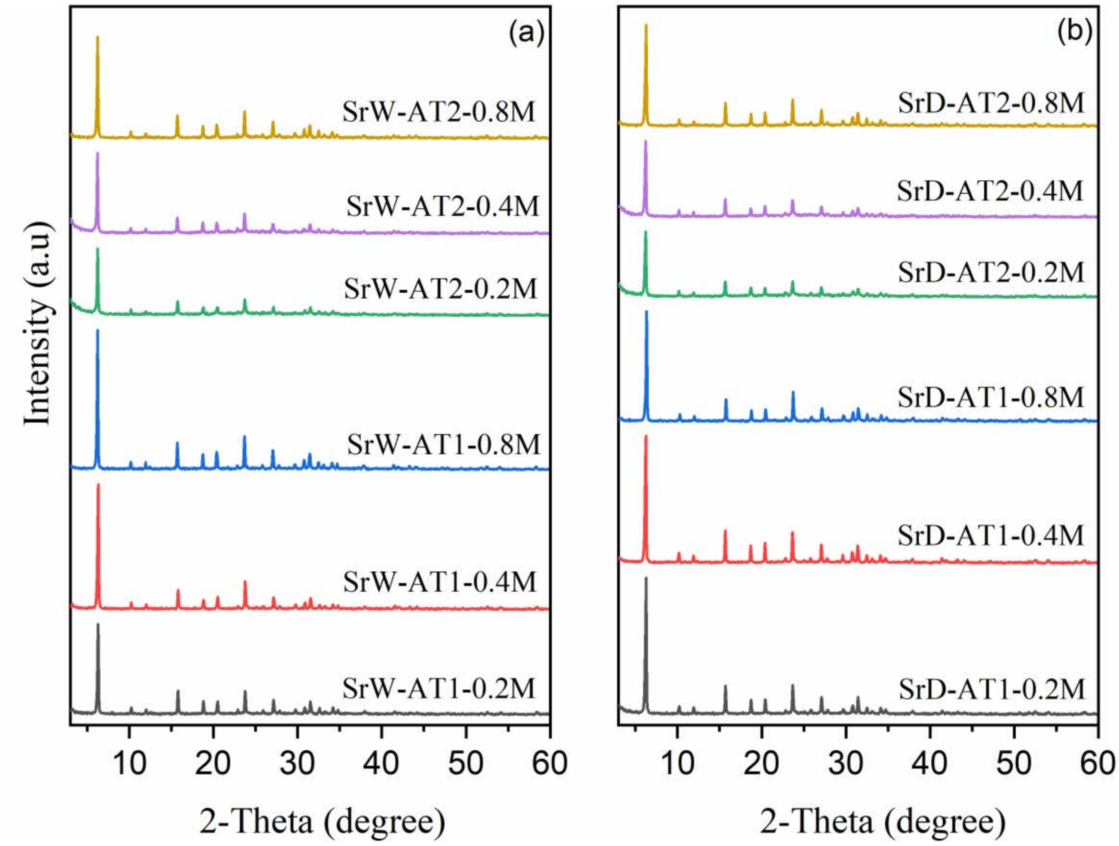

Figure 3.3. XRD characterization of strontium loaded Y-zeolite (a) Strontium loading via wet impregnation, 0.05M citric acid (AT1) and 0.1M citric acid (AT2); (b) Strontium loading via dry impregnation, 0.05M citric acid (AT1) and 0.1M citric acid (AT2).

Loading of strontium on dealuminated and desilicated samples caused a slight shift in XRD peaks at 2-Theta of 6.2°, 10.15°, 11.9°,20.4°, 23.7°, 31.45° and 34.75°, which can be attributed to the incorporation of strontium ion into zeolite framework (Figure 3.3). However, the presence of strontium oxide in the zeolite framework was not detected by XRD. The absence of relevant peaks cannot be considered as the absence of strontium oxide; instead, it may be regarded as the availability of strontium oxide at low concentrations. In addition, the possibility of uniform dispersion of strontium oxide into the zeolite framework cannot be overlooked [317, 318].

3.3.1.4 FTIR analysis

The FTIR analyses of parent, hierarchical, and strontium modified Y-zeolites are presented in Figure 3.4. All the samples showed predominant peaks at 440 cm^{-1}, 577 cm^{-1}, 577 $cm^{-1,}$ and 980-1030 cm^{-1}, as in the case of a typical Y-zeolite. The Y-zeolites consist of TO_4 tetrahedrons structure (T = Si, Al), and the Si/Al ratio of zeolites influences the strength of the vibration frequencies. The FTIR spectra at 440 cm^{-1} correspond to T-O-T bending vibration, and the peak at 577 cm^{-1} can be attributed to microporous zeolite [307]. The intensity of these peaks dropped after loading strontium, indicating a decrease in microporous volume. Since the wet impregnation method enhanced slightly the average microporous volume, the drop in peak intensity at 577 cm^{-1} was not high compared to the dry impregnation method. The bands noticed at 980 cm^{-1} and 1036 cm^{-1} can be attributed to the symmetric and asymmetric stretching vibration of framework O-T-O [319], respectively. The intensity of these peaks decreased after strontium loading, which confirms a reduction in zeolite crystallinity. As can be observed in Figure 4, with an increase in the NaOH concentration, all strontium loaded samples showed an increase in the intensity on FTIR spectra, supported by an increase in microporous volume due to the occurrence of recrystallization during desilication. The presence of Brønsted acid sites in parent Y-zeolite was observed at the broadband centre at 1449 cm^{-1}, but the intensity of this peak drops after adding strontium [320]. Reducing the number of acidic sites could decrease the catalytic activity [321]. However, the intensity of peak centred at 1631 cm^{-1} increased after loading strontium, which might be attributed to an increase in the number Lewis acid sites. The presence of Lewis acid sites can enhance ketonisation and aldol condensation activities during biomass catalytic pyrolysis [322]. An increase in the number of Lewis acid sites is supported by an increase in the mesoporous area after strontium loading.

FESEM monograph of parent, dealuminated-desilicated, and strontium loaded Y-zeolites are presented in Figure A.1 - Figure A.3. The parent Y-zeolite showed a well-defined octahedral structure. After sequential dealumination-desilication treatment, the sharp edges and overall morphology of Y-zeolite remained the same, but irregularly shaped particles were noticed. These irregular shapes were caused by removing aluminium and silicon from the framework, which was also confirmed by a drop in relative crystallinity compared with parent Y-zeolite [310]. AT1 samples showed a better resemblance with parent Y-zeolite than AT2 due to slightly higher aluminium removal caused by higher citric acid concentration. As shown in Figure A.1-Figure A.3, no noticeable morphological changes were observed after loading strontium, which confirms the relative crystallinity results. The EDS mapping (Figure A.4-Figure A.6) was used to analyse the dispersion of strontium, silicon, and aluminium on zeolite framework. According to the results, both wet and dry impregnation methods provided homogenous dispersion of strontium.

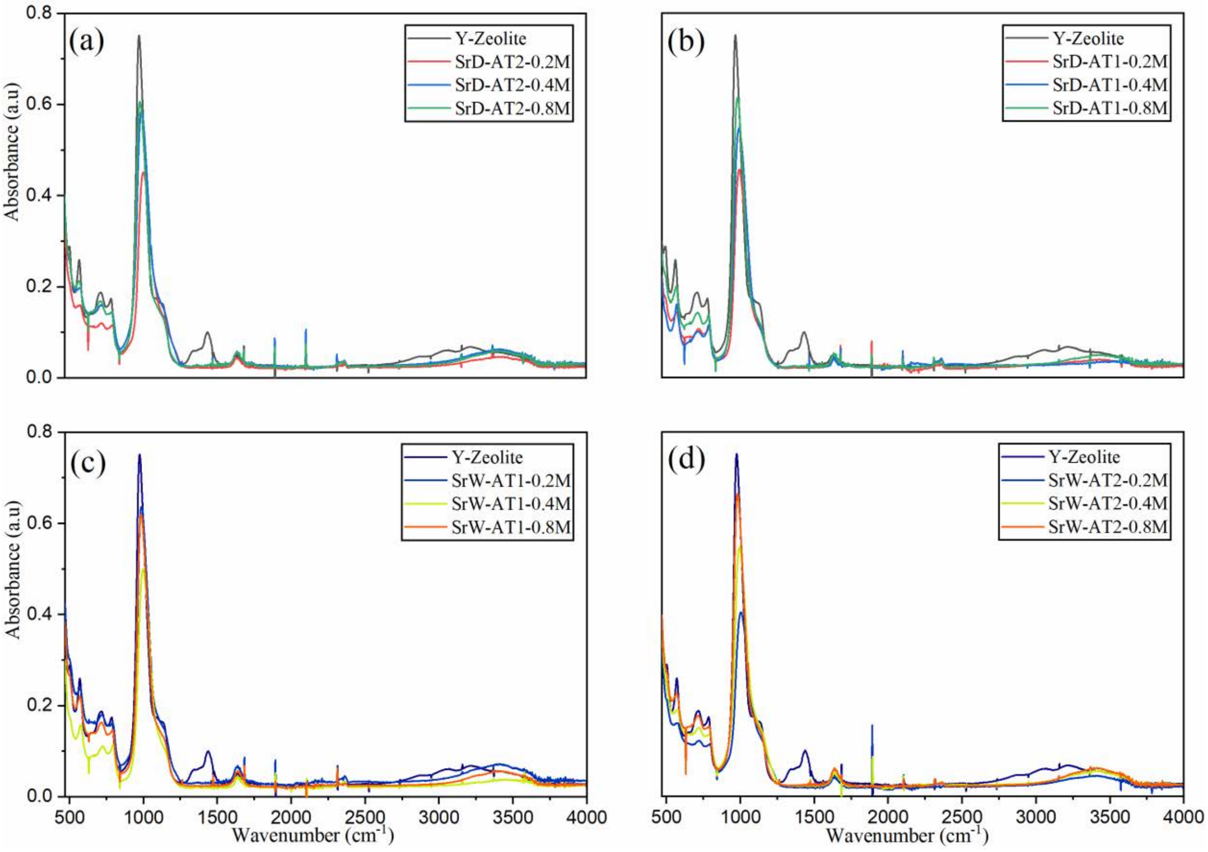

Figure 3.4. FITR spectra of strontium loaded Y-zeolite; (a) Dry impregnation, 0.1M citric acid (AT2); (b) Dry impregnation, 0.05M citric acid (AT1); (c) Wet impregnation, 0.05M citric acid (AT1); (d) Wet impregnation, 0.1M citric acid (AT2).

3.3.1.5 Effect of calcination temperature

The DSC/TGA analysis of parent Y-zeolite and uncalcined Sr loaded Y-zeolite was used to analyse phase change during calcination. As presented in Figure A.7, the DTG curves of uncalcined parent Y-zeolite and alkaline treated zeolite with different NaOH concentrations (0.2 M-0.8 M) in the presence of CTAB showed two main endothermic stages. The first stage was from room temperature to 170°C, which corresponds to the release of bounded and surface water from zeolite pore. The second stage took place from 280°C to 500°C, attributed to the removal of CTAB micelles from the zeolite matrix [323]. Parent Y-zeolite shows additional mass loss from 650-850ºC; this might be due to aluminium release from the zeolite framework, which probably defects the lattice structure [324].

Furthermore, to examine the calcination temperature for strontium loaded Y-zeolite, different quantities of strontium (4, 8, and 12%) were loaded onto the alkaline treated zeolite (0.8 M NaOH). The DSC curve indicated evaporation of bound water in the temperature range of 35°C to 180°C. The second stage took place in the temperature range of 300–650°C, which can be attributed to the dehydroxylation reaction of strontium nitrate on the surface zeolite [325]. Mass losses were observed at temperatures higher than 750°C, which might be due to the desorption of adsorbed strontium from the zeolite matrix [326]. On the other hand, as shown in Figure A.7b, the DSC curve of untreated strontium nitrate also showed a phase change in the temperature range between 550°C and 700°C, which can be attributed to the formation of SrO. Therefore, to obtain a better dispersion of SrO into the zeolite framework, the calcination temperature should be 700°C.

3.3.2 Pyrolysis characteristics

3.3.2.1 Thermal Analysis

Thermogravimetric analyses of IB, PW and their mixture (IB+PW) are shown in Figure 3.5. Thermal decomposition of IB can be divided into three stages; (stage I) in a temperature range of room temperature to 150°C; (stage II) 200°C to 450°C and (stage III) 450°C to 800°C for moisture removal, devolatilization and carbonization stages, respectively. The first stage is associated with removing moisture with a mass loss rate of 3.2 wt. % /min. The low moisture content (9.2 wt.%) of IB makes it suitable for pyrolysis and favours the production of bio-oil with high quality and yield [90]. The second stage causes the main decomposition between 200°C to 450°C with a weight loss of 51.3 wt.%. The weight loss is mainly attributed to the decomposition of hemicellulose, cellulose, part of lignin, and the formation of non-condensable gas (CO, CO_2, and CH_4) [327]. The second stage is further divided into intermediate shoulder peaks temperature zones, decomposition of hemicelluloses in the first zone (250°C to 305°C) with a maximum mass loss rate of 6.5 wt. % /min while cellulose and lignin degradation takes place in the second zone (305°C to 450°C) with a maximum mass loss rate of 14.52 wt. % /min at 340°C. The third stage, from 450°C to 800°C, corresponds to degradation of the remaining lignin with the final residue of 23.41 wt. %.

However, as shown in the DTG curve (Figure 3.5) the decomposition of PW has two main stages, from room temperature to 190°C and 300°C–420°C, which are attributed to water release (3.52 wt. %) and fast decomposition of PW (83.37 wt. %), respectively. The high moisture content of this PW sample compared with previous works is due to the nature of the waste sample used in this study. The DTG curve shows no significant decomposition up to 300°C due to the crystalline nature of PW, which imparts high thermal stability. DTG curve further reveals that PW showed a maximum weight loss rate of 31.17 wt. %/min at 390°C. The second stage of weight loss is mainly due to dehydrochlorination and decomposition of the polymer.

The TGA and DTG of IB: PW mixture is presented in Figure 3.5 a-b. In this study, 4:1 ratio of IB to PW was used based on previous literature to obtain an optimum devolatilization rate [305]. The mixture shows three successive weight loss stages, room temperature to 190°C, 250-450°C and 450-800°C. The moisture content of IB+PW mixture accounts for 6.31 wt. % that is removed up to 190°C. The second stage is the most significant temperature region (main decomposition) between 250-450°C with a weight loss of 57.94 wt. %, attributed to the devolatilization of both IB and PW. The maximum weight loss occurs at 387°C with 16.52 wt. % /min, which is shifted to the right compared to the IB. The right shift in temperature is due to the presence of PW that requires high energy for degradation. The third stage occurs from 450-800°C with a mass loss of 5.66 wt. % is comparatively similar to IB decomposition. The solid residue reduces from 23.4 wt. % (IB) to 13.4 wt. % (IB+PW) and can be explained by a high conversion of reactants due to synergic effect of PW that enhanced the devolatilization rate.

The effect of strontium loaded Y-zeolite on co-pyrolysis was investigated at a catalyst to biomass (IB and PW) ratio of 1:4, which was based on previous literature to obtain a better degree of aromatization and bio-oil yield [328]. As shown in Figure 3.5 c-j, the TGA and DTG curves revealed that decomposition of IB and PW mixture with the catalyst showed a similar trend like non-catalytic decomposition. The first stage (< 190 °C) corresponds to the removal of moisture in the range of 7.1-9.7 wt. %. The amount of moisture content of the mixture increased compared to PW due to the presence of sawdust biomass characterized by a higher moisture content [90]. The main decomposition occurred between 250-450°C; however, mass loss rate varies across the samples. The maximum weight loss rate ranges from 11.70 wt. % /min to 18.53 wt. % /min for catalytic co-pyrolysis. As shown in Figure 3.5, the weight loss rate increased with the increase in NaOH concentration during treatment, i.e., SrW-AT1-0.2M < SrW-AT1-0.4M < SrW-AT1-0.8M. The high mesoporous area of SrW-AT2-0.2M allows the IB and PW mixture to undergo a high devolatilization rate. The lower mass loss rate might be due to pore blockage caused by secondary reactions and coke formation during decarbonylation reaction [329].

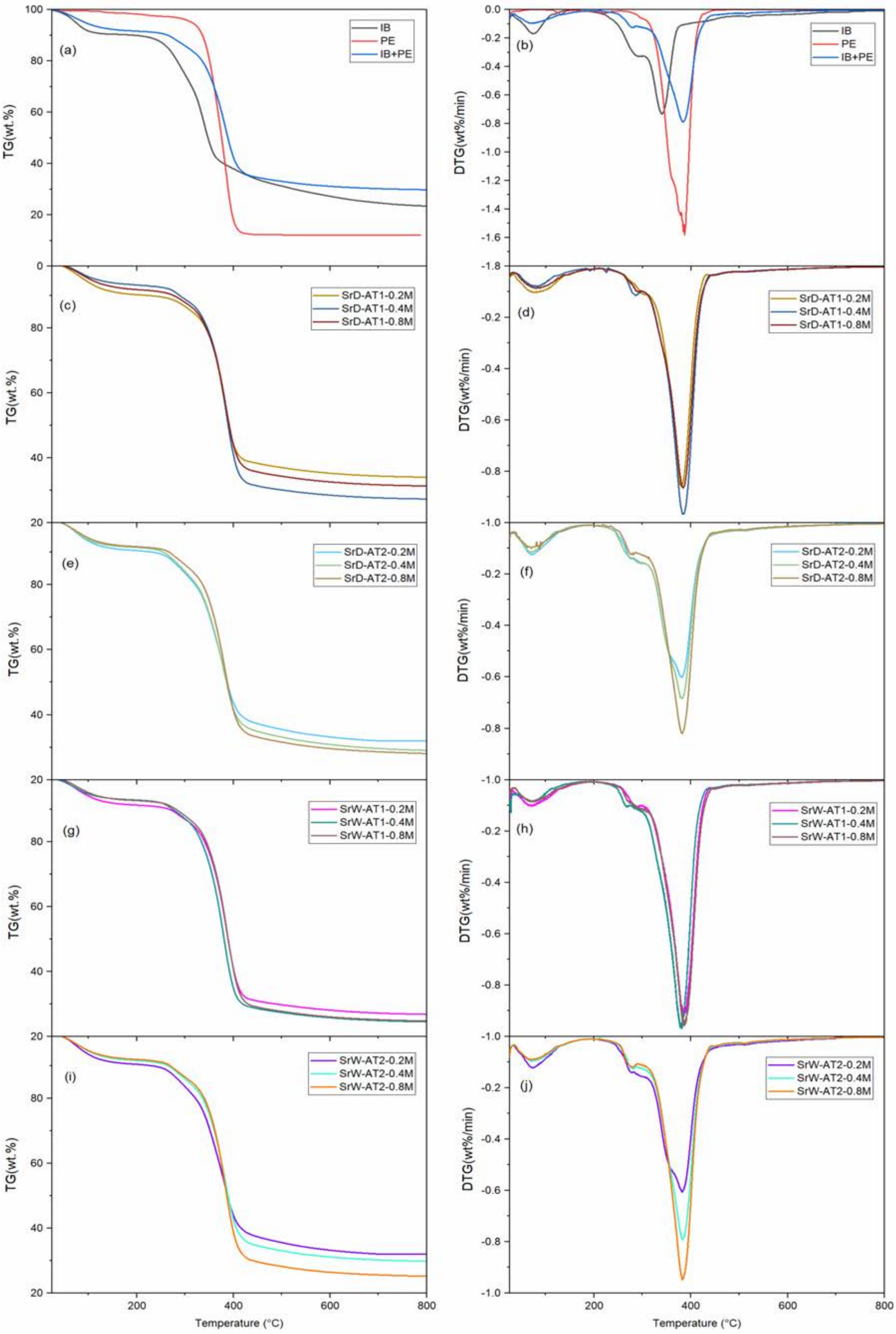

Figure 3.5. TGA/DTG curve of co-pyrolysis of IB and PW with and without catalyst; (a) TGA curves for IB and PW and mixture (IB+PW); (b) DTG curves for IB and PW and mixture

(IB+PW); (c) TGA curves of IB+PW and Y-zeolite loaded with strontium via dry impregnation, 0.05M citric acid and 0.2M-0.8M NaOH concentration; (d) DTG curves of IB+PW and Y-zeolite loaded with strontium via dry impregnation, 0.05M citric acid and 0.2M-0.8M NaOH concentration; (e) TGA curves of IB+PW and Y-zeolite loaded with strontium via dry impregnation , 0.1M citric acid and 0.2M-0.8M NaOH concentration; (f) DTG curves of IB+PW and Y-zeolite loaded with strontium via dry impregnation, 0.1M citric acid and 0.2M-0.8M NaOH concentration; (g) TGA curves of IB+PW and Y-zeolite loaded with strontium via wet impregnation, 0.05M citric acid and 0.2M-0.8M NaOH concentration; (h) DTG curves of IB+PW and Y-zeolite loaded with strontium via wet impregnation, 0.05M citric acid and 0.2M-0.8M NaOH concentration; (i) TGA curves of IB+PW and Y-zeolite loaded with strontium via wet impregnation , 0.1M citric acid and 0.2M-0.8M NaOH concentration; (j) DTG curves of IB+PW and Y-zeolite loaded with strontium via wet impregnation, 0.1M citric acid and 0.2M-0.8M NaOH concentration.

3.3.2.2 Kinetics study

The kinetic parameters, including apparent activation energy (E) and pre-exponential factor, were determined using Coasts-Redfern equation based on TGA/DTG data for IB, PW, IB+PW, and catalytic co-pyrolysis of IB and PW mixture are summarized in Table 3.4.

The kinetics parameters for catalytic co-pyrolysis were calculated for the main pyrolysis stage in the temperature range of 250-450°C, where the highest mass loss was noticed, as shown in Table S8. Plots of $\ln\left(g(\mathrm{x})/T^2\right)$ vs. $1/T$ for eight reaction mechanism functions (Table 3.4) result in a straight line; the slope and intercept can be used to calculate the activation energy and pre-exponential factor, respectively. The accuracy of the models was analysed based on R^2 value for each reaction mechanism. Therefore, among eight reaction mechanisms, the mechanism function with the highest R^2 value was considered for the discussion.

As shown in Table S8, non-catalytic IB showed the best linear fit of 0.965 (R^2) compared to other models, described by a second-order chemical reaction mechanism. Moreover, IB possesses apparent activation energy (E) of 52.12 kJ/mol, which is similar to previous studies reported for wood biomass [329]. For PW pyrolysis, the maximum R^2 value (0.971) was noticed for one-dimensional (1-D) diffusion reaction mechanism. The apparent activation energy (E) of PW is 199.2 kJ/mol, which is lower than the previously reported study (213-280 kJ/mol) [327]. The pre-treatment (grinding) of PW before the analysis may have reduced the thermal stability and lowered activation energy. However, the apparent activation energy (E) of IB and PW mixture is 74.64 kJ/mol and follows the one-dimensional (1-D) diffusion of reaction mechanism with R^2 value of 0.987.

Table 3.4. Kinetics parameters of catalytic and non-catalytic co-pyrolysis of iron bark and PW.

Sample Name	Slope	Y-Intercept	Activation Energy, KJ/mol	Pre-exponential factor, min^{-1}	R^2
Iron Bark	-6269	-2.33	52.12	$1.8x10^2$	0.965
PW	-23966	22.40	199.25	$3.7x10^{13}$	0.971
IB+PW (4:1)	-8978	-0.41	74.64	$1.7x10^3$	0.987
SrD-AT1-0.2M	-7295	-2.95	60.65	$1.1x10^2$	0.926
SrD-AT1-0.4M	-9123	0.33	75.85	$3.7x10^3$	0.952
SrD-AT1-0.8M	-8107	-1.81	67.40	$3.9x10^2$	0.943
SrW-AT1-0.2M	-8115	-1.79	67.47	$3.9 x10^2$	0.944
SrW-AT1-0.4M	-8977	-0.53	74.63	$1.5 x10^3$	0.960
SrW-AT1-0.8M	-8809	-0.79	73.24	$1.2 x10^3$	0.954
SrW-AT2-0.2M	-6804	-3.63	56.57	$5.3 x10^1$	0.974
SrW-AT2-0.4M	-8105	-2.14	67.38	$2.7 x10^2$	0.904
SrW-AT2-0.8M	-8325	-1.48	69.21	$5.5 x10^2$	0.952
SrD-AT2-0.2M	-8496	-1.16	70.64	$7.8x10^2$	0.935
SrD-AT2-0.4M	-7259	-2.94	60.35	$1.1 x10^2$	0.976
SrD-AT2-0.8M	-7929	-2.04	65.92	$3.0 x10^2$	0.961

SrD/W-ATn-mM, where D/W represents dry or wet impregnation, respectively, m represents NaOH concentration, and AT1 and AT2 are 0.05 M and 0.1 M concentration of citric acid, respectively.

The presence of strontium loaded Y-zeolite catalyst in the co-pyrolysis of IB and PW mixture follows a one-dimensional (1-D) diffusion reaction mechanism with R^2 value ranging from 0.926 to 0.976. In general, the addition of catalyst minimizes the activation energy. Based on the reaction mechanism (one-dimensional (1-D) diffusion), the hierarchical structure of Y-zeolite enhances macromolecular diffusion by providing additional porosity during the devolatilization stage [330]. Moreover, strontium catalyst prepared using 0.1 M citric acid (AT2) shows the lowest activation energy (56.5-69.2 kJ/mol) compared to the catalyst prepared using 0.05 M citric acid (AT1) (60.6-76.8 kJ/mol). According to previous literature, treatment with concentrated citric acid results in higher mesoporous volume by providing additional active sites to decompose high molecular weight components of biomass [331]. The lowest activation energy (56.5 kJ/mol) was achieved for catalyst sample SrW-AT2-0.2M, which has the highest mesoporous area and volume. Therefore, incorporating mesoporosity on Y-zeolite structure after sequential dealumination and desilication treatments was an effective strategy in reducing the activation energy. SrD-AT1-0.4M showed higher activation energy (75.85 kJ/mol) than IB+PW mixture. The higher activation energy might be due to blockage of pores caused by coke formation, as noticed in other studies [332].

Activation energy might be impacted by catalytic co-pyrolysis parameters such as catalyst loading, catalyst to feedstock ratio and biomass to plastic ratio; therefore, it is difficult to have a direct comparison with previous studies. However, Table 3.6 presents the comparison of SrW-AT2-0.2M with zeolite and metal oxide catalysts previously reported in the literature. The newly synthesised catalyst minimized the activation energy compared to results reported in previous studies. For instance, Zhong et al. [333] achieved lower activation energy of 38.63 kJ/mol using HZSM-5 catalyst for co-pyrolysis of water hyacinth and HDPE. However, the catalyst to feedstock ratio was 1:1, which highly affected the activation energy and composition of bio-oil. Therefore, it is recommended to optimise catalyst to feedstock ratio and strontium loading onto Sr/Y-zeolite, and investigating its impact on the catalytic co-pyrolysis process.

3.3.2.3 Bio-oil characterization

The bio-oil obtained from IB, IB+PW mixture, and catalytic co-pyrolysis over strontium modified Y-zeolite (SrW-AT2-0.2M) was further analysed to determine the available functional groups using ^{13}C NMR. The chemical shift assignment was done based on previous literature and typical ^{13}C NMR spectra for all the samples is presented in Figure A.8-Figure A.10 [334]. The percentage of carbon in different bio-oil constituent is presented in Table 3.5. Bio-oil obtained from IB is composed of 12.14% carbonyl, 3.94% aromatic C-O, 0.26 % aromatic C-C, 0.26 % aromatic C-C, 5.17% levoglucosan, 23% aliphatic C-O, 3.3% aliphatic C-C, 12.3% methyl-aromatic and 0.78% methyl-aromatic. Based on these results, it can be concluded that the bio-oil produced from IB pyrolysis contains more oxygenated species. Co-pyrolysis of IB and PW mixture showed less oxygenated functional groups; however, less aromatic carbon such as, 3.94% aromatic C-O, 0.26 % aromatic C-C, 0.26 % aromatic C-C were noticed. Therefore, by adding PW as co-feedstock, the total aliphatic carbon content increased while reducing the oxygen-containing functional groups [335].

Table 3.5. Integration results shown as percentage of carbon of bio-oil from IB, IB+PW and catalytic co-pyrolysis of IB+PW mixture.

Bio-oil component	Chemical Shift (ppm)	IB	IB+PE	Catalyst + IB+PW mixture
Carbonyl	215.0-166.5	12.14	11.07	16.04
Aromatic C-O	166.5-142.0	3.94	3.45	8.91
Aromatic C-C	125.0-95.8	0.26	0.54	0.46
Aromatic C-H	125.0-95.8	6.39	6.47	11.28
Levoglucosan	C_1 102.3, C_2 72.0, C_3 76.5, C_6 64.9	5.17	2.34	0.25
Aliphatic C-O	95.8-60.8	23.41	23.57	29.22
Methoxy/hydroxy	60.8-55.2	21.81	0.77	0.891
Aliphatic C-C (general)	55.2-0.0	27.09	17.61	17.45
Methyl-Aromatic	21.6-19.1	12.01	12.05	12.80
Methyl-Aromatic at ortho position of a hydroxyl or methoxy group	16.1-15.4	1.76	1.15	1.22

Compared with IB and IB+PW, strontium modified Y-zeolite catalysts enhanced the total aromatic carbon in the bio-oil. The catalytic co-pyrolysis increased aromatic C-H (11.28%), which is due to “hydrogen pool” pathways via the Diel-Alder reaction [336]. In the present study, the reaction between furans from ironbark and olefine gases from PW in the presence of SrW-AT2-0.2M may be the reason for an increase in the aromatic carbon content [337]. The increase in aromatic C-O during catalytic co-pyrolysis can be attributed to the radical reaction between the aliphatic and aromatic hydroxyl groups [338]. It has been also observed that SrW-

AT2-0.2M promotes ketonisation of acidic groups resulting in high-quality bio-oil. The ^{13}C NMR showed an increase in carbonyl from 12.14 to 16.04 %, which confirmed the formation of ketonic compounds such as acetone and 2-heptadecanone [339]. Therefore, the newly synthesised catalyst has effectively enhanced the quality of bio-oil from co-pyrolysis of ironbark and plastic waste.

Table 3.6. Comparison of catalyst used in this study and other catalytic co-pyrolysis from previous literature.

Catalyst	Biomass	Plastic	B:P (w/w)	C:F (w/w)	E (kJ/mol)	A (min^{-1})	R^2	Ref.
Mg/ Y-zeolite	-	Plastic waste	-	1:10	131	2.52	0.979	[340]
HZSM-5	Water hyacinth	HDPE	3:1	1:1	38.63	-	0.952	[333]
MgO	Rice husk	-	-	1:4	115	1.76×10^{9}	0.985	[341]
ZSM-5	Wood fuel	LDPE	1:1	1:4	108.12	1.92×10^{14}	0.973	[342]
ZSM-5	Cellulose	LDPE	4:1	1:4	89.51	6.73×10^{5}	0.950	[327]
Co/ZSM-5	Rice straw	LDPE	4:1	1:4	70.58	4.2×10^{2}	0.968	[343]
Sr/Y-zeolite	Ironbark	Plastic waste	4:1	1:4	56.57	5.29×10^{1}	0.974	This study

3.4 Conclusions

In this work, strontium loaded hierarchical Y-zeolite was prepared using sequential dealumination-desilication and wet and dry impregnation methods. Also, the catalyst was used in the co-pyrolysis of ironbark and plastic waste to understand its influence on the co-pyrolysis process and end-product (bio-oil). The dealumination process was carried out using citric acid, which resulted in an increase in the mesoporous surface area (53 m^2/g to 147 m^2/g) and Si/Al ratio (2.48 to 5.36), indicating the effectiveness of citric acid to act as a chelating agent in selectively removing extra-framework aluminium and contribute to the formation of mesoporosity. The sequential desilication process further enhanced the mesoporous volume, from 0.118 cm^3/g (AT1) to 0.192 cm^3/g (AT1-0.2M), 0.147 cm^3/g (AT2) to 0.314 cm^3/g (AT2-

0.2M). Wet and dry impregnation methods were used to load strontium in the Y-zeolite, and both methods showed a comparable result. The loading of strontium ions into the zeolite framework decreased the mesoporous volume and area. Strontium dispersion increased with decreasing Si/Al ratio due to the higher alkalinity of desilicated Y-zeolites. The wet impregnation method resulted in better strontium loading with an average of 6.78%, whereas the dry impregnation method gave a maximum of 5.33%. The kinetic parameters were calculated using Coasts-Redfern integral method. The non-catalytic pyrolysis of IB and PW mixture had an activation energy of 74.64 kJ/mol and followed one-dimensional (1-D) diffusion reaction mechanism. However, the presence of strontium loaded Y-zeolite catalyst significantly reduced the activation energy of the mixture and the lowest activation energy was noticed for sample SrW-AT2-0.2M (56.57 kJ/mol). The bio-oil collected from catalytic co-pyrolysis of IB+PW using sample SrW-AT2-0.2M showed a higher content of aromatic compounds and lower acidic fraction.

Catalytic pyrolysis has been used to enhance the yield and selectivity of by-products. The selection of catalyst materials, temperature control, catalyst loading, catalyst regeneration, and feedstock characteristics are all important factors that can impact the performance of catalytic pyrolysis. Both in-situ and ex-situ catalytic pyrolysis are two commonly used methods. In-situ catalytic pyrolysis involves the use of a single reactor where the biomass and catalyst are mixed and processed together while ex-situ catalytic pyrolysis separates the biomass and catalyst into different reactors. In-situ catalytic pyrolysis uses a single reactor, reducing costs and high yields of biofuels and chemicals can be achieved. However, catalyst deactivation and the formation of undesirable by-products can reduce the catalyst efficiency and quality of the final by-products. Ex-situ catalytic pyrolysis can overcome some of the challenges of in-situ catalytic pyrolysis by separating the biomass and catalyst into different reactors. In this approach, recycling and reusing of catalyst can be easily implemented, increasing catalyst lifespan. However, ex-situ catalytic pyrolysis requires more equipment and higher initial capital investment. The process can also be less efficient than in-situ catalytic pyrolysis, resulting in lower hydrocarbons yields. Recycling and reusing of the catalyst were not considered in this study as we employed an in-situ catalytic pyrolysis mode and separating the catalyst from biochar is challenging. However, despite this drawback, this study approach facilitated high selectivity towards aromatic hydrocarbons. Moving forward, it would be beneficial to explore both in-situ and ex-situ catalytic pyrolysis modes to advance towards an economical and environmentally sustainable solution.

4 High-quality bio-oil production and optimisation of process parameters

Abstract

Catalytic co-pyrolysis of IB and WCO over strontium oxide (SrO) loaded hierarchical Y-zeolite was performed using a fixed bed reactor. The effect of reaction temperature, IB:WCO ratio and SrO loading percentage on product distribution and quality was examined. The findings indicated that the highest bio-oil yield (55.3 %) was obtained at a pyrolysis temperature of 550°C. A further increase in the reaction temperature (650°C) initiated secondary cracking reactions, which reduced bio-oil yield. Simultaneously, the maximum aromatic yield (28.6 %) was obtained at an IB:WCO ratio of 1:1 and 10 wt. % SrO loading. Increasing the amount of WCO enhanced the aromatic yield by providing alkyl radicals and a hydrocarbon pool to promote the conversion of methoxy/hydroxyl, phenols, and levoglucosan into poly-aromatics. Basic sites introduced by SrO addition promoted the ketonisation of fatty acids to aliphatic ketones. The reaction mechanism of catalytic co-pyrolysis of IB and WCO showed that the acid sites on Y-zeolite and basic sites on SrO contribute to the conversion of oxygenated compounds to phenols and aromatic hydrocarbons. The present work indicates that SrO/Y-zeolite active sites increased the aromatic carbon yield.

Keywords: Biomass; Waste cooking oil; Hierarchal zeolite; Strontium oxide; Co-pyrolysis; Bifunctional catalyst

This work has been published as: Tewodros Kassa Dada, Anwarul Islam, Ravinder Kumar, Jason Scott, Elsa Antunes. Catalytic co-pyrolysis of ironbark and waste cooking oil using strontium oxide-modified Y-zeolite for high-quality bio-oil production, Chemical Engineering Journal, 2022, 138448.

4.1 Introduction

Replacing conventional fossil fuels with renewable energy sources is one of the priorities for all nations globally. In this regard, biomass is considered a sustainable and renewable feedstock to produce a variety of biofuels. Pyrolysis is an efficient technique to produce bio-oil from biomass [264]. However, the hydrogen-deficient nature of biomass affects the physicochemical properties of bio-oil, such as low heating value, low stability, and high oxygen content. The ratio of H/C molar ratio is an important parameter and can be expressed by equation (4.1).

$$\frac{\mathbf{H}}{\mathbf{C}} = \frac{\mathbf{H - 2O - 3N - 2S}}{\mathbf{C}} \tag{4.1}$$

The H/C ratio of biomass generally ranges between 0 and 0.3. As a result, the pyrolysis of biomass alone produces bio-oil with low or negligible hydrocarbons and high oxygen-containing compounds, making biomass alone an inefficient feedstock for producing high quality bio-oil [272, 273]. Co-feeding biomass with a hydrogen-rich feedstock is a viable solution to increase the H/C ratio and upgrade the bio-oil quality. Among hydrogen-rich feedstocks, WCO shows high potential as a hydrogen co-feed during co-pyrolysis, subsequently producing bio-oil rich in aromatic and aliphatic hydrocarbons. WCO is mainly utilized to produce biodiesel, which generates large amounts of by-products (glycerol) and requires an additional pre-treatment stage [5, 6]. Co-pyrolysis of WCO has advantages over transesterification processes, including low processing cost and high conversion rates to produce high energy value fuel. Consequently, it could be suggested that using WCO in the co-pyrolysis process is highly advantageous to obtaining high energy density bio-oil and should be preferred over biomass as the sole feedstock.

Catalytic co-pyrolysis (CCP) of biomass and hydrogen-rich materials is another attractive and significant approach to further enhance the calorific value and other physicochemical properties of bio-oil. The application of catalysts reduces the activation energy and promotes the formation of mono-cyclic aromatic hydrocarbons by favouring a number of deoxygenation reactions, such as decarboxylation, dehydration, and decarbonylation [126, 344]. Many heterogeneous catalysts have been studied to enhance bio-oil quality, including metal oxides [24], zeolites [167, 345], metal-loaded zeolite [181], and activated carbon (AC) [346]. In particular, zeolites have been excessively utilized in catalytic fast pyrolysis as well as CCP to obtain high energy density bio-oil. During CCP using an acid catalyst, the principal mechanism in the conversion of oxygenated compounds involves Diels–Alder reactions between biomass-derived furans, acetic acids, levoglucosan, xylose and hydrocarbon pool from olefins [277]. In contrast, CCP over a base catalyst upgrades the bio-oil quality via the ketonisation of acids and aldol condensation of aldehydes and smaller ketones [347, 348]. Generally, the active catalytic sites on a basic catalyst favour the formation of aromatic compounds by decreasing H_2O formation and producing CO_2 during the deoxygenation of the pyrolysis products. Alkaline metal oxides such as MgO and CaO have been successfully used to deoxygenate aldehydes and carboxylic acids to produce light hydrocarbon compounds via ketonisation and aldol condensation reactions [216, 349].

Ketonisation is one of the primary deoxygenation reactions for bio-oil upgrading, which mainly involves dehydration (H_2O) and decarboxylation (CO_2) reactions and enhances C-C interaction between acids. The presence of strong basic sites on a catalyst during the CCP process enables the ketonisation of carboxylic acids to upgrade pyrolytic vapours [7]. The basicity of a catalyst depends on the strength of the adsorption energy during the reaction. Metal oxide catalysts possess high energy such as SrO (2.85 eV), CaO (-2.05 eV) and MgO (-1.35 eV). SrO exhibits stronger adsorption energy, making it highly recommended for converting acid fractions into bio-oil [302]. However, a solely basic catalyst (SrO) is inefficient at converting the oxygenated components in bio-oil into aromatic molecules. Hence, impregnating a basic metal oxide on acidic support, such as a zeolite, has been suggested as an advantageous approach to produce a catalyst with dual acidic-basic physicochemical properties and consequently obtaining bio-oil with varying chemical components. In an earlier study, strontium-loaded hierarchical Y-zeolite catalyst was synthesised and tested for the CCP of ironbark and plastic waste [4]. The results showed that non-catalytic co-pyrolysis of ironbark and plastic waste generated a bio-oil with high oxygenated compounds, 3.9 % aromatic C–O and 0.3% aromatic C–C. CCP over the SrO-loaded Y-zeolite significantly enhanced the proportion of aromatic compounds, particularly an aromatic C–H content of 11.3 % was achieved in the bio-oil. Overall, it is anticipated that CCP using bifunctional catalysts with dual basic and acidic active sites seems to be beneficial to obtain a high-quality bio-oil.

Given that CCP is a promising approach for bio-oil upgrading, the application of a bifunctional catalyst could favour several deoxygenation reactions to produce a range of aromatic compounds. This study examines the application of SrO-loaded hierarchical Y-zeolite catalyst for bio-oil upgrading during in-situ co-pyrolysis of IB and WCO. The effect of SrO loading (5, 10, and 15 wt.%) on product distribution and CCP process parameters, including heating rate, reaction temperature, and IB:WCO mixture ratio on aromatic and carbonyl yields in bio-oil, was studied. The novelty of this work is to synthesise a catalyst with additional active sites (acid and alkaline) to convert the oxygenated fraction of bio-oil into aromatic compounds. Therefore, this study put forward a new idea by combining hierarchical Y-zeolites (acidic sites as support) loaded with SrO (alkaline sites). Previous studies used mainly a mono-catalytic system (acid or alkaline catalysts), which is unable to address all oxygenated compounds available in the bio-oil mixture. However, this new catalyst system addresses all oxygenated compounds by providing high mass transfer (hierarchical structure) and promotes ketonisation and aldol condensation reaction due to the presence of SrO. This will help to enhance the selectivity of aromatics C-C, resulting in high-quality bio-oil.

4.2 Materials and Methods

4.2.1 Materials

IB sawdust was collected from a local store in Townsville, Australia. The IB was sieved with a 100-mesh sieve prior to use in the pyrolysis experiments. The proximate and ultimate analysis of IB is presented in Table A.2. The WCO was collected from a local restaurant and stored at room temperature. This study used the mixture of IB:WCO for co-pyrolysis experiments. Dimethyl sulfoxide (DMSO), citric acid (99.5 %), cetyl-trimethylammonium bromide (CTAB), sodium hydroxide (NaOH), strontium nitrate, and Y-zeolite (Si/Al = 2.65) were purchased from Sigma-Aldrich. All used chemicals and reagents were of analytical grade and utilized as delivered without further purification.

4.2.2 Catalyst Preparation

Mesoporous Y-zeolite was synthesised via a sequential dealumination and desilication process of parent Y-zeolite as described in previous work [4]. SrO was loaded onto the mesoporous Y-zeolite using wet impregnation. The impregnation involved dispersing 10 g of mesoporous Y-zeolite in 100 mL of a solution containing different $Sr(NO_3)_2$ concentrations (5, 10, and 15 wt. % Sr). The solution was stirred at 400 rpm for 5 h at 80°C and then dried at 105°C overnight. The thermal decomposition of strontium nitrate to produce strontium oxide occurs at a temperature greater than 570°C [350]. Subsequently, for all samples, the calcination temperature was set at 600°C for 5 h with a ramp rate of 10°C/min. The obtained catalysts were labelled as SrO/Y-zeolite-N, where N represents the strontium percentage.

4.2.3 Experimental setup

As indicated in Figure A.11, a fixed bed reactor with two condensation systems was employed to collect bio-oil produced during the CCP process. The IB:WCO mixture was manually mixed at a ratio of 1:1, 2:1, and 4:1 before the co-pyrolysis process. Non-catalytic co-pyrolysis and CCP experiments were conducted using an in-situ pyrolysis mode, where feedstocks and catalysts were mixed and placed in a quartz tube. Nitrogen was used as the carrier gas at a flow rate of 1000 ml/min with a residence time of 30 min, based on previous literature [351]. A graham condenser was used to condense the pyrolytic vapor into bio-oil, and the biochar was collected after cooling the reactor to room temperature. The effect of co-pyrolysis temperature (450, 550, and 650ºC), IB:WCO ratio (1:1, 2:1, and 4:1), and SrO loading (5, 10, and 15 wt. %) was studied.

4.2.4 Characterization of catalyst and feedstock

4.2.4.1 X-ray diffraction (XRD)

The crystalline phases of the catalysts were analysed using a Rigaku Ultima IV X-ray instrument with a CU Kα radiation source. The samples were scanned across a 2θ range of 5 to 60° using a step size of 0.05º.

4.2.4.2 BET/BJH analysis

N_2 physisorption isotherms and the specific surface area of the parent and SrO-loaded Y-zeolite samples were determined using Micromeritics Tristar 3020 instrument at -196°C. The samples were degassed at 300°C for 6 h under vacuum prior to the analysis. The surface area was estimated using the Brunauer-Emmett-Teller (BET) model. Mesoporous diameter and volume were determined using the Barrett-Joyner-Halenda (BJH) method.

4.2.4.3 CO_2 and NH_3 Temperature Programmed Desorption (TPD)

TPD studies were conducted on a Micromeritics Autochem II. In the case of CO_2 TPD experiments, the sample was initially pre-treated in 20 mL/min He at 250°C for 30 min using a heating rate of 10°C/min. Following pre-treatment, the sample was cooled to 40°C, and 20 mL/min 50% CO_2 (balance He) passed through the sample for 60 min. The sample was then flushed with helium at 20 mL/min for 60 min, after which the temperature was increased to 850°C at a ramp rate of 10°C/min. In the case of NH_3 TPD experiments, the sample was initially pre-treated in 25 mL/min He at 550°C for 60 min using a ramp rate of 10°C/min. Following pre-treatment, the sample was cooled to 100°C, and 25 mL/min 1% NH_3 (balance He) passed through the sample for 30 min. The sample was then flushed with helium at 25 mL/min for 30 min, after which the temperature was increased to 550°C at a ramp rate of 10°C/min.

4.2.4.4 FTIR analysis

The FTIR spectra were recorded by PerkinElmer One FTIR spectrometer. The functional groups presented in SrO/Y-zeolite were analysed by collecting FTIR spectra at an average of 64 scans across the wavelength range of 100 to 4000 cm^{-1} with a resolution of 4 cm^{-1}.

4.2.4.5 SEM/EDS analysis

Particle morphology and elemental Sr, Si and Al distribution in the parent and SrO-loaded Y-zeolite were evaluated using SEM/EDS. The analyses were conducted on a Field Emission Scanning Electron Microscope (FESEM, SU5000, Hitachi) and measured at Vac=5.0kV, EC=115nA, WD=7.5mm.

4.2.4.6 TGA/DTG analysis

The thermal degradation of IB and WCO was analysed using thermogravimetric analysis (TGA) under a N_2 flow rate of 50 ml/min. The samples were placed in an Al_2O_3 crucible and heated from room temperature to 800°C using a 10°C/min ramp rate.

4.2.4.7 Pyrolysis product characterization

Quantification of the bio-oil chemical composition was performed using a ^{13}C NMR AVANCE III 600 MHz NMR spectroscope (Bruker Inc). Quantification of the bio-oil chemical composition was performed using a ^{13}C NMR AVANCE III 600 MHz NMR spectroscope (Bruker Inc). A representative bio-oil sample were taken, and 100 mg was weighed into a clean and dry NMR tube. Then a known amount of DMSO-d6 (450 µL) was added to dissolve the bio-oil sample. The amount of solvent used depends on the solubility of the bio-oil and the concentration desired for the NMR analysis. To ensure complete dissolution and to remove any impurities or particulate matter that may interfere with the NMR signals, the mixture was filtered using a syringe filter with a pore size of 0.2 µm, which was then transferred into a new NMR tube. Spectra were collected at room temperature with pulse angles of 90°, inverse gated decoupling pulse sequence, 8 s pulse delays, and 8000 scans. Estimation of bio-oil composition was calculated based on integrated ^{13}C spectra area, which is divided into ten chemical shift ranges. The solvent signal at 39.52 ppm was used as the internal reference. A detailed description of chemical shift ranges is presented in our previous work [4].

4.3 Results and discussion

4.3.1 Feedstock properties

The fatty acids composition of WCO analysed using ^1H NMR is shown in Table 4.1. The experiment was conducted by dissolving 50 mg of WCO sample in 600 μl deuterated chloroform and using tetramethylsilane (TMS) at 0.00 ppm as an internal reference. Bruker TopSpin software was used to determine the integration area of each type of resonance in the proton spectrum, and the calculation was based on a previous study [352]. The results revealed that the composition of WCO varies across the range C14:0 to C22:0 with significant components of palmitic acid (C16:0), oleic acid (C18:2), and linoleic acid (C18:2). Noticeably, approximately 77% of the fatty acids were found to be unsaturated (mono and poly), which has been highlighted in other studies [353]. However, saturated fatty acids (palmitic acid and stearic acid) account for only 14% of the make-up that defines the bio-oil cold flow properties. The presence of various unsaturated and saturated fatty acid groups confirms that the WCO is a suitable feedstock for CCP with a biomass feedstock.

Table 4.1. Fatty acids composition of WCO analysed by ^1H NMR.

Fatty acid component	Composition (wt. %)
Linoleic acid (C18:2)	53.0
Oleic acid (C18:1)	24.5
Palmitic acid (C16:0)	12.3
Linolenic acid (C18:3)	4.2
Stearic acid (C18:0)	2.0
Other	4.1

Figure A.12 presents the FTIR spectrum of WCO and confirms the high content of aliphatic groups. The peaks at 2950 and 2850 cm^{-1} correspond to the vibration of aliphatic CH and are preliminary indicators of high concentrations of aliphatic groups. The high intensity of the band at 1712 cm^{-1} indicates the presence of C=O stretching, predominantly corresponding to fatty acid groups. The vibrations for asymmetric deformations of the CH_2 and CH_3 groups are confirmed by the peak centred at 1460 cm^{-1}. The presence of aliphatic groups demonstrates that WCO is composed of both oxygen-containing groups and aromatic compounds. It is anticipated that hydrogen and carbon-rich compounds will help to produce high-quality bio-oil via CCP.

The TGA profiles for IB and WCO are shown in Figure 4.1. The thermo-degradation of IB can be grouped into three phases; room temperature to 150°C; 200°C to 450°C, and 450°C to 800°C. The first phase involves the removal of moisture and light volatile components. In the second phase, the bulk of the decomposition occurs between 200°C and 450°C, resulting in a weight loss of 51.3 wt. %. The substantial weight loss is primarily due to the degradation of hemicellulose, cellulose, a portion of lignin, and the formation of non-condensable gases (CO, CO_2, and CH_4). The third phase, which ranges from 450°C to 800°C, is characterized by the breakdown of residual lignin and carbonization, with a final solid residue of 23.4 wt. %. The largest weight loss occurs at 320°C, as evidenced by the DTG curve (Figure 4.1.b). The thermo-degradation of WCO has shown one main stage from 320°C to 505°C. It showed depolymerization of complex organic compounds with the maximum weight loss at 424 °C and a final solid residue of 0.74%. Individual IB and WCO exhibit a significant weight loss from 120°C to 650°C, which indicates the possibility of an interaction effect on bio-oil quality during CCP. On the other hand, thermal decomposition of IB:WCO mixture with the presence of catalyst shifts the maximum degradation temperature to 438°C. The catalyst pore size distribution plays an important role during the decomposition of the IB:WCO mixture. When the catalyst pore size is lower than the reactant molecule diameter, it hinders the diffusion of intermediates and increases degradation temperature [354].

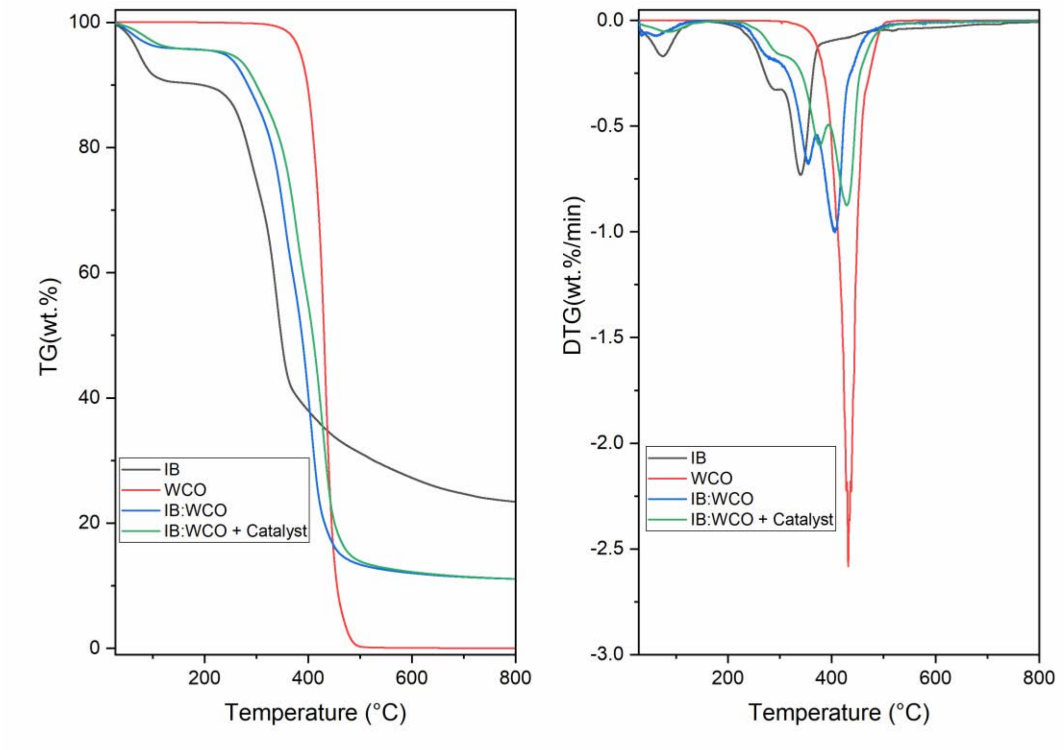

Figure 4.1. (a) TGA and (b) DTG curves for IB, WCO, IB: WCO (1:1) and IB:WCO (1:1) + Catalyst (SrO/Y-zeolite-10%) from room temperature to 800°C at a heating rate of 10°C/min.

Figure A.13 presents variations in ΔW (difference of mass loss) with temperature for non-catalytic co-pyrolysis of IB:WCO (1:1) mixture. The ΔW takes place in three stages; (1) 300 - 380°C; (2) 380 - 510°C; and (3) 510 - 800°C. There is no significant ΔW for temperatures below 300°C. This is because the main degradation process (main pyrolysis) requires temperatures above 300°C. In stage (1), the ΔW of IB:WCO mixture displays a positive correlation with temperature, which shows that decomposition of IB increases while increasing the WCO amount in the mixture. In stage (2), a major reduction in ΔW is observed with a peak at 420°C. In stage (3), there is an increasing trend of ΔW, indicating that the degradation rate of WCO increases compared to IB.

4.3.2 Catalyst characteristics

XRD patterns of the three catalysts are provided in Figure 4.2. All samples display high and low-intensity peaks at 2-theta values of 6.3°, 10.25°, 12.2°, 16°, 19.1°, 20.7°, and 23.3°, attributed to parent Y-zeolite (JCPDS-01-077-1551). Compared to the parent Y-zeolite [4], the XRD peak intensities are lower for the SrO-modified Y-zeolite catalysts, potentially arising from the incorporation of strontium cations that may change the parent Y-zeolite crystallinity and scattering properties [355]. For the SrO-impregnated catalysts, XRD peaks at 2-theta values of 10.15°, 11.9°,20.4°, 23.7°, 31.45° and 34.75° indicate the presence of SrO on the catalysts [356].

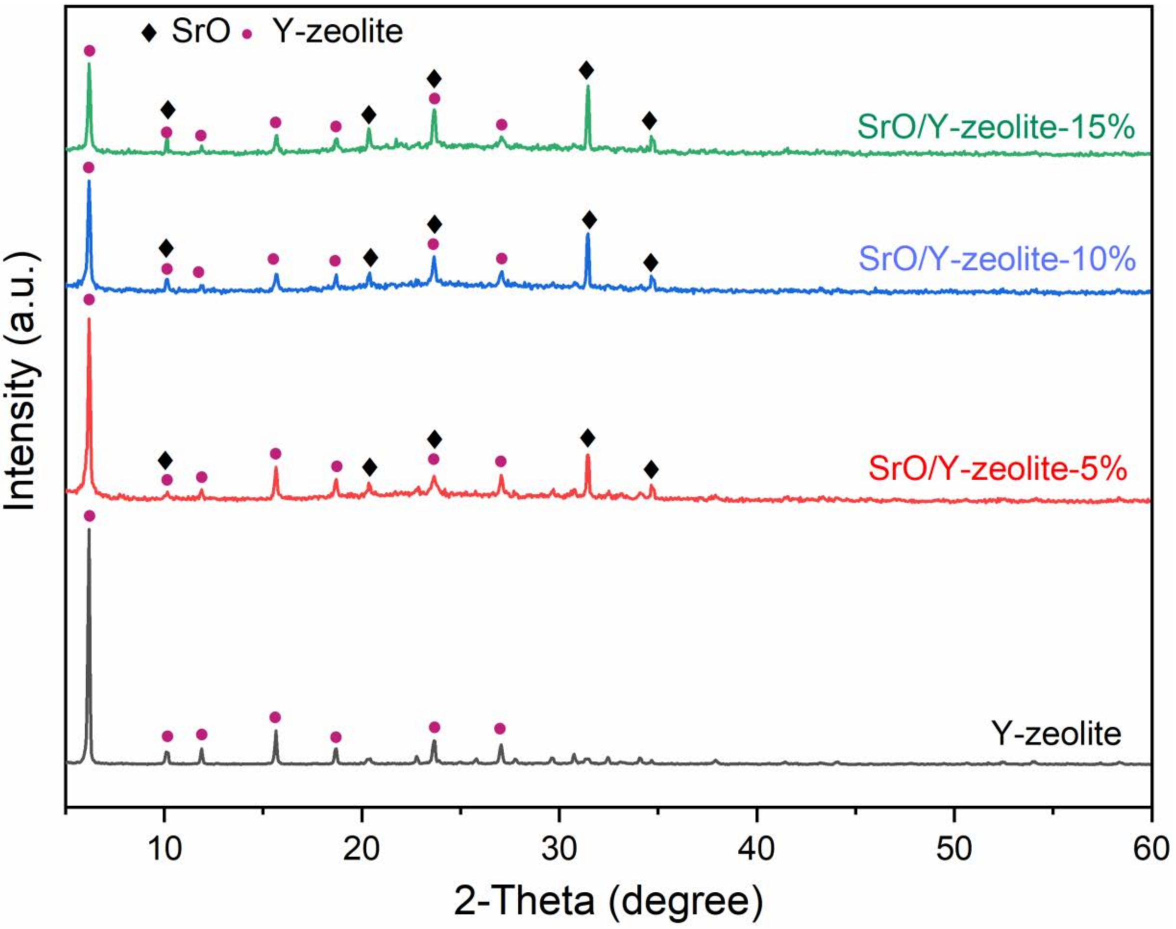

Figure 4.2. XRD profiles of parent Y-zeolite, SrO/Y-zeolite-5%, SrO/Y-zeolite-10%, and SrO/Y-zeolite-15%.

Nitrogen adsorption-desorption isotherms for SrO-loaded Y-zeolite catalysts are provided in Figure A.14, with the specific surface areas and pore volumes provided in Table 4.2. The parent Y-zeolite exhibits a type-I isotherm which corresponds to a microporous material according to the IUPAC classification [4]. All SrO-loaded Y-zeolite samples possess a hysteresis loop, indicating the presence of mesopores in the catalysts (Figure A.14). The parent Y-zeolite has the highest surface area (577.2 m^2/g), while SrO addition decreases the surface area with the loss in the surface area increases with increasing SrO loading (SrO/Y-zeolite-15%, 224.8m^2/g). As the SrO loading increases, there is an increasing potential for pore blockage in the zeolite framework. Further, a portion of the sodium cations was substituted by strontium cations, contributing to the overall decrease of the surface area. These results are in line with previous studies that also described a noticeable decrease in surface area after the addition of metal oxides onto the zeolite surface [357, 358].

Table 4.2. Specific surface areas and pore volumes for parent Y-zeolite and Y-zeolite loaded with 5 wt. %, 10 wt. % and 15 wt. % SrO.

Catalysts	S_{BET} (m^2/g)	S_{Meso} (m^2/g)	V_{total} (cm^3/g)	V_{micro} (cm^3/g)	V_{meso} (cm^3/g)	Sr wt.%*	
						Nominal loading	Actual loading
Y-zeolite	577.2	53.5	0.33	0.27	0.07	-	-
SrO/Y-zeolite-5	397.6	146.1	0.25	0.10	0.15	5	4.31
SrO/Y-zeolite-10	242.0	95.3	0.16	0.06	0.14	10	9.17
SrO/Y-zeolite-15	224.8	90.4	0.16	0.05	0.10	15	12.26

*Determined by EDS analysis.

The microporous volume (V_{micro}) also decreased from 0.10 cm^3/g to 0.05 cm^3/g as SrO loading increased from 10 wt. % to 15 wt. %. This showed that an increase in mesoporous volume was achieved by reducing microporous volume. The low microporous volume hinders the penetration of IB and WCO molecules during the co-pyrolysis, forcing the reaction to take place on the surface of the catalysts. The sequential dealumination and desilication further incorporated mesoporosity, which is confirmed by increasing mesoporous volume from 0.07 cm^3/g (Y-zeolite) to 0.15 cm^3/g (SrO/Y-zeolite-5). Incorporating mesoporous volume also enhances the mass transfer and allows IB and WCO molecules to react with the catalyst. All the SrO-loaded samples exhibit a higher mesoporous area than the parent Y-zeolite. SrO/Y-zeolite-5% exhibited the highest mesoporous surface area (146.1 m^2/g) and mesopore volume (0.15 cm^3/g). As the SrO loading increased from 10 wt. % to 15 wt. %, the mesoporous surface area decreased from 95.3 m^2/g to 90.4 m^2/g, which is due to the blockage of a portion of the Y-zeolite pores by the deposition of SrO. The presence of additional mesoporous surface area would impart more active sites for the deoxygenation reaction.

The FTIR spectra of SrO/Y-zeolites catalysts are presented in Figure A.15. All samples display peaks at 485 cm^{-1}, 577 cm^{-1}, 791 cm^{-1}, and 961 cm^{-1}, attributed to the parent Y-zeolite. Broad bands associated with asymmetric and symmetric stretching vibrations of framework O-T-O of the peak centred at 1030 cm^{-1} for the SrO/Y-zeolite become sharper and shift compared to the parent Y-zeolite. The occurrence of framework vibrations, which are typical of zeolite materials, confirms the mesoporous structure development. As the SrO loading increases, the intensity of the band associated with the O-T-O bond vibrations decreases. Figure A.16 provides SEM images of the parent and SrO-loaded Y-zeolite, highlighting the morphology of the particles. The parent Y-zeolite has an octahedral structure. The sharp edges and overall morphology of the Y-zeolite remain unaltered following SrO loading, while irregular-shaped particles are also apparent. However, no discernible morphological variations were observed after loading the SrO on the zeolite.

NH_3 and CO_2 TPDs for the SrO-loaded Y-zeolite catalysts are provided in Figure A.17, with the total acidity and basicity provided in Table 4.3. The acidity of the SrO/Y-zeolites was measured using NH_3-TPD; the intensity and position of the NH_3 desorption peaks represent the number of acid sites and their strength, respectively [359]. The NH_3 desorption peak in the range of 100°C-300°C is attributed to weak acid sites while peaks ranging from 300°C-600°C are attributed to strong acid sites [360]. SrO/Y-zeolite-5% and SrO/Y-zeolite-10% display-one desorption peak (weak acid sites) centred at a temperature of 225°C and 228°C with a total acidity of 0.291 and 0.288 mmol/g, respectively. In contrast, SrO/Y-zeolite-15% exhibits two desorption peaks at 228°C and 475°C, with a total acidity of 0.436 mmol/g.

Table 4.3. Qualitative analysis of NH_3-TPD and CO_2-TPD profiles for SrO/Y-zeolite catalysts.

Catalyst	NH_3-TPD			CO_2-TPD
	Weak acid (mmol/g)	Strong acid (mmol/g)	Total acidity (mmol/g)	Total basicity (mmol/g)
SrO/Y-zeolite-5%	0.291	-	0.291	0.948
SrO/Y-zeolite-10%	0.288	-	0.288	1.061
SrO/Y-zeolite-15%	0.402	0.034	0.436	0.889

In addition, the total basicity of the SrO/Y-zeolites was analysed by CO_2-TPD. Overlapping of the various CO_2 desorption peaks makes it difficult to clearly assign each peak to each basic site type (weak or strong); however, the overall high amount of CO_2 desorbed suggests strong total basicity within the samples [316]. In general, the CO_2-TPD analysis shows an opposite trend compared to the NH_3-TPD analysis. The SrO/Y-zeolite-10% possesses an intense peak in the range of 300°C -600°C with total CO_2 desorption of 1.061 mmol/g. Increasing the amount of strontium from 10% to 15% reduced the total basicity to 0.889 mmol/g. The result illustrates the presence of high basicity, revealing strong bonding strength between SrO and the zeolite framework for SrO/Y-zeolite-10% [361].

4.3.3 Pyrolysis product characteristics

4.3.3.1 Non-catalytic pyrolysis and bio-oil composition

Pyrolysis of individual feedstocks (IB and WCO) was performed in the fixed bed reactor, and the yield of pyrolysis products is summarized in Table 4.4. The pyrolysis products from the pyrolysis at 550°C of IB alone comprise bio-oil (29.1 wt. %), biochar (31.0 wt. %), and pyrolytic gas (39.9 wt. %). In contrast, WCO produced a bio-oil yield of 66.5 wt. % and a lower bio-char yield of 8.1 wt. %. The bio-char yield from IB was much higher than for WCO due to the higher ash content (23.4 wt.%) of IB. Cellulose and lignin decomposition during IB pyrolysis enhanced the formation of char and gaseous products [362]. The presence of alkali and alkaline earth metals in IB also promoted secondary cracking reactions of condensable vapor, which is converted into non-condensable gaseous products [363]. However, the bio-oil yield from IB pyrolysis was found to be lower than WCO. In previous studies, the pyrolysis of triglycerides-based materials, such as waste animal fats, beef tallow, and fish oil wastes, showed bio-oil yields of 77.9 wt. %, 77.1 wt. %, and 73 wt. %, respectively [136, 364, 365]. Accordingly, the addition of triglyceride-based materials to lignocellulose biomass is expected to increase the bio-oil yield during co-pyrolysis.

^{13}C NMR analyses were conducted to estimate the carbon percentage of aromatics and various oxygenates, including fatty acids and tiny acids, for individual and mixtures of IB and WCO. The pyrolytic organic products contained different oxygenated compounds. Figure 4.3 illustrates the percentage of carbon in aromatics, carbonyl, aliphatics, and levoglucosan. Non-catalytic pyrolysis of IB produced an aromatic carbon yield of 10.6 %. As expected, the bio-oil obtained from WCO was mainly composed of aliphatic C-C and aliphatic C-O with yields of 42.4 % and 17.1 %, respectively.

Table 4.4. Impact of reaction temperature, strontium loading and IB:WCO ratio on product yield during catalytic co-pyrolysis of mixed IB and WCO. Included are product yields for individual IB and WCO feedstocks. All experiments were performed at a residence time of 30 min.

Run	Reaction Temperature (°C)	Strontium loading (wt. %)	IB:WCO ratio	Product yield (wt. %)			Bio-oil moisture content (wt. %)
				Biochar	Bio-oil	Gases	
IB	550	-	-	23.4	29.1	47.5	31.7
WCO	550	-	-	8.1	66.5	25.4	6.5
IB+WCO	550	-	1:1	18.4	40.4	41.2	27.9
1	450	5	1:1	13.8	51.9	34.3	18.0
2	450	10	2:1	17.6	44.8	37.7	20.8
3	450	15	4:1	17.2	41.6	41.2	25.9
4	550	10	1:1	9.4	55.3	35.2	17.3
5	550	15	2:1	17.0	50.9	32.2	22.5
6	550	5	4:1	19.8	48.8	31.4	21.7
7	650	15	1:1	16.8	44.6	38.6	18.1
8	650	5	2:1	13.7	47.1	33.4	24.2
9	650	10	4:1	18.1	39.2	42.7	27.5

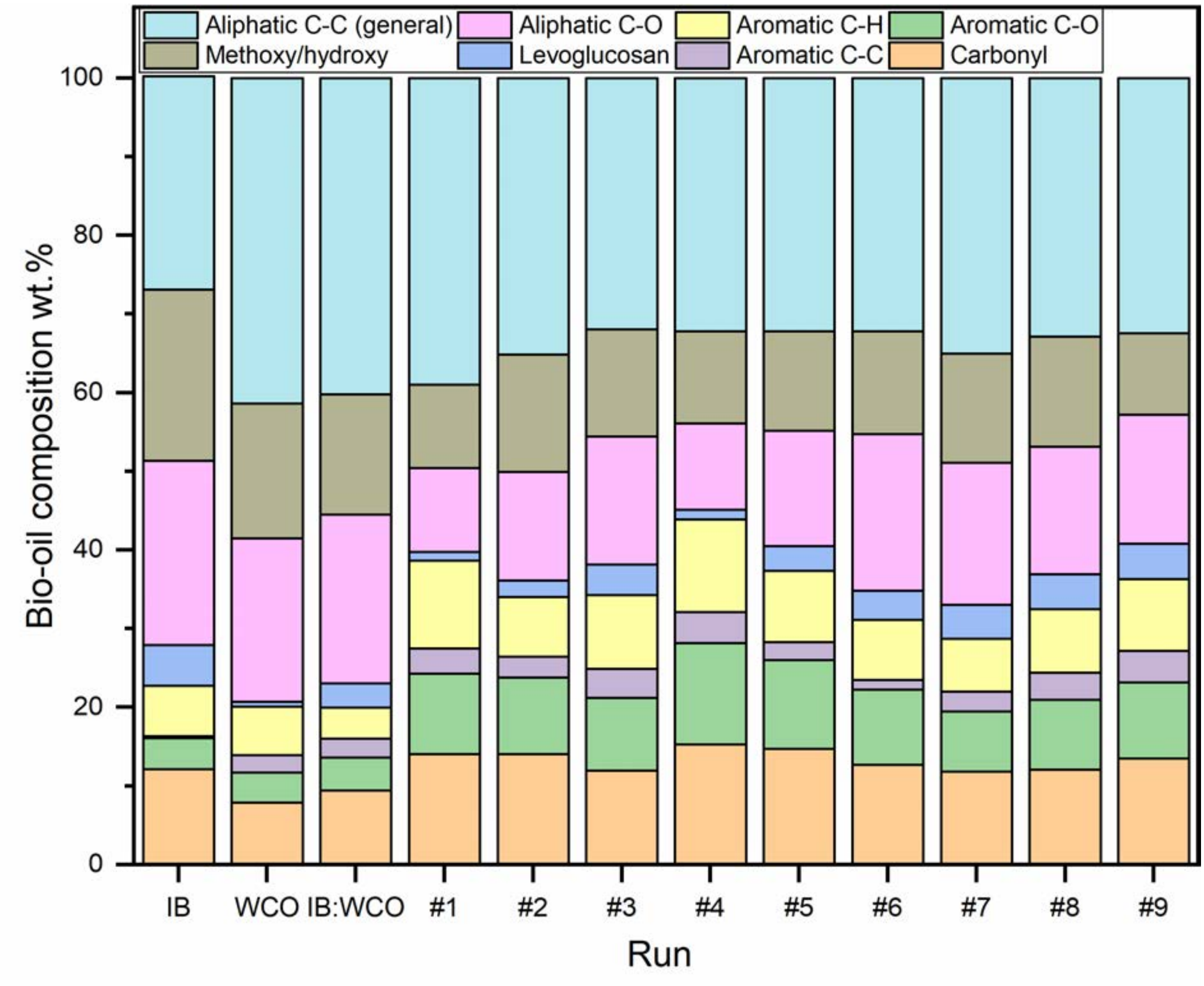

Figure 4.3. ^{13}C NMR representative chemical functional groups and their relative concentration in bio-oil obtained from individual IB, WCO and IB:WCO mixture via catalytic co-pyrolysis using SrO/Y-zeolite. The conditions for each run are described in Table 4.4.

4.3.3.2 Effect of reaction temperature on product distribution and bio-oil composition

CCP of IB and WCO mixture was performed at different reaction temperatures (450ºC, 550ºC, and 650ºC) with varying IB:WCO ratios to investigate the effect of reaction temperature on product distribution. When the reaction temperature increases from 450ºC to 650ºC, the bio-oil yield decreases by 15 %. The highest bio-oil yield (55.3 wt. %) was obtained at 550°C, which represents the optimum temperature where maximum devolatilization and bond breakage occurs. As the CCP temperature increases, an increasing number of secondary reactions of small molecular weight organic fractions in the IB and WCO mixture are initiated and decomposed into non-condensable gaseous products. As shown in Figure A.18, a high amount of WCO favours bio-oil production, with the yield increasing from 48.8 % to 55.3 % when the WCO percentage increases from 20 % to 50 % at 550°C. These results confirm that there is a possible interaction between CCP process parameters (temperature and IB:WCO ratio).

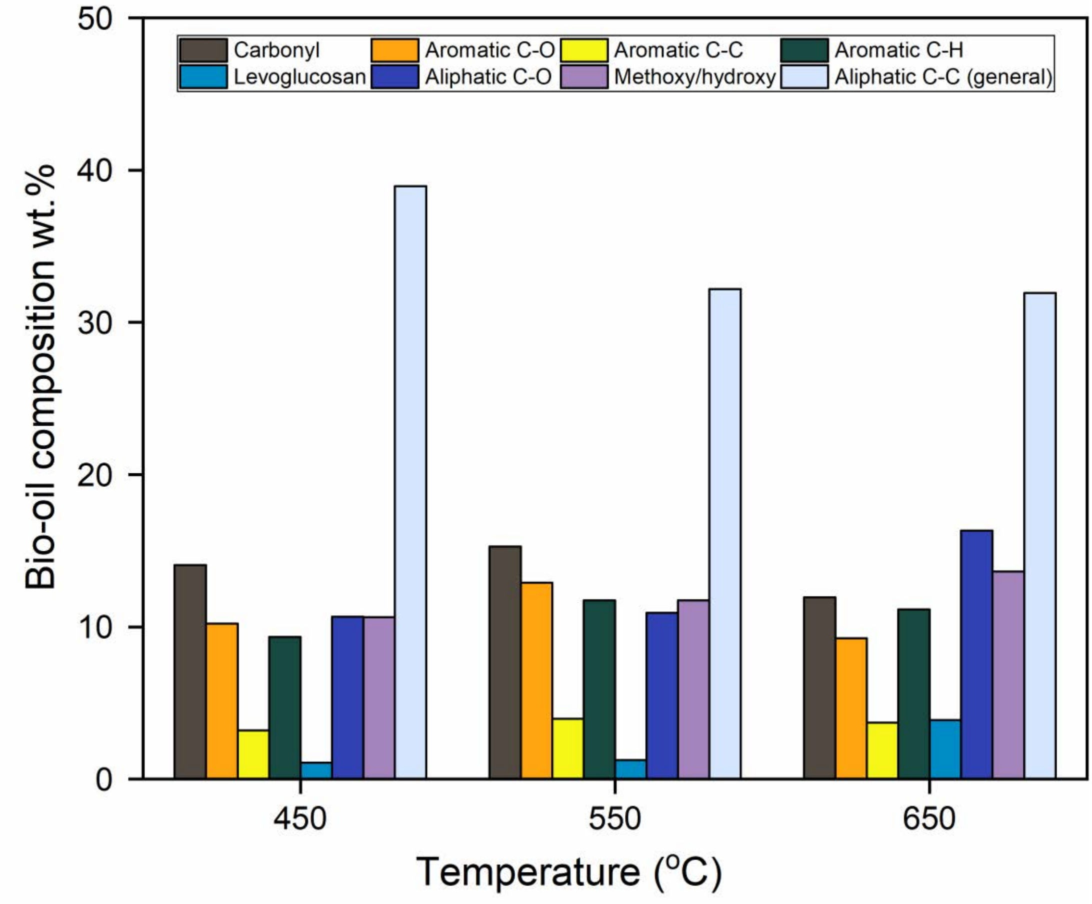

Figure 4.4. Effect of reaction temperature on bio-oil product composition obtained from CCP of IB and WCO mixture using SrO/Y-zeolite-10%, IB:WCO (1:1), a heating rate of 10°C/min and residence time of 30 min.

Non-catalytic individual IB and WCO produced mainly aliphatic and phenolic compounds, while the CCP of IB and WCO mixtures displayed an increase in aromatic yield. As shown in

Figure 4.4, the aromatic carbon yield first decreased and then increased as it reached a CCP temperature of 650°C. The maximum aromatic carbon yield (24.6 %) was obtained at 650°C, which is due to the endothermic nature of the CCP that is breaking down more organic matter and promoting secondary cracking reactions at 650°C [366]. SrO/Y-zeolite favored the catalytic cleavage of long-chain hydrocarbons into shorter molecules. The acidic sites of SrO/Y-zeolite removed hydrogen atoms from aliphatic hydrocarbons via the Diels–Alder process to produce short-chain hydrocarbons [367]. In the CCP of IB and WCO mixture, methoxy/hydroxy are the most active species, which accelerated aliphatic decomposition. These findings are in line with previous work by Xue et al. [368], who found that biomass-derived chemicals promote the decomposition of long-chain hydrocarbons.

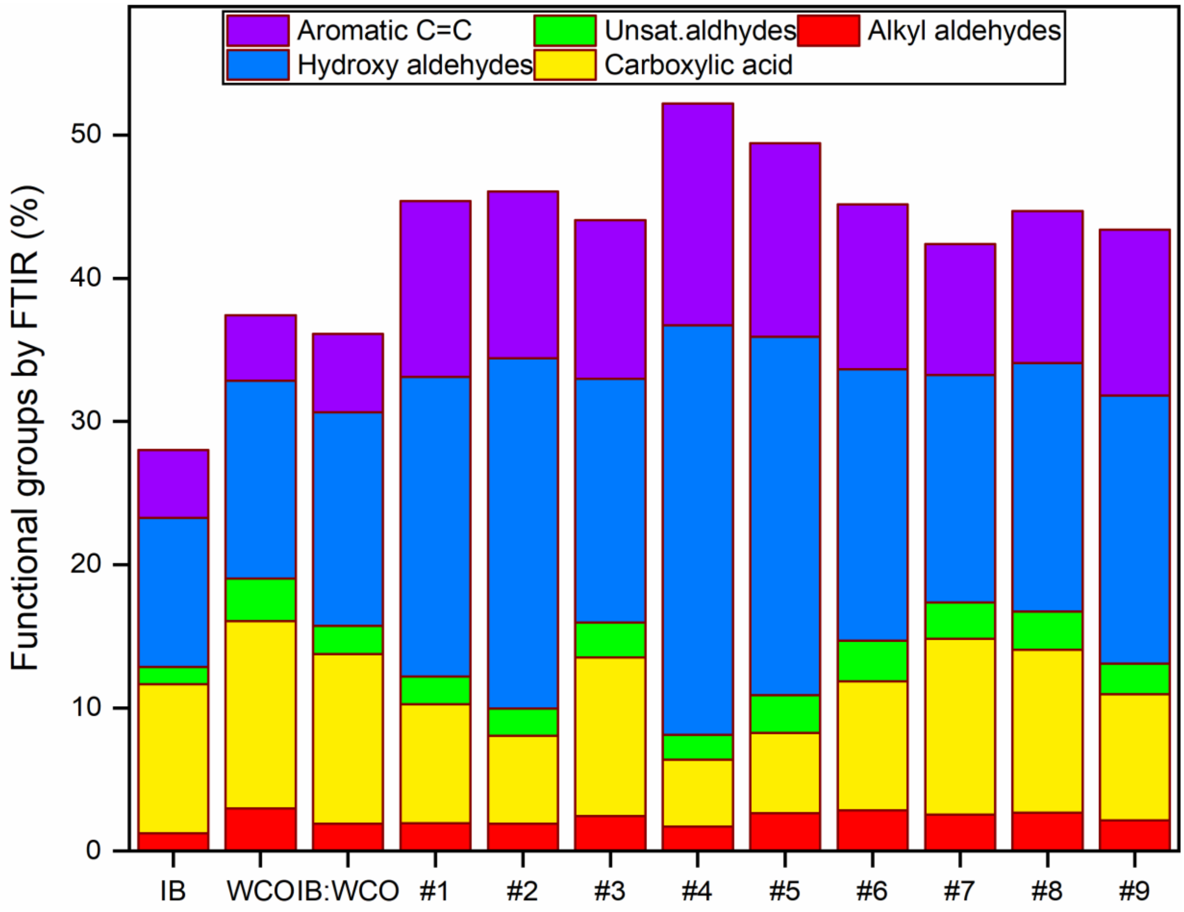

Figure 4.5. FTIR spectra in the region 1850 to 1490 cm^{-1} with characteristic peak deconvolution for IB, WCO, IB:WCO and catalytic co-pyrolysis using SrO/Y-zeolite catalysts. The conditions for each run are described in Table 4.4.

FTIR spectroscopy was performed to semi-quantify the different carbonyl groups in the aromatic components of the bio-oil that are represented by the spectral peaks between 1850 and 1490 cm^{-1}. Lievens et al. [369] stated that a better comparison of bio-oils may be obtained by peak fitting the spectra between 1850 and 1490 cm^{-1} to identify the relative amounts of functional groups. All the bio-oil samples obtained in this study were subject to the same peak deconvolution approach, with the results provided in Figure 4.5. The carboxylic acid group is represented by the band at 1710 cm^{-1} from the deconvoluted peak, which is considerably higher in the non-catalytic WCO and increases with temperature. The presence of a more prominent peak of 1696 cm^{-1} in the FTIR spectrum, which is attributed to the ketone group, shows that the carboxylic acids underwent C-C single bond coupling via the ketonisation process. As H_2O and CO_2 are by-products of the ketonisation reaction, it is suggested that decarboxylation and dehydration are the preferred deoxygenation pathways for removing oxygen from bio-oil.

4.3.3.3 Effect of IB:WCO ratio on product distribution and bio-oil composition

The effect of feedstock ratio on product distribution was examined for IB:WCO ratios of 1:1, 2:1 and 4:1 at CCP temperature of 550°C using SrO/Y-zeolite-10%, as shown in Figure 4.6. The amount of WCO played a significant role in bio-oil, pyrolytic gas, and bio-char yields (Figure A.18b), where increasing the amount of WCO in the mixture increased the bio-oil yield. The highest bio-oil yield was obtained using a 1:1 feedstock ratio at a CCP temperature of 550°C. Increasing IB:WCO ratio from 1:1 to 4:1 reduced biochar and pyrolytic gas yield to 9.4 % and 35.2 %, respectively. The results obtained in this study align with other literature, which stated that blending biomass with triglyceride-based material increases bio-oil yield [364, 365, 370]. Moreover, bio-oil yield decreased when the IB:WCO ratio increased from 2:1 to 4:1 at 650°C, mainly due to the secondary decomposition of the volatile matter prior to condensation [138].

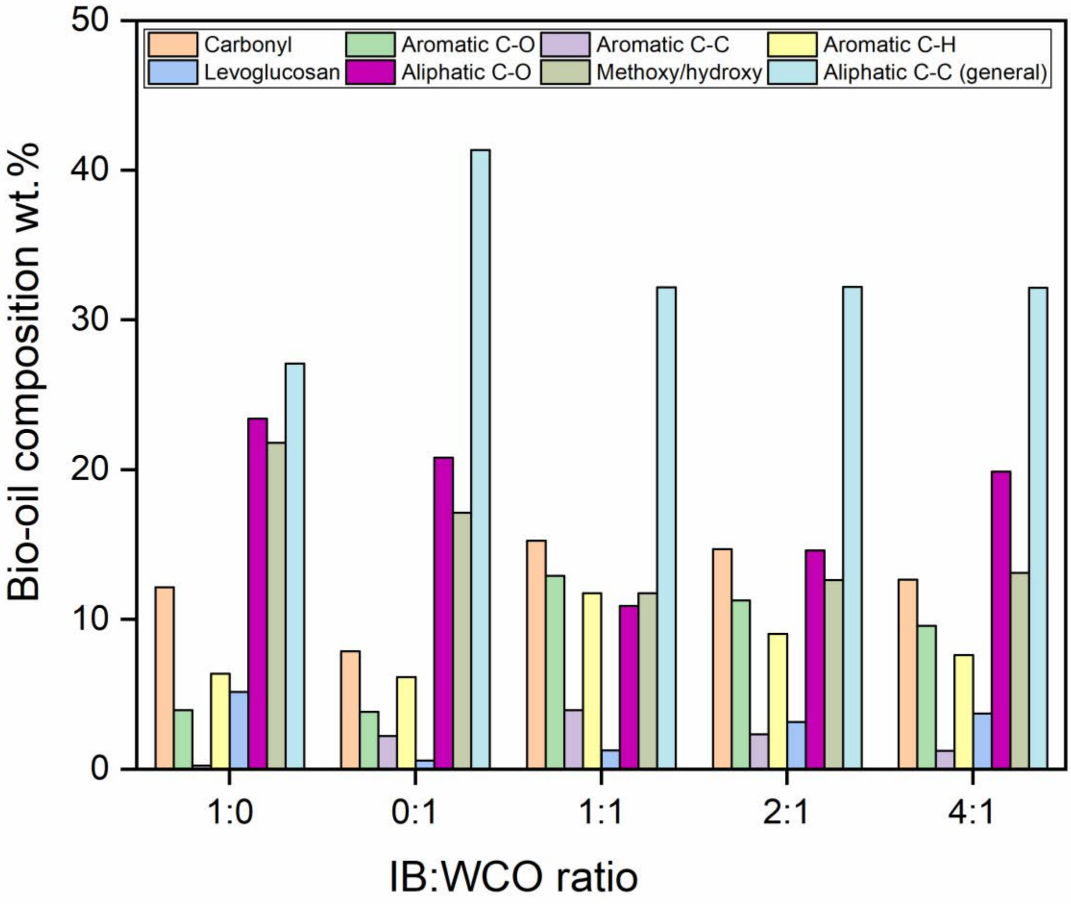

Figure 4.6. Effect of IB:WCO ratio on bio-oil product composition obtained from CCP of IB: WCO mixture at 550°C using SrO/Y-zeolite-10%.

As shown in Figure 4.6, thermal cracking of WCO enhanced the generation of aliphatics and produced a significant amount of aliphatics with a low IB:WCO ratio. In contrast, the CCP of the IB:WCO mixture generated more aromatic hydrocarbons (18.4 %-28.6 %) compared to non-catalytic pyrolysis for both IB (10.6 %) and WCO (12.2 %). The CCP also enhanced the conversion of additional oxygenated compounds into aromatics containing C-O and C-H. The lowest methoxy/hydroxy percentage occurred when the WCO proportion was increased. The IB:WCO (1:1) produced the maximum aromatic carbon yield and a low percentage of levoglucosan, which can be attributed to the formation of aromatics via the Diels–Alder reaction of glycerol moieties. The findings showed that adding WCO prevents the conversion of mono-aromatics into poly-aromatics. The increase in the IB:WCO ratio from 1:0 to 1:1 resulted in a decrease in the fraction of methoxy/hydroxy, which may be attributed to phenols deoxygenation to aromatics. The demethoxylation process slowed down the deoxygenation reactions as the IB:WCO ratio decreased from 1:1 to 2:1, while the presence of levoglucosan and methoxy/hydroxy was boosted. Increasing the WCO content increased alkanes and alkenes formation due to the generation of RCOO radicals via a decarboxylation reaction. The results from the FTIR analysis for carbonyl groups in aromatic compounds agreed closely with the ^{13}C NMR analysis indicating that as the IB:WCO ratio decreases, the aromatic content of the bio-oil increases.

4.3.3.4 Effect of strontium oxide loading on product distribution and bio-oil composition

The influence of SrO loading (5, 10, and 15 wt. %) onto Y-zeolite on bio-oil yield and quality is presented in Figure 4.7 and Figure A.18. Non-catalytic co-pyrolysis of IB:WCO (1:1) mixture produced an aromatic carbon yield of 10.6 %, which is higher than the individual feedstocks. However, the bio-oil obtained was mainly composed of aliphatic C-C and aliphatic C-O with yields of 40.23 % and 15.29 %, respectively. The addition of catalyst, SrO/Y-zeolite-10% at 550°C produced the highest bio-oil yield (55.3 %), while SrO/Y-zeolite-5% generated a maximum bio-oil yield of 48.8 % at an IB:WCO ratio of 1:1, and SrO/Y-zeolite-15% produced a bio-oil yield of 50.9 %. It is apparent that increasing the SrO loading increased the bio-oil yield until reaching a maximum of 10 wt. %, whilst a further increase to 15 wt. % decreased the bio-oil yield. However, at a low reaction temperature (450°C), the bio-oil yield decreased as the SrO loading increased. The basic sites on the SrO/Y-zeolite catalyst (SrO) can convert the fatty acids to poly-aromatics through decarboxylation, decarbonylation and dehydration reactions and remove oxygen in the forms of CO_2, CO, and H_2O. Therefore, increasing the SrO amount promoted decarboxylation reactions, ketonisation and aldol condensation, which caused a decrease in the bio-oil yield and increased the pyrolysis gas yield. The results are in good agreement with previous studies, which stated that increasing the catalyst loading enhances CO and CO_2 production via decarbonylation and decarboxylation processes, consequently reducing the bio-oil yield [371].

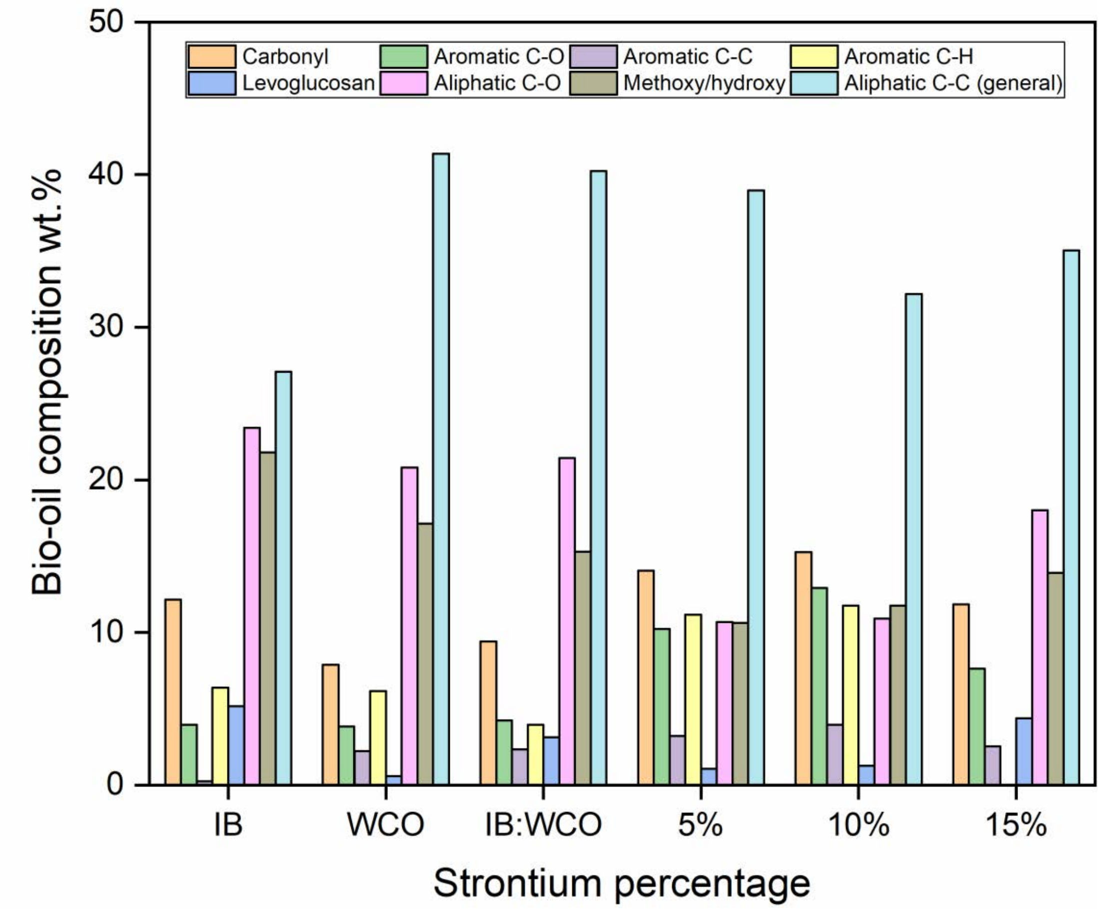

Figure 4.7. Bio-oil product composition for non-catalytic IB, WCO, IB:WCO and the effect of SrO loading on Y-zeolite on bio-oil composition obtained from IB:WCO (1:1).

The physicochemical properties of the SrO/Y-zeolite catalysts, such as surface area, pore volume, and acidic and basic active sites, influenced the bio-oil yield [372]. The impact of SrO loading on the carbon composition within the bio-oil yield is shown in Figure 4.7. The aromatic carbon yield of bio-oil increased with increasing SrO loading from 5 wt. % (24.6 % yield) to 10 wt. % (28.6 % yield) at an IB:WCO of 1:1. The rate of the catalytic cracking reaction is directly related to the availability of active sites on the catalyst whereby the 10 wt. % SrO-loaded Y-zeolite provides the optimum number of total active catalytic sites to conduct the cracking and deoxygenation reactions. The acid sites in mesoporous Y-zeolite convert long-chain hydrocarbons and acids produced from lignin and cellulose into aromatics through cracking and deoxygenation reactions [373]. However, adding SrO introduced additional basic sites on the hierarchical Y-zeolite catalyst, increasing the aromatic carbon yield by converting ketones, aldehydes and fatty acids into mono-aromatics. Therefore, increasing the SrO content until it reaches an optimum loading (10 wt. %) enhanced the aromatic carbon yield and decreased the aliphatic compound carbon yield. The yield of aromatic C-H and aromatic C-C decreased when the SrO loading was increased to 15 wt. %. This may derive from further increases in the SrO loading that might lead to SrO agglomeration on the active sites of the Y-zeolite surface, in turn, reduced the catalytic activity.

4.3.3.5 Reaction mechanism

Compiling the findings from the IB and WCO CCP in the presence of the SrO/Y-zeolite catalyst, a reaction mechanism describing aromatics formation is proposed, as shown in Figure 4.8. During CCP, the components of IB undergo thermal depolymerization into smaller intermediate products. The results in Figure 4.6 verified that levoglucosan present in the bio-oil was due to the addition of IB. The complex structure of lignin breaks into free radical benzene rings, which bond with hydrogen radicals from SrO/Y-zeolite acidic sites to form phenols and methoxy–substituents. Meanwhile, during thermal decomposition, WCO converted into alkyl radicals and olefins via β-scission in the presence of the SrO/Y-zeolite catalysts. As shown in Figure 4.8, the aliphatic fatty acid (R) present in the triglycerides, such as oleic acid, linoleic acid, palmitic and stearic acid, underwent thermal degradation to convert into wax and oxygenated compounds. The oxygenated compounds are simultaneously converted into light alkanes and aromatic hydrocarbons via catalytic cracking and aromatization reactions [374]. The oleic acid present in WCO first decomposes into acrolein and fatty aldehydes [375]. Then intermediate products such as phenylbutylene and propylene benzene are produced that promote the formation of olefins, which are converted into low-chain hydrocarbons. The acid sites on the Y-zeolite assist with producing carbanions by abstracting hydrogen from aliphatic C-C in WCO. The unstable carbanions further undergo β-scission to form olefins and a hydrocarbon pool [376, 377]. The resulting short olefins are subsequently converted to aromatics via the Diels-Alder reaction. The intermediate products further undergo decarbonylation and dehydration reactions and combine with short chains of olefins to produce aromatic compounds instead of undergoing polymerization. The oxygenated compounds are mainly removed in the form of water during dehydration, decarboxylation, and thermal cracking [378]. Decarboxylation reactions release water by converting fatty acids and esters into CO_2, water, and ketones [379]. Water is also produced by a dehydration reaction, which involves the breakdown of the C-O bond of triglycerides and the removal of oxygen in the form of H_2O. Overall, the alkyl radicals and hydrocarbon pool provided by the WCO promote the conversion of methoxy/hydroxyl, phenols and levoglucosan from the IB into poly-aromatics.

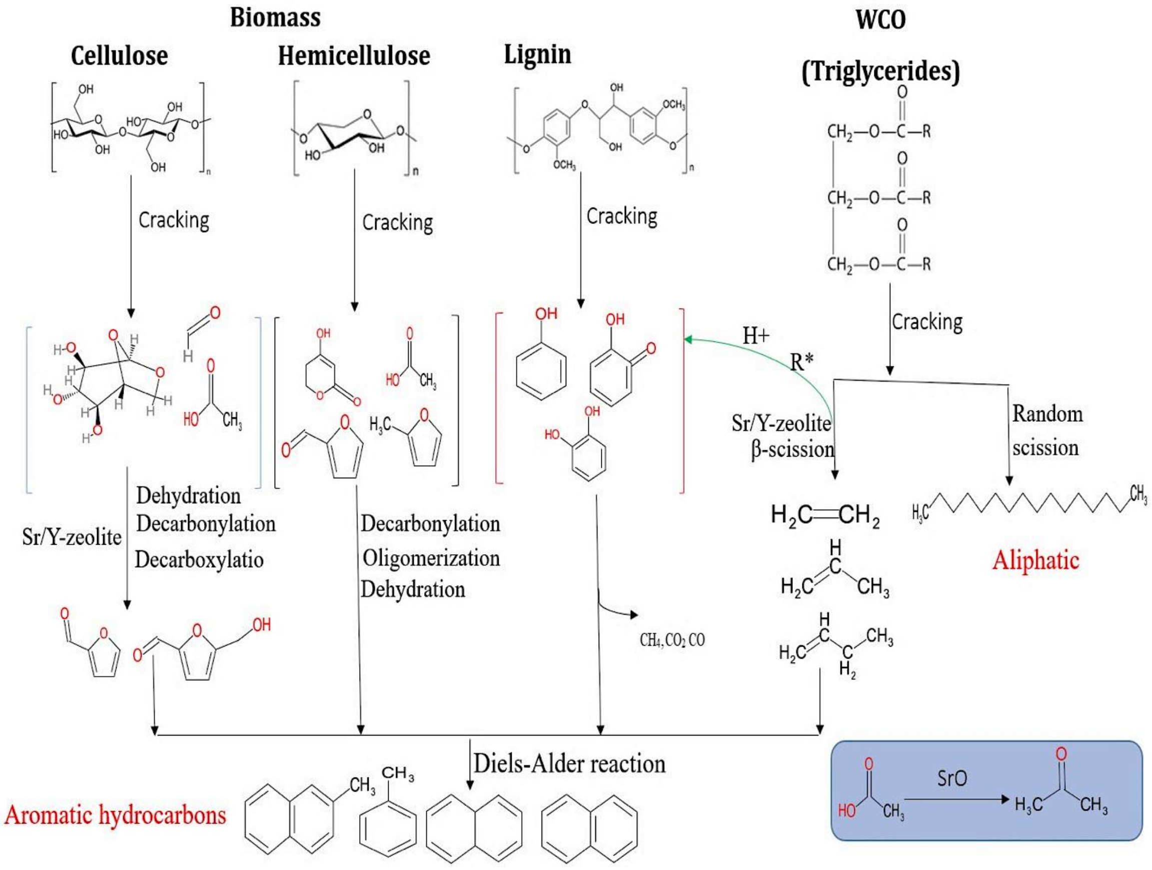

Figure 4.8. Proposed reaction mechanism for catalytic co-pyrolysis of IB:WCO mixture in the presence of SrO/Y-zeolite.

The overall cost-effectiveness and environmental sustainability of the catalytic co-pyrolysis process can be significantly influenced by the selection of catalyst and its recyclability. Therefore, research on catalyst deactivation, regeneration, and reusability is critical to optimize the process. However, due to the in-situ catalytic pyrolysis mode used in our study, the catalyst could not be separated from the final product, which is biochar. Nevertheless, the use of in-situ catalytic pyrolysis mode has the advantage of being more cost-effective due to its single reactor operation. On the other hand, ex-situ catalytic pyrolysis mode enables catalyst recovery and reuse, which can be more environmentally sustainable. Therefore, future research should aim to combine the advantages of both in-situ and ex-situ catalytic pyrolysis modes to optimize the catalytic co-pyrolysis process and minimize its environmental impact.

4.4 Conclusions

In this work, the impact of SrO-modified hierarchical Y-zeolite catalyst on upgrading bio-oil quality was investigated via CCP of IB and WCO mixture. Various unsaturated and saturated fatty acids groups are presented in the WCO, which makes it suitable for CCP in combination with biomass feedstock. The effect of CCP temperature, SrO loading and IB:WCO ratio on bio-oil yield was explored, with the results demonstrating that a 550°C reaction temperature, 10 wt. % SrO loading and IB:WCO ratio of 1:1 delivered the highest bio-oil yield. In terms of aromatic yield, while the individual non-catalytic pyrolysis of IB and WCO produced aromatic carbon yields of 10.6% and 12.2%, respectively; however, CCP of IB:WCO (1:1) mixture with a 10 wt. % SrO loading Y-zeolite at 550°C offered the highest aromatic yield of 28.6%. Increasing the SrO loading to 15 wt. % reduced aromatic C-H and aromatic C-C yield. The IB:WCO ratio of 4:1 increased the formation of alkanes and alkenes due to the generation of the RCOO radical via the decarboxylation reaction. The acidic sites on the SrO/Y-zeolite remove hydrogen atoms from aliphatic hydrocarbons via the Diels–Alder process to produce short-chain hydrocarbons. Loading SrO onto the Y-zeolite created new basic active sites, in turn increasing the aromatic carbon yield by converting ketones, aldehydes, and fatty acids into mono-aromatics. Overall, the aromatics were synergistically generated from methoxy/hydroxyl, phenols and levoglucosan from the IB with the assistance of alkyl radicals and the hydrocarbon pool provided by WCO. The results demonstrated that SrO/Y-zeolite is a potential catalyst to produce high-quality bio-oil from co-pyrolysis of IB and WCO.

5 Examining the effect of bimetallic catalyst on bio-oil product distribution

Abstract

Catalytic co-pyrolysis (CCP) of IB and WCO over bimetallic (Ni, Cu, Zn, Ag, and Fe) strontium oxide (SrO)-loaded hierarchical Y-zeolite was performed using Py-GC/MS. The effect of bimetallic catalyst on kinetics, reaction mechanisms and product distribution of CCP was examined. The bimetallic catalysts were prepared via wet impregnation and characterized using N_2 adsorption-desorption, SEM, XPS and FTIR. CCP using Ag-SrO/Y-zeolite showed the lowest activation energy of 163.1 kJ/mol compared to non-catalytic co-pyrolysis (193.21 kJ/mol). The results indicated that Cu-SrO/Y-zeolite produced the highest aromatic yield of 65.43% at a temperature of 750°C with a catalyst to feedstock ratio of 1:1. The present work indicates that Cu-SrO/Y-zeolite active sites increased the aromatic yield.

Keywords: Biomass; Bimetallic catalyst; Aromatics; Kinetics; Py-GC/MS

This work has been published as: Tewodros Kassa Dada, Md Anwarul Islam, Alex Xiaofei Duan, Elsa Antunes. Catalytic co-pyrolysis of ironbark and waste cooking oil using X-strontium /Y-zeolite (X= Ni, Cu, Zn, Ag, and Fe), Journal of the Energy Institute, 2022.

5.1 Introduction

Thermochemical conversion of biomass into liquid fuel has shown potential for feedstock to replace fossil fuel due to their carbon-neutral properties. Among thermochemical processes, pyrolysis is predominantly used to produce hydrocarbons fuel at a low cost [126, 380]. Bio-oil produced via pyrolysis has potential as a fuel for various applications and as a feedstock for the production of hydrocarbons that may be easily incorporated into existing petroleum refineries or future bio-refineries [381, 382]. However, biomass pyrolysis limits the yield of aromatic hydrocarbon compounds found in the liquid fuel. Consequently, to overcome these issues, many studies focus on enhancing bio-oil quality by increasing the hydrocarbons yield [1, 383]. Co-pyrolysis of biomass with hydrogen-rich wastes (polymeric and triglycerides wastes) are used as alternative pathways to enhance the bio-oil quality [384, 385].

Co-pyrolysis is a cost-effective way to convert biomass and wastes into non-fossil fuels due to the positive synergistic effects between feedstock constituents [272, 386]. Triglyceride wastes, such as waste cooking oil, have a simple structure and higher hydrogen–carbon ratio than biomass feedstock and hence have a greater potential to be converted into biofuel with a high calorific value [387]. Co-pyrolysis of triglyceride wastes such as WCO produces small molecular hydrocarbons, acids, ketones and aldehydes [383]. The main composition of WCO is a free fatty acid (FFA) and triglyceride, which makes it a vital feedstock to upgrade bio-oil quality [388]. Several researchers have studied the potential of triglyceride wastes to produce high-quality bio-oil [389-391]. Thermochemical conversion of WCO mainly depends on process parameters such as temperature, biomass to WCO ratio, catalyst to feedstock ratio and types of catalyst [392-394]. The oxygenated compounds in WCO are removed as H_2O and CO_2, and CO via decarboxylation, aromatization, ketonization, and decarboxylation [395, 396]. Similarly, the co-feeding of WCO with biomass also promotes the conversion of methoxy/hydroxyl, phenols, and levoglucosan from the biomass into poly-aromatics. The intermediate products, short olefins produced during thermal conversion of WCO and biomass mixture converted into aromatic hydrocarbons with C8-C14 [397]. Therefore, bio-oil obtained from co-pyrolysis of biomass and WCO has a tremendous advantage over biomass alone; it still has a high amount of aliphatic and oxygenated compounds.

Catalytic co-pyrolysis (CCP) of biomass and hydrogen-rich material reduces the activation energy and promotes the formation of aromatic hydrocarbons [126, 344]. CCP improves the bio-oil quantity and quality concisely and effectively, thus making the process cost-competitive and energy conservation. Many heterogeneous catalysts were studied to enhance bio-oil quality ranging from metal oxides [24], zeolites [167, 345], metal-loaded zeolites [181] and activated carbon (AC) [346]. The presence of catalysts during co-pyrolysis of biomass and WCO could remove the oxygen-containing compounds through ketonisation, aromatization, decarbonylation, decarboxylation and cracking [395, 398, 399]. Wang et al. [400] studied the CCP of mushroom and waste oil using HZSM-5. Results showed that increasing WCO would increase aromatics and olefins content and enhance synergetic effects between tea residual and WCO. In another study, metal oxide (MgO) loaded ZSM-5 resulted in higher amount of aromatics [367]. The basicity of MgO improves decarboxylation via ketonisation reaction; however, aromatization by acid sites of zeolites converts phenols to aromatic compounds. The presence of strong basic sites in the catalyst favours the formation of aromatic compounds by decreasing H_2O formation and producing CO_2 during the deoxygenation of the pyrolysis products [216, 349]. Strontium oxide imparts basicity to the zeolite framework by enhancing the Lewis basic sites [401]. In our previous study [397], we investigated the effect of the application of SrO-loaded hierarchical Y-zeolite catalyst for bio-oil upgrading during in-situ co-pyrolysis of IB and WCO. The effect of SrO loading (5, 10, and 15 wt.%) on product distribution has also been examined. The results showed that basic sites on SrO contributed to the conversion of oxygenated compounds to phenols and aromatic hydrocarbons [397, 402]. Considering that CCP using a basic monometallic catalyst is a promising approach for bio-oil upgrading, the application of a bimetallic catalyst could favour a number of deoxygenation reactions to produce a range of aromatic compounds [403-406].

Bimetallic catalysts using transition metals such as Ni, Cu, Zn, Ag and Fe loaded on zeolite have been studied for CCP [407, 408]. Loading of transition metals onto zeolite could enhance monocyclic aromatic hydrocarbons formation [409]. Guo et al. [410] studied the performance of mono- and bimetallic modified HZSM-5 for catalytic fast pyrolysis of *Arundo donax*. The results showed that Mo–Zn/HZSM-5 catalyst produced bio-oil with a high calorific value of 34.12 MJ/kg and the oxygen content in bio-oil decreased from 36.07 wt.% to 15.05 wt.%. This indicates that Zn-loading would be suitable to produce light hydrocarbon fuels with high octane number. In another study, Putro et al. [411] reported that bimetallic Ni-Cu enhanced the bio-oil quality and reduced coke formation. Increasing Cu amount promotes the formation of olefins and phenols via demethylation and dehydration. However, higher Ni loading onto the catalyst increases the amount of aromatic hydrocarbons and alkanes via decarbonylation, decarboxylation and aromatization. Razzaq et al. [185] investigated the effect of metals for the formation mono-aromatic compounds during CCP of wheat straw and polystyrene. Results showed that Fe-ZSM-5 produced the highest mono-aromatic hydrocarbons content (83.3%) and de-oxygenation (97.4%). The presence of Fe favoured decarbonylation and decarboxylation, which helped to remove oxygenated compounds. The cook formation during the CCP also decreased by 50% after loading Fe on ZSM-5, due to the lower acid sites strength of metal modified catalysts.

Recently some studies have been conducted on CCP of biomass and waste cooking oil using a different group of catalysts, but there is no literature on kinetics analysis and product distribution using any catalyst. Thus, addressing this knowledge gap will help to understand: (1) reaction mechanisms, (2) product formation during CCP of biomass and (3) WCO and IB promote wealth from the waste approach via commercialization. This study analyses the synthesis and characterization of mono-metallic (SrO/Y-zeolite) and bimetallic (X-SrO/Y-zeolite) catalysts and their impact on the co-pyrolysis of IB and WCO. The effect of X (Ni, Cu, Zn, Ag, and Fe) on kinetics parameters, product distribution and aromatic yield in pyrolytic vapor has been investigated using both TGA and Py-GC/MS techniques.

5.2 Materials and methods

5.2.1 Materials

The pyrolysis feedstocks used in this study are ironbark (IB) and waste cooking oil (WCO). The ironbark was collected from Townsville, Australia and sieved with 100 mesh, then dried in an oven at 105°C for 12 h. The WCO was collected from a local restaurant and stored at room temperature. IB:WCO (1:1) mixture were used for all co-pyrolysis experiments in this study. Y-zeolite (Si/Al=2.65), $Sr(NO3)_2$, $AgNO_3$, $Cu(NO_3)_2 \cdot 3H_2O$, $Ni(NO_3)_2 \cdot 6H_2O$, $Zn(NO_3)_2 \cdot 6H_2O$ and $Fe(NO_3)_3 \cdot 9H_2O$ were all purchased from Sigma-Aldrich.

5.2.2 Catalyst preparation

Mesoporous Y-zeolite synthesis via sequential dealumination and desilication was carried out based on the previous work [4]. SrO/Y-zeolite as the mono-metallic catalyst and X-SrO/Y-zeolite as a bimetallic catalyst were prepared by the incipient wetness impregnation method, where X is Ni, Cu, Zn, Ag, and Fe. To prepare 15 g of a bimetallic catalyst, a known amount of mesoporous Y-zeolite, $Sr(NO_3)_2$ and metal nitrate salt of the second metal was dissolved in 30 ml Milli Q water. The solution was kept in ultrasonic vibration at 40 kHz for 2 h. Then the slurry was held for 22 h at room temperature and then dried overnight at 110°C. Subsequently, for all samples, the calcination temperature was set at 600°C for 5 h with a ramp rate of 10°C/min. The obtained catalysts were marked as X-SrO/Y-Zeolite.

5.2.3 Catalyst characterisation

The total surface area and pore size distribution of the parent and bimetallic catalyst were determined by N_2 physisorption. Moreover, the average mesoporous diameter and volume were determined by N_2 sorption using Barrett-Joyner-Halenda (BJH) pore size distribution. SEM-EDS was used to determine the amount of Strontium (Sr), Nickel (Ni), Zinc (Zn), Iron (Fe), Copper (Cu) and Silver (Ag) loaded into Y-zeolite. This analysis was essential to understand the nominal and actual metal amounts in the Y-zeolite. TGA was performed using a TG analyzer (TA instrument, SD 600). The feedstock mixture (10 mg) and the catalyst (5 mg) were blended before performing thermal analysis. The furnace was heated from ambient temperature to 1000°C at a heating rate of 10, 20, 30°C/min under a nitrogen atmosphere at 50 mL/min. XPS measurements were carried out on Kratos Axis Supra to determine the oxidation states and elemental composition of mono- and bimetallic catalysts.

5.2.4 Pyrolysis GC/MS

Py-GC/MS was carried out in a CDS Pyroprobe 6150 pyrolyser. During the experiment, the desired pyrolysis temperature was held (at 550, 650 or 750°C) for 30 s with a heating rate of 10°C/ms. The interface, valve oven and GC transfer line were all set at 300°C. The pyrolysis by-products flowed from the quartz furnace tube into a gas chromatography mass spectrometer (6890/5973N, Agilent) via the helium sweeper gas stream. The GC/MS injector temperature was 250°C. The GC separation was carried out using an HP-5MS with ultra-purity helium (99.999%) at 1.0 mL/min. Typical operating conditions of MS included ionization energy at 70 eV and m/z scanning mode over a range of 25–550 amu.

5.2.5 Kinetic parameters and reaction mechanism

The kinetic parameters and reaction mechanism for co-pyrolysis of IB and WCO using bimetallic Y–zeolite catalysts were studied using TGA data. The catalyst to feedstock ratio of 1:2 was selected based on previous work to obtain better product distribution [4]. The thermal decomposition of CCP of IB and WCO mixture can be expressed by the Arrhenius equation; the rate constant can be described as a function of temperature:

$$\mathrm{k} = \mathrm{A}e^{-\mathrm{Ea}/\mathrm{RT}} \tag{5.1}$$

where A is called the pre-exponential factor in min^{-1}, E_a is the activation energy of the reaction in kJ/mol, R represents the universal gas constant (8.314 J/mol K), and T is the absolute temperature of the pyrolysis process in K.

The rate of thermal degradation of biomass to volatiles is given below:

$$\frac{d\alpha}{dt} = k(T).f(\alpha) \tag{5.2}$$

Here, α represents the conversion ratio, and f (α) is a function of the conversion ratio.

$$\alpha = \frac{(m_i - m_t)}{(m_i - m_f)} \tag{5.3}$$

m_i is the initial mass of biomass before reaction, m_f is the final mass left at the end of the reaction, while m_t is mass reacted at any time t.

$$f(\alpha) = (1 - \alpha)^n \tag{5.4}$$

Where n represents the reaction order.

At a particular heating rate (β), the temperature is a function of time and increases with the increase in time at a constant value of heating rate (β), given as:

$$T = T_0 + \beta t \tag{5.5}$$

T_0 is the starting temperature, β is the heating rate in °C/min, and t is time in minutes.

$$\beta = \frac{dT}{dt} = \frac{d\alpha}{dt}.\frac{dT}{d\alpha} \tag{5.6}$$

By substitution of Equation. (5.3) and (5.5) to Equation (5.4), the conversion ratio (α) is defined as a function of temperature (T):

$$\frac{d\alpha}{dT} = \frac{A}{\beta} e^{(-E_a/RT)}.f(\alpha) \tag{5.7}$$

On integrating the above equation:

$$g(\alpha) = \int_0^\alpha \frac{d\alpha}{f(\alpha)} = \frac{A}{\beta}\int_{T_0}^{T} e^{-\frac{E_a}{RT}} dT = \int_0^T e^{-\frac{E_a}{RT}} dT = \frac{E_a A}{R\beta} p(u) \tag{5.8}$$

Where, g(α) is an integral function of the conversion rate (α) and f(α) is the algebraic function that relates to different physical models representing solid-state reactions. Here, u = E_a/RT and p(u) is a temperature integral that does not have any exact solution. Therefore, it can be solved through numerical methods or certain approximations. The activation energy was estimated using iso-conversional methods by employing non-isothermal thermogravimetric data obtained at three heating rates (10, 20, and 30°C/min). At the same time, the mechanism of pyrolysis reaction was predicted by master plots using different expressions for f(α) and g(α) functions.

Iso-conversional (model free) method does not require any kinetic reaction model but calculates activation energy and pre-exponential factors using multiple heating rates at different conversion rates. There are two model-free methods: Ozawa Flynn Wall (OFW) and Kissinger Akahira Sunose (KAS), which were used in this study. These methods are based on different mathematical approximations assumed for the p(u) temperature integral. Due to simplicity, good adaptability and authenticity, these methods are the most preferable for calculating activation energy.

Ozawa Flynn Wall (OFW) is an integral method based on certain mathematical assumptions of term p(u). It uses Doyle's approximation: $p(u) = \exp(-2.315 + 0.456\ u)$, where $u = E_a/RT$. OFW Equation (5.9) is given as:

$$\ln\beta \ = \ \ln\left(\frac{A.E_a}{R.g(\alpha)}\right) - 5.331 - 1.052\frac{E_a}{R.T} \tag{5.9}$$

The slope of the lnβ vs 1/T plot is $1.052E_a/R$, which was used to calculate activation energy for the reaction at different conversion rates.

Kissinger Akahira Sunose (KAS) is the most accurate method for predicting the value of activation energy [412]. It uses Murray and White's approximation: $p(u) = e^u/u^2$ for integral term p(u) in Equation (5.8). After replacing p(u) and some rearrangements in Equation (9) and taking the logarithm to both sides:

$$\ln\left(\frac{\beta}{T^2}\right) = \ln\left(\frac{A.R}{E_a.g(\alpha)}\right) - \frac{E_a}{R.T} \tag{5.10}$$

Activation energy can be determined from the slope (E_a/R) of the curve plotted of $\ln(\beta/T^2)$ versus 1/T. All calculations were done on a molar basis. The activation energy was calculated in units of J/mol using the universal gas constant value of 8.314 J/mol K.

5.3 Results and discussion

5.3.1 Characterisation of catalyst

Nitrogen adsorption-desorption isotherms for the parent Y-zeolite and bimetallic catalysts, the specific surface areas, and pore volumes are provided in Table 5.1 and Figure A.19. The parent Y-zeolite exhibits a type-I isotherm that indicates the presence of a microporous material according to the IUPAC classification [308]. All bimetallic catalysts possess a hysteresis loop, indicating the presence of mesopores in the catalysts. The parent Y-zeolite has the highest surface area, while the other catalytic materials demonstrated a decrease in surface area, which may be attributed to the loading of SrO and the second metal oxide on the zeolite surface. The higher the ionic radii of metal, the higher the potential for blockage of pores in the zeolite framework. Therefore, Cu-SrO/Y-zeolite exhibited the highest surface area due to the smallest ionic radii of Cu^{2+} and distribution on the Y-zeolite surface. Further, a portion of the sodium cations was substituted by strontium cations, resulting in an overall decrease in the surface area [357, 358]. The mesoporous surface area was also affected by the types of metal-doped into SrO/Y-zeolite catalyst. Cu-SrO/Y-zeolite showed the highest mesoporous surface area of 171.72 m^2/g.

Table 5.1. Surface area and pore volume of parent Y-zeolite and bimetallic catalysts.

Sample	S_{BET} (m^2/g)	S_{Meso} (m^2/g)	V_{total} (cm^3/g)	V_{micro} (cm^3/g)	V_{meso} (cm^3/g)
Y-zeolite	577.20	53.50	0.330	0.2670	0.066
Ni-SrO/Y-zeolite	267.78	114.12	0.1998	0.0611	0.1387
Cu-SrO/Y-zeolite	436.32	171.72	0.3448	0.987	0.2461
Zn-SrO/Y-zeolite	153.36	65.73	0.2388	0.0349	0.2039
Ag-SrO/Y-zeolite	166.85	35.01	0.1212	0.0505	0.0707
Fe-SrO/Y-zeolite	113.82	77.85	0.1079	0.0143	0.0936

XPS was employed to investigate the chemical states and elemental compositions of bimetallic catalysts, and the results are shown in Figure 5.1 and Table 5.2. The XPS spectra of SrO/Y-zeolite for Sr showed two binding energies for Sr $3d_{5/2}$ (132.9 eV and 134.4 eV) and Sr 3P (280.7 eV), which showed that Sr was mainly in the Sr^{2+} state. For all bimetallic catalysts, the XPS curve fitting of Sr presents three peaks at 133.2 eV, 134.4 eV and 280.9 eV. Moreover, the actual loading of Sr on hierarchical Y-zeolite ranges between 10.87 to 7.25%, similar to the nominal loading of 10% average. Loading of the second metal in SrO/Y-zeolite changed the content of the lattice oxygen, which caused a slight shifting in the shape of the spectrum and the binding energy due to the Al and Si species in the zeolite. Similarly, the Ni-SrO/Y-zeolite catalyst showed two binding energies for Ni 2p3/2 (856.1 eV and 856.9 eV) and Ni 2p1/2 (873.8 eV). This indicates that Ni is presented in the form of NiO with actual loading of 5.77%. Similarly, Cu-SrO/Y-zeolite, Zn-SrO/Y-zeolite, Ag-SrO/Y-zeolite, and Fe-SrO/Y-zeolite confirm that the second metal is presented in the form of CuO, ZnO, AgO, and Fe_2O_3, respectively. Meanwhile, the O1s regions of bimetallic catalysts show the formation of M-O-M species at approximately 530.94 eV. However, the binding energy shifted to the left (528.10

eV) for the mono-metallic catalyst, indicating an electron transfer from the support and SrO (M to Sr) via the M-O-Sr structure. The lower binding energy can be explained by the appearance of surface oxygen vacancies due to its removal from the oxide lattice via hydrogen-rich feedstock, removing oxygen from M-O-Sr to form M-Sr.

Table 5.2. Surface elemental composition (%) and surface chemistry of mono- and bimetallic catalysts.

	SrO/ Y-zeolite	Ni-SrO/ Y-zeolite	Cu-SrO/ Y-zeolite	Zn-SrO/ Y-zeolite	Ag-SrO/ Y-zeolite	Fe-SrO/ Y-zeolite
O 1s	64.9	53.5	56.5	61.2	62.2	53.4
C 1s	5.9	10.6	7.12	8.9	7.8	19.4
Al 2p	3.9	9.2	10.1	3.1	3.2	1.21
Si 2p	17.2	9.9	13.9	13.1	15.1	11.1
Sr 3d	7.9	10.8	8.9	7.2	7.6	8.1
Ni 2p	-	5.7	-	-	-	-
Cu 2p3	-	-	3.5	-	-	-
Zn 2p3	-	-	-	6.3	-	-
Ag 3d	-	-	-	-	3.9	-
Fe	-	-	-	-	-	4.6

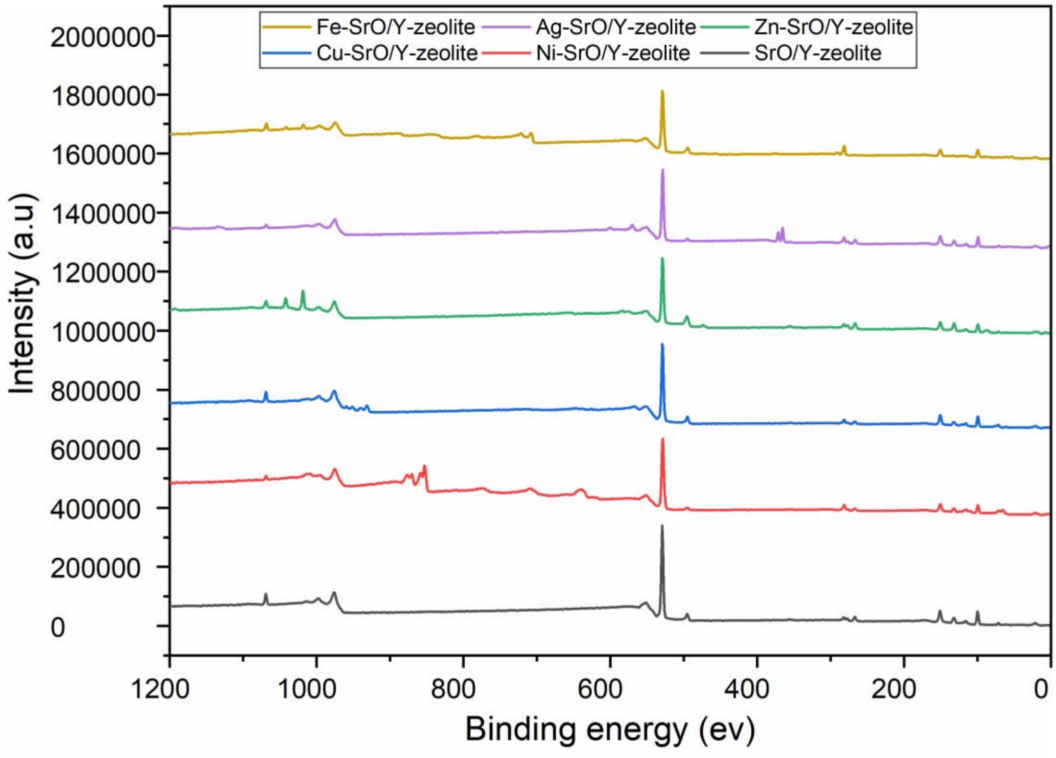

Figure 5.1. X-ray photoelectron spectra of mono- and bimetallic catalysts.

5.3.2 Thermal behaviour of non-catalytic and catalytic co-pyrolysis

The TGA and DTG curves of non-catalytic pyrolysis of individual IB and WCO are shown in Figure A.20. The thermo-degradation of WCO has two main stages, room temperature to 170°C and 170 to 505°C. The first stage (< 170°C) is attributed to the removal of moisture. The second stage showed depolymerization of complex organic compounds from 170°C to 505°C, with the maximum weight loss at 424°C and a final solid residue of 0.74%. The thermal depolymerization of IB occurred mainly between 280 and 400°C, and the DTG curve showed that the maximum degradation occurs at 342.1°C. The degradation of IB ranges from 450 to 800°C and is characterized by the breakdown of residual lignin and carbonization. As shown in Figure, the thermal decomposition of the IB:WCO mixture can be divided into three stages; room temperature to 150°C, 200 to 450°C and 450 to 800°C. The first stage is associated with the removal of moisture and volatile light components. In the second phase, the bulk of the decomposition occurs between 200 and 450°C resulting in a weight loss of 51.3 wt. %. The third phase, which ranges from 450 to 800°C, is characterized by the breakdown of residual lignin and carbonisation, with a final solid residue of 23.4 wt. %.

The thermal decomposition profile of catalytic co-pyrolysis of IB:WCO mixture using bimetallic catalysts could be divided into three stages. The first stage (room temperature to 250°C) resulted from the volatilization of moisture. The second stage (250°C - 450°C) was the main decomposition stage of cellulose and higher molecular weight compounds in WCO. The presence of bimetallic catalysts promotes dehydrogenation reaction and increases the degree of ring-opening reaction of oleic acid, thereby enhancing the formation of gases and coke. The strong electron acceptance tendency of the second metal in X-SrO/Y-zeolite reduces the bond angles and length of C─C and C─O presented in the IB:WCO mixture, which contributes to the formation of cyclic hydrocarbons [329]. Moreover, the presence of second metal helps to degrade the hydrogen bonds in the cellulose and reduces the condensation point of volatile substances at a lower temperature than in non-catalytic co-pyrolysis. Ni-SrO/Y-zeolite showed the highest weight loss of 86.74%. Cu-SrO/Y-zeolite showed the lowest thermal decomposition temperature mainly because Cu may weaken the crystalline structure of cellulose and break down the hydrogen bonds. Fe-SrO/Y-zeolite displayed the highest solid content. The high thermal stability of Fe^{3+} decreases the precipitation of volatile compounds that contributes to the formation of ash and coke.

5.3.3 Kinetic analysis

5.3.3.1 Estimation of activation energy using a model-free method

The apparent activation energy (Ea, kJ/mol) of the IB:WCO mixture using bimetallic catalysts was studied using two iso-conversional methods (OFW and KAS) based on the corresponding TG experimental data. The correction coefficients (R^2) of both models were above 0.98 for various conversion rates (α) ranging from 0.1 to 0.9, confirming that the two models fit the experimental results well. The average correlation coefficient of the OFW model is relatively high, whereas KAS model results were scattered compared to OFW. Therefore, the results obtained from the OFW model were used for the discussion. For both models, the average apparent activation energy (Ea) is presented in Figure 5.2 and Table A.3. In general, the average Ea ranges from 193.21 to 164.99 kJ/mol for the OFW model and 192.41 to 163.10 kJ/mol for the KAS model.

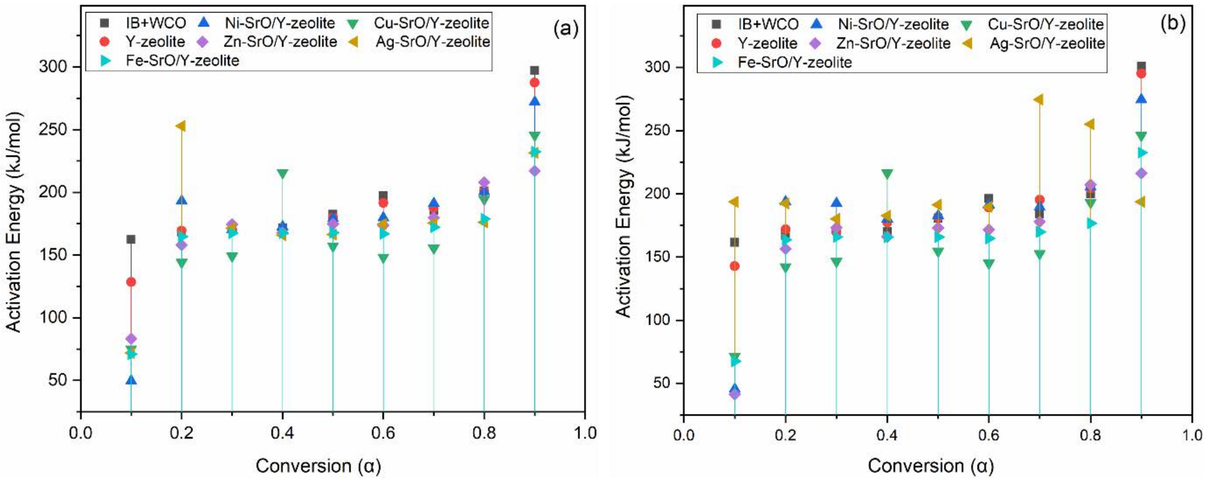

Figure 5.2. The apparent activation energy of CCP of IB:WCO mixture; IB:WCO with Y-zeolite, and IB:WCO with bimetallic catalysts using (a) OFW and (b) KAS models.

Non-catalytic IB:WCO mixture shows the highest Ea of 193.21 and 192.41 kJ/mol from OFW and KAS models, respectively. The Ea values of CCP using Ni-SrO/Y-zeolite, Cu-SrO/Y-zeolite, Zn-SrO/Y-zeolite, Ag-SrO/Y-zeolite, and Fe-SrO/Y-zeolite catalysts were found to be 184.11, 164.99, 170.77, 176.27, 165.43 kJ/mol using OFW model; and 183.95, 163.10, 164.77, 189.45, and 163.56 kJ/mol using KAS model, respectively. Both models showed comparatively similar trends of apparent activation energy.

The average Ea of all CCP is lower than non-catalytic co-pyrolysis of IB and WCO mixture, which showed that the catalysts effectively enhanced the degradation of feedstocks. The order of Ea for CCP based on the second metal is as follows; Ni> Ag> Zn> Fe> Cu. These findings showed that lower ionic radii of the second metal and redox properties on the surface of hierarchical Y-zeolite lower the Ea. The Cu^{2+} has the strongest oxidation properties and smallest ionic radius (0.177 nm). As a result, the Cu ion enhances the degradation of IB, decreases the oxygen-containing functional groups, and promotes the co-pyrolysis of the IB:WCO mixture. The presence of high mesoporous surface (171.72 m^2/g) of Cu-SrO/Y-zeolite also enhances the mass transfer phenomena by allowing more macromolecules to pass through the catalyst thus reducing the activation energy. Furthermore, the copper atom on the Y-zeolite surface shows a strong tendency to accept electrons due to the dispersion of electron unsaturated energy levels, which is highly active and unstable [413]. Meanwhile, during thermal decomposition, WCO converts into olefins, alkenes, and alkyl radicals via β-scission in the presence of the Cu-SrO/Y-zeolite [414].

The apparent activation energy significantly varied with the conversion ratio (α) for different catalysts used for CCP. In non-catalytic co-pyrolysis of IB and WCO mixture, the Ea was first increased from 162.4 to 197.31 kJ/mol for the conversion range of 0.1 – 0.6; the Ea was lower because of lower molecular bond energy degradation. Thereafter, the Ea was decreased to 184 kJ/mol at $\alpha = 0.7$ and increased significantly to 297.35 kJ/mol at high conversions ($\alpha = 0.9$). The Ea increased with a higher conversion due to the degradation of high molecular weight WCO components in a temperature range of 400 – 450°C. The variation of activation energy for Ni-SrO/Y-zeolite is divided into three stages. The first stage ($0.1 \leq \alpha \leq 0.3$) occurred in the temperature range of 150 – 345°C. In this stage, the activation energy decreased for lower conversion. The second stage ($0.3 \leq \alpha \leq 0.6$) occurred in the temperature range of 345 – 392°C, and the devolatilization of IB and WCO reached the maximum. Higher temperatures (392 - 459°C) and activation energy were required for the third stage ($0.7 < \alpha \leq 0.9$). This could be attributed to the degradation of lignin and higher molecular weight compounds presented in WCO [415]. During CCP using Ag-SrO/Y-zeolite catalyst, the Ea showed similar trends with the variation of conversions. The first stage ($0.1 \leq \alpha \leq 0.3$) occurred in the temperature range of 114 – 339°C, and the second stage ($0.4 \leq \alpha \leq 0.9$) occurred in the temperature range of 361–457°C with the highest activation energy of 245.52 kJ/mol ($\alpha = 0.9$). However, Cu-SrO/Y-zeolite displayed low activation energy of 245.52 kJ/mol at high conversion ($\alpha = 0.8$) and enhanced aromatic formation, as shown in section 5.3.4.1.

5.3.3.2 Predication of reaction mechanism using criado z master plot

The catalytic degradation of the IB and WCO mixture is a complicated process with hundreds of reactions; therefore, predicting the reaction mechanism is challenging. However, mathematical models based on various approximations have been established (Figure 5.3). The Z-Master plot examined solid reaction processes using Criado's technique. The Z-Master plot $[(Z(\alpha)/Z(0.5)]$ was constructed using the Ea acquired from the OFW model for co-pyrolysis of IB and WCO mixture over bimetallic catalysts since no approximation is required with the OFW model. The reaction mechanism of CCP was determined by comparing the theoretical curves with the experimental curves based on their closeness.

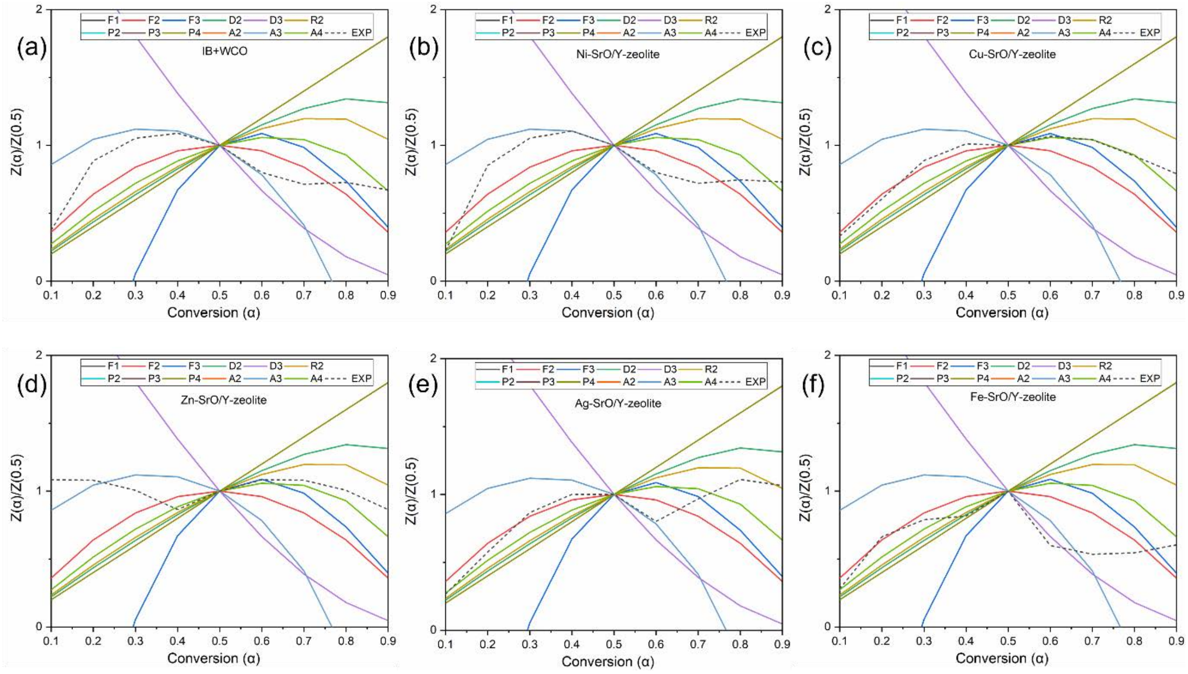

Figure 5.3. Master plots of co-pyrolysis of IB:WCO mixture without and with the presence of bimetallic catalysts (a) IB:WCO mixture; (b) Ni-SrO/Y-zeolite; (c) Cu-SrO/Y-zeolite; (d) Zn-SrO/Y-zeolite; (e) Ag-SrO/Y-zeolite; (f) Fe-SrO/Y-zeolite.

Non-catalytic co-pyrolysis of IB and WCO followed different models, namely nucleation and growth (α = 0.1-0.6), phase boundary (contacting area) controlled reaction (α = 0.7-0.9). The CCP of IB and WCO using Ni-SrO/Y-zeolite followed nucleation and growth (α = 0.1-0.6) and tended to resemble 2-D diffusion (α = 0.7-0.9). However, CCP using Cu-SrO/Y-zeolite showed second-order random nucleation (α = 0.1-0.5), and the reaction mechanism changed to nucleation and growth (α = 0.5-0.9). On the other side, CCP using Ag-SrO/Y-zeolite showed three different mechanisms, namely second-order random nucleation (α = 0.1-0.5), nucleation and growth (α = 0.5-0.6) and phase boundary (contacting area) controlled reaction (α = 0.6-0.9).

5.3.4 Product distribution and composition of catalytic co-pyrolysis products

5.3.4.1 Effect of catalyst on product distribution

Py-GC/MS experiments were carried out to understand the product distribution from CCP of IB and WCO mixture using bimetallic catalysts. The products could be classified based on their chemical structures, hydrocarbons, acids, phenols, aldehydes, ketones, and esters. A detailed description of relative area percentages of product compositions using bimetallic catalysts is presented in Table A.4. The SrO/Y-zeolite produced aromatic hydrocarbons (19.96 %), phenolic compounds (13.67 %) and high acid content (44.92%) mainly oleic acids. After doping the SrO/Y-zeolite with a second metal, the relative aromatic hydrocarbons amount increased to 32.97 % at 550°C and reached a maximum of 65.43 % at 750°C; Cu-SrO/Y-zeolite mainly reduced the acids, phenols, and ketones. The presence of high mesoporous volume (0.2461 cm^3/g) and strong interaction between Cu-SrO help to convert higher molecular weight compounds into aromatic hydrocarbons. Cu can also supply acidic sites, enhancing aromatization and increasing aromatic hydrocarbons synthesis [416].

As shown in Figure 5.4, Ag-, Fe-, and Zn-SrO/Y-zeolite catalysts increased aliphatic and aromatic hydrocarbons. Ag-SrO/Y-zeolite showed the highest hydrocarbons content (34.27 %) compared with the mono-metallic SrO/Y-zeolite catalyst (19.96%) because Ag promoted hydrogenation of the C–O bond. As confirmed by XPS results, the surface oxygen vacancies in Ag-SrO/Y-zeolite promoted the formation of additional active sites to enhance hydrocarbons production. Also, Ag-SrO/Y-zeolite improved the phenolic content to 15.79% compared with non-catalytic co-pyrolysis (11.26%). Phenols are primarily produced via the decomposition of lignin and hemicellulose from IB, mainly composed of alkyl and methoxy phenols [417]. It could be observed that the selectivity of light phenol was 33.45% higher than alkoxy phenols in the CCP of IB and WCO mixture using Ag-SrO/Y-zeolite. Moreover, the presence of a base (SrO) could promote the homolysis of O-CH_3 presented in guaiacol and enhance the amount of alkyl phenols [418]. As a result, SrO enhanced the conversion of alkoxy phenols to light phenols by demethoxylation, decarbonylation, and cracking, indicating that it has significant potential for improving light phenol production.

Fe-SrO/Y-zeolite catalyst generated 29.43% of hydrocarbons. Also, it significantly reduced other components compared to non-catalytic pyrolysis, with 42.23 % of acids, 10.30% of phenols, and 3.93% of ketones. The presence of Fe contributes to the hydrogenation of the C-O bond and the transformation of oxygen-containing compounds to aromatic hydrocarbons [419]. Due to its higher acid sites, Fe was more favourable to the formation of simple phenols via deoxygenation and rearrangement processes. Furthermore, the alkylmethoxyphenols generated from biomass degradation would be demethoxylated and dealkylated to create phenol at the Fe-SrO/Y-zeolite active sites [420]. The presence of low mesoporous volume (0.093 cm^3/g) on Fe-SrO/Y-zeolite hinders the conversion of higher molecular weight compounds, mainly acids (42.23 %). Zn-SrO/Y-zeolite produced 25.82% hydrocarbons, 13.26% phenols, 53.53% acids, 3.15% ketones and 1.80% aldehydes. As shown on the TGA result, Zn-SrO/Y-zeolite produces high solid residual, which lowers the conversion of acids. Zn species enhanced surface acidity by creating Lewis acid sites (Zn-L), resulting in high aromatic yields [421].

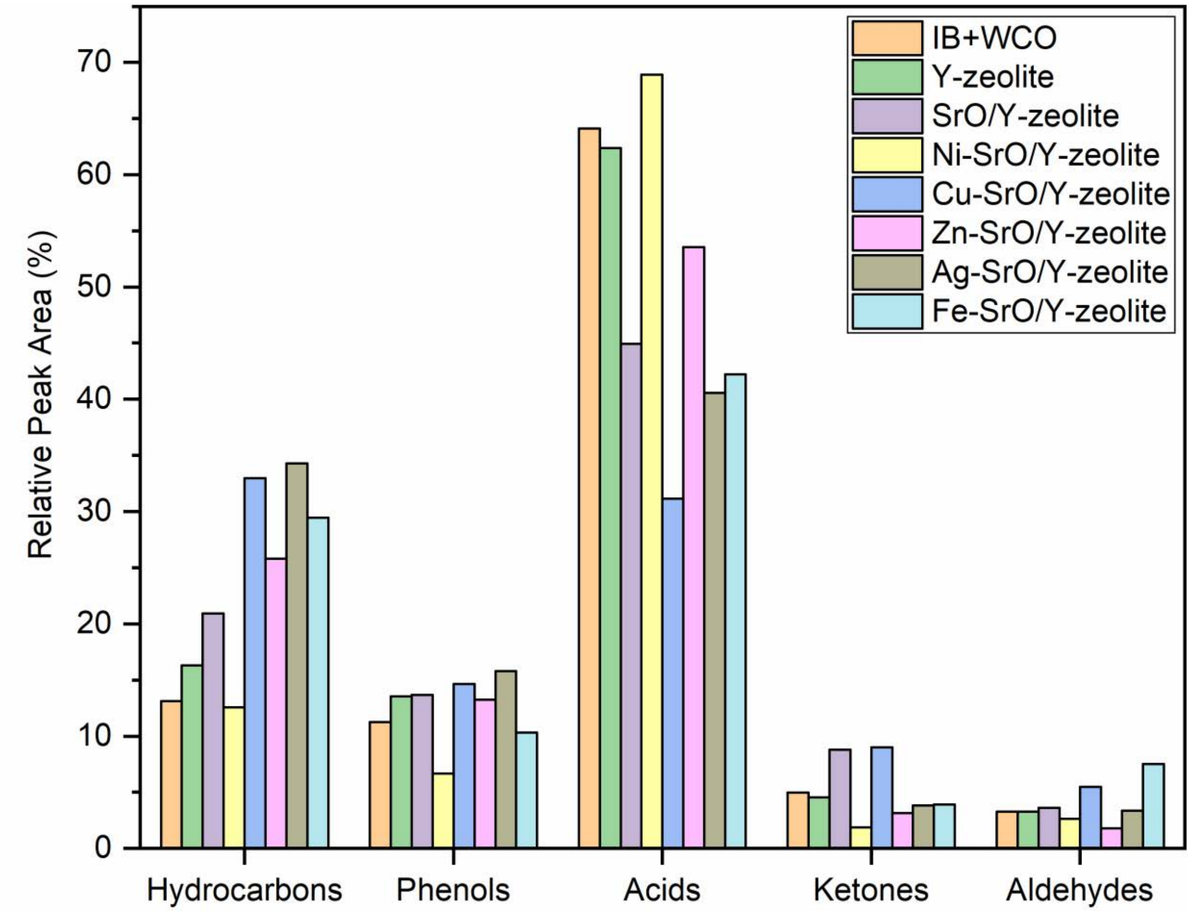

Figure 5.4. Product distribution obtained from non-catalytic and catalytic co-pyrolysis of Ironbark (IB) and waste cooking oil (WCO) mixture using mono- and bimetallic catalysts via Py-GC/MS.

As shown in Figure 5.5, the product distribution and hydrocarbons selectivity is affected by the second metal doped into SrO/Y-zeolite. Zn- and Ag-SrO/Y-zeolite catalysts mainly produced light hydrocarbons (C9-C12) and non-condensable gas products. The result suggested that the catalysts favor aromatization reactions of higher molecular weight intermediates to form aromatics [405]. Fe-SrO/Y-zeolite catalyst favors the selectivity of higher molecular weight hydrocarbons (C15-C23). More crucially, these novel Fe-SrO/Y-zeolite active sites were more conducive to the formation of mono-aromatics rather than poly-aromatics. The Cu-SrO/Y-zeolite catalyst showed a higher yield of C17-C20 (jet fuel range) than the mono-metallic

SrO/Y-zeolite catalyst. These results indicated that the doping of Cu on SrO/Y-zeolite promotes the formation of additional active sites for deoxygenation reaction.

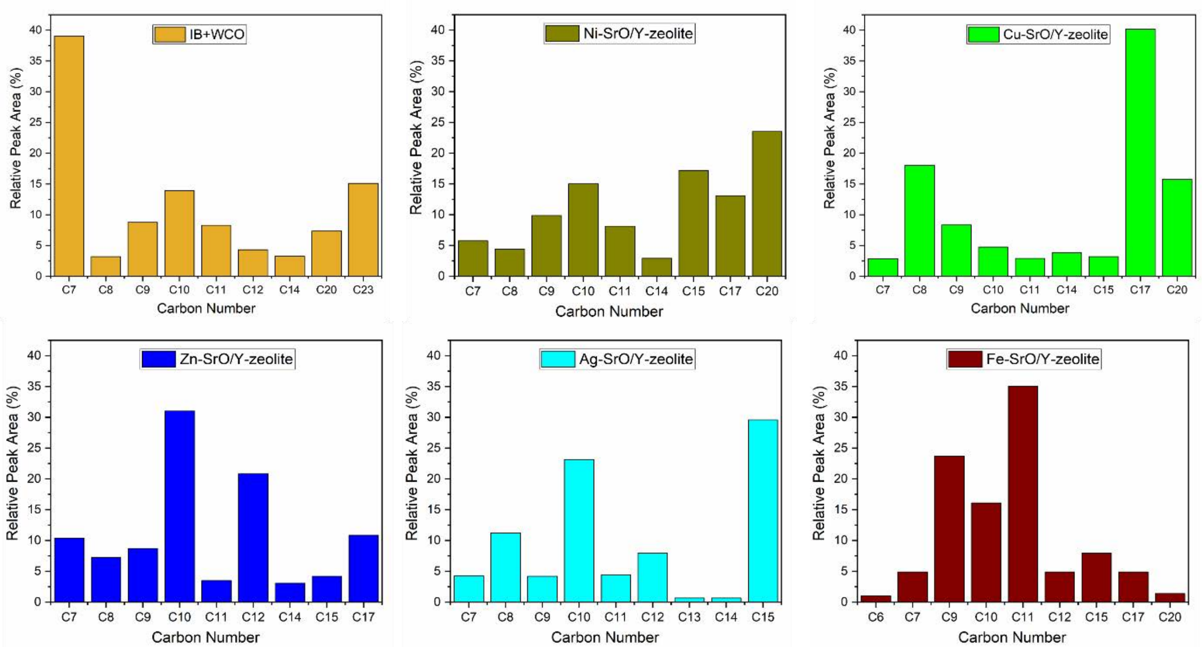

Figure 5.5. Carbon number and aromatic selectivity of IB:WCO (1:1) mixture without and with the addition of bimetallic catalysts.

5.3.4.2 Effect of temperature on product composition

CCP temperature predominantly affects the selectivity and composition of aromatic compounds. To understand the effect of temperature, CCP has been conducted using Cu-SrO/Y-zeolite bimetallic catalyst (catalyst with the best performance) at three different temperatures of 550, 650, and 750ºC. As shown in Figure 5.6 (a) and (b), increasing temperature from 550 to 750ºC increased the relative aromatic yield from 32.97 to 65.43 %. [422]. At high temperatures, the degradation of the strong organic bonds presented in the IB:WCO mixture increases, which also enhances the formation of aromatic compounds. Ketones were produced by pyrolysis of lignin and depolymerized hemicellulose; the presence of SrO also initiated a ketonisation reaction for the conversion of acetic acids into acetone and cyclic aliphatic ketones. However, at high temperatures (750ºC), ketones and acids yield decreased to 1.09 and 12.56%, respectively. These results can be explained by the decarbonylation of ketones and decarboxylation of acids [422]. The CCP at 750ºC produced maximum aromatic hydrocarbons yield of C17-C20 (86.72%), much higher than SrO/Y-zeolite C17-C20 (43.71%).

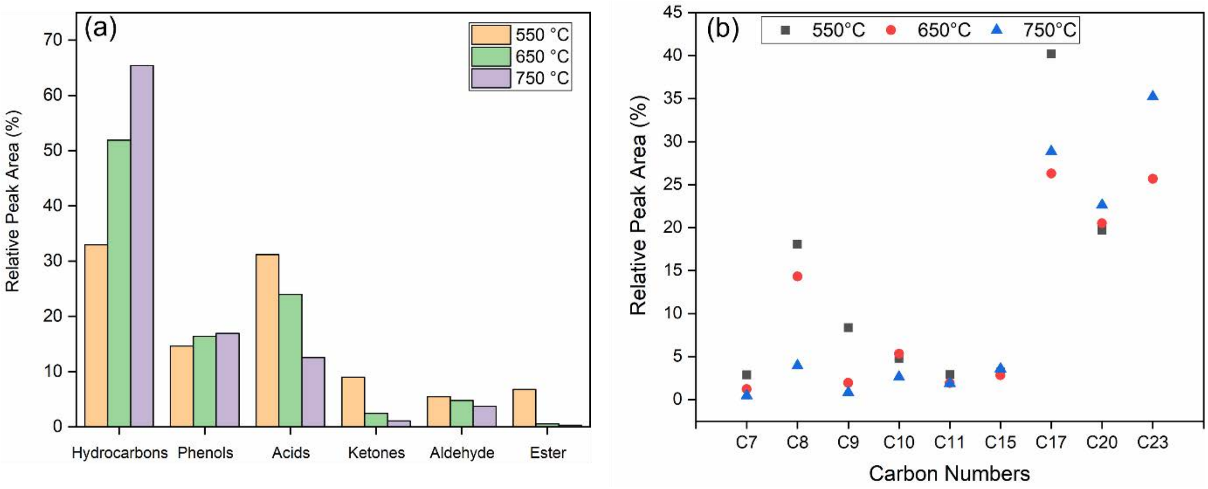

Figure 5.6. Effect of temperature on (a) product distribution of CCP of IB:WCO (1:1) mixture using Cu-SrO/Y-zeolite; (b) aromatic hydrocarbon selectivity obtained from CCP of IB:WCO (1:1) mixture using Cu-SrO/Y-zeolite.

5.4 Conclusions

This work used mono-metallic SrO/Y-zeolite and bimetallic catalyst (X-SrO/Y-zeolite; X = Ni, Cu, Zn, Ag and Fe) for catalytic co-pyrolysis of IB:WCO (1:1) mixture. The thermal decomposition of the IB:WCO (1:1) mixture occurred mainly between 280 and 400°C at a peak temperature of 342.1°C. The presence of a second metal in X-SrO/Y-zeolite enhances the degradation of cellulose hydrogen bonds, weakens the interaction force, and reduces the pyrolysis peak temperature. The average activation energy (Ea) ranges from 193.21 to 164.99 kJ/mol for the OFW model and 192.41 to 163.10 kJ/mol for the KAS model. The average Ea of all CCP was lower than the non-catalytic co-pyrolysis of the IB:WCO mixture, which showed that the catalysts effectively enhanced the degradation of feedstocks. The order of Ea for CCP was as follow; Ni> Ag> Zn> Fe> Cu. Non-catalytic co-pyrolysis of IB and WCO followed different models, namely nucleation and growth (α = 0.1-0.6), phase boundary (contacting area) controlled reaction (α = 0.7-0.9). CCP using Cu-SrO/Y-zeolite showed second-order random nucleation (α = 0.1-0.5) and growth (α = 0.5-0.9).

The Py-GC/MS results demonstrated that the CCP using SrO/Y-zeolite produced mainly acids (44.92%), including oleic acids, followed by aromatic hydrocarbons (19.96%) and phenolic compounds (13.67%). However, after loading the second metal, the relative aromatic hydrocarbons amount increased to 32.97% at 550°C and reached a maximum of 65.43 % at 750°C, while the acids, phenols, and ketones were mainly reduced with the presence of Cu-

SrO/Y-zeolite. Fe-SrO/Y-zeolite catalyst favors the selectivity of higher molecular weight hydrocarbons (C15-C23). The Cu-SrO/Y-zeolite catalyst showed a higher yield of C17-C20 (jet fuel range) than the mono-metallic SrO/Y-zeolite catalyst. This work demonstrates that bimetallic catalysts are promising and efficient catalysts for converting IB:WCO mixture into bio-oil with high aromatic yield. The Cu-SrO/Y-zeolite catalyst exhibited the best performance.

6 Effect of catalyst supports on bio-oil product distribution

Abstract

In this work, Cu-SrO bimetallic catalyst was synthesised and examined for catalytic co-pyrolysis of ironbark (IB) and waste cooking oil (WCO) using Py-GC/MS. The effect of catalyst support (ZSM-5, Y-zeolite, activated carbon, Al_2O_3, and ZrO_2) on aromatic hydrocarbon yield was studied. The effect of catalyst support on the selectivity of gasoline (C8-C14), diesel (C15-C17), and heavy oil (> C20) components of bio-oil were studied. Non-catalytic co-pyrolysis of IB and WCO produced a heavy oil component of 58.7% (> C20). SrO initiated a ketonisation reaction that converted carboxylic acids into new C-C bonds. The addition of Cu effectively promoted secondary cracking and aromatization reactions enhancing the hydrocarbon yield. Cu-SrO/ZSM-5 and Cu-SrO/Y-zeolite produced low acid content of 4.43% and 12.5%, respectively. Overall, the bimetallic catalyst Cu-SrO/ZSM-5 significantly increased the amount of C8-C14 compounds to 87.28% and reduced compounds over C20 to 1.19%.

Keywords: Biomass; Waste cooking oil; Catalytic co-pyrolysis; Bifunctional catalyst; Hydrocarbons; Aromatics

This work has been published as: Tewodros Kassa Dada, Arun Vuppaladadiyam, Alex Xiaofei Duan, Ravinder Kumar, Elsa Antunes. Probing the effect of Cu-SrO loading on catalyst supports (ZSM-5, Y-zeolite, activated carbon, Al_2O_3, and ZrO_2) for aromatics production during catalytic co-pyrolysis of biomass and waste cooking oil, Bioresource Technology, Volume 360, 2022, 127515

6.1 Introduction

The International Energy Agency reported that the global economy is largely dependent on fossil-based fuels [423]. The current production and consumption trends may cause depletion of fossil reserves in another 50 years [265]. Depletions of fossil based reserves may result in serious economic issues, both national and international [424]. In recent years, the development of alternative fuel sources, such as biofuels, is taken significant priority to support the world economy and environmental conservation [383]. Bio-oil can be used as a fuel and as a feedstock for the production of valuable chemicals[382]. The target product yield and selectivity mainly depend upon feedstock types (biomass, polymeric, and triglycerides wastes) and process parameters [425]. However, single feedstock pyrolysis is characterized by limited yield of aromatic hydrocarbon compounds in bio-oil.

Co-pyrolysis has been extensively studied and is recommended to upgrade bio-oil quality [426]. Due to the possibility of creating synergy between various feedstocks, co-pyrolysis can effectively enhance bio-oil quality [427]. The hydrogen transfer reaction that occurs during co-pyrolysis can increase the calorific value of bio-oil by converting heavy hydrocarbons (> C20) into light hydrocarbons (C8-C14) [428]. Among hydrogen-rich feedstocks, WCO demonstrated a high potential as additional hydrogen source during co-pyrolysis. For example, co-pyrolysis of WCO demonstrated high conversion rates and low processing cost to produce high energy fuel [383]. Therefore, co-pyrolysis of biomass and WCO has a tremendous benefit over single biomass pyrolysis to obtain bio-oil with a high energy density.

Catalytic pyrolysis, by selectively improving a specific reaction, has been recognized as a method to enhance the product distribution. For instance, reactions such as aromatization, dehydrogenation, deoxygenation, and cracking can be induced by adding an appropriate catalyst, which facilitates the formation of targeted products [426]. The yield and selectivity of aromatic hydrocarbon during catalytic co-pyrolysis (CCP) is affected by catalyst physicochemical properties such as acidity/basicity, surface area, and metal loading [429, 430]. Many heterogeneous catalysts, ranging from metal oxides (MgO, SrO, CaO, ZrO_2, Fe_2O_3, ZnO) [24], zeolites (HY-zeolite, HZSM-5, H-beta) [426], activated carbon (AC) [431]and alkali ceramics [432], were studied to understand their influence on pyrolysis products.

ZSM-5 is the most widely used zeolite due to its remarkable deoxygenation and aromatization capabilities. Catalytic pyrolysis of rapeseed oil with the addition of HZSM-5 demonstrated an increase in the formation of light hydrocarbon , which mainly consisted of alkenes (C9-C26), alkanes, aliphatic, and long-chain fatty acids [433]. Recently, many researchers focused on loading metal oxides into ZSM-5. These studies indicated that the synergistic effects between ZSM-5 and metal oxides can significantly impact composition of bio-oil. Wu et al. examined the viability of combining ZSM-5 with metal oxides during catalytic pyrolysis of waste oils to produce aromatic rich bio-oil [395]. At 550°C, the amount of monocyclic hydrocarbons increased and promoted the formation of BTEX (benzene, toluene, ethylbenzene and xylene). ZSM-5 alone increased the polycyclic aromatic hydrocarbons to 9.18% while the addition of CaO/ZSM-5 further increased to 35.47%. Wang et al. investigated the co-pyrolysis of WCO and tea residue with the addition of HZSM-5 catalyst [434]. The findings implied that the co-pyrolysis produced a 6.3% aromatic carbon; however, catalytic co-pyrolysis (CCP) significantly increased the aromatics yield to 26%. The Brønsted acid sites on zeolites act as active catalytic sites to conduct various deoxygenation and aromatization reactions during CCP to produce aromatic hydrocarbons and enhance the product distribution [435].

Activated carbon (AC) demonstrates a significant role in converting biomass into diesel grade bio-oil [363]. Carbon-based catalysts have high a large surface area, resulting in better catalytic performance [431]. Lam et al. discussed the effect of modified char for catalytic pyrolysis of waste engine oil and indicated that the use of catalyst enhanced pyrolysis-gas yields, but reduced pyrolysis-oil and metallic–char yields [436]. In addition, the presence of metal induced char enhanced the aromatic content but reduce aliphatic content in the liquid product. The authors explained that the extra active sites introduced by metallic-char catalyst promoted secondary cracking reactions to convert waste engine oil to diesel fuel range hydrocarbons (C8 to C14). Catalysts doped with metal oxides, such as ZrO_2-based catalysts, are the current research focus due to their distinct thermal stability and catalytic activity [437]. However, low surface area and lack of active sites limited their application in catalytic pyrolysis [438].

This work reports the non-catalytic and catalytic co-pyrolysis of biomass (ironbark) and waste cooking oil. Mono (SrO) and bimetallic (Cu-SrO) catalysts over different catalyst supports (ZSM-5, Y-zeolite, AC, Al_2O_3, and ZrO_2) were synthesised and the characterization is reported. The catalyst supports were selected to represent different classification of catalyst group such as acid catalyst (ZSM-5), Mesoporous catalyst (Y-zeolite), carbon-based catalyst (activated carbon). Acid metal oxide (Al_2O_3), and basic metal oxide (ZrO_2). The catalysts and pyrolysis products were analysed by N_2 physisorption isotherms, XRD, and XPS. The catalytic co-pyrolysis products were analysed based on the area percentage of peak obtained via Py-GC/MS. The effect of catalyst support on product distribution, aromatic selectivity, and carbon yield has been investigated. This research establishes a novel theoretical foundation and technological support to produce gasoline and diesel-grade bio-oil and demonstrates the potential of biomass and waste cooking oil as feedstock for renewable energy production.

6.2 Materials and methods

6.2.1 Materials

In this work IB and WCO were used as feedstock [397]. A mixing ratio of IB:WCO of 1:1 was used for all experiments in this study. Y-zeolite (Si/Al=2.65), ZSM-5, Al_2O_3, ZrO_2, $Sr(NO3)_2$, and $Cu(NO_3)_2{\cdot}3H_2O$ were all purchased from Sigma-Aldrich. The AC was purchased from Carbon Activated Australia.

6.2.2 Catalyst preparation

6.2.2.1 Synthesis of zeolite support catalyst

Mesoporous Y-zeolite synthesis was carried out via sequential dealumination and desilication and the detailed procedure is reported in our previous work [4]. Mono-metallic (SrO) and bimetallic (Cu-SrO) catalysts were prepared by impregnation method. To prepare 15 g of a bimetallic catalyst, a known amount of $Sr(NO_3)_2$ and of $Cu(NO_3)_2.3H2O$ were dissolved in water, followed by the loading of the required amount of Y-zeolite/ZSM-5 in the metal solution. The commercially available ZSM-5 was calcined at 550°C for 2.5 h before using it for catalyst preparation. The mixture was subjected to ultrasonic vibration at 40 kHz for 2 h. Then the slurry held for 22 h at room temperature and then dried overnight at 110°C. The dried catalysts were then calcined under N_2 atmosphere at 600°C for 4 h.

6.2.2.2 Synthesis of AC support catalyst

The activated carbon was sieved into granules using a 125µm mesh, washed several times, and dried overnight at 110°C. Pre-treatment with nitric acid was carried out at 80°C for 10 h to increase active acid sites. After being washed to a pH of *ca.* 7, the sample was dried overnight at 110°C. In the impregnation process, $Cu(NO_3)_2$ and $Sr(NO_3)_2$ were added to obtain a total weight of metal of 5 wt% and 10 wt%, respectively. For better dispersion, the mixture was placed in an ultrasonic vibration for 30 min and subjected to heating at 50°C for 8 h. The resultant mixture was dried at 110°C overnight. The dried catalysts were then calcined under N_2 atmosphere at 600°C for 4 h. The final products were marked as SrO/AC and Cu-SrO/AC.

6.2.2.3 Synthesis of metal oxide support catalyst

ZrO_2 and γ-Al_2O_3 were used as supporting catalysts to impregnate the desired amounts of copper ($Cu(NO_3)_2$) and strontium $Sr(NO_3)_2$). The mixture of ceramic and metal salts was subjected to 50°C for 8 h, subsequently dried at 110°C overnight. The dried catalysts were then calcined at 600°C for 6 h. The materials obtained after the calcination process were characterized and used for catalytic co-pyrolysis.

6.2.3 Catalyst characterization

XRD was employed to characterize the crystalline phases of mono- and bimetallic catalysts using a Rigaku Ultima IV. The samples were scanned across a 2θ range of 5 to 70° using a step size of 0.05°. The total surface area and pore size distribution of the mono- and bimetallic catalysts were determined by N_2 physisorption. SEM-EDS was used to determine the amount of Strontium (Sr), and Copper (Cu) loaded into catalyst supports. XPS were carried out to determine elemental composition and the oxidation states of mono- and bimetallic catalysts using Kratos Axis Supra measurements. XPS peak processing software was used to deconvolute the peaks to separate different species of the same element.

6.2.4 Pyrolysis GC/MS

Py-GC/MS analysis was carried out using Agilent 6890 GC 5973N MS couple with CDS Pyroprobe 6150 pyrolyser. The pyrolysis temperature was set at 750°C for 30 s with heating rate of 10°C /ms. The GC separation was carried out using HP-5MS column with a constant helium flow of 1.0 mL/min and the injector temperature was maintained at 250°C. Typical operating conditions of MS include ionization energy at 70 eV and m/z scanning mode over a range of 25–550 amu. The relative content of catalytic co-pyrolysis products was identified based on chromatograph peak area (%), which also reported by previous studies [439]. Compounds that have similarity factor greater than 80% with NIST library were used for the analysis. The relative selectivity of aromatic hydrocarbon (As) was calculated based on equation (6.1). Before each sample injection, three blank injections were performed to reduce the retention effect and background signal.

$$\mathrm{As} = \frac{\mathrm{Hs}}{\sum \mathrm{Ht}} \tag{6.1}$$

Where Hs is the peak area of specific aromatic hydrocarbon, ΣHt is the total peak area of hydrocarbons.

6.3 Results and discussion

6.3.1 Catalyst characterization

The XRD spectra of mono- and bimetallic catalysts prepared with different catalyst supports are presented (Figure A.22). The XRD profile of parent Y-zeolite exhibited typical peaks of zeolite at 6.3°, 10.25°, 12.2°, 16°, 19.1°, 20.7°, and 23.3°, which are indexed as the [111], [331], [533], and [555] planes [4]. The XRD profile of ZSM-5 displayed peaks with high intensity for 2-theta values 8.1° and 23° and were in-line with previous reports [440]. The AC sample indicated a single peak at 2-theta of 26.5° and could be attributed to the amorphous nature of the carbon sample [441]. There were predominant peaks for crystalline ZrO_2 at 2-theta values 30.3°, 35.1°, 50.4°, and 60°, which are indexed as the [101], [110], [200], and [211] planes [442].

Table 6.1. Elemental composition of Cu-SrO catalyst prepared with various catalyst supports using SEM-EDS.

Catalysts	Copper loading (wt. %)		Strontium loading (wt. %)	
	Actual	Nominal	Actual	Nominal
SrO/AC	-	-	10	8.48
Cu-SrO/AC	5	4.51	10	8.59
SrO/Y-zeolite	-	-	10	7.91
Cu-SrO/Y-zeolite	5	3.51	10	8.90
SrO/ZSM-5	-	-	10	8.91
Cu-SrO/ZSM-5	5	4.75	10	8.30
SrO/Al_2O_3	-	-	10	9.27
Cu-SrO/Al_2O_3	5	4.36	10	9.11
SrO/ZrO_2	-	-	10	7.32
Cu-SrO/ZrO_2	5	3.74	10	7.44

After loading of SrO and CuO into the catalyst supports, both mono- and bimetallic catalysts displayed Sr peaks at 2-theta values of 11.9°, 20.4°, 23.7°, 31.45° and 34.75° and Cu peaks at 2-theta values of 33.2°, 47.9°, and 53.7°, which confirms that Sr and Cu were successfully loaded on the catalyst supports. Particularly for the Y-zeolite and ZSM-5 the diffraction peak shifted to a lower angle and the half-peak width increased gradually. This indicates that the loading of SrO and CuO caused partial structural damage to the catalyst supports [315]. In addition, the loading of SrO and CuO on catalyst supports is confirmed by EDS analysis (Table 6.1). The actual Sr and Cu loadings were in between 7.32 to 9.27 wt.% and 3.51 to 4.75 wt.%, respectively. For all the synthesised catalysts, copper to strontium ratio was comparable with the nominal ratio.

Nitrogen adsorption-desorption isotherms for the mono-metallic and bimetallic catalysts prepared from five different catalyst support materials are provided (Figure 6.1). To better understand the surface properties, the catalyst supports were grouped in two groups for discussion: microporous (AC, Al_2O_3, and ZrO_2) and mesoporous (ZSM-5 and Y-zeolite). The parent catalyst supports AC, Al_2O_3, and ZrO_2 exhibited a type I isotherm that indicating the presence of a microporous material [308]. The pore structure of parent catalyst supports did not change after loading with Sr and Cu. The total surface area (S_{BET}) for AC, Al_2O_3, and ZrO_2 are 835.18 m^2/g, 128.35 m^2/g and 13.92 m^2/g, respectively (Table 6.2). However, ZSM-5 and Y-zeolite catalyst supports showed type IV adsorption curves, showing the presence of mesopores in the catalysts (Figure 6.1). The mesoporous surface area (S_{meso}) was also affected by the types of catalyst support. ZSM showed the highest S_{meso} of 237.07 m^2/g, which might enhance the number of active sites and allow more macromolecules to pass through the catalyst. Y-zeolite also produce low microporous volume of 0.066 cm^3/g compare with ZSM-5. The presence of low microporous volume hinder penetration of IB and WCO molecule during the co-pyrolysis, which force the reaction to take place on the surface of the catalysts.

The mono- and bimetallic of ZSM-5 and Y-zeolite catalysts had a type IV adsorption-desorption isotherm curve, indicating mainly a mesoporous structure. Furthermore, both catalysts showed substantially wide pore size distribution, while the addition of Sr and Cu to mesoporous catalysts (ZSM-5 and Y-zeolite) reduced the specific surface area, but an increase in the pore size that might be due to metals loading. The metals were deposited onto the active sites of the catalysts, and consequently blocking pores. Furthermore, the total average aperture increased because micropores and mesopores account for most blocked pores. These results align with previous studies that described a noticeable decrease in surface area after loading metal oxides onto zeolites [443]. The ZSM-5, SrO/ZSM-5, and Cu-SrO/ZSM-5 samples have different textural qualities. In addition, for the mono-metallic catalyst, the pore volume and surface area were noticed to decrease, and in general, particles size of mono-metallic SrO is smaller than Cu-O-Sr, therefore they can easily penetrate to the inner part of the catalyst and lower surface area. However, the large particle size of bimetallic catalyst (Cu-O-Sr) reduced the surface area and impacted pore diameter to a lower extent than mono-metallic. SrO/AC and Cu-SrO/AC catalysts showed high surface area, and average pore diameter compared to the other samples.

Table 6.2. Specific surface area and pore volume for Cu-SrO catalysts prepared with various catalyst supports.

Sample	S_{BET} (m^2/g)	S_{Meso} (m^2/g)	V_{total} (cm^3/g)	V_{micro} (cm^3/g)	V_{meso} (cm^3/g)
AC	835.18	196.81	0.397	0.251	0.146
SrO/AC	1272.32	492.75	0.627	0.332	0.295
Cu-SrO/AC	806.46	200.27	0.465	0.256	0.209
Y-zeolite	577.20	53.50	0.330	0.267	0.066
SrO/Y-zeolite	436.32	171.72	0.345	0.098	0.246
Cu-SrO/Y-zeolite	397.60	146.10	0.250	0.100	0.150
Al_2O_3	128.35	84.38	0.277	0.033	0.244
SrO/Al_2O_3	183.61	170.51	0.298	0.041	0.257
Cu-SrO/Al_2O_3	137.03	135.45	0.297	0.044	0.253
ZSM-5	440.72	237.07	0.293	0.086	0.207
SrO/ZSM-5	425.33	195.96	0.229	0.095	0.134
Cu-SrO/ZSM-5	364.01	39.56	0.197	0.137	0.060
ZrO_2	13.92	9.42	0.020	0.004	0.016
SrO/ZrO_2	24.58	16.91	0.031	0.005	0.026
Cu-SrO/ZrO_2	13.951	12.818	0.021	0.001	0.020

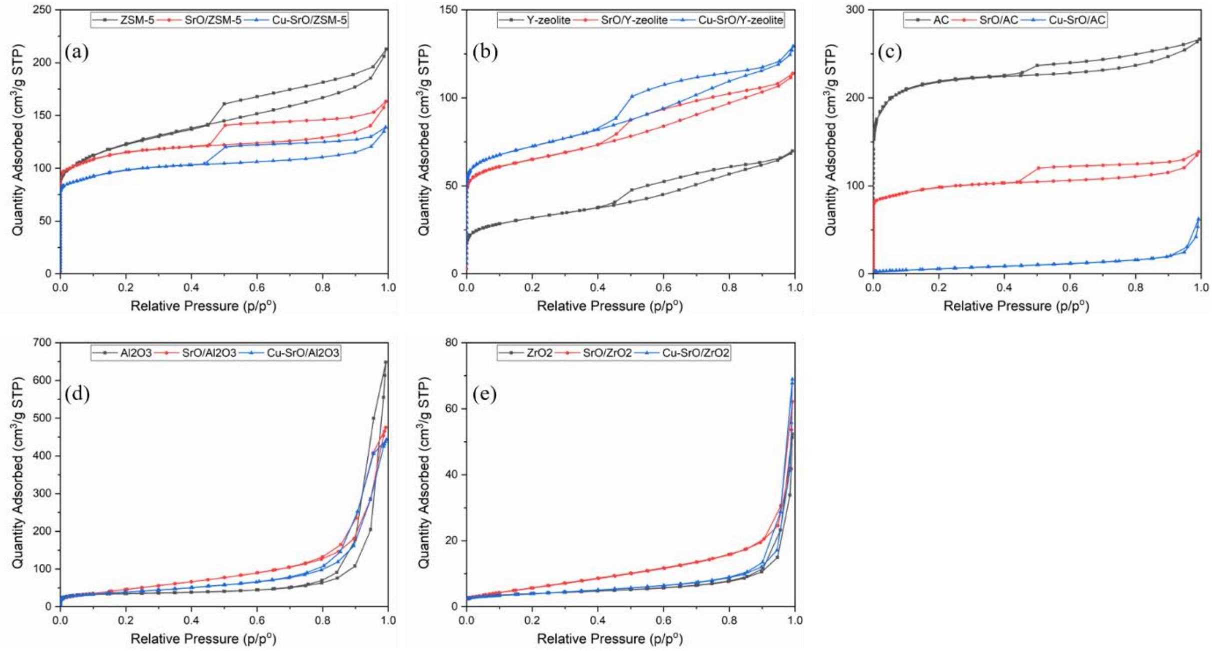

Figure 6.1. N_2 adsorption-desorption isotherms of: (a) ZSM-5 catalyst support; (b) Y-zeolite catalyst support; (C) Activated carbon (AC) catalyst support; (d) Al_2O_3 catalyst support. (e) ZrO_2 catalyst support.

XPS was employed to investigate mono- and bimetallic catalysts chemical states and elemental compositions. The XPS spectra of SrO/ZSM-5 for Sr were at Sr $3d_{5/2}$ (134.1 and 135.6 eV) and Sr 3P (270.3 and 280.7 eV), indicating the presence of Sr^{2+}. Similarly, for SrO/Y-zeolite, XPS spectra for Sr $3d_{5/2}$ (132.9 and 134.4 eV) and Sr 3P (271.1 and 280.7 eV) also indicated that Sr was mainly in the Sr^{2+} state. In addition, XPS curve fitting for Sr $3d_{5/2}$ SrO/AC (133.8 and 135.9 eV), SrO/Al_2O_3 (133.5 and 135.7 eV) and SrO/ZrO_2 (133.3 and 135.6 eV) confirmed the presence of SrO. For bimetallic catalysts, the position of Sr $3d_{5/2}$ and Sr 3P XPS peaks shifted to lower energy, in the range of 129.7 to 132.7 eV and 133.1 to 134.5 eV, respectively. Loading of copper on mono-metallic catalyst changed the content of the lattice oxygen, which may have caused a slight shift in the binding energy and thus, a change in the shape of the spectrum. The XPS absorption peaks for Cu^0 were noticed at 932.6, 933.3, and 932.8 eV, and the peak at 936.2 eV was attributed to Cu^+, showed that Cu^0 and Cu^+ are present in the sample. Meanwhile, the O1s regions of bimetallic catalysts of all samples showed the formation of Cu-O-Cu species *ca.* at 532.8 eV. However, the binding energy shifted to the left (528.1 eV) for mono-metallic catalysts, which indicated the possibility of an electron transfer from Cu to Sr via the Cu-O-Sr structure.

6.3.2 Pyrolysis product composition

The product distribution of the non-catalytic and catalytic co-pyrolysis (CCP) of IB:WCO mixture with different catalyst supports is presented in Figure 6.2. The operational parameters considered for the reaction are as follows; temperature: 750°C, IB:WCO ratio of 1:1, a reaction time of 30 min, and catalyst to feedstock ratio 1:2. The pyrolysis products were classified based on their chemical structures as acids, hydrocarbons, phenols, ketones, aldehydes, and esters. The major compounds produced during the non-catalytic co-pyrolysis were acids (64.1%, mainly oleic acids), followed by aromatic hydrocarbons (13.1%), phenolic compounds (11.3%), and ketones (4.9%).

Mono-metallic catalysts enhanced the hydrocarbon yield and reduced the formation of acids and oxygenated compounds. The order of hydrocarbon yield was as follow: SrO/ZSM-5 (56.7%) > SrO/Y-zeolite (40.9%) > SrO/ Al_2O_3 (32.9%) > SrO/ZrO_2 (30.4%) > SrO/AC (28.1%). The acid sites in mesoporous Y-zeolite and ZSM-5 may have converted long-chain hydrocarbons and acids (produced from lignin and cellulose) into aromatics via secondary cracking [444]. In addition, oxygenated compounds from WCO were converted into aromatics via ketonisation, aldol condensation, β-scission, and hydrogen transfer reactions [443]. As shown in Figure 6.2, SrO/ZSM-5 and SrO/Y-zeolite produced bio-oil with low acid content of 9.1% and 24.9%, respectively. The addition of SrO resulted in additional basic sites on the zeolite catalyst supports, increasing the hydrocarbon yield by converting ketones, aldehydes, and fatty acids into mono-aromatics. Among mono-metallic catalysts, SrO/AC produced oil with high acid content of 38.7% [436], while SrO/ZrO_2 and SrO/Al_2O_3 catalysts favoured the ketonisation of carboxylic acids.

Bimetallic catalysts significantly enhanced the hydrocarbons yield and decreased the acids content in pyrolytic vapour. The order of hydrocarbon yield was as follows: Cu-SrO/ZSM-5 (70.06%) > Cu-SrO/Y-zeolite (65.43%) > Cu-SrO/Al_2O_3 (46.51%) > Cu-SrO/ZrO_2 (45.42%) > Cu-SrO/AC (34.20%). Bimetallic catalysts also decreased the oxygenated compounds by reducing the acid content in the following order: Cu-SrO/ZSM-5 (4.43%) < Cu-SrO/Y-zeolite (12.5%) < Cu-SrO/ZrO_2 (18.2%) < Cu-SrO/Al_2O_3 (24.5%) < Cu-SrO/AC (30.6%). Copper (Cu-SrO/ZSM-5) enhanced the formation of primary oxygenic products via deoxygenation [445]. Moreover, Diels–Alder reaction at acid sites converted olefins into cycloalkanes [446]. Zeolites may have removed oxygen as CO, CO_2 and H_2O through dehydroxylation, decarboxylation, and decarbonylation [435]. In summary, among the mono-metallic catalysts, SrO/ZSM-5 produced the lowest acid content of 9.1% via ketonisation and aldol condensation reactions. Moreover, Cu-SrO/ZSM-5 showed the highest hydrocarbon yield of 70.06% by converting oxygenated compounds (acidic compounds) via Diels–Alder reaction.

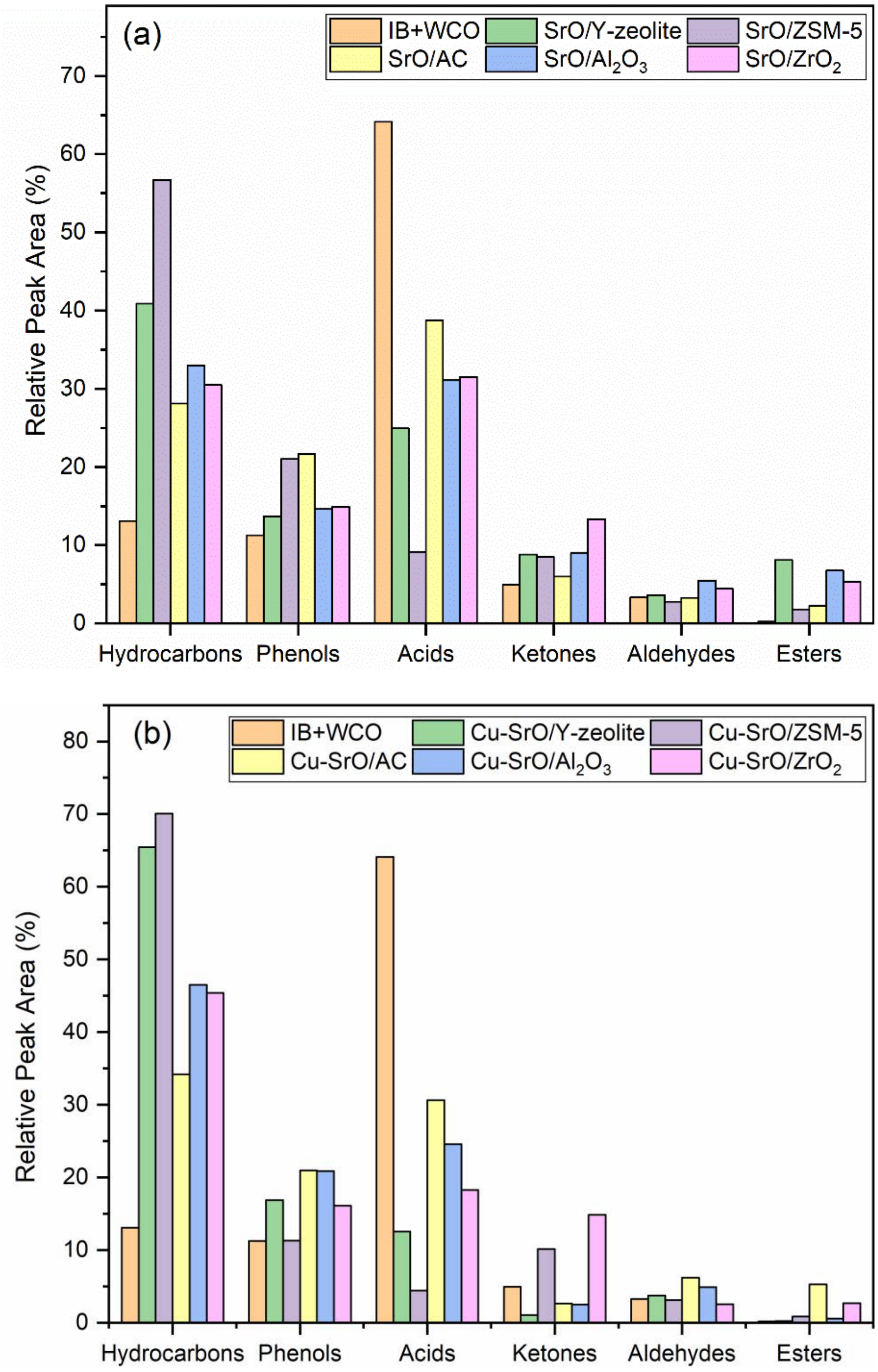

Figure 6.2. Product distribution obtained from non-catalytic and catalytic co-pyrolysis of IB and WCO mixture (a) Mono-metallic catalyst with different support; (b) Bimetallic catalyst with different catalyst supports.

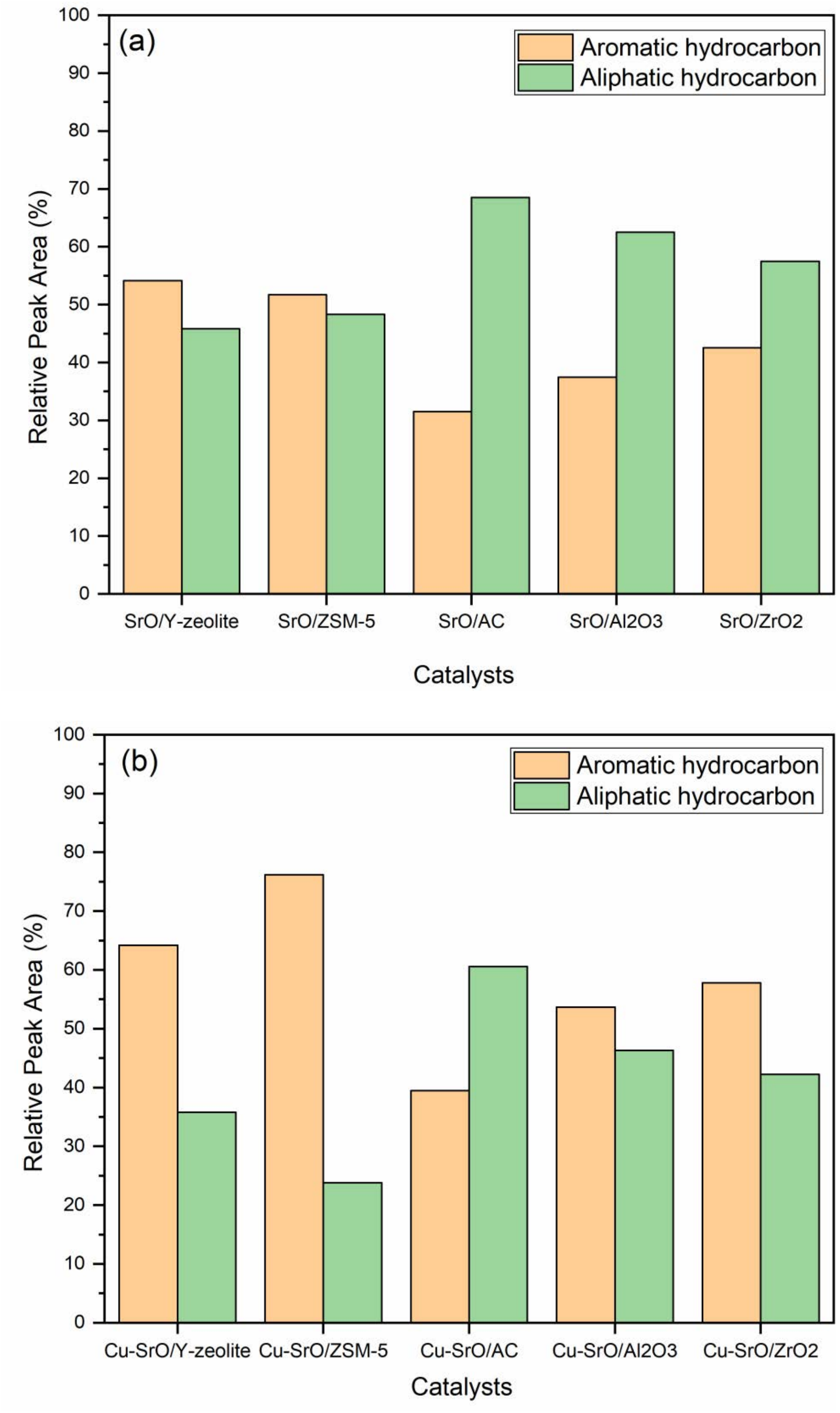

Figure 6.3. Effect of catalyst support on aromatic and aliphatic content: (a) Mono-metallic (SrO) catalysts prepared with different catalyst supports; (b) Bimetallic catalysts (Cu-SrO) prepared with different catalyst supports.

6.3.3 Effect of catalyst on selectivity of Aromatic hydrocarbon

The percentage of aromatic hydrocarbons produced using different catalyst supports is presented in Figure 6.3. In non-catalytic co-pyrolysis of IB:WCO mixture, the percentage of aromatic hydrocarbons was only 2.7%, the liquid hydrocarbons product was predominantly composed of aliphatic hydrocarbons (alkanes and alkenes). The aliphatic hydrocarbons were alkanes (65%), ranging from Nonane (C_9H_{20}) to Dodecane ($C_{12}H_{26}$), and alkenes (18%), ranging from 1-pentadecene ($C_{15}H_{30}$) to 1-nonadecene ($C_{19}H_{38}$). The content of aromatic hydrocarbons was noticed to increase after adding catalysts prepared with different catalyst supports (Figure 6.4). The order of aromatic hydrocarbons yield for mono-metallic catalysts was as follows: SrO/Y-zeolite (54.2%) > SrO/ZSM-5 (51.7%) > SrO/ZrO_2 (42.5%) SrO/Al_2O_3 (37.4%) > SrO/AC (31.5%). Zeolite catalysts with high Lewis acid content favoured the conversion of IB:WCO mixture into aromatic hydrocarbon , resulting in the highest conversion rate. The aromatic hydrocarbons dominated the composition for SrO/ZSM-5 and SrO/Y-zeolite mainly toluene, benzene, and xylene. However, SrO/AC catalyst showed mainly aliphatic hydrocarbons due to the lack of acid sites to promote deoxygenation reaction. The selectivity towards aromatization and removal of heteroatoms increased significantly with bimetallic catalysts. The order of aromatic hydrocarbon percentage was as follows: Cu-SrO/ZSM-5 (76.2%) > Cu-SrO/Y-zeolite (64.4%) > Cu-SrO/ZrO_2 (57.7%) > Cu-SrO/Al_2O_3 (53.9%) > Cu-SrO/AC (39.4%). In general, Cu-SrO/ZSM-5 shows better selectivity and yield towards aromatic hydrocarbons.

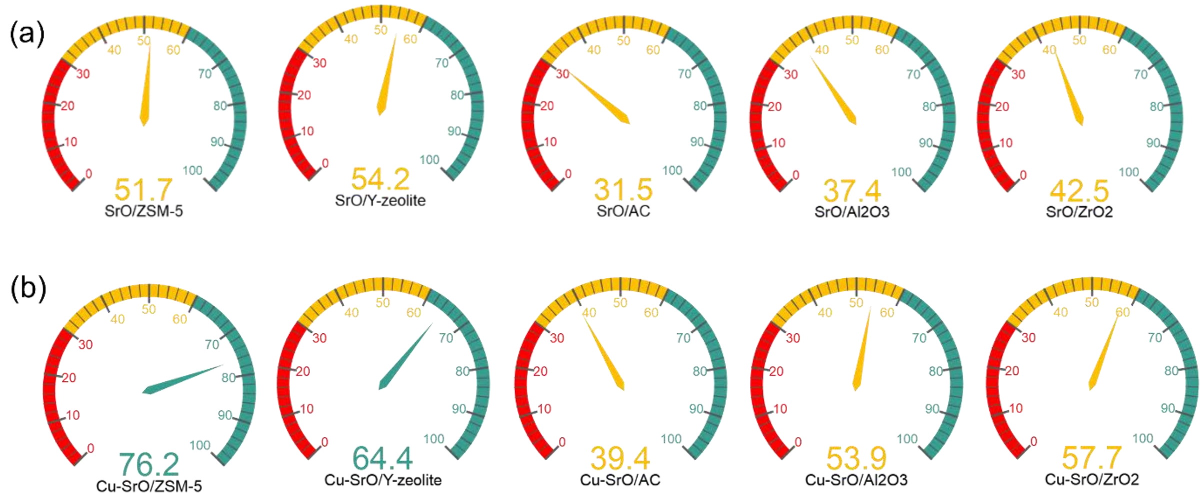

Figure 6.4. Effect of catalyst support (ZSM-5, Y-zeolite, AC, Al_2O_3, and ZrO_2) on aromatic yield and selectivity :(a) Mono-metallic (SrO) catalyst with different catalyst supports; (b) Bimetallic catalyst (Cu-SrO) with different catalyst supports.

6.3.4 Effect of catalyst on selectivity and carbon number yield

The effect of catalyst on the selectivity of gasoline components (C8-C14), diesel components (C15-C17), and heavy oil components (> C20) is showed in Figure 6.5. As shown in this figure, the addition of catalysts enhanced the hydrocarbon selectivity while reducing the high molecular weight components (heavy oil). The non-catalytic co-pyrolysis produced a heavy oil component of 58.7% (> C20). During the co-pyrolysis process, cellulose, hemicellulose and lignin undergo thermal depolymerization into small intermediate products. Cellulose produces intermediate products such as levoglucosan, furfural, 5-hydroxymethylfurfural, and other small molecules [447]. In addition, the triglycerides presented in WCO are also converted into alkanes, alkenes, paraffin, and unsaturated compounds [448].

ZSM-5 catalyst support favoured the formation of C8-C14 and reduced the formation of compounds over C20. The hydrocarbon selectivity is influenced by catalyst physicochemical properties such as acidity, metal loading and surface area [274]. As shown in Figure 4(a), SrO/ZSM-5 promoted cracking of IB:WCO mixture, resulting in an increase in C8-C14 compounds (61.45%), and reduced the formation of compounds over C20 (6.35%) compared with non-catalytic co-pyrolysis (58.7%). This improvement is due to the presence of strong acid sites on ZSM-5 catalyst created by the addition of metals, which favour pyrolytic vapor decomposition into small hydrocarbon molecules. The main reaction pathways involved to produce gasoline range compounds are decarboxylation, cyclization, aromatization, and Diels-Alder reactions [378]. Moreover, Cu-SrO/ZSM-5 significantly increased the content of C8-C14 compounds to 87.28% while reducing compounds over the range of C20 to 1.19%. The addition of copper promoted the deoxygenation reaction in the conversion of aliphatic C-O in WCO resulting in the formation of olefins and a hydrocarbon pool [449]. The pore size of ZSM-5 also played an important role in facilitating secondary cracking and cyclization of lower-chain phenolic compounds to generate gasoline range compounds [378]. However, the selectivity of Cu-SrO/ZSM-5 for C17 was low (6.21%), which implies low selectivity towards decarbonylation and decarboxylation reaction pathways. This low selectivity can be explained by the contribution of decarbonylation of octadecanol and decarboxylation of stearic acid to the formation of C17 compounds [450].

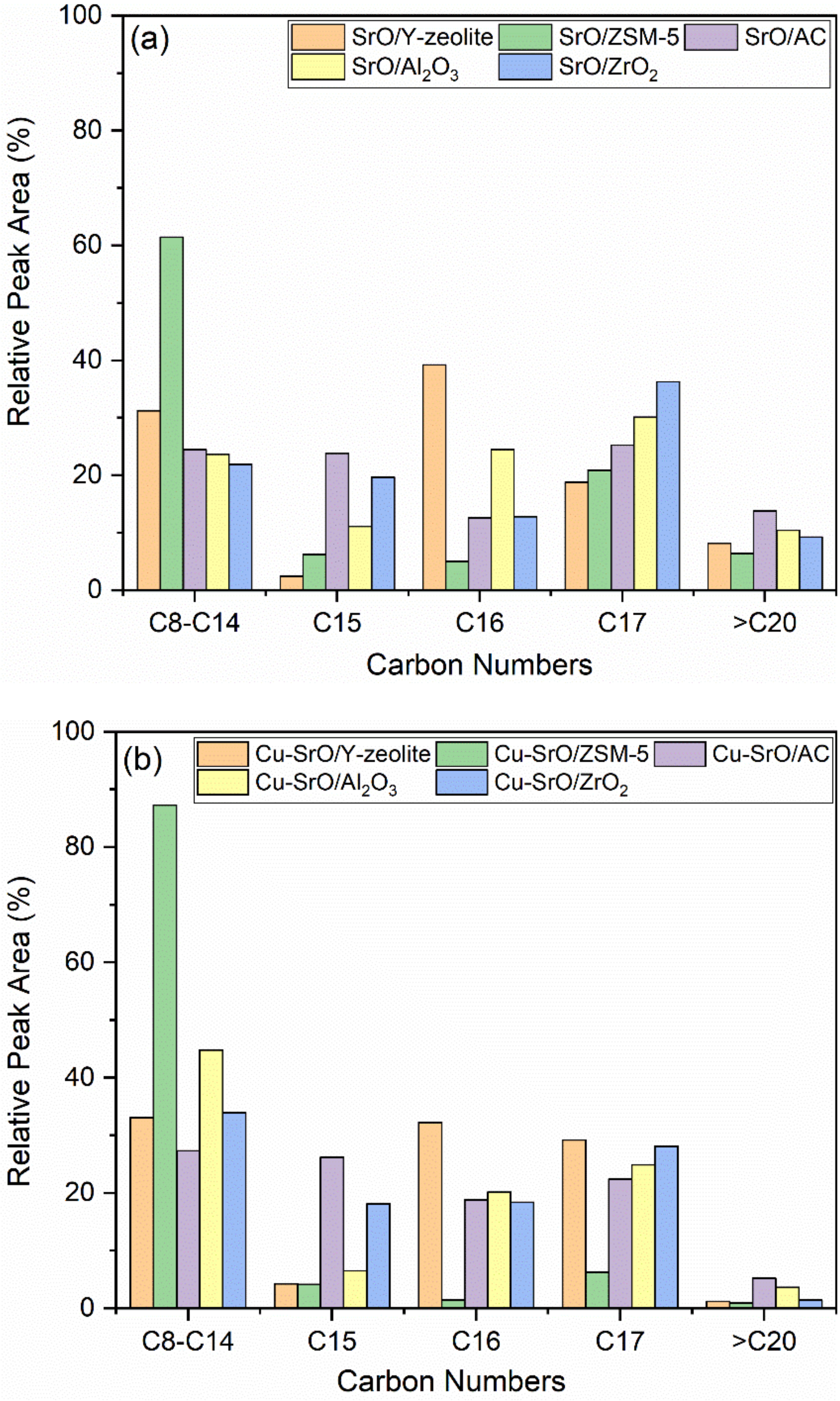

Figure 6.5. Effect of catalyst support on carbon yield and selectivity (a) Mono-metallic catalyst with different catalyst supports; (b) Bimetallic catalyst with different catalyst supports.

SrO/Y-zeolite displayed higher selectivity towards C16-C17 (59.4%) and C8-C14 (31.2%) compounds. The complex structure of IB breaks into free radical benzene rings, which bond with hydrogen radicals from hierarchical Y-zeolite acidic sites to form phenols and methoxy–substituents such as phenol, methoxyl phenoxide, guaiacol, cresol, and 3-methoxy-4 hydroxybenzaldehyde. Meanwhile, during thermal decomposition, WCO may have been converted into olefins, hydrogen, and alkyl radicals via β-scission in the presence of the SrO/Y-zeolite catalysts. The acid sites on the Y-zeolite assisted the extraction of hydrogen from aliphatic C-C in WCO to produce carbanions. The unstable carbanions undergo β-scission to form olefins and a hydrocarbon pool. Cu-SrO/Y-zeolite showed a better selectivity towards higher molecular weight hydrocarbons. Cu-SrO/Y-zeolite produced maximum aromatic hydrocarbons yield for C8-C14 (46.72%), which was much higher than SrO/Y-zeolite (31.2%). The addition of Cu on SrO/Y-zeolite enhanced the deoxygenation and product selectivity, which may be due to the formation of strong active acid sites. Cu promoted the formation of mono-aromatics through decarbonylation, demethoxylation, and decarboxylation reactions of oxygenate compounds.

The basic SrO/ZrO_2 catalyst showed high selectivity towards C17 (36.28%) and low selectivity for C8-C14 compounds (21.93%). The Lewis acid sites in SrO/ZrO2 favoured decarbonylation and hydrogenation reactions, mainly producing C17 hydrocarbons [449]. The lack of active Brönsted acid sites also hindered the conversion of oleic acids and levoglucosan into C8-C14 compounds. However, bimetallic modification (Cu-SrO/ZrO_2) further increased the production of C8-C14 compounds to 33.94%, but reduced C17 compounds to 28.1%. Loading of Cu initiated secondary cracking reactions and enhanced hydrogenation reactions. Similarly, loading of Cu on ZrO2 support resulted in the reduction of compounds over C20 from 9.27% (SrO/ZrO_2,) to 1.44% (Cu-SrO/ZrO_2).

Activated carbon (AC) catalyst support provided a high surface area with homogeneous active sites, which promoted Fischer-Tropsch synthesis reaction [451]. The content of C8-C14 compounds from mono-metallic (SrO/AC) was 24.45%, while the content of compounds over C20 range reduced from 58.7% to 13.82%. Sample with bimetallic Cu-SrO/AC catalyst showed total selectivity of 27.34% and 22.41% for C8-C14 and C17, respectively. This suggests that Cu-SrO/AC promoted the conversion of compounds over C20 range into CO and CH_4 via a cracking reaction [452].

Metal oxide (Al_2O_3) support favoured the reduction-deoxidation reaction. Cu-SrO/Al_2O_3 increased the selectivity towards C8-C14 compounds from 23.67% to 44.79%, while C17 and compounds over C20 range decreased to 24.92% and 3.62%, respectively. The C8-C14 compounds yield increased due to deoxygenation of phenolic compounds and triglycerides on Lewis acid sites of Al_2O_3 [394]. γ-hydrogen transfer and β-elimination reaction pathways may have reduced the contents of carboxylic acids and C20 compounds. In general, ZSM-5 catalyst support favoured pyrolytic vapour decomposition into small hydrocarbon molecules, which produced gasoline range compounds via aromatization, cyclization, decarboxylation, and Diels-Alder reactions. The addition of copper enhanced the formation of strong active acid sites and favoured deoxygenation reaction in the conversion of aliphatic C-O in WCO to olefins and aromatic hydrocarbons.

6.3.5 Role of catalyst support on reaction mechanism and product distribution

The catalyst support promotes various reaction pathways to remove oxygenated compounds and enhance bio-oil quality. In particular ZSM-5 and Y-zeolite promote aromatization and Diels–Alder reaction to produce high amount of aromatic hydrocarbon [446]. However, Al_2O_3 and ZrO_2 favoured ketonisation and aldol condensation, and AC followed demethoxylation and dealkylation reactions [436]. Among the catalyst support, ZSM-5 catalyst support mainly favoured the formation of C8-C14 compounds and reduced the formation of compounds over C20 [453, 454]. The Brönsted acid sites on zeolites act as active catalytic sites to conduct various deoxygenation and aromatization reactions during CCP to produce aromatic hydrocarbons and enhance the product distribution [282, 283, 455]. Meanwhile, Y-zeolite assists with producing carbanions by abstracting hydrogen from aliphatic C-C in WCO [397]. The unstable carbanions further undergo β-scission to form olefins and a hydrocarbon pool [377]. The resulting short olefins are subsequently converted to aromatics via the Diels-Alder reaction. The Y-zeolite catalyst support plays a major role in the reaction mechanism and product distribution as intermediate products formed during CCP of IB further undergo dehydration, decarboxylation, decarbonylation, and oligomerization, then combine with short chains olefins (generated from the thermal degradation of WCO) to form aromatic compounds. Undesirably, furans from cellulose and hemicellulose are likely to polymerize and react with smaller phenols to form coke [377]. However, short olefins originated from WCO in the reaction converted into aromatics instead of undergoing polymerization, reducing coke formation for the CCP of IB and WCO. The oxygen is mainly removed from the oxygen containing compounds in the form of H_2O, CO, and CO_2 during dehydration, decarbonylation, decarboxylation, and thermal cracking [456, 457].

AC catalyst supports exhibit microporous material with a high surface of 835.18 m^2/g. As evident from previous studies, the AC has low acid sites, and the CCP occurs at the surface of the catalyst support [441]. The thermal degradation IB and WCO produce intermediate products such as guaiacols, anhdrosugars, and fatty acids. AC promotes decarbonylation and dehydration reactions to convert anhdrosugars into simple phenol, methylphenol via decarbonylation and dehydration reactions, which creates a phenol pool. The functional groups present in AC (C–O, OH, and O–C=O groups) promote the generation of non-methoxy phenols [452]. Then the cyclopentenones undergo demethoxylation and dealkylation reactions to form a phenol pool. Meanwhile, WCO thermal cracked into olefin compounds with the assistance of active sites on the AC catalyst surface. The synergetic effect between WCO-derived olefins and phenol pool from IB produces aromatic hydrocarbons by Diels-Alder reaction [446]. The metal oxide ZrO_2-based catalyst support (acid and base) promotes the formation of high molecular weight alkanes and favours aldol condensation and ketonisation reactions to remove oxygenated compounds [434]. During the CCP of WCO and IB, the carboxylic acids formed are converted into large molecular weight ketones, which could then be coupled in the aldol condensation reaction to form aldehyde. The acid sites on the ZrO_2 catalyst surface and the hydrogen donor from pyrolysis of WCO favour hydrogenation/ dehydration of the aldol condensation products to produce fuel-grade alkanes [437].

6.4 Conclusions

This work studied the effect of mono- (SrO) and bimetallic (Cu-SrO) catalysts prepared with different supports (ZSM-5, Y-zeolite, activated carbon, Al_2O_3, and ZrO_2) to produce gasoline-range bio-oil from IB:WCO mixture. Loading of SrO introduced additional basic sites on the catalyst supports, increasing the hydrocarbon yield by converting ketones, aldehydes, and fatty acids into mono-aromatics. Cu-SrO/ZSM-5 promoted secondary cracking and aromatization reactions and enhanced the hydrocarbon content to 70.06%. Bimetallic catalysts showed high selectivity towards gasoline range (C8-C14) compounds with the following order: Cu-SrO/ZSM-5 (87.28%) > Cu-SrO/Y-zeolite (46.72%) > Cu-SrO/Al_2O_3 (44.79%) > Cu-SrO/ZrO_2 (33.94%) > Cu-SrO/AC (27.34%). Therefore, this study contributes to a better understanding of the effect of catalyst supports and metal oxides to produce bio-oil rich aromatic compounds from lignocellulose biomass and waste.

7 CONCLUSIONS AND RECOMMENDATIONS

The overall objective of this research thesis has been successfully achieved and this chapter reports the overall conclusions of this research thesis. Conclusions are described sequentially, chapter by chapter. The implications of this research are then presented. Finally, recommendations for future work are outlined.

7.1 Probing the impact of catalyst synthesis conditions on the preparation of catalyst with high mesoporous surface and volume catalyst.

In this chapter, the preparation of a bifunctional (acidic-basic) SrO/Y-zeolite using sequential dealumination-desilication to create hierarchal structure and subsequently loading of strontium via wet and dry impregnation methods was discussed. Parent Y-zeolite was used as a precursor to create a hierarchical structure. Dealumination process (acid treatment) was performed with two different concentrations of citric acid of 0.05 M (ATl) and 0.1 M (AT2). The dealumination process increased the mesoporous surface area from 53 m^2/g to 147 m^2/g and the Si/Al ratio (2.48 to 5.36), which confirms the effectiveness of citric acid in selectively removing aluminium from the Y-zeolite framework and consequently enhancing the formation of mesoporosity. The desilication process was carried out with different NaOH concentrations (0.2 M, 0.4 M, and 0.8 M) in the presence of cetyltrimethyl ammonium bromide (CTAB). The desilication process enhanced mesoporosity by removing the debris remaining in the zeolite framework from the dealumination treatment. The use of CTAB in the desilication process provided stability to the zeolite framework by removing silicon atoms and restoring the microporosity. Wet and dry impregnation methods were then used to load strontium in the Y-zeolite, and both methods showed comparable average strontium loading. Both methods showed a decrease in mesoporous volume and surface area with the loading of Sr ion into the zeolite framework. Among all samples, SrW-AT2-0.2M displayed the highest mesoporous surface area (379.7 m^2/g). These results confirm that sequential dealumination and desilication processes are effective pathways to create hierarchical catalysts with high mesoporous surface area and volume. The wet impregnation method resulted in higher strontium loading with an average of 6.8%, while the dry impregnation method resulted in a strontium loading of 5.3%.

7.2 High-quality bio-oil production and optimisation of process parameters

In this chapter, catalyst with the highest mesoporous surface area and volume from chapter 3 was used to produce high-quality bio-oil by using a fixed bed reactor. The bio-oil quality and yield were also enhanced through the optimisation of process parameters such as SrO loading into Y-zeolite, IB:WCO ratio, and pyrolysis temperature. Catalyst characterisation results confirm the successful loading of strontium on Y-zeolite and the presence of both acidic and basic active sites on the catalysts. Among the process parameters, the temperature of 550ºC, IB:WCO of 1:1, and Sr Loading of 10% produced a bio-oil yield of 55.3% with low moisture content (17.3%). The chemical compounds present in the bio-oil were grouped into aromatics, carbonyl, aliphatic, methoxy, and levoglucosan. Non-catalytic pyrolysis of IB produced an aromatic carbon yield of 10.6%. In contrast, non-catalytic pyrolysis of WCO produced an aliphatic yield of 59.5%. After adding a catalyst to IB:WCO mixture, the aromatic C-H content in the bio-oil increased to 28.6%.

The pyrolysis temperature played a significant role in the decomposition of long-chain hydrocarbons present in the bio-oil. The maximum aromatic hydrocarbon yield of 28.6% was obtained at 550°C, representing the optimum temperature where maximum devolatilisation and bond breakage occur. On the other hand, SrO loading (basic sites) on Y-zeolite catalyst increases the aromatic carbon yield by converting fatty acids into poly-aromatics. Results showed that increasing the SrO amount promoted decarboxylation, ketonisation, and aldol condensation reactions; particularly, 10% SrO produced high aromatic hydrocarbons yield. Because of the availability of an optimum number of total active sites (acidic and basic) to perform the cracking and deoxygenation reactions. The proposed reaction mechanism also showed that aromatics were synergistically generated from methoxy/hydroxyl, phenols and levoglucosan from the IB and the hydrocarbon pool provided by WCO. Overall, the results demonstrated that SrO/Y-zeolite is a potential catalyst to produce high-quality bio-oil from co-pyrolysis of IB and WCO.

7.3 Examining the effect of bimetallic catalyst on bio-oil product distribution

In this chapter, the effect of adding a second metal (Ni, Cu, Zn, Ag, and Fe) on SrO/Y-zeolite to upgrade bio-oil quality was examined. The second metals (5%) were selected based on their performance in upgrading bio-oil quality and contribution to acidity. The catalyst characterisation results showed that loading of a second metal decreases the surface area, which might be due to blockage of pores in the zeolite framework by SrO and the second metal. Among the bimetallic catalysts, Cu-SrO/Y-zeolite showed the highest mesoporous surface area (171.7 m^2/g) because of the smallest ionic radii of Cu^{2+} and its distribution on the Y-zeolite surface. All prepared catalysts were mixed with IB:WCO mixture for Py-GC/MS tests to study product distribution, and TGA analysis for kinetic parameters investigation. The kinetics study showed that the non-catalytic IB:WCO mixture shows the highest average activation energy of 193.2 kJ/mol. However, adding catalysts effectively reduced the average activation energy in the following order (based on the second metal): Ni> Ag> Zn> Fe> Cu.

The Py-GC/MS results indicated that bimetallic catalyst selectivity enhanced the aromatic hydrocarbons yield. Ag-SrO/Y-zeolite selectively increased the phenolic content to 15.8% by promoting hydrogenation of C–O bond in lignin and converting into phenol. Cu-SrO/Y-zeolite produced bio-oil with a high aromatic content of 65.43% at 750°C and the lowest acid content. Cu-SrO/Y-zeolite also showed better selectivity towards jet fuel range hydrocarbons (C17-C20) with a maximum yield of 86.72%. The high mesoporous area and strong interaction between Cu-SrO helped in the conversion of higher molecular weight compounds into aromatic hydrocarbons.

7.4 Effect of catalyst supports on bio-oil product distribution

This chapter investigates the effect of mono- (SrO) and bimetallic (Cu-SrO) catalysts prepared with different catalyst supports on product distribution, aromatic selectivity, and carbon yield. Catalyst supports were selected from different catalyst groups: zeolite (ZSM-5), mesoporous catalyst (Y-zeolite), biomass-derived catalyst (AC), basic catalyst (ZrO_2), and acidic catalyst (Al_2O_3). All catalysts were characterized using BET, SEM, XPS, and FTIR. All bimetallic catalysts significantly enhanced the hydrocarbon yield and decreased the acid content in the pyrolytic vapour. Hydrocarbon yield: Cu-SrO/ZSM-5 (70.06%) > Cu-SrO/Y-zeolite (65.43%) > Cu-SrO/Al_2O_3 (46.51%) > Cu-SrO/ZrO_2 (45.42%) > Cu-SrO/AC (34.20%). Among the catalyst supports, ZSM-5 produced the maximum aromatic hydrocarbon yield by converting long-chain hydrocarbons and acids (produced from lignin and cellulose) into aromatics via secondary cracking. Bimetallic catalyst (Cu-SrO) revealed high selectivity towards gasoline range (C8-C14) compounds. This chapter establishes a novel theoretical foundation and technological support to produce gasoline-grade bio-oil.

7.5 Implications of this research

This research work introduces for the first time a new SrO/Y-zeolite catalyst for bio-oil upgradation and production of high–quality bio-oil. The presence of acidic and basic active sites on the catalyst converts various oxygenated compounds in bio-oil into aromatic hydrocarbons. This research has been successful in combining hierarchical Y-zeolites (acidic sites as support) with alkaline metals oxides such as SrO (alkaline sites). This new catalyst system addresses all oxygenated compounds by providing high mass transfer (hierarchical structure) and promotes ketonisation and aldol condensation reactions due to the presence of SrO. This combination resulted in enhancing both the aromatic yield and bio-oil quality.

The research work also demonstrates the flexibility and selectivity of bimetallic catalysts towards specific bio-oil chemical groups and different fuel ranges. Among the bimetallic catalyst, Ag-SrO/Y-zeolite showed high selectivity towards phenolic compounds producing a phenol-rich bio-oil, which can be used as a precursor to produce synthetic phenol-formaldehyde resins, bioplastics, and polyurethane materials. Moreover, the research findings from this work demonstrate the capability to tailor-made catalysts with selectivity towards different fuel ranges in bio-oil: gasoline (C8-C14), diesel (C15-C17) and jet fuel range (C17-C20). Cu-SrO/Y-zeolite catalyst showed high selectivity towards jet fuel range while Cu-SrO/ZSM-5 showed high selectivity towards gasoline fuel range. Fine-tuning catalyst physicochemical properties is fundamental for the economical production of different fuel grades.

This research demonstrates the potential of combining biomass and waste cooking oil feedstocks for renewable energy production, which establishes an essential pathway for the "wealth from waste approach" by converting waste cooking oil from household and industrial waste into bio-oil. This research work also contributes towards a circular bioeconomy strategy to initiate a low carbon economy by reducing greenhouse gases footprint, and holds great prospects for a sustainable and greener world. Overall, this research establishes a novel theoretical foundation and technological support to produce high-quality bio-oil with high selectivity towards jet and gasoline-grade fuels.

7.6 Recommendations

The catalyst synthesis methods affect the surface properties and structures of catalysts. Therefore, it is important to explore robust catalyst synthesis methods to enhance catalyst activity. Synthesis methods such as single atom catalyst, metal-organic framework (MOF), and ion exchange can be used. Further creating hierarchical structure on the catalyst support enhances mass transfer during catalytic pyrolysis. Thus, research should be focused on fine-tuning the catalyst structure via 3D technology (additive manufacturing). 3D printed catalysts have several advantages, have a better hierarchical structure, can be used in-situ and ex-situ, can be regenerated and reused multiple times. In addition, understanding detailed fundamental reaction mechanisms inside catalyst pores is pivotal to upgrading bio-oil quality. Future work should investigate reaction mechanisms using representative chemical substances from each potential feedstock.

Our study proposed a new idea by combining hierarchical Y-zeolites (acidic sites as support) loaded with SrO (alkaline sites). It was carried out using solely in-situ catalytic pyrolysis mode, making it difficult to separate the catalyst from the final product (biochar). Since in-situ catalytic pyrolysis is operated in a single reactor, it saves associated capital costs. However, ex-situ catalytic pyrolysis enables the recovery and reusability of catalysts. Therefore, future research should utilise both ex-situ catalytic pyrolysis advantages for economical and environmental benefits. In this research, ironbark and waste cooking oil were used to produce bio-oil, but other feedstocks with a high H/C ratio should be considered to diversify raw material acquisition and expand the bio-oil precursors, which may enhance the quality of bio-oil produced.

References

1. Dai, L., et al., *Integrated process of lignocellulosic biomass torrefaction and pyrolysis for upgrading bio-oil production: A state-of-the-art review.* Renewable and Sustainable Energy Reviews, 2019. **107**: p. 20-36.
2. Altalhi, A.A., et al., *Pyrolytic conversion of waste edible oil into biofuel using sulphonated modified alumina.* Alexandria Engineering Journal, 2022. **61**(6): p. 4847-4861.
3. Zhang, X., et al., *Gasoline-range hydrocarbons produced from microwave-induced pyrolysis of low-density polyethylene over ZSM-5.* Fuel, 2015. **144**: p. 33-42.
4. Dada, T.K., et al., *Thermo-catalytic co-pyrolysis of ironbark sawdust and plastic waste over strontium loaded hierarchical Y-zeolite.* Journal of Environmental Management, 2021. **299**: p. 113610.
5. Chen, G., et al., *Co-pyrolysis of corn cob and waste cooking oil in a fixed bed.* Bioresource Technology, 2014. **166**: p. 500-507.
6. Karmee, S.K., *Liquid biofuels from food waste: current trends, prospect and limitation.* Renewable and Sustainable Energy Reviews, 2016. **53**: p. 945-953.
7. Stefanidis, S.D., et al., *Natural magnesium oxide (MgO) catalysts: A cost-effective sustainable alternative to acid zeolites for the in situ upgrading of biomass fast pyrolysis oil.* Applied Catalysis B: Environmental, 2016. **196**: p. 155-173.
8. Bridgwater, A.V., *Renewable fuels and chemicals by thermal processing of biomass.* Chemical Engineering Journal, 2003. **91**(2): p. 87-102.
9. Asadullah, M., et al., *Production and detailed characterization of bio-oil from fast pyrolysis of palm kernel shell.* Biomass and bioenergy, 2013. **59**: p. 316-324.
10. Kang, Q., et al., *Bioethanol from lignocellulosic biomass: current findings determine research priorities.* The Scientific World Journal, 2014. **2014**.
11. Kobayashi, N. and L.-S. Fan, *Biomass direct chemical looping process: a perspective.* Biomass and Bioenergy, 2011. **35**(3): p. 1252-1262.
12. Panwar, N.L., R. Kothari, and V.V. Tyagi, *Thermo chemical conversion of biomass – Eco friendly energy routes.* Renewable and Sustainable Energy Reviews, 2012. **16**(4): p. 1801-1816.
13. Torres, W., S.S. Pansare, and J.G. Goodwin, *Hot Gas Removal of Tars, Ammonia, and Hydrogen Sulfide from Biomass Gasification Gas.* Catalysis Reviews, 2007. **49**(4): p. 407-456.
14. Morrin, S., et al., *Two stage fluid bed-plasma gasification process for solid waste valorisation: Technical review and preliminary thermodynamic modelling of sulphur emissions.* Waste management, 2012. **32**(4): p. 676-684.
15. Antunes, E., et al., *Biochar produced from biosolids using a single-mode microwave: Characterisation and its potential for phosphorus removal.* Journal of Environmental Management, 2017. **196**: p. 119-126.
16. Di Blasi, C., et al., *Pyrolytic behavior and products of some wood varieties.* Combustion and Flame, 2001. **124**(1): p. 165-177.
17. Mythili, R., et al., *Characterization of bioresidues for biooil production through pyrolysis.* Bioresource Technology, 2013. **138**: p. 71-78.
18. Laird, D.A., et al., *Review of the pyrolysis platform for coproducing bio-oil and biochar.* Biofuels, bioproducts and biorefining, 2009. **3**(5): p. 547-562.

19. Yang, H., et al., *Characteristics of hemicellulose, cellulose and lignin pyrolysis.* Fuel, 2007. **86**(12): p. 1781-1788.

20. Alvarez, J., et al., *Bio-oil production from rice husk fast pyrolysis in a conical spouted bed reactor.* Fuel, 2014. **128**: p. 162-169.

21. Iliopoulou, E.F., K.S. Triantafyllidis, and A.A. Lappas, *Overview of catalytic upgrading of biomass pyrolysis vapors toward the production of fuels and high-value chemicals.* Wiley Interdisciplinary Reviews: Energy and Environment, 2019. **8**(1): p. e322.

22. Wang, K., P.A. Johnston, and R.C. Brown, *Comparison of in-situ and ex-situ catalytic pyrolysis in a micro-reactor system.* Bioresource Technology, 2014. **173**: p. 124-131.

23. Stephanidis, S., et al., *Catalytic upgrading of lignocellulosic biomass pyrolysis vapours: Effect of hydrothermal pre-treatment of biomass.* Catalysis Today, 2011. **167**(1): p. 37-45.

24. Stefanidis, S., et al., *In-situ upgrading of biomass pyrolysis vapors: catalyst screening on a fixed bed reactor.* Bioresource technology, 2011. **102**(17): p. 8261-8267.

25. van Donk, S., et al., *Generation, Characterization, and Impact of Mesopores in Zeolite Catalysts.* Catalysis Reviews, 2003. **45**(2): p. 297-319.

26. Deng, Y., et al., *Large-pore ordered mesoporous materials templated from non-Pluronic amphiphilic block copolymers.* Chemical Society Reviews, 2013. **42**(9): p. 4054-4070.

27. Li, W., et al., *Ordered mesoporous materials based on interfacial assembly and engineering.* Advanced Materials, 2013. **25**(37): p. 5129-5152.

28. Guo, X., et al., *Analysis of coke precursor on catalyst and study on regeneration of catalyst in upgrading of bio-oil.* Biomass and Bioenergy, 2009. **33**(10): p. 1469-1473.

29. Zarnegar, S., *A review on catalytic-pyrolysis of coal and biomass for value-added fuel and chemicals.* Energy Sources, Part A: Recovery, Utilization, and Environmental Effects, 2018. **40**(12): p. 1427-1433.

30. Yang, Y., et al., *Ce-promoted Ni/SBA-15 catalysts for anisole hydrotreating under mild conditions.* Applied Catalysis B: Environmental, 2016. **197**: p. 206-213.

31. Linares, N., et al., *Incorporation of chemical functionalities in the framework of mesoporous silica.* Chemical Communications, 2011. **47**(32): p. 9024-9035.

32. Nava, R., et al., *Upgrading of bio-liquids on different mesoporous silica-supported CoMo catalysts.* Applied Catalysis B: Environmental, 2009. **92**(1): p. 154-167.

33. Han, T., et al., *Catalytic pyrolysis of lignin using low-cost materials with different acidities and textural properties as catalysts.* Chemical Engineering Journal, 2019. **373**: p. 846-856.

34. Balat, M., *Production of bioethanol from lignocellulosic materials via the biochemical pathway: a review.* Energy conversion and management, 2011. **52**(2): p. 858-875.

35. Tsai, W., M. Lee, and Y. Chang, *Fast pyrolysis of rice straw, sugarcane bagasse and coconut shell in an induction-heating reactor.* Journal of analytical and applied pyrolysis, 2006. **76**(1-2): p. 230-237.

36. Dhyani, V. and T. Bhaskar, *A comprehensive review on the pyrolysis of lignocellulosic biomass.* Renewable Energy, 2018. **129**: p. 695-716.

37. Mullen, C.A. and A.A. Boateng, *Chemical Composition of Bio-oils Produced by Fast Pyrolysis of Two Energy Crops.* Energy & Fuels, 2008. **22**(3): p. 2104-2109.

38. Prasad, S., A. Singh, and H. Joshi, *Ethanol as an alternative fuel from agricultural, industrial and urban residues.* Resources, Conservation and Recycling, 2007. **50**(1): p. 1-39.

39. Imam, T. and S. Capareda, *Characterization of bio-oil, syn-gas and bio-char from switchgrass pyrolysis at various temperatures.* Journal of Analytical and Applied Pyrolysis, 2012. **93**: p. 170-177.

40. Stefanidis, S.D., et al., *A study of lignocellulosic biomass pyrolysis via the pyrolysis of cellulose, hemicellulose and lignin.* Journal of Analytical and Applied Pyrolysis, 2014. **105**: p. 143-150.

41. Zhang, L., et al., *Catalytic Pyrolysis of Biomass and Polymer Wastes.* Catalysts, 2018. **8**(12): p. 659.

42. Chang, S., et al., *Effect of hydrothermal pretreatment on properties of bio-oil produced from fast pyrolysis of eucalyptus wood in a fluidized bed reactor.* Bioresource Technology, 2013. **138**: p. 321-328.

43. Abdullah, N. and H. Gerhauser, *Bio-oil derived from empty fruit bunches.* Fuel, 2008. **87**(12): p. 2606-2613.

44. Piskorz, J., et al., *Liquid products from the fast pyrolysis of wood and cellulose*, in *Research in thermochemical biomass conversion*. 1988, Springer. p. 557-571.

45. Isahak, W.N.R.W., et al., *A review on bio-oil production from biomass by using pyrolysis method.* Renewable and Sustainable Energy Reviews, 2012. **16**(8): p. 5910-5923.

46. Braga, R.M., et al., *Characterization and comparative study of pyrolysis kinetics of the rice husk and the elephant grass.* Journal of Thermal Analysis and Calorimetry, 2014. **115**(2): p. 1915-1920.

47. Shi, X. and J. Wang, *A comparative investigation into the formation behaviors of char, liquids and gases during pyrolysis of pinewood and lignocellulosic components.* Bioresource Technology, 2014. **170**: p. 262-269.

48. Alper, K., K. Tekin, and S. Karagöz, *Pyrolysis of agricultural residues for bio-oil production.* Clean Technologies and Environmental Policy, 2015. **17**(1): p. 211-223.

49. Hameed, Z., et al., *Gasification of municipal solid waste blends with biomass for energy production and resources recovery: Current status, hybrid technologies and innovative prospects.* Renewable and Sustainable Energy Reviews, 2021. **136**: p. 110375.

50. Lyu, G., S. Wu, and H. Zhang, *Estimation and comparison of bio-oil components from different pyrolysis conditions.* Frontiers in Energy Research, 2015. **3**: p. 28.

51. Setter, C., et al., *Energy quality of pellets produced from coffee residue: Characterization of the products obtained via slow pyrolysis.* Industrial Crops and Products, 2020. **154**: p. 112731.

52. Luo, Z., et al., *Research on biomass fast pyrolysis for liquid fuel.* Biomass and Bioenergy, 2004. **26**(5): p. 455-462.

53. Zhang, Q., Z. Yang, and W. Wu, *Role of crop residue management in sustainable agricultural development in the North China Plain.* Journal of Sustainable Agriculture, 2008. **32**(1): p. 137-148.

54. Tsai, W., M. Lee, and Y. Chang, *Fast pyrolysis of rice husk: Product yields and compositions.* Bioresource technology, 2007. **98**(1): p. 22-28.

55. Torri, C., et al., *Comparative analysis of pyrolysate from herbaceous and woody energy crops by Py-GC with atomic emission and mass spectrometric detection.* Journal of Analytical and Applied Pyrolysis, 2010. **88**(2): p. 175-180.

56. Zanzi, R., K. Sjöström, and E. Björnbom, *Rapid pyrolysis of agricultural residues at high temperature.* Biomass and Bioenergy, 2002. **23**(5): p. 357-366.

57. Theis, M., et al., *Fouling tendency of ash resulting from burning mixtures of biofuels. Part 1: Deposition rates.* Fuel, 2006. **85**(7-8): p. 1125-1130.

58. Elliott, D.C., et al., *Catalytic hydroprocessing of biomass fast pyrolysis bio-oil to produce hydrocarbon products.* Environmental Progress & Sustainable Energy, 2009. **28**(3): p. 441-449.

59. Şensöz, S. and M. Can, *Pyrolysis of pine (Pinus brutia Ten.) chips: 1. Effect of pyrolysis temperature and heating rate on the product yields.* Energy Sources, 2002. **24**(4): p. 347-355.

60. Boateng, A.A., et al., *Bench-Scale Fluidized-Bed Pyrolysis of Switchgrass for Bio-Oil Production.* Industrial & Engineering Chemistry Research, 2007. **46**(7): p. 1891-1897.

61. Bartoli, M., et al., *Production of bio-oils and bio-char from Arundo donax through microwave assisted pyrolysis in a multimode batch reactor.* Journal of Analytical and Applied Pyrolysis, 2016. **122**: p. 479-489.

62. Chen, D., J. Zhou, and Q. Zhang, *Effects of heating rate on slow pyrolysis behavior, kinetic parameters and products properties of moso bamboo.* Bioresource Technology, 2014. **169**: p. 313-319.

63. Li, L.I.N. and H. Zhang, *Production and Characterization of Pyrolysis Oil from Herbaceous Biomass (Achnatherum Splendens).* Energy Sources, 2005. **27**(4): p. 319-326.

64. Sahoo, D., et al., *Value-addition of water hyacinth and para grass through pyrolysis and hydrothermal liquefaction.* Carbon Resources Conversion, 2019. **2**(3): p. 233-241.

65. Kojima, Y., et al., *Pyrolysis characteristic of kenaf studied with separated tissues, alkali pulp, and alkali lignin.* Biofuel Res. J, 2015. **8**: p. 317-323.

66. Cao, J.-P., et al., *Preparation and characterization of bio-oils from internally circulating fluidized-bed pyrolyses of municipal, livestock, and wood waste.* Bioresource technology, 2011. **102**(2): p. 2009-2015.

67. Heo, H.S., et al., *Bio-oil production from fast pyrolysis of waste furniture sawdust in a fluidized bed.* Bioresource technology, 2010. **101**(1): p. S91-S96.

68. Weldekidan, H., et al., *Energy Conversion Efficiency of Pyrolysis of Chicken Litter and Rice Husk Biomass.* Energy & Fuels, 2019. **33**(7): p. 6509-6514.

69. Chaiwong, K., et al., *Study of bio-oil and bio-char production from algae by slow pyrolysis.* Biomass and Bioenergy, 2013. **56**: p. 600-606.

70. Adamczyk, M. and M. Sajdak, *Pyrolysis behaviours of microalgae Nannochloropsis gaditana.* Waste and biomass valorization, 2018. **9**(11): p. 2221-2235.

71. Yang, W., et al., *Direct hydrothermal liquefaction of undried macroalgae Enteromorpha prolifera using acid catalysts.* Energy Conversion and Management, 2014. **87**: p. 938-945.

72. Torres-Mayanga, P.C., et al., *Production of biofuel precursors and value-added chemicals from hydrolysates resulting from hydrothermal processing of biomass: A review.* Biomass and Bioenergy, 2019. **130**: p. 105397.

73. Zhang, L., C. Xu, and P. Champagne, *Overview of recent advances in thermo-chemical conversion of biomass.* Energy Conversion and Management, 2010. **51**(5): p. 969-982.

74. Bridgwater, A., *Thermal conversion of biomass and waste: the status.* Birmingham (UK): Bio-Energy Research Group, Aston University, 2001.

75. Effendi, A., H. Gerhauser, and A.V. Bridgwater, *Production of renewable phenolic resins by thermochemical conversion of biomass: A review.* Renewable and Sustainable Energy Reviews, 2008. **12**(8): p. 2092-2116.

76. Amen-Chen, C., H. Pakdel, and C. Roy, *Production of monomeric phenols by thermochemical conversion of biomass: a review.* Bioresource Technology, 2001. **79**(3): p. 277-299.

77. Jenkins, B., et al., *Combustion properties of biomass.* Fuel processing technology, 1998. **54**(1-3): p. 17-46.

78. Bok, J.P., et al., *Fast pyrolysis of coffee grounds: Characteristics of product yields and biocrude oil quality.* Energy, 2012. **47**(1): p. 17-24.

79. Soloiu, V., et al., *Combustion characteristics of a charcoal slurry in a direct injection diesel engine and the impact on the injection system performance.* Energy, 2011. **36**(7): p. 4353-4371.

80. Hoekman, S.K., *Biofuels in the US–challenges and opportunities.* Renewable energy, 2009. **34**(1): p. 14-22.

81. Gopirajan, P.V., et al., *Optimization of hydrothermal liquefaction process through machine learning approach: process conditions and oil yield.* Biomass Conversion and Biorefinery: p. 1-10.

82. Barreiro, D.L., et al., *Hydrothermal liquefaction (HTL) of microalgae for biofuel production: state of the art review and future prospects.* Biomass and Bioenergy, 2013. **53**: p. 113-127.

83. Ruiz, J.A., et al., *Biomass gasification for electricity generation: Review of current technology barriers.* Renewable and Sustainable Energy Reviews, 2013. **18**: p. 174-183.

84. Damartzis, T. and A. Zabaniotou, *Thermochemical conversion of biomass to second generation biofuels through integrated process design—A review.* Renewable and Sustainable Energy Reviews, 2011. **15**(1): p. 366-378.

85. Franco, C., et al., *The study of reactions influencing the biomass steam gasification process☆.* Fuel, 2003. **82**(7): p. 835-842.

86. Chan, Y.H., et al., *An overview of biomass thermochemical conversion technologies in Malaysia.* Science of The Total Environment, 2019. **680**: p. 105-123.

87. Jiang, X., et al., *Investigation into advantage of pyrolysis over combustion of sewage sludge in PCDD/Fs control.* Fresenius Environmental Bulletin, 2014. **23**(2a): p. 550-557.

88. Collard, F.-X. and J. Blin, *A review on pyrolysis of biomass constituents: Mechanisms and composition of the products obtained from the conversion of cellulose, hemicelluloses and lignin.* Renewable and Sustainable Energy Reviews, 2014. **38**: p. 594-608.

89. McGrath, T.E., W.G. Chan, and M.R. Hajaligol, *Low temperature mechanism for the formation of polycyclic aromatic hydrocarbons from the pyrolysis of cellulose.* Journal of Analytical and Applied Pyrolysis, 2003. **66**(1-2): p. 51-70.

90. Van de Velden, M., et al., *Fundamentals, kinetics and endothermicity of the biomass pyrolysis reaction.* Renewable energy, 2010. **35**(1): p. 232-242.

91. Collard, F.-X., et al., *Influence of impregnated metal on the pyrolysis conversion of biomass constituents.* Journal of Analytical and Applied Pyrolysis, 2012. **95**: p. 213-226.

92. Garcia-Perez, M., et al., *Characterization of bio-oils in chemical families.* Biomass and Bioenergy, 2007. **31**(4): p. 222-242.

93. López, M.B., et al., *Composition of gases released during olive stones pyrolysis.* Journal of analytical and applied pyrolysis, 2002. **65**(2): p. 313-322.

94. Yanik, J., et al., *Fast pyrolysis of agricultural wastes: Characterization of pyrolysis products.* Fuel Processing Technology, 2007. **88**(10): p. 942-947.

95. Antal, M.J. and M. Grønli, *The Art, Science, and Technology of Charcoal Production.* Industrial & Engineering Chemistry Research, 2003. **42**(8): p. 1619-1640.

96. Eke, J., J.A. Onwudili, and A.V. Bridgwater, *Influence of Moisture Contents on the Fast Pyrolysis of Trommel Fines in a Bubbling Fluidized Bed Reactor.* Waste and Biomass Valorization, 2019: p. 1-12.

97. Balat, M., et al., *Main routes for the thermo-conversion of biomass into fuels and chemicals. Part 1: Pyrolysis systems.* Energy Conversion and Management, 2009. **50**(12): p. 3147-3157.

98. Bridgwater, A.V. and G.V.C. Peacocke, *Fast pyrolysis processes for biomass.* Renewable and Sustainable Energy Reviews, 2000. **4**(1): p. 1-73.

99. Heo, H.S., et al., *Fast pyrolysis of rice husk under different reaction conditions.* Journal of Industrial and Engineering Chemistry, 2010. **16**(1): p. 27-31.

100. Wei, L., et al., *Characteristics of fast pyrolysis of biomass in a free fall reactor.* Fuel Processing Technology, 2006. **87**(10): p. 863-871.

101. Czernik, S. and A. Bridgwater, *Overview of applications of biomass fast pyrolysis oil.* Energy & fuels, 2004. **18**(2): p. 590-598.

102. Venderbosch, R. and W. Prins, *Fast pyrolysis technology development.* Biofuels, Bioproducts and Biorefining, 2010. **4**(2): p. 178-208.

103. Li, Y. and S.K. Khanal, *Bioenergy: principles and applications*. 2016: John Wiley & Sons.

104. Garcìa-Pérez, M., et al., *Vacuum pyrolysis of softwood and hardwood biomass: Comparison between product yields and bio-oil properties.* Journal of Analytical and Applied Pyrolysis, 2007. **78**(1): p. 104-116.

105. Singh, N.R., et al., *Estimation of liquid fuel yields from biomass.* Environmental science & technology, 2010. **44**(13): p. 5298-5305.

106. Galiasso, R., Y. González, and M. Lucena, *New inverted cyclone reactor for flash hydropyrolysis.* Catalysis Today, 2014. **220**: p. 186-197.

107. Resende, F.L.P., *Recent advances on fast hydropyrolysis of biomass.* Catalysis Today, 2016. **269**: p. 148-155.

108. Basu, P., *Biomass gasification and pyrolysis: practical design and theory*. 2010: Academic press.

109. Guedes, R.E., A.S. Luna, and A.R. Torres, *Operating parameters for bio-oil production in biomass pyrolysis: A review.* Journal of analytical and applied pyrolysis, 2018. **129**: p. 134-149.

110. Goyal, H., D. Seal, and R. Saxena, *Bio-fuels from thermochemical conversion of renewable resources: a review.* Renewable and sustainable energy reviews, 2008. **12**(2): p. 504-517.

111. Zhang, Q., et al., *Fractioned preparation of bio-oil by biomass vacuum pyrolysis.* International journal of green energy, 2010. **7**(3): p. 263-272.

112. Akhtar, J. and N. Saidina Amin, *A review on operating parameters for optimum liquid oil yield in biomass pyrolysis.* Renewable and Sustainable Energy Reviews, 2012. **16**(7): p. 5101-5109.

113. Beis, S., Ö. Onay, and Ö. Koçkar, *Fixed-bed pyrolysis of safflower seed: influence of pyrolysis parameters on product yields and compositions.* Renewable energy, 2002. **26**(1): p. 21-32.

114. Angın, D., *Effect of pyrolysis temperature and heating rate on biochar obtained from pyrolysis of safflower seed press cake.* Bioresource Technology, 2013. **128**: p. 593-597.

115. Fu, P., et al., *Effect of temperature on gas composition and char structural features of pyrolyzed agricultural residues.* Bioresource Technology, 2011. **102**(17): p. 8211-8219.

116. Açıkalın, K., F. Karaca, and E. Bolat, *Pyrolysis of pistachio shell: Effects of pyrolysis conditions and analysis of products.* Fuel, 2012. **95**: p. 169-177.

117. Sricharoenchaikul, V. and D. Atong, *Thermal decomposition study on Jatropha curcas L. waste using TGA and fixed bed reactor.* Journal of Analytical and Applied Pyrolysis, 2009. **85**(1): p. 155-162.

118. Lam, S.S., et al., *Microwave-heated pyrolysis of waste automotive engine oil: Influence of operation parameters on the yield, composition, and fuel properties of pyrolysis oil.* Fuel, 2012. **92**(1): p. 327-339.

119. Pütün, A.E., E. Apaydın, and E. Pütün, *Rice straw as a bio-oil source via pyrolysis and steam pyrolysis.* Energy, 2004. **29**(12-15): p. 2171-2180.

120. Paenpong, C. and A. Pattiya, *Effect of pyrolysis and moving-bed granular filter temperatures on the yield and properties of bio-oil from fast pyrolysis of biomass.* Journal of Analytical and Applied Pyrolysis, 2016. **119**: p. 40-51.

121. Ji-lu, Z., *Bio-oil from fast pyrolysis of rice husk: Yields and related properties and improvement of the pyrolysis system.* Journal of Analytical and Applied Pyrolysis, 2007. **80**(1): p. 30-35.

122. Bridgewater, A.V., *Biomass fast pyrolysis.* Thermal science, 2004. **8**(2): p. 21-50.

123. Ateş, F., E. Pütün, and A. Pütün, *Fast pyrolysis of sesame stalk: yields and structural analysis of bio-oil.* Journal of Analytical and Applied Pyrolysis, 2004. **71**(2): p. 779-790.

124. Tripathi, M., J.N. Sahu, and P. Ganesan, *Effect of process parameters on production of biochar from biomass waste through pyrolysis: A review.* Renewable and Sustainable Energy Reviews, 2016. **55**: p. 467-481.

125. Varma, A.K. and P. Mondal, *Pyrolysis of sugarcane bagasse in semi batch reactor: Effects of process parameters on product yields and characterization of products.* Industrial Crops and Products, 2017. **95**: p. 704-717.

126. Bhoi, P.R., et al., *Recent advances on catalysts for improving hydrocarbon compounds in bio-oil of biomass catalytic pyrolysis.* Renewable and Sustainable Energy Reviews, 2020. **121**: p. 109676.

127. Jahirul, M.I., et al., *Biofuels production through biomass pyrolysis—a technological review.* Energies, 2012. **5**(12): p. 4952-5001.

128. Akhtar, J. and N.S. Amin, *A review on operating parameters for optimum liquid oil yield in biomass pyrolysis.* Renewable and Sustainable Energy Reviews, 2012. **16**(7): p. 5101-5109.

129. Choi, H.S., Y.S. Choi, and H.C. Park, *Fast pyrolysis characteristics of lignocellulosic biomass with varying reaction conditions.* Renewable Energy, 2012. **42**: p. 131-135.

130. Mohamed, A.R., et al., *The Effects of Holding Time and the Sweeping Nitrogen Gas Flowrates on the Pyrolysis of EFB using a Fixed–Bed Reactor.* Procedia Engineering, 2013. **53**: p. 185-191.

131. Strezov, V., B. Moghtaderi, and J. Lucas, *Thermal study of decomposition of selected biomass samples.* Journal of Thermal Analysis and Calorimetry, 2003. **72**(3): p. 1041-1048.

132. Debdoubi, A., et al., *The effect of heating rate on yields and compositions of oil products from esparto pyrolysis.* International Journal of Energy Research, 2006. **30**(15): p. 1243-1250.

133. Huber, G.W., S. Iborra, and A. Corma, *Synthesis of Transportation Fuels from Biomass: Chemistry, Catalysts, and Engineering.* Chemical Reviews, 2006. **106**(9): p. 4044-4098.

134. Vardon, D.R., et al., *Complete Utilization of Spent Coffee Grounds To Produce Biodiesel, Bio-Oil, and Biochar.* ACS Sustainable Chemistry & Engineering, 2013. **1**(10): p. 1286-1294.

135. Jacobson, K., K.C. Maheria, and A. Kumar Dalai, *Bio-oil valorization: A review.* Renewable and Sustainable Energy Reviews, 2013. **23**: p. 91-106.

136. Demirbas, A., *The influence of temperature on the yields of compounds existing in bio-oils obtained from biomass samples via pyrolysis.* Fuel Processing Technology, 2007. **88**(6): p. 591-597.

137. Debdoubi, A., et al., *The effect of heating rate on yields and compositions of oil products from esparto pyrolysis.* International Journal of Energy Research, 2006. **30**(15): p. 1243-1250.

138. Onay, O., *Influence of pyrolysis temperature and heating rate on the production of bio-oil and char from safflower seed by pyrolysis, using a well-swept fixed-bed reactor.* Fuel processing technology, 2007. **88**(5): p. 523-531.

139. Oasmaa, A. and S. Czernik, *Fuel oil quality of biomass pyrolysis oils state of the art for the end users.* Energy & Fuels, 1999. **13**(4): p. 914-921.

140. Dickerson, T. and J. Soria, *Catalytic fast pyrolysis: a review.* Energies, 2013. **6**(1): p. 514-538.

141. Kumar, R. and V. Strezov, *Thermochemical production of bio-oil: A review of downstream processing technologies for bio-oil upgrading, production of hydrogen and high value-added products.* Renewable and Sustainable Energy Reviews, 2021. **135**: p. 110152.

142. Clauser, N.M., et al., *Biomass Waste as Sustainable Raw Material for Energy and Fuels.* Sustainability, 2021. **13**(2): p. 794.

143. Boucher, M., A. Chaala, and C. Roy, *Bio-oils obtained by vacuum pyrolysis of softwood bark as a liquid fuel for gas turbines. Part I: Properties of bio-oil and its blends with methanol and a pyrolytic aqueous phase.* Biomass and Bioenergy, 2000. **19**(5): p. 337-350.

144. Diebold, J.P., *A review of the chemical and physical mechanisms of the storage stability of fast pyrolysis bio-oils*. 1999, National Renewable Energy Lab., Golden, CO (US).

145. Cai, J., et al., *Viscosity of aged bio-oils from fast pyrolysis of beech wood and Miscanthus: shear rate and temperature dependence.* Energy & Fuels, 2016. **30**(6): p. 4999-5004.

146. Meng, J., et al., *Thermal and storage stability of bio-oil from pyrolysis of torrefied wood.* Energy & Fuels, 2015. **29**(8): p. 5117-5126.

147. Zhang, Q., et al., *Review of biomass pyrolysis oil properties and upgrading research.* Energy Conversion and Management, 2007. **48**(1): p. 87-92.

148. Thangalazhy-Gopakumar, S., et al., *Physiochemical properties of bio-oil produced at various temperatures from pine wood using an auger reactor.* Bioresource technology, 2010. **101**(21): p. 8389-8395.

149. Park, Y.-K., et al., *Wild reed of Suncheon Bay: Potential bio-energy source.* Renewable Energy, 2012. **42**: p. 168-172.

150. Kim, J.-S., *Production, separation and applications of phenolic-rich bio-oil–a review.* Bioresource technology, 2015. **178**: p. 90-98.

151. Wei, Y., et al., *Liquid–liquid extraction of biomass pyrolysis bio-oil.* Energy & Fuels, 2014. **28**(2): p. 1207-1212.

152. Fini, E.H., et al., *Chemical characterization of biobinder from swine manure: Sustainable modifier for asphalt binder.* Journal of Materials in Civil Engineering, 2011. **23**(11): p. 1506-1513.

153. Zhang, S., et al., *Liquefaction of biomass and upgrading of bio-oil: a review.* Molecules, 2019. **24**(12): p. 2250.

154. Mathimani, T., et al., *Review on cultivation and thermochemical conversion of microalgae to fuels and chemicals: Process evaluation and knowledge gaps.* Journal of Cleaner Production, 2019. **208**: p. 1053-1064.

155. Shan Ahamed, T., et al., *Upgrading of bio-oil from thermochemical conversion of various biomass – Mechanism, challenges and opportunities.* Fuel, 2021. **287**: p. 119329.

156. Gollakota, A.R.K., et al., *A review on the upgradation techniques of pyrolysis oil.* Renewable and Sustainable Energy Reviews, 2016. **58**: p. 1543-1568.

157. Wang, S., et al., *Lignocellulosic biomass pyrolysis mechanism: A state-of-the-art review.* Progress in Energy and Combustion Science, 2017. **62**: p. 33-86.

158. Aho, A., et al., *Catalytic upgrading of woody biomass derived pyrolysis vapours over iron modified zeolites in a dual-fluidized bed reactor.* Fuel, 2010. **89**(8): p. 1992-2000.

159. Foster, A.J., et al., *Optimizing the aromatic yield and distribution from catalytic fast pyrolysis of biomass over ZSM-5.* Applied Catalysis A: General, 2012. **423-424**: p. 154-161.

160. Ruddy, D.A., et al., *Recent advances in heterogeneous catalysts for bio-oil upgrading via "ex situ catalytic fast pyrolysis": catalyst development through the study of model compounds.* Green Chemistry, 2014. **16**(2): p. 454-490.

161. Luo, G. and F.L. Resende, *In-situ and ex-situ upgrading of pyrolysis vapors from beetle-killed trees.* Fuel, 2016. **166**: p. 367-375.

162. Wan, S. and Y. Wang, *A review on ex situ catalytic fast pyrolysis of biomass.* Frontiers of Chemical Science and Engineering, 2014. **8**(3): p. 280-294.

163. Gamliel, D.P., et al., *Investigation of in situ and ex situ catalytic pyrolysis of miscanthus × giganteus using a PyGC–MS microsystem and comparison with a bench-scale spouted-bed reactor.* Bioresource Technology, 2015. **191**: p. 187-196.

164. Stefanidis, S.D., et al., *Catalyst hydrothermal deactivation and metal contamination during the in situ catalytic pyrolysis of biomass.* Catalysis Science & Technology, 2016. **6**(8): p. 2807-2819.

165. Shirazi, Y., S. Viamajala, and S. Varanasi, *In situ and ex situ catalytic pyrolysis of microalgae and integration with pyrolytic fractionation.* Frontiers in chemistry, 2020. **8**: p. 786.

166. Hemberger, P., et al., *Understanding the mechanism of catalytic fast pyrolysis by unveiling reactive intermediates in heterogeneous catalysis.* Nature Communications, 2017. **8**: p. 15946.

167. Rahman, M.M., R. Liu, and J. Cai, *Catalytic fast pyrolysis of biomass over zeolites for high quality bio-oil – A review.* Fuel Processing Technology, 2018. **180**: p. 32-46.

168. Adjaye, J. and N. Bakhshi, *Production of hydrocarbons by catalytic upgrading of a fast pyrolysis bio-oil. Part II: Comparative catalyst performance and reaction pathways.* Fuel Processing Technology, 1995. **45**(3): p. 185-202.

169. Nie, L., et al., *Selective conversion of m-cresol to toluene over bimetallic Ni–Fe catalysts.* Journal of Molecular Catalysis A: Chemical, 2014. **388**: p. 47-55.

170. Shafaghat, H., P.S. Rezaei, and W.M.A.W. Daud, *Catalytic hydrodeoxygenation of simulated phenolic bio-oil to cycloalkanes and aromatic hydrocarbons over bifunctional metal/acid catalysts of Ni/HBeta, Fe/HBeta and NiFe/HBeta.* Journal of industrial and engineering chemistry, 2016. **35**: p. 268-276.

171. Yuan, G. and M.A. Keane, *Aqueous-Phase Hydrodechlorination of 2,4-Dichlorophenol over Pd/Al2O3: Reaction under Controlled pH.* Industrial & Engineering Chemistry Research, 2007. **46**(3): p. 705-715.

172. Mahata, N. and V. Vishwanathan, *Influence of Palladium Precursors on Structural Properties and Phenol Hydrogenation Characteristics of Supported Palladium Catalysts.* Journal of Catalysis, 2000. **196**(2): p. 262-270.

173. Zhao, C., et al., *Aqueous-phase hydrodeoxygenation of bio-derived phenols to cycloalkanes.* Journal of Catalysis, 2011. **280**(1): p. 8-16.

174. Echeandia, S., et al., *Synergy effect in the HDO of phenol over Ni–W catalysts supported on active carbon: Effect of tungsten precursors.* Applied Catalysis B: Environmental, 2010. **101**(1): p. 1-12.

175. Patel, M. and A. Kumar, *Production of renewable diesel through the hydroprocessing of lignocellulosic biomass-derived bio-oil: A review.* Renewable and Sustainable Energy Reviews, 2016. **58**: p. 1293-1307.

176. Nishu, et al., *A review on the catalytic pyrolysis of biomass for the bio-oil production with ZSM-5: Focus on structure.* Fuel Processing Technology, 2020. **199**: p. 106301.

177. Mihalcik, D.J., C.A. Mullen, and A.A. Boateng, *Screening acidic zeolites for catalytic fast pyrolysis of biomass and its components.* Journal of Analytical and Applied Pyrolysis, 2011. **92**(1): p. 224-232.

178. French, R. and S. Czernik, *Catalytic pyrolysis of biomass for biofuels production.* Fuel Processing Technology, 2010. **91**(1): p. 25-32.

179. Zhang, H., et al., *Comparison of non-catalytic and catalytic fast pyrolysis of corncob in a fluidized bed reactor.* Bioresource Technology, 2009. **100**(3): p. 1428-1434.

180. Valle, B., et al., *Selective Production of Aromatics by Crude Bio-oil Valorization with a Nickel-Modified HZSM-5 Zeolite Catalyst.* Energy & Fuels, 2010. **24**(3): p. 2060-2070.

181. Iliopoulou, E.F., et al., *Catalytic upgrading of biomass pyrolysis vapors using transition metal-modified ZSM-5 zeolite.* Applied Catalysis B: Environmental, 2012. **127**: p. 281-290.

182. Sun, L., et al., *Comparision of catalytic fast pyrolysis of biomass to aromatic hydrocarbons over ZSM-5 and Fe/ZSM-5 catalysts.* Journal of Analytical and Applied Pyrolysis, 2016. **121**: p. 342-346.

183. Zheng, Y., et al., *Study on aromatics production via the catalytic pyrolysis vapor upgrading of biomass using metal-loaded modified H-ZSM-5.* Journal of Analytical and Applied Pyrolysis, 2017. **126**: p. 169-179.

184. Iliopoulou, E.F., et al., *Catalytic upgrading of biomass pyrolysis vapors using transition metal-modified ZSM-5 zeolite.* Applied Catalysis B: Environmental, 2012. **127**: p. 281-290.

185. Razzaq, M., et al., *Investigating use of metal-modified HZSM-5 catalyst to upgrade liquid yield in co-pyrolysis of wheat straw and polystyrene.* Fuel, 2019. **257**: p. 116119.

186. Taylor, M.J., et al., *Highly selective hydrogenation of furfural over supported Pt nanoparticles under mild conditions.* Applied Catalysis B: Environmental, 2016. **180**: p. 580-585.

187. Li, X., et al., *Recent advances in aqueous-phase catalytic conversions of biomass platform chemicals over heterogeneous catalysts.* Frontiers in Chemistry, 2019. **7**.

188. Busetto, L., et al., *Application of the Shvo catalyst in homogeneous hydrogenation of bio-oil obtained from pyrolysis of white poplar: New mild upgrading conditions.* Fuel, 2011. **90**(3): p. 1197-1207.

189. Kaewpengkrow, P., D. Atong, and V. Sricharoenchaikul, *Selective catalytic fast pyrolysis of Jatropha curcas residue with metal oxide impregnated activated carbon for upgrading bio-oil.* International Journal of Hydrogen Energy, 2017. **42**(29): p. 18397-18409.

190. Yarulina, I., et al., *Recent trends and fundamental insights in the methanol-to-hydrocarbons process.* Nature Catalysis, 2018. **1**(6): p. 398-411.

191. Wang, Z., et al., *Direct, single-step synthesis of hierarchical zeolites without secondary templating.* Journal of Materials Chemistry A, 2015. **3**(3): p. 1298-1305.

192. Rahman, M.M., R. Liu, and J. Cai, *Catalytic fast pyrolysis of biomass over zeolites for high quality bio-oil–a review.* Fuel Processing Technology, 2018. **180**: p. 32-46.

193. Yue, Y., et al., *From natural aluminosilicate minerals to hierarchical ZSM-5 zeolites: A nanoscale depolymerization–reorganization approach.* Journal of catalysis, 2014. **319**: p. 200-210.

194. Cho, K., et al., *Zeolite Synthesis Using Hierarchical Structure-Directing Surfactants: Retaining Porous Structure of Initial Synthesis Gel and Precursors.* Chemistry of Materials, 2012. **24**(14): p. 2733-2738.

195. Kantarelis, E., et al., *Engineering the Catalytic Properties of HZSM5 by Cobalt Modification and Post-synthetic Hierarchical Porosity Development.* Topics in Catalysis, 2019. **62**(7): p. 773-785.

196. Hellinger, M., et al., *Catalytic hydrodeoxygenation of guaiacol over platinum supported on metal oxides and zeolites.* Applied Catalysis A: General, 2015. **490**: p. 181-192.

197. Hellinger, M., et al., *Catalytic hydrodeoxygenation of guaiacol over platinum supported on metal oxides and zeolites.* Applied Catalysis A: General, 2015. **490**: p. 181-192.

198. Jin, X., et al., *Lattice-matched bimetallic CuPd-graphene nanocatalysts for facile conversion of biomass-derived polyols to chemicals.* Acs Nano, 2013. **7**(2): p. 1309-1316.

199. Lup, A.N.K., et al., *A review on reactivity and stability of heterogeneous metal catalysts for deoxygenation of bio-oil model compounds.* Journal of industrial and engineering chemistry, 2017. **56**: p. 1-34.

200. Bulushev, D.A. and J.R. Ross, *Catalysis for conversion of biomass to fuels via pyrolysis and gasification: a review.* Catalysis today, 2011. **171**(1): p. 1-13.

201. Nilsen, M.H., et al., *Investigation of the effect of metal sites in Me–Al-MCM-41 (Me=Fe, Cu or Zn) on the catalytic behavior during the pyrolysis of wooden based biomass.* Microporous and Mesoporous Materials, 2007. **105**(1): p. 189-203.

202. Shen, Y., et al., *In-situ catalytic conversion of tar using rice husk char-supported nickel-iron catalysts for biomass pyrolysis/gasification.* Applied Catalysis B: Environmental, 2014. **152**: p. 140-151.

203. Guan, G., et al., *Catalytic steam reforming of biomass tar over iron- or nickel-based catalyst supported on calcined scallop shell.* Applied Catalysis B: Environmental, 2012. **115-116**: p. 159-168.

204. Hensley, A.J., et al., *Enhanced Fe2O3 reducibility via surface modification with Pd: characterizing the synergy within Pd/Fe catalysts for hydrodeoxygenation reactions.* Acs Catalysis, 2014. **4**(10): p. 3381-3392.

205. Li, J., et al., *Catalytic fast pyrolysis of biomass with mesoporous ZSM-5 zeolites prepared by desilication with NaOH solutions.* Applied Catalysis A: General, 2014. **470**: p. 115-122.

206. Ding, K., et al., *Effects of alkali-treated hierarchical HZSM-5 zeolites on the production of aromatic hydrocarbons from catalytic fast pyrolysis of waste cardboard.* Journal of Analytical and Applied Pyrolysis, 2017. **125**: p. 153-161.

207. Puértolas, B., et al., *Porosity–Acidity Interplay in Hierarchical ZSM-5 Zeolites for Pyrolysis Oil Valorization to Aromatics.* ChemSusChem, 2015. **8**(19): p. 3283-3293.

208. Asadieraghi, M. and W.M.A. Wan Daud, *In-situ catalytic upgrading of biomass pyrolysis vapor: Using a cascade system of various catalysts in a multi-zone fixed bed reactor.* Energy Conversion and Management, 2015. **101**: p. 151-163.

209. Antonakou, E., et al., *Evaluation of various types of Al-MCM-41 materials as catalysts in biomass pyrolysis for the production of bio-fuels and chemicals.* Fuel, 2006. **85**(14): p. 2202-2212.

210. Twaiq, F.A., A.R. Mohamed, and S. Bhatia, *Liquid hydrocarbon fuels from palm oil by catalytic cracking over aluminosilicate mesoporous catalysts with various Si/Al ratios.* Microporous and Mesoporous Materials, 2003. **64**(1): p. 95-107.

211. Liang, J., et al., *Heterogeneous catalysis in zeolites, mesoporous silica, and metal–organic frameworks.* Advanced Materials, 2017. **29**(30): p. 1701139.

212. Jeon, M.-J., et al., *Catalytic pyrolysis of biomass components over mesoporous catalysts using Py-GC/MS.* Catalysis Today, 2013. **204**: p. 170-178.

213. Lu, Q., et al., *Catalytic upgrading of biomass fast pyrolysis vapors with Pd/SBA-15 catalysts.* Industrial & Engineering Chemistry Research, 2010. **49**(6): p. 2573-2580.

214. Du, L., et al., *A comparison of monomeric phenols produced from lignin by fast pyrolysis and hydrothermal conversions.* International Journal of Chemical Reactor Engineering, 2013. **11**(1): p. 135-145.

215. Wang, C., et al., *Integrated harvest of phenolic monomers and hydrogen through catalytic pyrolysis of biomass over nanocellulose derived biochar catalyst.* Bioresource Technology, 2021. **320**: p. 124352.

216. Wang, D., et al., *Comparison of catalytic pyrolysis of biomass with MCM-41 and CaO catalysts by using TGA–FTIR analysis.* Journal of Analytical and Applied Pyrolysis, 2010. **89**(2): p. 171-177.

217. Brunelli, N.A., K. Venkatasubbaiah, and C.W. Jones, *Cooperative catalysis with acid–base bifunctional mesoporous silica: impact of grafting and co-condensation synthesis methods on material structure and catalytic properties.* Chemistry of Materials, 2012. **24**(13): p. 2433-2442.

218. Qiang, L., et al., *Analytical pyrolysis–gas chromatography/mass spectrometry (Py–GC/MS) of sawdust with Al/SBA-15 catalysts.* Journal of Analytical and Applied Pyrolysis, 2009. **84**(2): p. 131-138.

219. Tang, Y., et al., *Enhancement of Pt catalytic activity in the hydrogenation of aldehydes.* Applied Catalysis A: General, 2011. **406**(1): p. 81-88.

220. Yin, Y., et al., *Modification of as synthesized SBA-15 with Pt nanoparticles: Nanoconfinement effects give a boost for hydrogen storage at room temperature.* Scientific reports, 2017. **7**(1): p. 1-10.

221. Adam, J., et al., *Pyrolysis of biomass in the presence of Al-MCM-41 type catalysts.* Fuel, 2005. **84**(12-13): p. 1494-1502.

222. Kim, H., et al., *Catalytic copyrolysis of particle board and polypropylene over Al-MCM-48.* Materials Research Bulletin, 2016. **82**: p. 61-66.

223. Triantafyllidis, K.S., et al., *Hydrothermally stable mesoporous aluminosilicates (MSU-S) assembled from zeolite seeds as catalysts for biomass pyrolysis.* Microporous and Mesoporous Materials, 2007. **99**(1-2): p. 132-139.

224. Liu, W.-J., et al., *Facile synthesis of highly efficient and recyclable magnetic solid acid from biomass waste.* Scientific reports, 2013. **3**: p. 2419.

225. Tessarolo, N.S., et al., *Characterization of thermal and catalytic pyrolysis bio-oils by high-resolution techniques: 1H NMR, GC×GC-TOFMS and FT-ICR MS.* Journal of Analytical and Applied Pyrolysis, 2016. **117**: p. 257-267.

226. Staš, M., et al., *Overview of Analytical Methods Used for Chemical Characterization of Pyrolysis Bio-oil.* Energy & Fuels, 2014. **28**(1): p. 385-402.

227. Eschenbacher, A., et al., *Insights into the scalability of catalytic upgrading of biomass pyrolysis vapors using micro and bench-scale reactors.* Sustainable Energy & Fuels, 2020. **4**(7): p. 3780-3796.

228. Naik, S., et al., *Supercritical CO2 fractionation of bio-oil produced from wheat–hemlock biomass.* Bioresource technology, 2010. **101**(19): p. 7605-7613.

229. Ingram, L., et al., *Pyrolysis of wood and bark in an auger reactor: physical properties and chemical analysis of the produced bio-oils.* Energy & Fuels, 2008. **22**(1): p. 614-625.

230. Ren, S., et al., *Analysis of switchgrass-derived bio-oil and associated aqueous phase generated in a semi-pilot scale auger pyrolyzer.* Journal of Analytical and Applied Pyrolysis, 2016. **119**: p. 97-103.

231. Bertero, M., G. de la Puente, and U. Sedran, *Fuels from bio-oils: Bio-oil production from different residual sources, characterization and thermal conditioning.* Fuel, 2012. **95**: p. 263-271.

232. Barnés, M.C., et al., *A new approach for bio-oil characterization based on gel permeation chromatography preparative fractionation.* Journal of analytical and applied pyrolysis, 2015. **113**: p. 444-453.

233. Sfetsas, T., et al., *Qualitative and quantitative analysis of pyrolysis oil by gas chromatography with flame ionization detection and comprehensive two-dimensional gas chromatography with time-of-flight mass spectrometry.* Journal of chromatography A, 2011. **1218**(21): p. 3317-3325.

234. Auersvald, M., et al., *Quantitative Study of Straw Bio-oil Hydrodeoxygenation over a Sulfided NiMo Catalyst.* ACS Sustainable Chemistry & Engineering, 2019. **7**(7): p. 7080-7093.

235. Lewis, A.J., et al., *Hydrogen production from switchgrass via an integrated pyrolysis–microbial electrolysis process.* Bioresource technology, 2015. **195**: p. 231-241.

236. Hui-Peng, L., et al., *Effects of phenols on the stability of FCC diesel fuel.* Petroleum Science and Technology, 2009. **27**(5): p. 486-497.

237. Gellerstedt, G., et al., *Chemical structures present in biofuel obtained from lignin.* Energy & Fuels, 2008. **22**(6): p. 4240-4244.

238. Joseph, J., et al., *Compositional changes to low water content bio-oils during aging: an NMR, GC/MS, and LC/MS study.* Energy & Fuels, 2016. **30**(6): p. 4825-4840.

239. Moraes, M.S.A., et al., *Analysis of products from pyrolysis of Brazilian sugar cane straw.* Fuel processing technology, 2012. **101**: p. 35-43.

240. Venkatramani, C., J. Xu, and J.B. Phillips, *Separation orthogonality in temperature-programmed comprehensive two-dimensional gas chromatography.* Analytical chemistry, 1996. **68**(9): p. 1486-1492.

241. Murray, J.A., *Qualitative and quantitative approaches in comprehensive two-dimensional gas chromatography.* Journal of Chromatography A, 2012. **1261**: p. 58-68.

242. Negahdar, L., et al., *Characterization and comparison of fast pyrolysis bio-oils from pinewood, rapeseed cake, and wheat straw using 13C NMR and comprehensive GC× GC.* ACS sustainable chemistry & engineering, 2016. **4**(9): p. 4974-4985.

243. Mattsson, C., et al., *Using 2D NMR to characterize the structure of the low and high molecular weight fractions of bio-oil obtained from LignoBoost™ kraft lignin depolymerized in subcritical water.* Biomass and bioenergy, 2016. **95**: p. 364-377.

244. Mullen, C.A., G.D. Strahan, and A.A. Boateng, *Characterization of various fast-pyrolysis bio-oils by NMR spectroscopy.* Energy & Fuels, 2009. **23**(5): p. 2707-2718.

245. Hao, N., et al., *Review of NMR characterization of pyrolysis oils.* Energy & Fuels, 2016. **30**(9): p. 6863-6880.

246. Bharti, S.K. and R. Roy, *Quantitative 1H NMR spectroscopy.* TrAC Trends in Analytical Chemistry, 2012. **35**: p. 5-26.

247. Kanaujia, P.K., et al., *Review of analytical strategies in the production and upgrading of bio-oils derived from lignocellulosic biomass.* Journal of Analytical and Applied Pyrolysis, 2014. **105**: p. 55-74.

248. David, K., et al., *31P-NMR analysis of bio-oils obtained from the pyrolysis of biomass.* Biofuels, 2010. **1**(6): p. 839-845.

249. Tessarolo, N.S., et al., *Characterization of thermal and catalytic pyrolysis bio-oils by high-resolution techniques: 1H NMR, GC× GC-TOFMS and FT-ICR MS.* Journal of analytical and applied pyrolysis, 2016. **117**: p. 257-267.

250. Joseph, J., et al., *Chemical shifts and lifetimes for nuclear magnetic resonance (NMR) analysis of biofuels.* Energy & fuels, 2010. **24**(9): p. 5153-5162.

251. Christensen, E.D., et al., *Analysis of oxygenated compounds in hydrotreated biomass fast pyrolysis oil distillate fractions.* Energy & Fuels, 2011. **25**(11): p. 5462-5471.

252. Wang, Y., et al., *Analytical strategies for chemical characterization of bio-oil.* Journal of Separation Science, 2020. **43**(1): p. 360-371.

253. Schnitzer, M.I., et al., *The conversion of chicken manure to biooil by fast pyrolysis I. Analyses of chicken manure, biooils and char by 13C and 1H NMR and FTIR spectrophotometry.* Journal of Environmental Science and Health Part B, 2007. **42**(1): p. 71-77.

254. Jiang, X., N. Ellis, and Z. Zhong, *Fuel properties of bio-oil/bio-diesel mixture characterized by TG, FTIR and 1H NMR.* Korean Journal of Chemical Engineering, 2011. **28**(1): p. 133-137.

255. Kanaujia, P.K., et al., *Analytical approaches to characterizing pyrolysis oil from biomass.* TrAC Trends in Analytical Chemistry, 2013. **42**: p. 125-136.

256. Hu, X., et al., *Coke Formation during Thermal Treatment of Bio-oil.* Energy & Fuels, 2020. **34**(7): p. 7863-7914.

257. El-Sayed, S.A. and M.E. Mostafa, *Thermal pyrolysis and kinetic parameter determination of mango leaves using common and new proposed parallel kinetic models.* RSC Advances, 2020. **10**(31): p. 18160-18179.

258. Mureddu, M., et al., *Air-and oxygen-blown characterization of coal and biomass by thermogravimetric analysis.* Fuel, 2018. **212**: p. 626-637.

259. Hu, J., et al., *Combustion behaviors of three bamboo residues: Gas emission, kinetic, reaction mechanism and optimization patterns.* Journal of Cleaner Production, 2019. **235**: p. 549-561.

260. Müller-Hagedorn, M. and H. Bockhorn, *Pyrolytic behaviour of different biomasses (angiosperms)(maize plants, straws, and wood) in low temperature pyrolysis.* Journal of Analytical and Applied Pyrolysis, 2007. **79**(1-2): p. 136-146.

261. Branca, C., A. Albano, and C. Di Blasi, *Critical evaluation of global mechanisms of wood devolatilization.* Thermochimica Acta, 2005. **429**(2): p. 133-141.

262. Varsha, S., et al., *Methane production from anaerobic mono-and co-digestion of kitchen waste and sewage sludge: synergy study on cumulative methane production and biodegradability.* Biomass Conversion and Biorefinery, 2020: p. 1-9.

263. Vuppaladadiyam, A.K., et al., *Discernment of synergy during the co-pyrolysis of lipid-extracted microalgae and digested municipal solid waste: a thermogravimetric–mass spectrometric study.* Journal of Chemical Technology & Biotechnology, 2021.

264. Dada, T.K., et al., *A review on catalytic pyrolysis for high-quality bio-oil production from biomass.* Biomass Conversion and Biorefinery, 2021.

265. Vuppaladadiyam, A.K., et al., *Influence of microalgae on synergism during co-pyrolysis with organic waste biomass: A thermogravimetric and kinetic analysis.* Renewable energy, 2021. **167**: p. 42-55.

266. Lin, X., et al., *Catalytic co-pyrolysis of waste corn stover and high-density polyethylene for hydrocarbon production: The coupling effect of potassium and HZSM-5 zeolite.* Journal of Analytical and Applied Pyrolysis, 2020. **150**: p. 104895.

267. Ghorbannezhad, P., S. Park, and J.A. Onwudili, *Co-pyrolysis of biomass and plastic waste over zeolite- and sodium-based catalysts for enhanced yields of hydrocarbon products.* Waste Management, 2020. **102**: p. 909-918.

268. Zhang, H., et al., *Catalytic pyrolysis of black-liquor lignin by co-feeding with different plastics in a fluidized bed reactor.* Bioresource technology, 2015. **192**: p. 68-74.

269. Dorado, C., C.A. Mullen, and A.A. Boateng, *Origin of carbon in aromatic and olefin products derived from HZSM-5 catalyzed co-pyrolysis of cellulose and plastics via isotopic labeling.* Applied Catalysis B: Environmental, 2015. **162**: p. 338-345.

270. Rezaei, P.S., et al., *In-situ catalytic co-pyrolysis of yellow poplar and high-density polyethylene over mesoporous catalysts.* Energy Conversion and Management, 2017. **151**: p. 116-122.

271. Xue, X., et al., *Segmented catalytic co-pyrolysis of biomass and high-density polyethylene for aromatics production with MgCl2 and HZSM-5.* Journal of Analytical and Applied Pyrolysis, 2018. **134**: p. 209-217.

272. Uzoejinwa, B.B., et al., *Co-pyrolysis of biomass and waste plastics as a thermochemical conversion technology for high-grade biofuel production: Recent progress and future directions elsewhere worldwide.* Energy conversion and management, 2018. **163**: p. 468-492.

273. Gin, A.W., et al., *Recent progress on catalytic co-pyrolysis of plastic waste and lignocellulosic biomass to liquid fuel: The influence of technical and reaction kinetic parameters.* Arabian Journal of Chemistry, 2021. **14**(4): p. 103035.

274. Wang, Z., et al., *Co-pyrolysis of waste plastic and solid biomass for synergistic production of biofuels and chemicals-A review.* Progress in Energy and Combustion Science, 2021. **84**: p. 100899.

275. Zhou, L., et al., *Thermogravimetric characteristics and kinetic of plastic and biomass blends co-pyrolysis.* Fuel Processing Technology, 2006. **87**(11): p. 963-969.

276. Cheng, Y.-T. and G.W. Huber, *Production of targeted aromatics by using Diels–Alder classes of reactions with furans and olefins over ZSM-5.* Green Chemistry, 2012. **14**(11): p. 3114-3125.

277. Xue, Y., S. Zhou, and X. Bai, *Role of hydrogen transfer during catalytic copyrolysis of lignin and tetralin over HZSM-5 and HY zeolite catalysts.* ACS Sustainable Chemistry & Engineering, 2016. **4**(8): p. 4237-4250.

278. Li, H., P. Yu, and B. Shen, *Biofuel potential production from cottonseed oil: a comparison of non-catalytic and catalytic pyrolysis on fixed-fluidized bed reactor.* Fuel processing technology, 2009. **90**(9): p. 1087-1092.

279. Zhang, H., et al., *Catalytic fast pyrolysis of biomass in a fluidized bed with fresh and spent fluidized catalytic cracking (FCC) catalysts.* Energy & Fuels, 2009. **23**(12): p. 6199-6206.

280. Mihalcik, D.J., et al., *Packed-bed catalytic cracking of oak-derived pyrolytic vapors.* Industrial & Engineering Chemistry Research, 2011. **50**(23): p. 13304-13312.

281. Asadieraghi, M., W.M. Ashri Wan Daud, and H.F. Abbas, *Heterogeneous catalysts for advanced bio-fuel production through catalytic biomass pyrolysis vapor upgrading: a review.* RSC Advances, 2015. **5**(28): p. 22234-22255.

282. Zhang, X., et al., *Catalytic co-pyrolysis of lignocellulosic biomass with polymers: a critical review.* Green Chemistry, 2016. **18**(15): p. 4145-4169.

283. Li, X., et al., *Improving the aromatic production in catalytic fast pyrolysis of cellulose by co-feeding low-density polyethylene.* Applied Catalysis A: General, 2013. **455**: p. 114-121.

284. Serrano-Ruiz, J.C. and J.A. Dumesic, *Catalytic routes for the conversion of biomass into liquid hydrocarbon transportation fuels.* Energy & Environmental Science, 2011. **4**(1): p. 83-99.

285. Taufiqurrahmi, N., A.R. Mohamed, and S. Bhatia, *Nanocrystalline zeolite Y: synthesis and characterization.* IOP Conference Series: Materials Science and Engineering, 2011. **17**(1): p. 012030.

286. In, S., et al., *Performance test of residential heat pump after partial optimization using low GWP refrigerants.* Applied Thermal Engineering, 2014. **72**(2): p. 315-322.

287. Carlson, T.R., et al., *Production of green aromatics and olefins by catalytic fast pyrolysis of wood sawdust.* Energy & Environmental Science, 2011. **4**(1): p. 145-161.

288. Wei, Y., et al., *Tailoring and visualizing the pore architecture of hierarchical zeolites.* Chemical Society Reviews, 2015. **44**(20): p. 7234-7261.

289. Holm, M.S., et al., *Assessing the acid properties of desilicated ZSM-5 by FTIR using CO and 2, 4, 6-trimethylpyridine (collidine) as molecular probes.* Applied Catalysis A: General, 2009. **356**(1): p. 23-30.

290. Kosinov, N., et al., *Engineering of transition metal catalysts confined in zeolites.* Chemistry of Materials, 2018. **30**(10): p. 3177-3198.

291. Zheng, J., et al., *The hierarchical effects of zeolite composites in catalysis.* Catalysis Today, 2011. **168**(1): p. 124-132.

292. Khan, W., et al., *Incorporating Hierarchy into Conventional Zeolites for Catalytic Biomass Conversions: A Review.* Catalysts, 2019. **9**(2): p. 127.

293. Yan, Y., et al., *Future of nano-/hierarchical zeolites in catalysis: gaseous phase or liquid phase system.* Catalysis Science & Technology, 2015. **5**(2): p. 772-785.

294. García-Martínez, J., et al., *Mesostructured zeolite Y—high hydrothermal stability and superior FCC catalytic performance.* Catalysis Science & Technology, 2012. **2**(5): p. 987-994.

295. Verboekend, D., G. Vilé, and J. Pérez-Ramírez, *Hierarchical Y and USY zeolites designed by post-synthetic strategies.* Advanced functional materials, 2012. **22**(5): p. 916-928.

296. Wang, Y., et al., *Effect of post treatment on the local structure of hierarchical Beta prepared by desilication and the catalytic performance in Friedel–Crafts alkylation.* Microporous and Mesoporous Materials, 2015. **206**: p. 42-51.

297. Santos, V., et al., *Evidence of surface active sites on NaY zeolite by a model reaction.* Applied surface science, 2007. **253**(13): p. 5688-5691.

298. Pérez-Ramírez, J., et al., *Hierarchical zeolites: enhanced utilisation of microporous crystals in catalysis by advances in materials design.* Chemical Society Reviews, 2008. **37**(11): p. 2530-2542.

299. Li, H., et al., *Catalytic performance of strontium oxide supported by MIL–100(Fe) derivate as transesterification catalyst for biodiesel production.* Energy Conversion and Management, 2019. **180**: p. 401-410.

300. Ono, Y., *Solid base catalysts for the synthesis of fine chemicals.* Journal of Catalysis, 2003. **216**(1): p. 406-415.

301. Naor, E.O., M. Koberg, and A. Gedanken, *Nonaqueous synthesis of SrO nanopowder and SrO/SiO2 composite and their application for biodiesel production via microwave irradiation.* Renewable Energy, 2017. **101**: p. 493-499.

302. Calatayud, M., A.M. Ruppert, and B.M. Weckhuysen, *Theoretical study on the role of surface basicity and Lewis acidity on the etherification of glycerol over alkaline earth metal oxides.* Chemistry–A European Journal, 2009. **15**(41): p. 10864-10870.

303. Zhang, R., et al., *Using ultrasound to improve the sequential post-synthesis modification method for making mesoporous Y zeolites.* Frontiers of Chemical Science and Engineering, 2020: p. 1-13.

304. Pérez-Ramírez, J., et al., *Zeolite catalysts with tunable hierarchy factor by pore-growth moderators.* Advanced Functional Materials, 2009. **19**(24): p. 3972-3979.

305. Zhang, H., et al., *Catalytic Co-pyrolysis of Biomass and Different Plastics (Polyethylene, Polypropylene, and Polystyrene) To Improve Hydrocarbon Yield in a Fluidized-Bed Reactor.* Energy & Fuels, 2014. **28**(3): p. 1940-1947.

306. Yu, J., et al., *Isothermal differential characteristics of gas–solid reaction in micro-fluidized bed reactor.* Fuel, 2013. **103**: p. 29-36.

307. Aghaei, E., et al., *Improving the physicochemical properties of Y zeolite for catalytic cracking of heavy oil via sequential steam-alkali-acid treatments.* Microporous and Mesoporous Materials, 2020. **294**: p. 109854.

308. Fang, Y., et al., *Dealumination and desilication for Al-rich HZSM-5 zeolite via steam-alkaline treatment and its application in methanol aromatization.* Frontiers of Chemical Science and Engineering, 2019. **13**(3): p. 543-553.

309. Li, X., et al., *Combined modification of ultra-stable Y zeolites via citric acid and phosphoric acid.* Applied Petrochemical Research, 2014. **4**(4): p. 343-349.

310. Qiao, K., et al., *An efficient modification of ultra-stable Y zeolites using citric acid and ammonium fluosilicate.* Applied Petrochemical Research, 2014. **4**(4): p. 373-378.

311. Wei, Q., et al., *Citric Acid-Treated Zeolite Y (CY)/Zeolite Beta Composites as Supports for Vacuum Gas Oil Hydrocracking Catalysts: High Yield Production of Highly-Aromatic Heavy Naphtha and Low-BMCI Value Tail Oil.* Frontiers in chemistry, 2019. **7**: p. 705.

312. Xing, C., et al., *Hierarchical zeolite Y supported cobalt bifunctional catalyst for facilely tuning the product distribution of Fischer–Tropsch synthesis.* Fuel, 2015. **148**: p. 48-57.

313. Oruji, S., R. Khoshbin, and R. Karimzadeh, *Preparation of hierarchical structure of Y zeolite with ultrasonic-assisted alkaline treatment method used in catalytic cracking of middle distillate cut: The effect of irradiation time.* Fuel Processing Technology, 2018. **176**: p. 283-295.

314. Sulikowski, B., et al., *Acidity and Catalytic Properties of Realuminated Zeolite Y.* The Journal of Physical Chemistry B, 1997. **101**(35): p. 6929-6932.

315. Verboekend, D., et al., *Synthesis, characterisation, and catalytic evaluation of hierarchical faujasite zeolites: milestones, challenges, and future directions.* Chemical Society Reviews, 2016. **45**(12): p. 3331-3352.

316. Cha, J., et al., *Highly monodisperse sub-nanometer and nanometer Ru particles confined in alkali-exchanged zeolite Y for ammonia decomposition.* Applied Catalysis B: Environmental, 2021. **283**: p. 119627.

317. Veses, A., et al., *Catalytic upgrading of biomass derived pyrolysis vapors over metal-loaded ZSM-5 zeolites: Effect of different metal cations on the bio-oil final properties.* Microporous and Mesoporous Materials, 2015. **209**: p. 189-196.

318. Yaman, E., et al., *Catalytic upgrading of pyrolysis vapours: Effect of catalyst support and metal type on phenolic content of bio-oil.* Journal of Cleaner Production, 2018. **185**: p. 52-61.

319. Duan, T.-W. and B. Yan, *Photophysical Properties of Metal Ion Functionalized NaY Zeolite.* Photochemistry and Photobiology, 2014. **90**(3): p. 503-510.

320. Liu, M.-C., et al., *Impact of Pt and V2O5 on Ethanol Removal from Moist Air Using Pellet Silica-Bound NaY.* Industrial & Engineering Chemistry Research, 2015. **54**(35): p. 8678-8689.

321. Ding, Y.-L., et al., *The Effect of Ni-ZSM-5 Catalysts on Catalytic Pyrolysis and Hydro-Pyrolysis of Biomass.* Frontiers in Chemistry, 2020. **8**(790).

322. Hernando, H., et al., *Engineering the acidity and accessibility of the zeolite ZSM-5 for efficient bio-oil upgrading in catalytic pyrolysis of lignocellulose.* Green Chemistry, 2018. **20**(15): p. 3499-3511.

323. Hasan, F., et al., *Direct synthesis of hierarchical LTA zeolite via a low crystallization and growth rate technique in presence of cetyltrimethylammonium bromide.* Journal of Colloid and Interface Science, 2012. **382**(1): p. 1-12.

324. Trigueiro, F.E., et al., *Thermal stability of Y zeolites containing different rare earth cations.* Journal of Alloys and Compounds, 2002. **344**(1): p. 337-341.

325. Ramli, N.A.S. and N.A.S. Amin, *Fe/HY zeolite as an effective catalyst for levulinic acid production from glucose: Characterization and catalytic performance.* Applied Catalysis B: Environmental, 2015. **163**: p. 487-498.

326. Li, H., et al., *Calcium oxide functionalized with strontium as heterogeneous transesterification catalyst for biodiesel production.* Fuel, 2016. **176**: p. 63-71.

327. Zhang, X., et al., *Thermal behavior and kinetic study for catalytic co-pyrolysis of biomass with plastics.* Bioresource Technology, 2016. **220**: p. 233-238.

328. Wu, F., et al., *Effects of Different Conditions on Co-Pyrolysis Behavior of Corn Stover and Polypropylene.* Polymers, 2020. **12**(4): p. 973.

329. Goenka, R., et al., *Kinetic analysis of biomass and comparison of its chemical compositions by thermogravimetry, wet and experimental furnace methods.* Waste and biomass valorization, 2015. **6**(6): p. 989-1002.

330. Liu, S.-N., et al., *Effect of zeolite structure on light aromatics formation during upgrading of cellulose fast pyrolysis vapor.* Journal of the Energy Institute, 2019. **92**(5): p. 1567-1576.

331. Cai, R., et al., *Biomass Catalytic Pyrolysis over Zeolite Catalysts with an Emphasis on Porosity and Acidity: A State-of-the-Art Review.* Energy & Fuels, 2020. **34**(10): p. 11771-11790.

332. Wang, Z., et al., *Co-pyrolysis of lignin and polyethylene with the addition of transition metals - Part I: Thermal behavior and kinetics analysis.* Journal of the Energy Institute, 2020. **93**(1): p. 281-291.

333. Zhong, S., et al., *Mechanism of synergistic effects and kinetics analysis in catalytic co-pyrolysis of water hyacinth and HDPE.* Energy Conversion and Management, 2021. **228**: p. 113717.

334. Ben, H. and A.J. Ragauskas, *Pyrolysis of kraft lignin with additives.* Energy & Fuels, 2011. **25**(10): p. 4662-4668.

335. Jin, Z., et al., *Co-pyrolysis characteristics of typical components of waste plastics in a falling film pyrolysis reactor.* Chinese Journal of Chemical Engineering, 2018. **26**(10): p. 2176-2184.

336. Ghorbannezhad, P., S. Park, and J.A. Onwudili, *Co-pyrolysis of biomass and plastic waste over zeolite-and sodium-based catalysts for enhanced yields of hydrocarbon products.* Waste Management, 2020. **102**: p. 909-918.

337. Cheng, Y.-T. and G.W. Huber, *Chemistry of furan conversion into aromatics and olefins over HZSM-5: a model biomass conversion reaction.* ACS catalysis, 2011. **1**(6): p. 611-628.

338. Ben, H., et al., *A comprehensive characterization of pyrolysis oil from softwood barks.* Polymers, 2019. **11**(9): p. 1387.

339. Gupta, J., et al., *CaO catalyst for multi-route conversion of oakwood biomass to value-added chemicals and fuel precursors in fast pyrolysis.* Applied Catalysis B: Environmental, 2021. **285**: p. 119858.

340. Miskolczi, N., T. Juzsakova, and J. Sója, *Preparation and application of metal loaded ZSM-5 and y-zeolite catalysts for thermo-catalytic pyrolysis of real end of life vehicle plastics waste.* Journal of the Energy Institute, 2019. **92**(1): p. 118-127.

341. Yuan, R. and Y. Shen, *Catalytic pyrolysis of biomass-plastic wastes in the presence of MgO and MgCO3 for hydrocarbon-rich oils production.* Bioresource Technology, 2019. **293**: p. 122076.

342. Garba, M.U., et al., *Thermogravimetric characteristic and kinetic of catalytic co-pyrolysis of biomass with low-and high-density polyethylenes.* Biomass Conversion and Biorefinery, 2018. **8**(1): p. 143-150.

343. Xiang, Z., et al., *Thermal behavior and kinetic study for co-pyrolysis of lignocellulosic biomass with polyethylene over Cobalt modified ZSM-5 catalyst by thermogravimetric analysis.* Bioresource technology, 2018. **247**: p. 804-811.

344. Kalogiannis, K.G., et al., *First pilot scale study of basic vs acidic catalysts in biomass pyrolysis: deoxygenation mechanisms and catalyst deactivation.* Applied Catalysis B: Environmental, 2018. **238**: p. 346-357.

345. Wang, K., K.H. Kim, and R.C. Brown, *Catalytic pyrolysis of individual components of lignocellulosic biomass.* Green Chemistry, 2014. **16**(2): p. 727-735.

346. Liu, W.-J., et al., *Facile synthesis of highly efficient and recyclable magnetic solid acid from biomass waste.* Scientific Reports, 2013. **3**(1): p. 2419.

347. Chen, X., et al., *Pyrolysis characteristics of lignocellulosic biomass components in the presence of CaO.* Bioresource technology, 2019. **287**: p. 121493.

348. Fan, L., et al., *Ex-situ catalytic upgrading of vapors from microwave-assisted pyrolysis of low-density polyethylene with MgO.* Energy Conversion and Management, 2017. **149**: p. 432-441.

349. Fan, L., et al., *Fast microwave-assisted catalytic co-pyrolysis of lignin and low-density polyethylene with HZSM-5 and MgO for improved bio-oil yield and quality.* Bioresource technology, 2017. **225**: p. 199-205.

350. Culas, S. and J. Samuel, *γ-Irradiation effects on the non-isothermal decomposition of strontium nitrate by model-free and model-fitting methods.* Radiation Physics and Chemistry, 2013. **86**: p. 90-95.

351. Gunasee, S.D., et al., *Co-pyrolysis of LDPE and cellulose: Synergies during devolatilization and condensation.* Journal of Analytical and Applied Pyrolysis, 2017. **126**: p. 307-314.

352. Barison, A., et al., *A simple methodology for the determination of fatty acid composition in edible oils through 1H NMR spectroscopy.* Magnetic resonance in chemistry, 2010. **48**(8): p. 642-650.

353. Di Pietro, M.E., A. Mannu, and A. Mele, *NMR Determination of Free Fatty Acids in Vegetable Oils.* Processes, 2020. **8**(4): p. 410.

354. Yang, H., et al., *Influence of the porosity and acidic properties of aluminosilicate catalysts on coke formation during the catalytic pyrolysis of lignin.* Journal of Analytical and Applied Pyrolysis, 2022. **165**: p. 105536.

355. Graça, I., et al., *Desilicated NaY zeolites impregnated with magnesium as catalysts for glucose isomerisation into fructose.* Applied Catalysis B: Environmental, 2018. **224**: p. 660-670.

356. Lee, H., et al., *Heterogeneous Catalysts Using Strontium Oxide Agglomerates Depositing upon Titanium Plate for Enhancing Biodiesel Production.* Catalysts, 2021. **11**(1): p. 30.

357. Ryu, H.W., et al., *Catalytic co-pyrolysis of cellulose and linear low-density polyethylene over MgO-impregnated catalysts with different acid-base properties.* Chemical Engineering Journal, 2019. **373**: p. 375-381.

358. Gupta, S. and P. Mondal, *Catalytic pyrolysis of pine needles with nickel doped gamma-alumina: Reaction kinetics, mechanism, thermodynamics and products analysis.* Journal of Cleaner Production, 2021. **286**: p. 124930.

359. Xue, X., et al., *Dual-catalyst catalytic pyrolysis of poplar sawdust: A systematic study on first-layered catalysts.* Chemical Engineering Journal, 2022. **431**: p. 134251.

360. Frusteri, F., et al., *Multifunctionality of Cu–ZnO–ZrO2/H-ZSM5 catalysts for the one-step CO2-to-DME hydrogenation reaction.* Applied Catalysis B: Environmental, 2015. **162**: p. 57-65.

361. Deka, R.C., R.K. Roy, and K. Hirao, *Basicity of the framework oxygen atom of alkali and alkaline earth-exchanged zeolites: a hard–soft acid–base approach.* Chemical Physics Letters, 2000. **332**(5-6): p. 576-582.

362. Ross, A., et al., *Classification of macroalgae as fuel and its thermochemical behaviour.* Bioresource technology, 2008. **99**(14): p. 6494-6504.

363. Norouzi, O., et al., *Promotion of hydrogen-rich gas and phenolic-rich bio-oil production from green macroalgae Cladophora glomerata via pyrolysis over its bio-char.* Bioresource technology, 2016. **219**: p. 643-651.

364. Hassen-Trabelsi, A.B., et al., *Pyrolysis of waste animal fats in a fixed-bed reactor: Production and characterization of bio-oil and bio-char.* Waste management, 2014. **34**(1): p. 210-218.

365. Wisniewski Jr, A., et al., *Biofuels from waste fish oil pyrolysis: Chemical composition.* Fuel, 2010. **89**(3): p. 563-568.

366. Zhang, B., et al., *Catalytic fast co-pyrolysis of biomass and food waste to produce aromatics: Analytical Py–GC/MS study.* Bioresource Technology, 2015. **189**: p. 30-35.

367. Wang, J., et al., *Catalytic fast co-pyrolysis of bamboo residual and waste lubricating oil over an ex-situ dual catalytic beds of MgO and HZSM-5: Analytical PY-GC/MS study.* Energy Conversion and Management, 2017. **139**: p. 222-231.

368. Xue, Y., A. Kelkar, and X. Bai, *Catalytic co-pyrolysis of biomass and polyethylene in a tandem micropyrolyzer.* Fuel, 2016. **166**: p. 227-236.

369. Lievens, C., et al., *An FT-IR spectroscopic study of carbonyl functionalities in bio-oils.* Fuel, 2011. **90**(11): p. 3417-3423.

370. Önal, E., B.B. Uzun, and A.E. Pütün, *Bio-oil production via co-pyrolysis of almond shell as biomass and high density polyethylene.* Energy conversion and management, 2014. **78**: p. 704-710.

371. Asadullah, M., et al., *Production of bio-oil from fixed bed pyrolysis of bagasse.* Fuel, 2007. **86**(16): p. 2514-2520.

372. Smith, G.V. and F. Notheisz, *Heterogeneous catalysis in organic chemistry*. 1999: Academic Press.

373. Gao, N., et al., *TG–FTIR and Py–GC/MS analysis on pyrolysis and combustion of pine sawdust.* Journal of Analytical and Applied Pyrolysis, 2013. **100**: p. 26-32.

374. Wang, J., et al., *Successive desilication and dealumination of HZSM-5 in catalytic conversion of waste cooking oil to produce aromatics.* Energy Conversion and Management, 2017. **147**: p. 100-107.

375. Ma, W., et al., *Co-upgrading of raw bio-oil with kitchen waste oil through fluid catalytic cracking (FCC).* Applied Energy, 2018. **217**: p. 233-240.

376. Liu, C., et al., *Effect of ZSM-5 on the aromatization performance in cracking catalyst.* Journal of molecular catalysis A: Chemical, 2004. **215**(1-2): p. 195-199.

377. Kelkar, S., et al., *A survey of catalysts for aromatics from fast pyrolysis of biomass.* Applied Catalysis B: Environmental, 2015. **174**: p. 85-95.

378. He, S., et al., *Catalytic conversion of free fatty acids to bio-based aromatics: a model investigation using oleic acid and an H-ZSM-5/Al2O3 catalyst.* ACS sustainable chemistry & engineering, 2021. **9**(3): p. 1128-1141.

379. Melero, J.A., et al., *Production of Biofuels via the Catalytic Cracking of Mixtures of Crude Vegetable Oils and Nonedible Animal Fats with Vacuum Gas Oil.* Energy & Fuels, 2010. **24**(1): p. 707-717.

380. Galadima, A. and O. Muraza, *In situ fast pyrolysis of biomass with zeolite catalysts for bioaromatics/gasoline production: a review.* Energy Conversion and Management, 2015. **105**: p. 338-354.

381. Aysu, T. and A. Sanna, *Nannochloropsis algae pyrolysis with ceria-based catalysts for production of high-quality bio-oils.* Bioresource technology, 2015. **194**: p. 108-116.

382. Dada, T.K., et al., *A review on catalytic pyrolysis for high-quality bio-oil production from biomass.* Biomass Conversion and Biorefinery, 2021: p. 1-20.

383. Wang, Y., et al., *Review on the catalytic pyrolysis of waste oil for the production of renewable hydrocarbon fuels.* Fuel, 2021. **283**: p. 119170.

384. Singh, S., et al., *Studies on individual pyrolysis and co-pyrolysis of corn cob and polyethylene: Thermal degradation behavior, possible synergism, kinetics, and thermodynamic analysis.* Science of The Total Environment, 2021. **783**: p. 147004.

385. Park, Y.-K., et al., *Co-feeding effect of waste plastic films on the catalytic pyrolysis of Quercus variabilis over microporous HZSM-5 and HY catalysts.* Chemical Engineering Journal, 2019. **378**: p. 122151.

386. Chen, J., et al., *A study on catalytic co-pyrolysis of kitchen waste with tire waste over ZSM-5 using TG-FTIR and Py-GC/MS.* Bioresource Technology, 2019. **289**: p. 121585.

387. Yu, Z., et al., *Microwave-assisted catalytic pyrolysis of Chinese tallow kernel oil for aromatic production in a downdraft reactor.* Journal of Analytical and Applied Pyrolysis, 2018. **133**: p. 16-21.

388. Atabani, A., et al., *Non-edible vegetable oils: a critical evaluation of oil extraction, fatty acid compositions, biodiesel production, characteristics, engine performance and emissions production.* Renewable and sustainable energy reviews, 2013. **18**: p. 211-245.

389. Mahari, W.A.W., et al., *Microwave co-pyrolysis of waste polyolefins and waste cooking oil: influence of N2 atmosphere versus vacuum environment.* Energy Conversion and Management, 2018. **171**: p. 1292-1301.

390. Kraiem, T., et al., *Production and characterization of bio-oil from the pyrolysis of waste frying oil.* Environmental Science and Pollution Research, 2017. **24**(11): p. 9951-9961.

391. Kraiem, T., et al., *Characterization of the liquid products obtained from Tunisian waste fish fats using the pyrolysis process.* Fuel Processing Technology, 2015. **138**: p. 404-412.

392. Gad, M.S., et al., *Effect of oil blends derived from catalytic pyrolysis of waste cooking oil on diesel engine performance, emissions and combustion characteristics.* Energy, 2021. **223**: p. 120019.

393. Shitao, Y., et al., *Effective pyrolysis of waste cooking oils into hydrocarbon rich biofuel on novel mesoporous catalyst with acid and alkali coexisting.* Industrial Crops and Products, 2020. **150**: p. 112362.

394. Chiaramonti, D., et al., *Bio-hydrocarbons through catalytic pyrolysis of used cooking oils and fatty acids for sustainable jet and road fuel production.* Biomass and Bioenergy, 2016. **95**: p. 424-435.

395. Wu, Q., et al., *Microwave-assisted pyrolysis of waste cooking oil for hydrocarbon bio-oil over metal oxides and HZSM-5 catalysts.* Energy Conversion and Management, 2020. **220**: p. 113124.

396. Al Alwan, B., S.O. Salley, and K.S. Ng, *Biofuels production from hydrothermal decarboxylation of oleic acid and soybean oil over Ni-based transition metal carbides supported on Al-SBA-15.* Applied Catalysis A: General, 2015. **498**: p. 32-40.

397. Dada, T.K., et al., *Catalytic Co-Pyrolysis of Ironbark and Waste Cooking Oil Using Strontium Oxide-Modified Y-Zeolite for High-Quality Bio-Oil Production.* Available at SSRN 4074333.

398. Yinhui, W., et al., *The impact of fuel compositions on the particulate emissions of direct injection gasoline engine.* Fuel, 2016. **166**: p. 543-552.

399. Li, X., et al., *Heterogeneous sulfur-free hydrodeoxygenation catalysts for selectively upgrading the renewable bio-oils to second generation biofuels.* Renewable and Sustainable Energy Reviews, 2018. **82**: p. 3762-3797.

400. Wang, J., et al., *Catalytic fast co-pyrolysis of mushroom waste and waste oil to promote the formation of aromatics.* Clean Technologies and Environmental Policy, 2016. **18**(8): p. 2701-2708.

401. Yuan, C., et al., *High-grade biofuel production from catalytic pyrolysis of waste clay oil using modified activated seaweed carbon-based catalyst.* Journal of Cleaner Production, 2021: p. 127928.

402. Kassa Dada, T., et al., *Probing the effect of Cu-SrO loading on catalyst supports (ZSM-5, Y-zeolite, activated carbon, Al2O3, and ZrO2) for aromatics production during catalytic co-pyrolysis of biomass and waste cooking oil.* Bioresource Technology, 2022. **360**: p. 127515.

403. Sun, B., et al., *Preparation and catalysis of carbon-supported iron catalysts for Fischer–Tropsch synthesis.* ChemCatChem, 2012. **4**(10): p. 1498-1511.

404. Duan, D., et al., *Renewable jet-fuel range hydrocarbons production from co-pyrolysis of lignin and soapstock with the activated carbon catalyst.* Waste Management, 2019. **88**: p. 1-9.

405. Zhang, Y., et al., *Jet fuel production from waste plastics via catalytic pyrolysis with activated carbons.* Applied Energy, 2019. **251**: p. 113337.

406. Duan, D., et al., *Renewable phenol production from lignin with acid pretreatment and ex-situ catalytic pyrolysis.* Journal of cleaner production, 2019. **231**: p. 331-340.

407. Ochoa, A., et al., *Deactivation dynamics of a Ni supported catalyst during the steam reforming of volatiles from waste polyethylene pyrolysis.* Applied Catalysis B: Environmental, 2017. **209**: p. 554-565.

408. Yang, H., et al., *Role of porous structure and active O-containing groups of activated biochar catalyst during biomass catalytic pyrolysis.* Energy, 2020. **210**: p. 118646.

409. Vichaphund, S., et al., *Production of aromatic compounds from catalytic fast pyrolysis of Jatropha residues using metal/HZSM-5 prepared by ion-exchange and impregnation methods.* Renewable Energy, 2015. **79**: p. 28-37.

410. Guo, X., et al., *Catalytic fast pyrolysis of Arundo donax in a two-stage fixed bed reactor over metal-modified HZSM-5 catalysts.* Biomass and Bioenergy, 2022. **156**: p. 106316.

411. Zheng, Y., et al., *Activity and selectivity of Ni–Cu bimetallic zeolites catalysts on biomass conversion for bio-aromatic and bio-phenols.* Journal of the Energy Institute, 2021. **97**: p. 58-72.

412. Clemente-Castro, S., et al., *Pyrolysis kinetic, thermodynamic and product analysis of different leguminous biomasses by Kissinger-Akahira-Sunose and pyrolysis-gas chromatography-mass spectrometry.* Journal of Analytical and Applied Pyrolysis, 2022. **162**: p. 105457.

413. Xing, S., et al., *Characterization of the decomposition behaviors of catalytic pyrolysis of wood using copper and potassium over thermogravimetric and Py-GC/MS analysis.* Energy, 2016. **114**: p. 634-646.

414. Rashidi, M., et al., *TiN-Cu Heterogeneous Nanocatalysts for Effective Depolymerisation of Oxidised Lignin.* ChemistrySelect, 2018. **3**(12): p. 3379-3385.

415. Kim, B.-S., et al., *Catalytic copyrolysis of cellulose and thermoplastics over HZSM-5 and HY.* ACS Sustainable Chemistry & Engineering, 2016. **4**(3): p. 1354-1363.

416. Li, M., et al., *A novel catalyst with variable active sites for the direct hydrogenation of waste oils into jet fuel.* Applied Catalysis B: Environmental, 2020. **260**: p. 118114.

417. Yang, H., et al., *Biomass-based pyrolytic polygeneration system for bamboo industry waste: evolution of the char structure and the pyrolysis mechanism.* Energy & Fuels, 2016. **30**(8): p. 6430-6439.

418. Liu, X., et al., *Selective hydrodeoxygenation of lignin-derived phenols to cyclohexanols over Co-based catalysts.* ACS Sustainable Chemistry & Engineering, 2017. **5**(10): p. 8594-8601.

419. Sitthisa, S., W. An, and D.E. Resasco, *Selective conversion of furfural to methylfuran over silica-supported NiFe bimetallic catalysts.* Journal of catalysis, 2011. **284**(1): p. 90-101.

420. Huang, X., et al., *Selective Production of Biobased Phenol from Lignocellulose-Derived Alkylmethoxyphenols.* ACS Catalysis, 2018. **8**(12): p. 11184-11190.

421. Pan, Y., et al., *BTEX recovery from waste rubbers by catalytic pyrolysis over Zn loaded tire derived char.* Waste Management, 2021. **131**: p. 214-225.

422. Xin, S., et al., *Assessment of pyrolysis polygeneration of biomass based on major components: Product characterization and elucidation of degradation pathways.* Fuel, 2013. **113**: p. 266-273.

423. Hongloi, N., P. Prapainainar, and C. Prapainainar, *Review of green diesel production from fatty acid deoxygenation over Ni-based catalysts.* Molecular Catalysis, 2021: p. 111696.

424. Fawzy, S., et al., *Strategies for mitigation of climate change: a review.* Environmental Chemistry Letters, 2020. **18**(6): p. 2069-2094.

425. Aysu, T. and H. Durak, *Thermochemical conversion of Datura stramonium L. by supercritical liquefaction and pyrolysis processes.* The Journal of Supercritical Fluids, 2015. **102**: p. 98-114.

426. Ahmed, M.H., et al., *A review on advanced catalytic co-pyrolysis of biomass and hydrogen-rich feedstock: Insights into synergistic effect, catalyst development and reaction mechanism.* Bioresource Technology, 2020. **310**: p. 123457.

427. Gouws, S.M., et al., *Co-pyrolysis of coal and raw/torrefied biomass: A review on chemistry, kinetics and implementation.* Renewable and Sustainable Energy Reviews, 2021. **135**: p. 110189.

428. Jin, X., J.H. Lee, and J.W. Choi, *Catalytic co-pyrolysis of woody biomass with waste plastics: Effects of HZSM-5 and pyrolysis temperature on producing high-value pyrolytic products and reducing wax formation.* Energy, 2022. **239**: p. 121739.

429. Aysu, T. and H. Durak, *Catalytic pyrolysis of liquorice (Glycyrrhiza glabra L.) in a fixed-bed reactor: Effects of pyrolysis parameters on product yields and character.* Journal of Analytical and Applied Pyrolysis, 2015. **111**: p. 156-172.

430. Alayont, Ş., et al., *The role of acidic, alkaline and hydrothermal pretreatment on pyrolysis of wild mustard (Sinapis arvensis) on the properties of bio-oil and bio-char.* Bioresource Technology Reports, 2022. **17**: p. 100980.

431. Zou, R., et al., *Biochar: From by-products of agro-industrial lignocellulosic waste to tailored carbon-based catalysts for biomass thermochemical conversions.* Chemical Engineering Journal, 2022. **441**: p. 135972.

432. Vuppaladadiyam, A.K., et al., *Pyrolysis of anaerobic digested residues in the presence of catalyst-sorbent bifunctional material: Pyrolysis characteristics, kinetics and evolved gas analysis.* Bioresource Technology, 2022: p. 127022.

433. Omar, R. and J.P. Robinson, *Conventional and microwave-assisted pyrolysis of rapeseed oil for bio-fuel production.* Journal of analytical and applied pyrolysis, 2014. **105**: p. 131-142.

434. Wang, J., et al., *Upgraded bio-oil production via catalytic fast co-pyrolysis of waste cooking oil and tea residual.* Waste Management, 2017. **60**: p. 357-362.

435. Hakimian, H., et al., *Increased aromatics production by co-feeding waste oil sludge to the catalytic pyrolysis of cellulose.* Energy, 2022. **239**: p. 122331.

436. Lam, S.S., et al., *Catalytic microwave pyrolysis of waste engine oil using metallic pyrolysis char.* Applied Catalysis B: Environmental, 2015. **176**: p. 601-617.

437. Jiang, J., et al., *Defect-rich ZrO2 anchored Pd nanoparticles for selective hydrodeoxygenation of bio-models at room temperature.* Fuel, 2022. **318**: p. 123529.

438. Xue, Z., et al., *Performance of Catalytic Fast Pyrolysis Using a γ-Al2O3 Catalyst with Compound Modification of ZrO2 and CeO2.* Catalysts, 2019. **9**(10): p. 849.

439. Chen, L., et al., *Co-pyrolysis of chlorella vulgaris and kitchen waste with different additives using TG-FTIR and Py-GC/MS.* Energy Conversion and Management, 2018. **177**: p. 582-591.

440. Zhou, G., et al., *Optimizing the distribution of aromatic products from catalytic fast pyrolysis of cellulose by ZSM-5 modification with boron and co-feeding of low-density polyethylene.* Applied Catalysis A: General, 2014. **487**: p. 45-53.

441. Yuan, C., et al., *High-grade biofuel production from catalytic pyrolysis of waste clay oil using modified activated seaweed carbon-based catalyst.* Journal of Cleaner Production, 2021. **313**: p. 127928.

442. Fan, Y., et al., *Olefin reduction of FCC gasoline via hydroisomerization aromatization over modified HMOR/HZSM-5/Hβ composite carriers.* Applied catalysis A: general, 2004. **275**(1-2): p. 61-71.

443. Naji, S.Z., C.T. Tye, and A.A. Abd, *State of the art of vegetable oil transformation into biofuels using catalytic cracking technology: Recent trends and future perspectives.* Process Biochemistry, 2021. **109**: p. 148-168.

444. Long, X., et al., *Magnesia modified H-ZSM-5 as an efficient acidic catalyst for steam reforming of dimethyl ether.* Applied Catalysis B: Environmental, 2013. **134**: p. 381-388.

445. Zhang, J., et al., *Enhancement of aromatics production via cellulose fast pyrolysis over Ru modified hierarchical zeolites.* Renewable Energy, 2022. **184**: p. 280-290.

446. Zhang, X., et al., *Catalytic co-pyrolysis of microwave pretreated chili straw and polypropylene to produce hydrocarbons-rich bio-oil.* Bioresource Technology, 2021. **319**: p. 124191.

447. Lee, H.W., et al., *Production of aromatic hydrocarbons via catalytic co-pyrolysis of torrefied cellulose and polypropylene.* Energy Conversion and Management, 2016. **129**: p. 81-88.

448. Seifi, H. and S.M. Sadrameli, *Bound cleavage at carboxyl group-glycerol backbone position in thermal cracking of the triglycerides in sunflower oil.* Journal of Analytical and Applied Pyrolysis, 2016. **121**: p. 1-10.

449. Wang, Y., et al., *Catalytic co-pyrolysis of waste vegetable oil and high density polyethylene for hydrocarbon fuel production.* Waste Management, 2017. **61**: p. 276-282.

450. Wu, J., et al., *Mechanism for the controllable production of heptadecane by hydrothermal in-situ hydrogenation and decarboxylation of oleic acid with methanol.* Energy and Environment Focus, 2016. **5**(3): p. 163-168.

451. Saheli, S., et al., *Design of mixed metal oxides with increased catalytic activity for Fischer–Tropsch synthesis.* Catalysis Letters, 2019. **149**(12): p. 3257-3267.

452. Luo, W., et al., *Catalytic co-pyrolysis of herb residue and polypropylene for pyrolysis products upgrading and diversification using nickel-X/biochar and ZSM-5 (X = iron, cobalt, copper).* Bioresource Technology, 2022. **349**: p. 126845.

453. Wang, Y., et al., *Characteristics of the catalytic fast pyrolysis of vegetable oil soapstock for hydrocarbon-rich fuel.* Energy Conversion and Management, 2020. **213**: p. 112860.

454. Zheng, Y., et al., *Insights into pyrolysis and catalytic co-pyrolysis upgrading of biomass and waste rubber seed oil to promote the formation of aromatics hydrocarbon.* International Journal of Hydrogen Energy, 2018. **43**(34): p. 16479-16496.

455. Ryu, H.W., et al., *Recent advances in catalytic co-pyrolysis of biomass and plastic waste for the production of petroleum-like hydrocarbons.* Bioresource Technology, 2020. **310**: p. 123473.

456. Kumar, R., et al., *Bio-oil upgrading with catalytic pyrolysis of biomass using Copper/zeolite-Nickel/zeolite and Copper-Nickel/zeolite catalysts.* Bioresour Technol, 2019. **279**: p. 404-409.

457. Kumar, R., et al., *Investigating the Effect of Mono- and Bimetallic/Zeolite Catalysts on Hydrocarbon Production during Bio-oil Upgrading from Ex Situ Pyrolysis of Biomass.* Energy & Fuels, 2019. **34**(1): p. 389-400.

APPENDIX

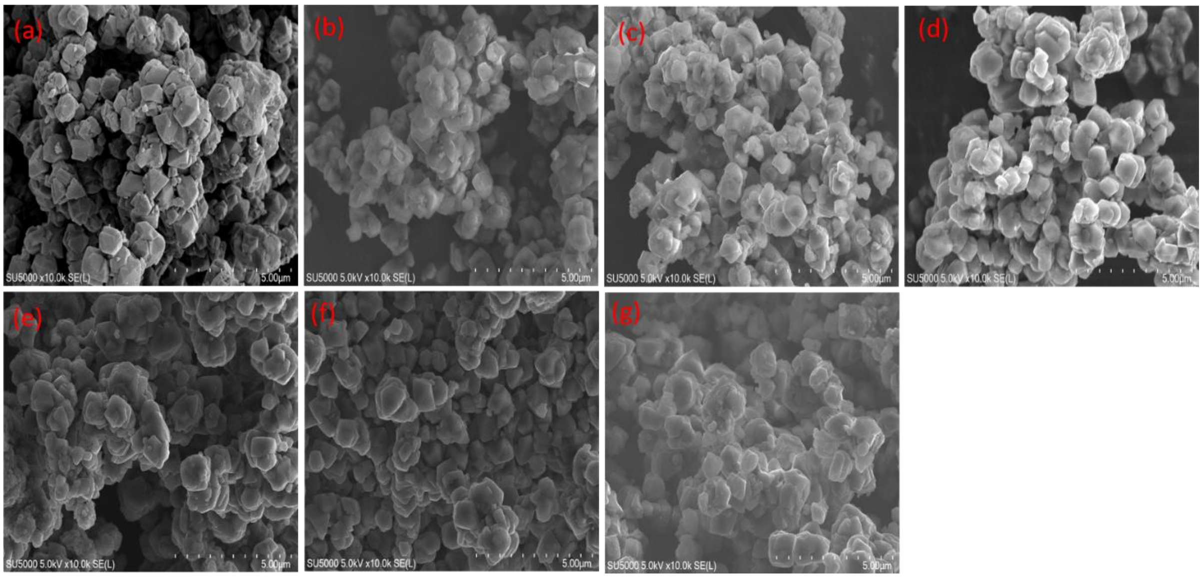

Figure A.1. SEM monograph of modified Y-zeolite after sequential acid and alkaline treatment; (a) Parent Y-zeolite; (b) 0.05M citric acid and 0.2M NaOH concentration (AT1-0.2M); (c) 0.05M citric acid and 0.4M NaOH concentration (AT1-0.4M) (c) 0.05M citric acid and 0.8M NaOH concentration (AT1-0.8M); (d) 0.1M citric acid with 0.2M NaOH concentration (AT2-0.2M);(e) 0.1M citric acid and 0.4M NaOH (AT2-0.4M) concentration; (f) 0.1M citric acid and 0.8M NaOH concentration (AT2-0.8M).

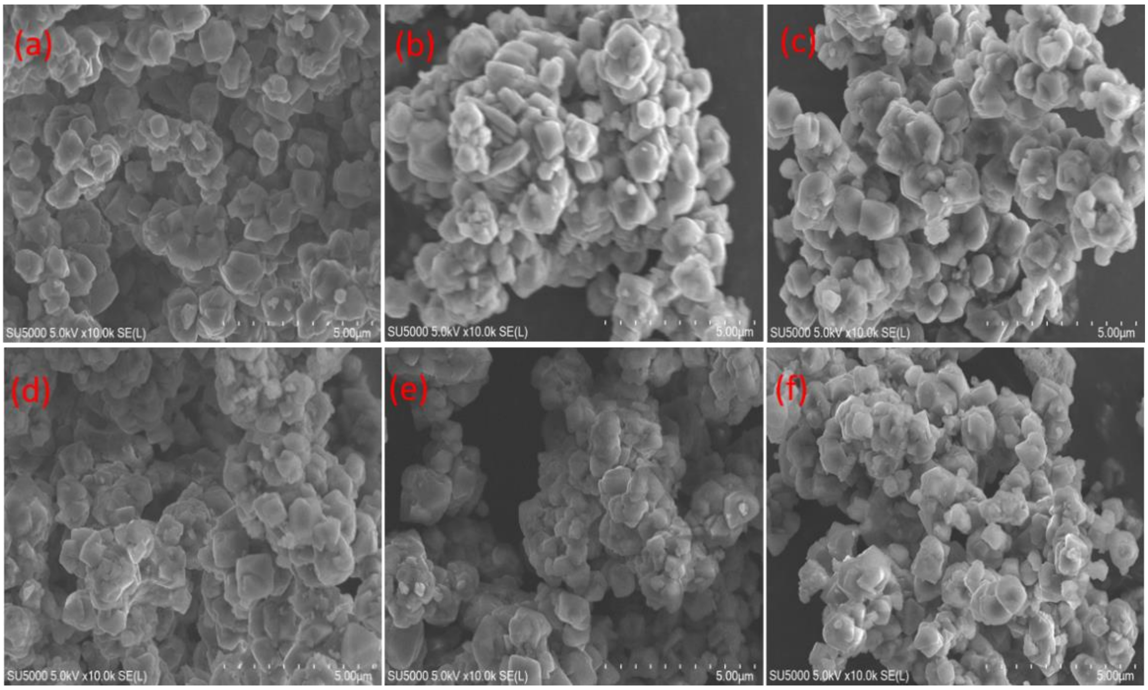

Figure A.2. SEM monograph of Y-zeolite modified by strontium (8%) via dry impregnation; (a) 0.05M citric acid and 0.2M NaOH concentration (SrD-AT1-0.2M); (b) 0.05M citric acid and 0.4M NaOH concentration (SrD-AT1-0.4M); (c) 0.05M (citric acid) and 0.8M NaOH concentration (SrD-AT1-0.8M); (d) 0.1M citric acid with 0.2M NaOH concentration (SrD-AT2-0.2M); (e) 0.1M citric acid and 0.4M NaOH concentration (SrD-AT2-0.4M); (f) 0.1M citric acid and 0.8M NaOH concentration (SrD-AT2-0.8M).

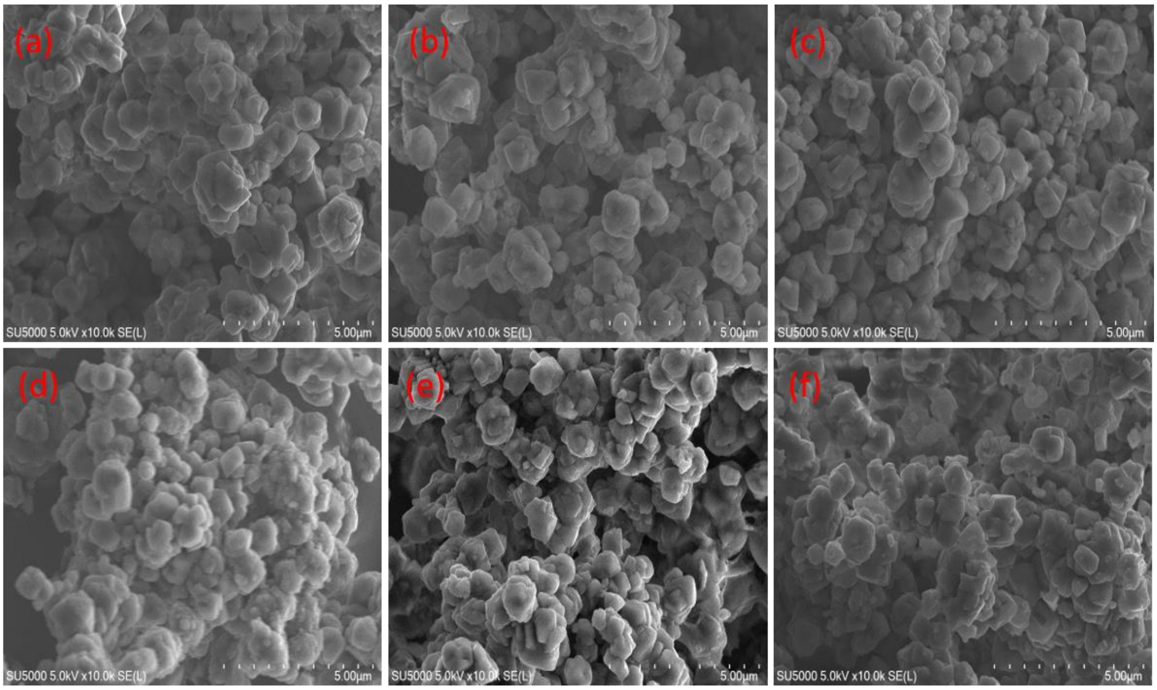

Figure A.3. SEM monograph of Y-zeolite modified by strontium (8%) via wet impregnation; (a) 0.05M citric acid and 0.2M NaOH concentration (SrW-AT1-0.2M); (b) 0.05M citric acid and 0.4M NaOH concentration (SrW-AT1-0.4M); (c) 0.05M (citric acid) and 0.8M NaOH concentration (SrW-AT1-0.8M); (d) 0.1M citric acid with 0.2M NaOH concentration (SrW-A2-0.2M); (e) 0.1M citric acid and 0.4M NaOH concentration (SrW-A2-0.4M); (f) 0.1M citric acid and 0.8M NaOH concentration (SrW-A2-0.8M).

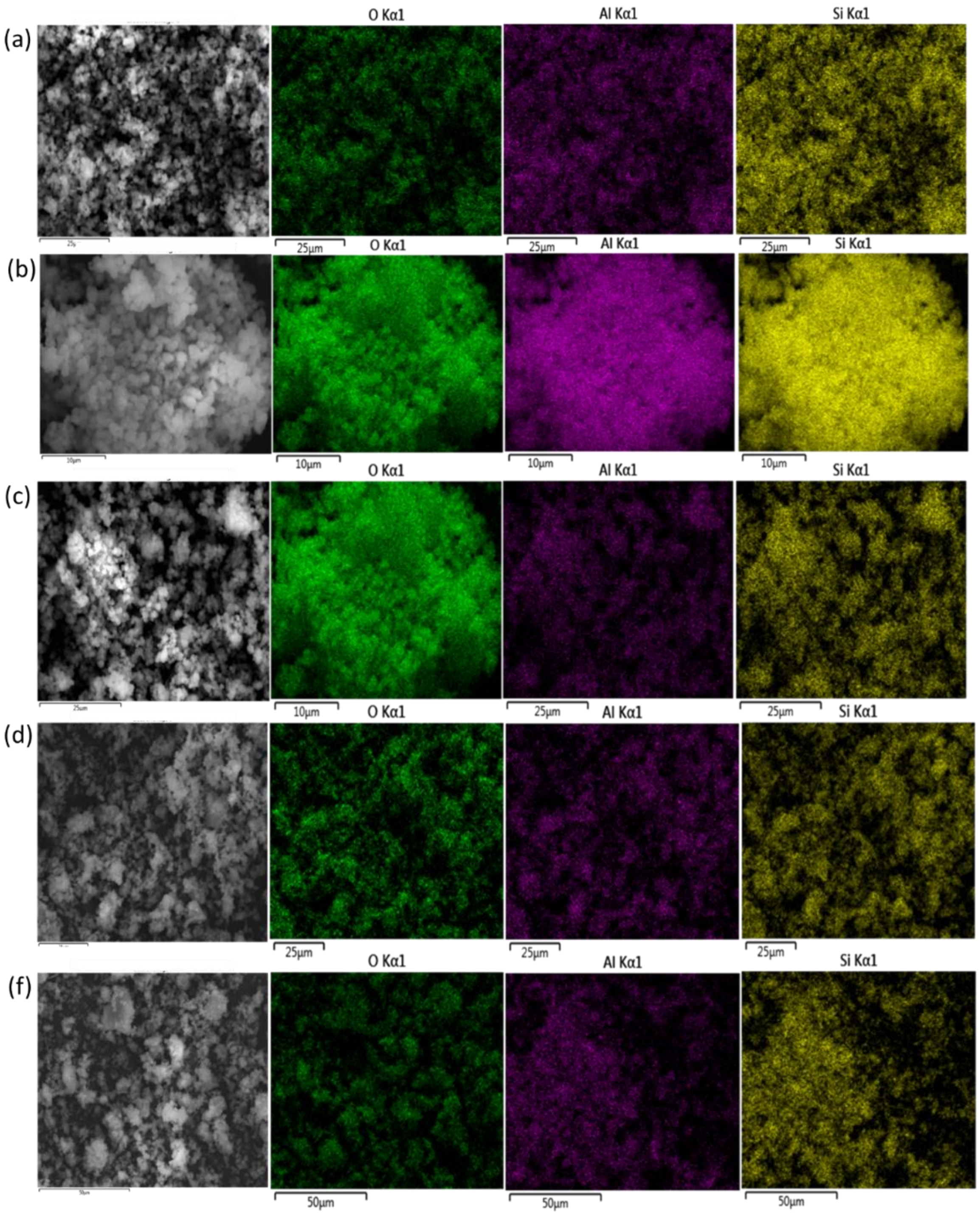

Figure A.4. EDS mapping of y-zeolite after sequential acid and alkaline treatment; (a) 0.05M citric acid and 0.2M NaOH concentration (AT1-0.2M); (b) 0.05M citric acid and 0.4M NaOH concentration (AT1-0.4M); (c) 0.05M citric acid and 0.8M NaOH concentration (AT1-0.8M); (d) 0.1M citric acid with 0.2M NaOH concentration (AT2-0.2M);(e) 0.1M citric acid and 0.4M NaOH (AT2-0.4M) concentration; (f) 0.1M citric acid and 0.8M NaOH concentration (AT2-0.8M).

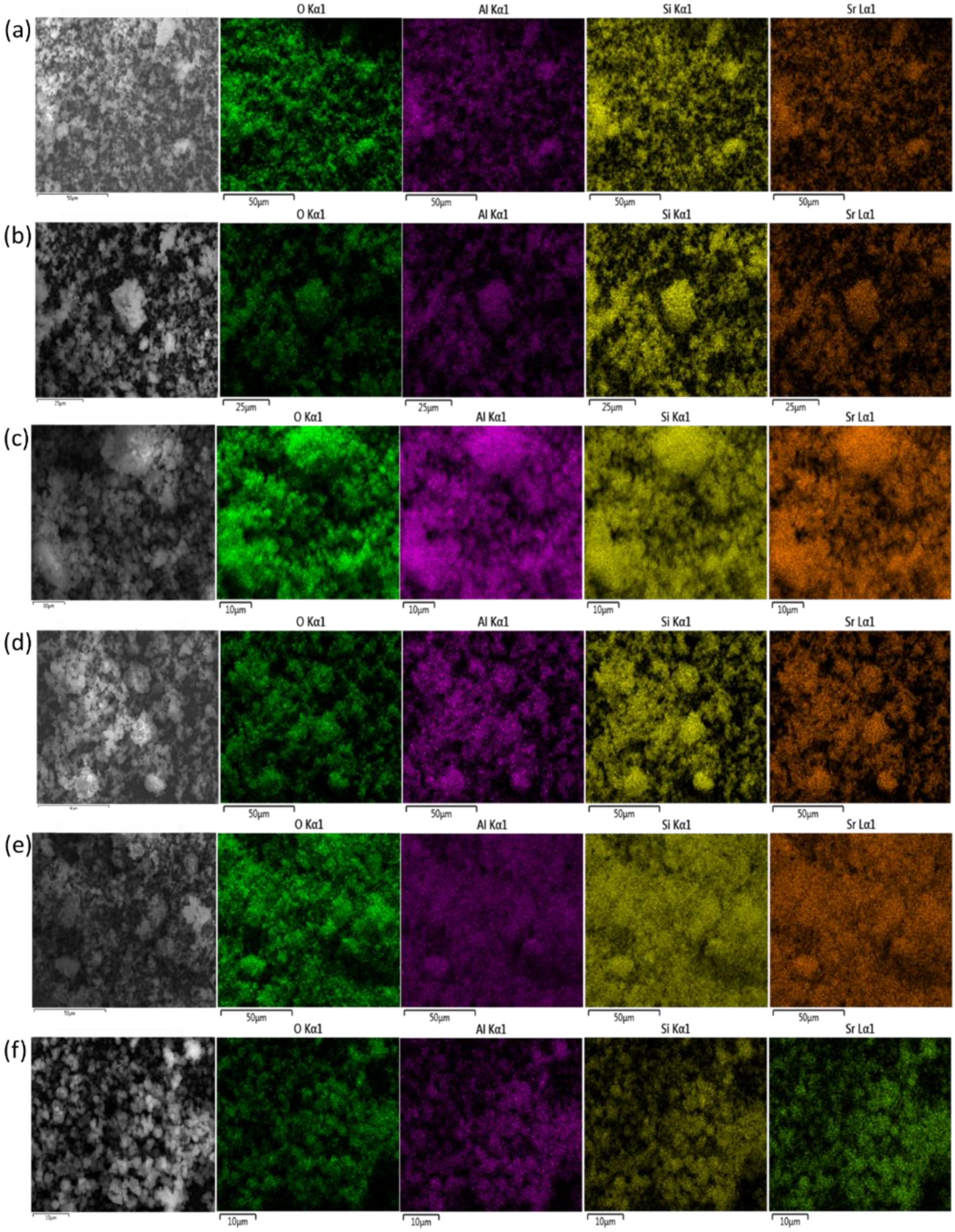

Figure A.5. EDS mapping of Y-zeolite modified by strontium (8%) via dry impregnation; (a) 0.05M citric acid and 0.2M NaOH concentration (SrD-AT1-0.2M); (b) 0.05M citric acid and 0.4M NaOH concentration (SrD-AT1-0.4M); (c) 0.05M (citric acid) and 0.8M NaOH concentration (SrD-AT1-0.8M); (d) 0.1M citric acid with 0.2M NaOH concentration (SrD-AT2-0.2M); (e) 0.1M citric acid and 0.4M NaOH concentration (SrD-AT2-0.4M); (f) 0.1M citric acid and 0.8M NaOH concentration (SrD-AT2-0.8M).

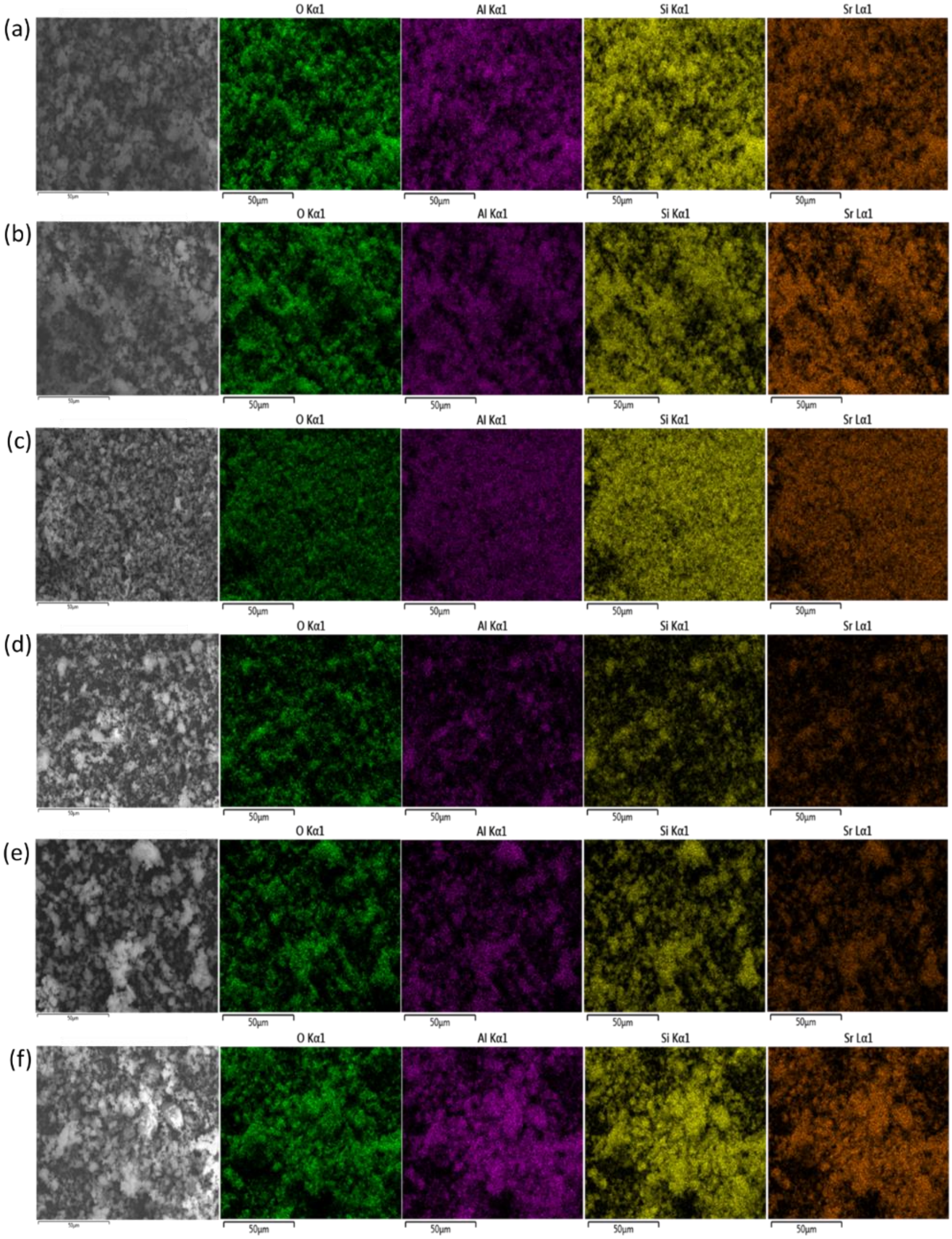

Figure A.6. EDS mapping of Y-zeolite modified by strontium (8%) via wet impregnation; (a) 0.05M citric acid and 0.2M NaOH concentration (SrW-AT1-0.2M); (b) 0.05M citric acid and 0.4M NaOH concentration (SrW-AT1-0.4M); (c) 0.05M (citric acid) and 0.8M NaOH concentration (SrW-AT1-0.8M); (d) 0.1M citric acid with 0.2M NaOH concentration (SrW-A2-0.2M); (e) 0.1M citric acid and 0.4M NaOH concentration (SrW-A2-0.4M); (f) 0.1M citric acid and 0.8M NaOH concentration (SrW-A2-0.8M).

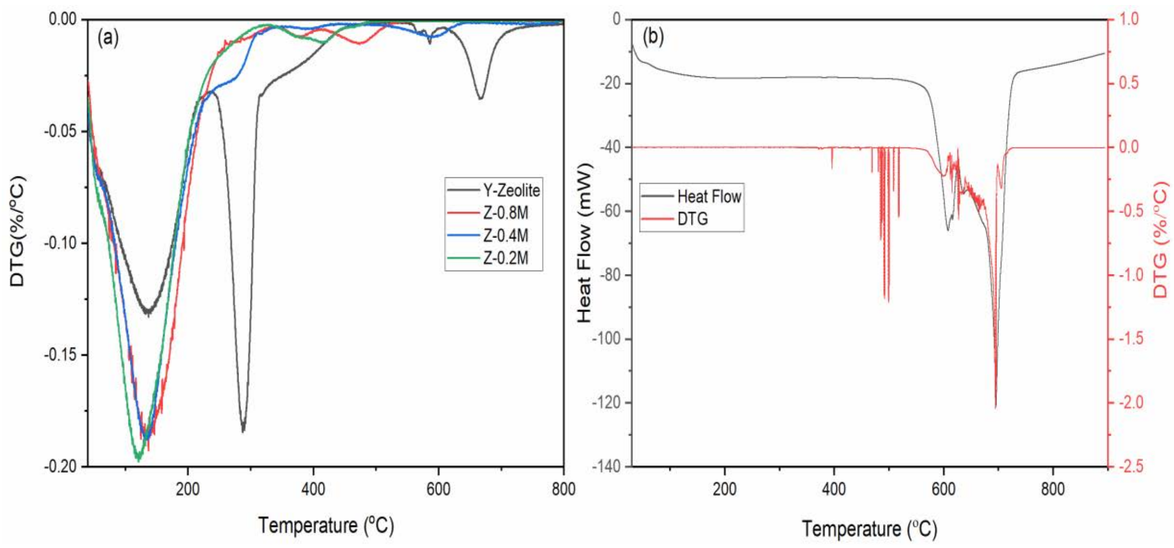

Figure A.7. DTG/DSC curve; a) DTG curve of parent Y-zeolite and uncalcined Sr loaded Y-zeolite; b) DTG/DSC curve of $Sr(NO_3)_2$.

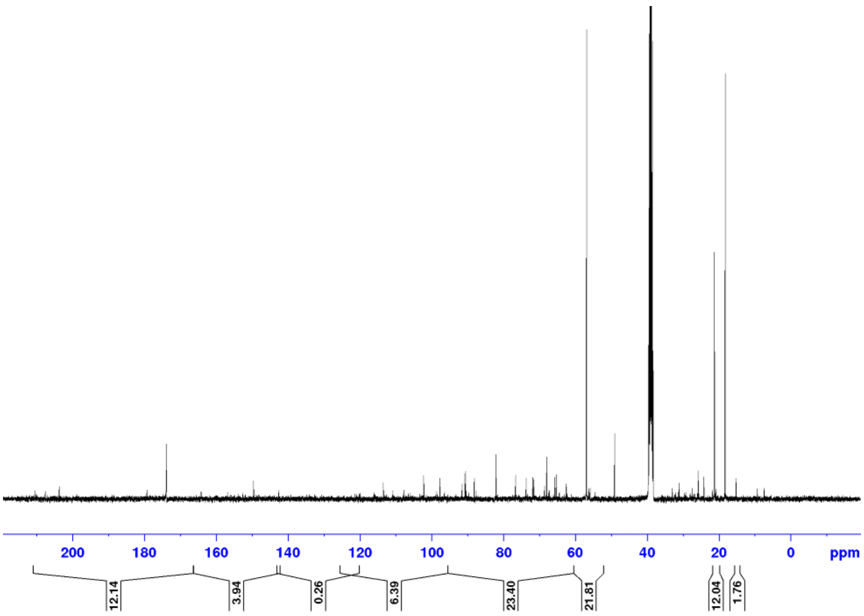

Figure A.8. Quantitative ^{13}C NMR spectrum of bio-oil produces from IB.

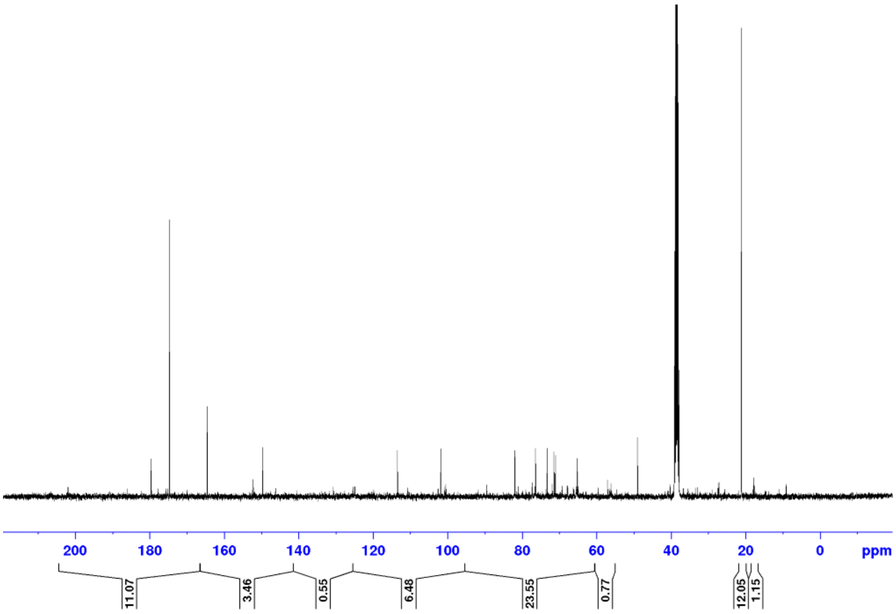

Figure A.9. Quantitative ^{13}C NMR spectrum of bio-oil produces from Ironbark and plastic waste mixture at 4:1 ratio (IB: PW).

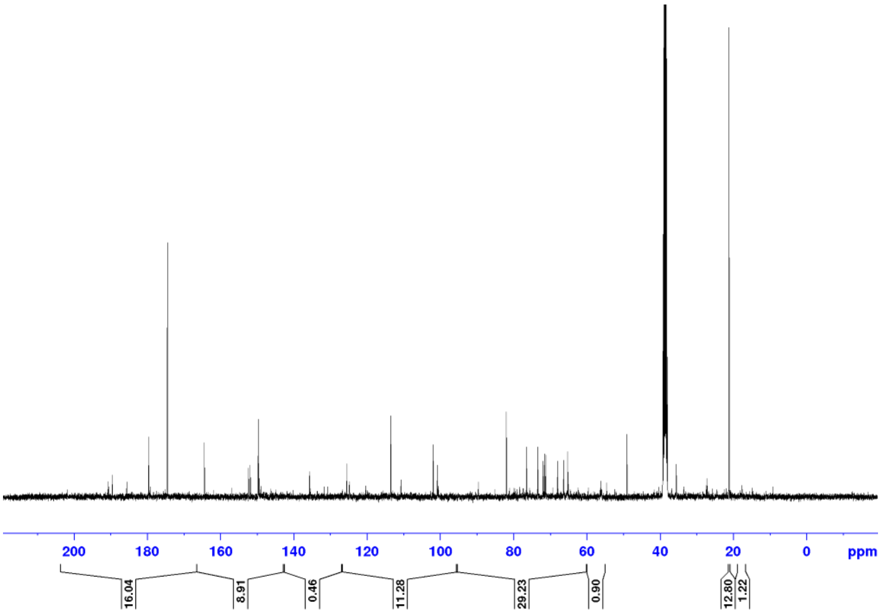

Figure A.10. Quantitative ^{13}C NMR spectrum of bio-oil produces from catalytic co-pyrolysis of ironbark and plastic waste mixture at 4:1 ratio (IB: PW) and 1:4 ratio of catalyst to feedstock.

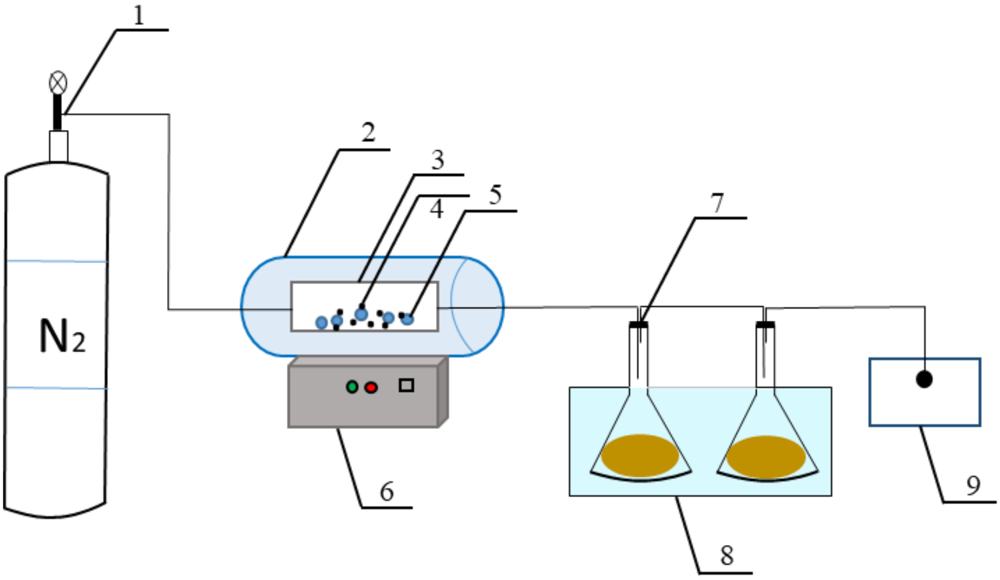

Figure A.11. Schematic diagram for the pyrolysis experiment setup used in this study (1 - Rotameter; 2 - Heat tape; 3 - Quartz tube; 4 - Catalyst; 5 - Biomass; 6 - Furnace control unit; 7 - Liquid bottle; 8 - Condenser; 9 - Gas collecting bag).

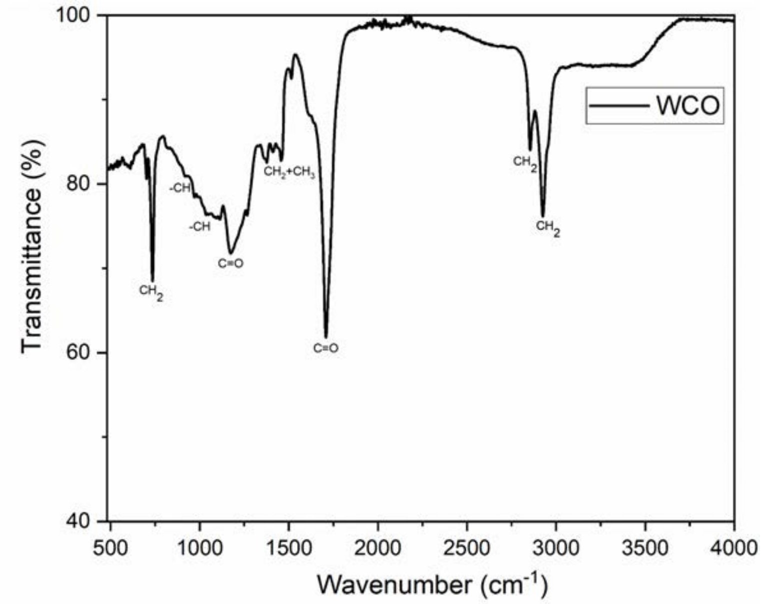

Figure A.12. FTIR spectrum of WCO.

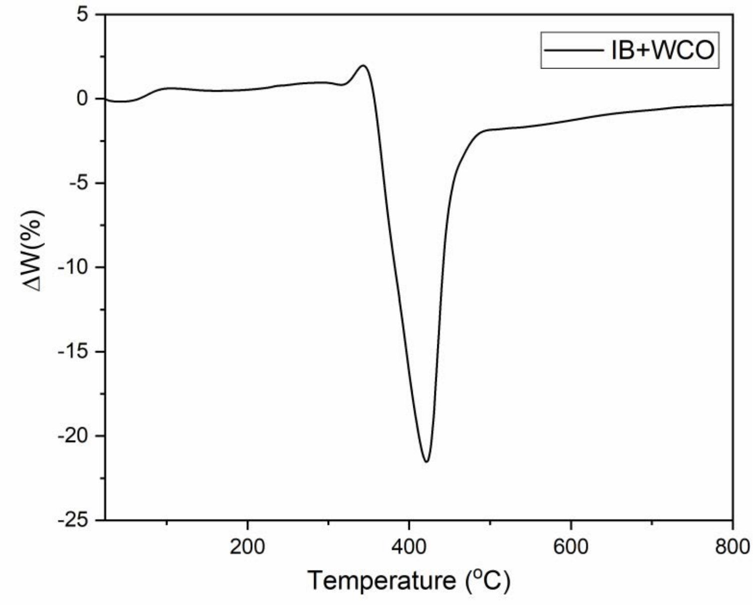

Figure A.13. Mass loss curve (ΔW) during IB:WCO (1:1) co-pyrolysis carried by TGA.

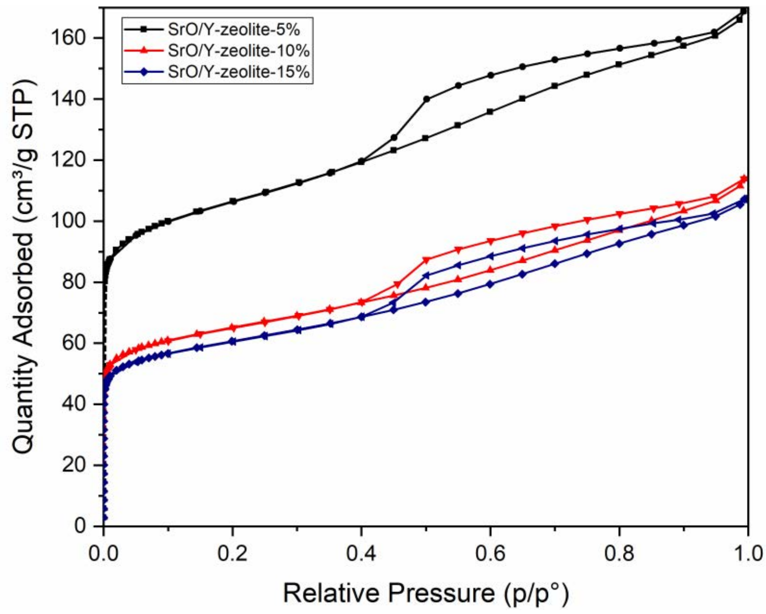

Figure A.14. N_2 adsorption-desorption isotherms of SrO/Y-zeolite catalysts.

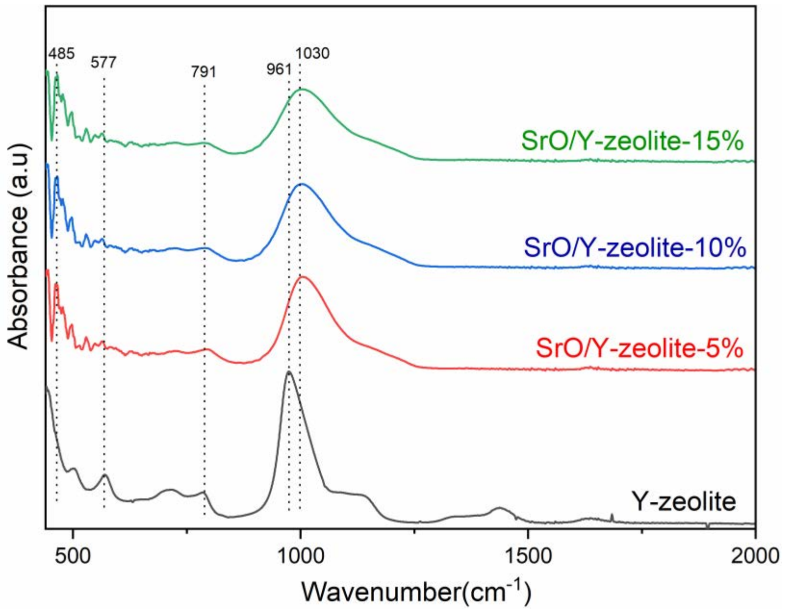

Figure A.15. FTIR characterization of catalysts used in the catalytic co-pyrolysis: Y-zeolite; parent Y-zeolite loaded with 5% strontium (SrO/Y-zeolite-5%); parent Y-zeolite loaded with 10% strontium (SrO/Y-zeolite-10%); parent Y-zeolite loaded with 15% strontium (SrO/Y-zeolite-15%).

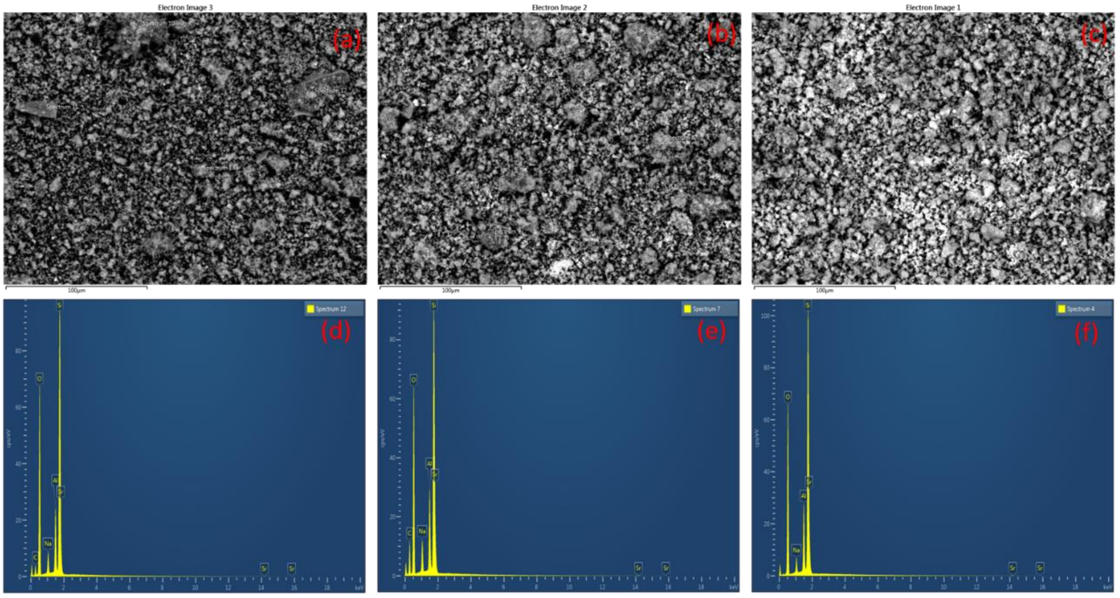

Figure A.16. SEM and EDS results of strontium loaded Y-zeolite: (a) and (d) SEM and EDS of Y-zeolite loaded with 5% strontium (SrO/Y-zeolite-5%); (b) and (e) SEM and EDS of Y-zeolite loaded with 10% strontium (SrO/Y-zeolite-10%); (c) and (f) SEM and EDS of Y-zeolite loaded with 15% strontium (SrO/Y-zeolite-15%).

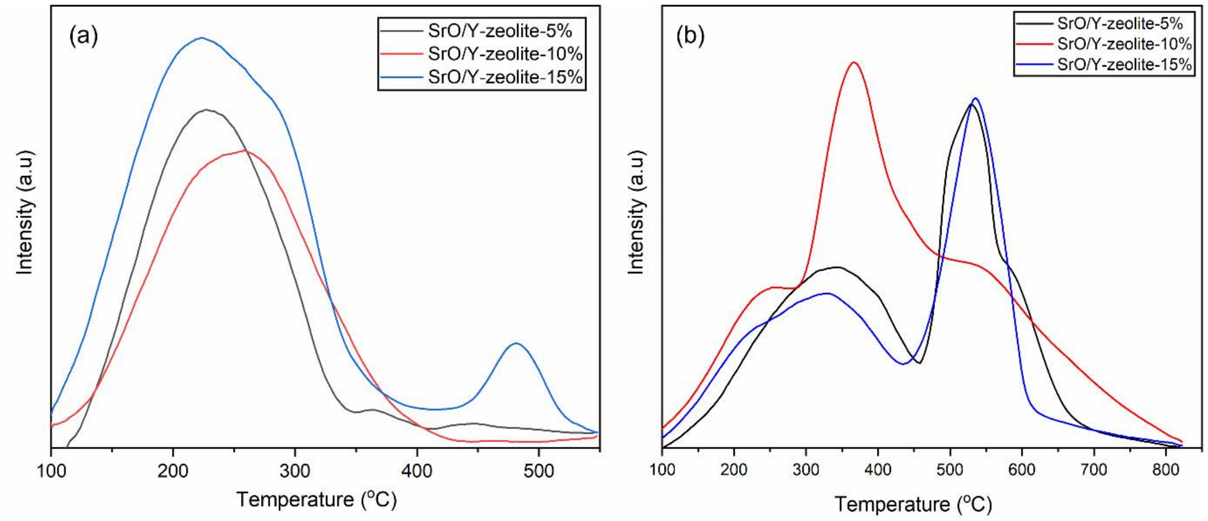

Figure A.17. Temperature Programmed Desorption (TPD) profile for SrO/Y-zeolite catalysts: (a) NH_3-TPD and (b) CO_2-TPD.

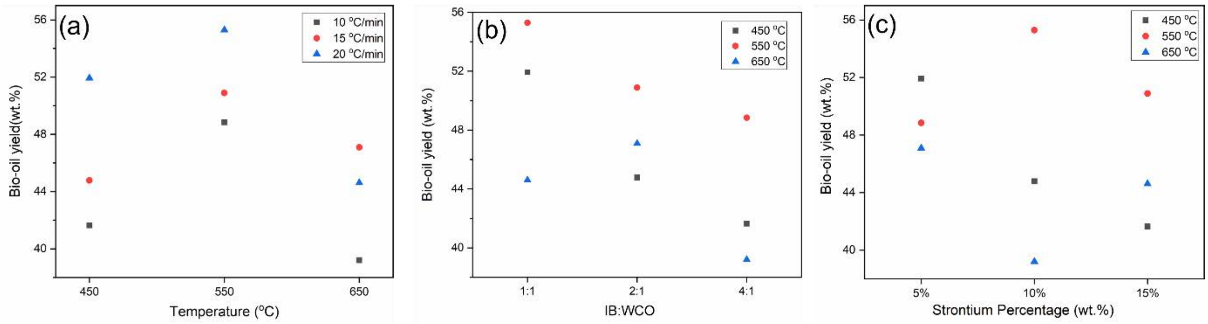

Figure A.18. Study of the effect of several variables on bio-oil yield: (a) effect of temperature on bio-oil yield at IB:WCO ratio of 1:1 and 550°C using SrO/Y-zeolite-10%; (b) effect of IB:WCO ratio on bio-oil yield at 550°C and heating rate of 10°C/min using SrO/Y-zeolite-10%; (c) effect of strontium percentage on bio-oil yield at IB:WCO ratio of 1:1, 550°C and heating rate of 10°C/min using SrO/Y-zeolite-10%.

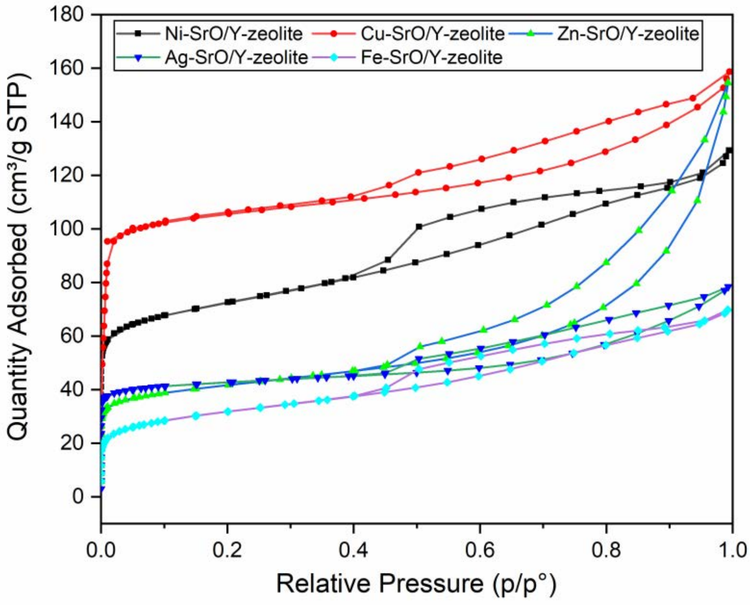

Figure A.19. N_2 adsorption-desorption isotherms of bimetallic catalysts (M-SrO/Y-zeolite).

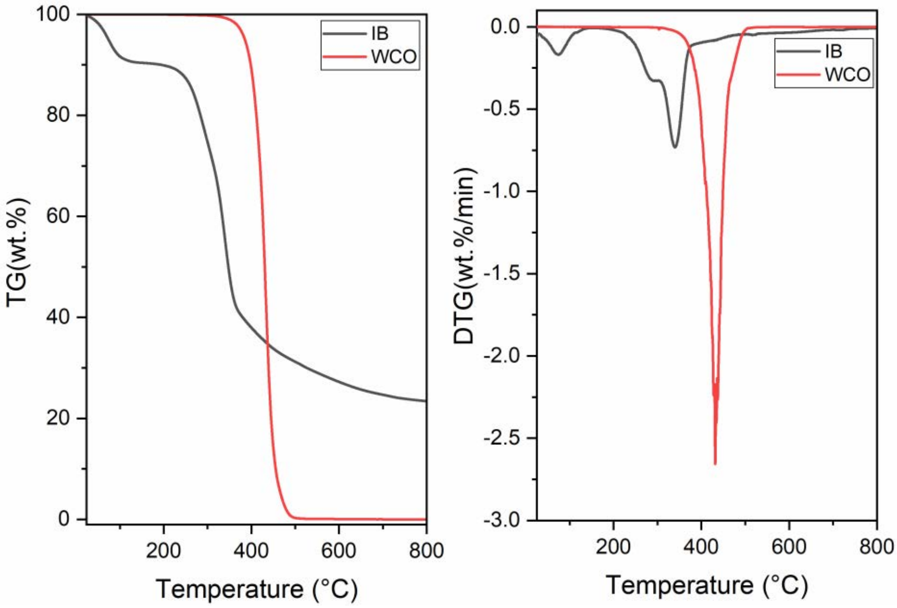

Figure A.20. TG/DTG curve of non-catalytic co-pyrolysis of individual IB and WCO.

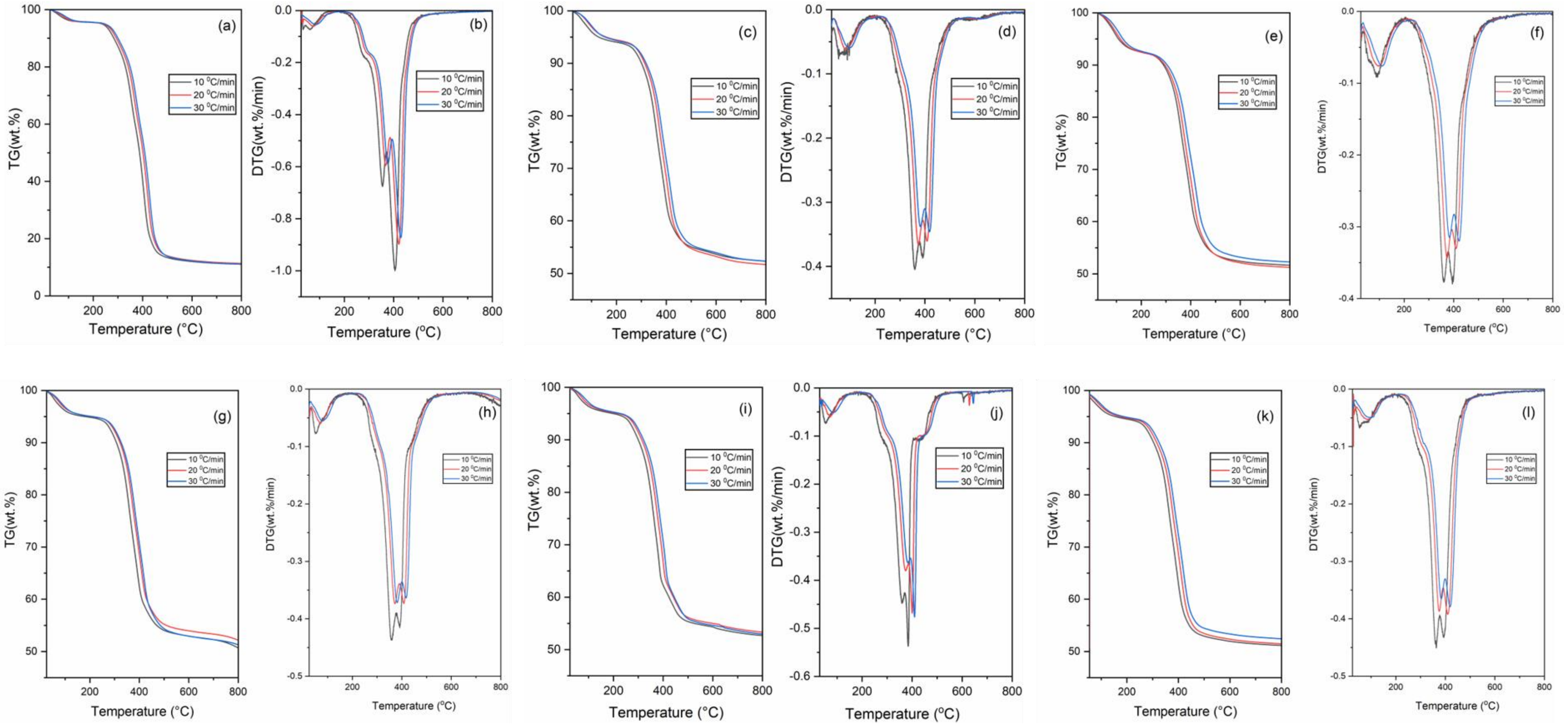

Figure A.21. TG/DTG curve of co-pyrolysis of IB and WCO mixture with and without catalyst at different heating rate ; (a) TG curves for IB and WCO (IB:WCO) mixture; (b) DTG curves for IB and WCO (IB:WCO) mixture; (c) TG curves of IB:WCO and Ni-SrO/Y-zeolite; (d) DTG curves of IB:WCO and Ni-SrO/Y-zeolite; (e) TG curves of IB:WCO and Cu-SrO/Y-zeolite; (f) DTG curves of IB:WCO and Cu-SrO/Y-zeolite; (g) TG curves of IB:WCO and Zn-SrO/Y-zeolite; (h) DTG curves of IB:WCO and Zn-SrO/Y-zeolite; (i) TG curves of IB:WCO and Ag-SrO/Y-zeolite; (j) DTG curves of IB:WCO and Ag-SrO/Y-zeolite ; (k) TG curves of IB:WCO and Fe-SrO/Y-zeolite; (i) DTG curves of IB:WCO and Fe-SrO/Y-zeolite.

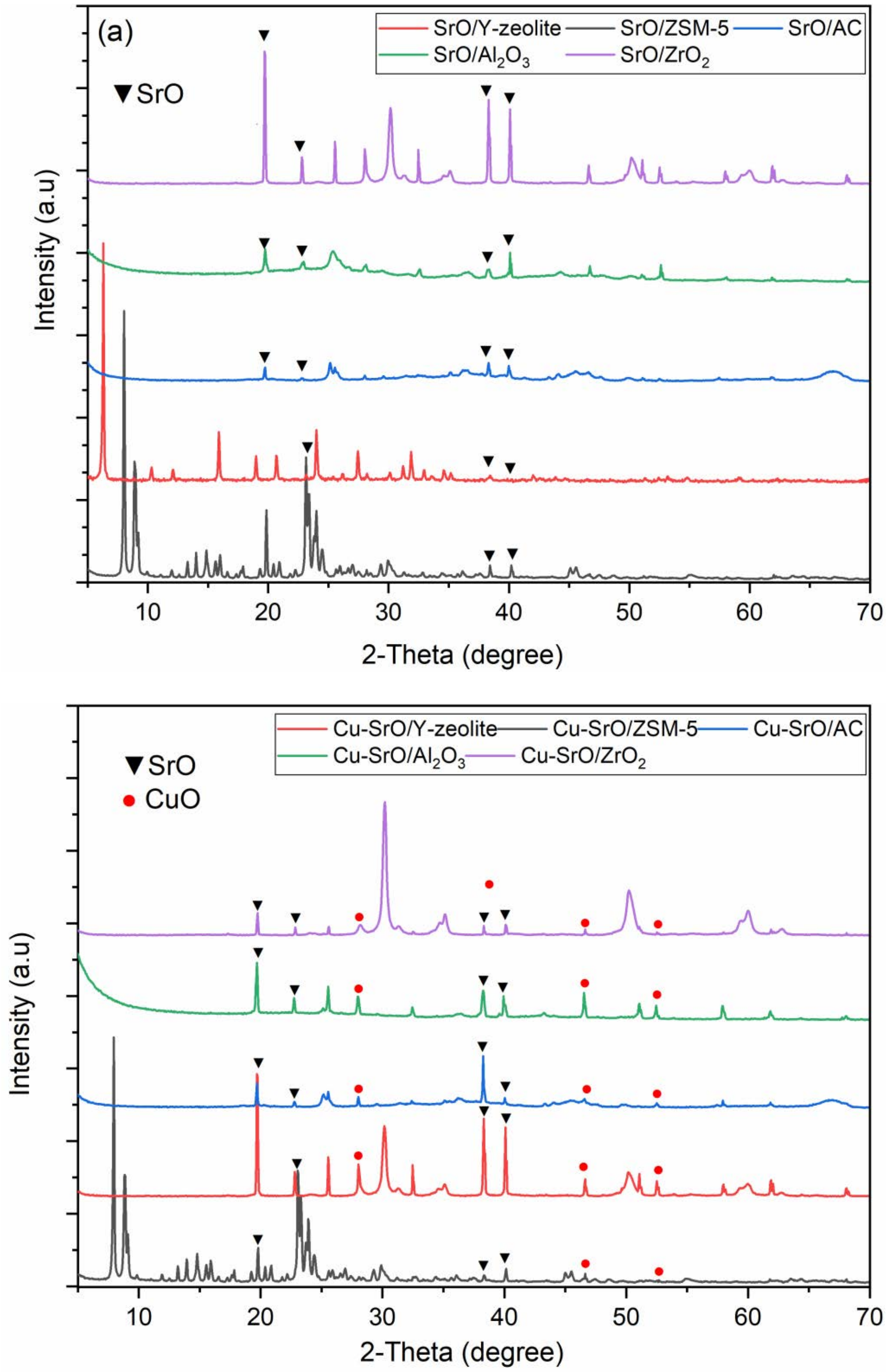

Figure A.22. XRD patterns of Cu-SrO modified catalysts (a) Mono-metallic catalysts prepared with different catalyst supports; (b) Bimetallic catalysts prepared with different catalyst supports.

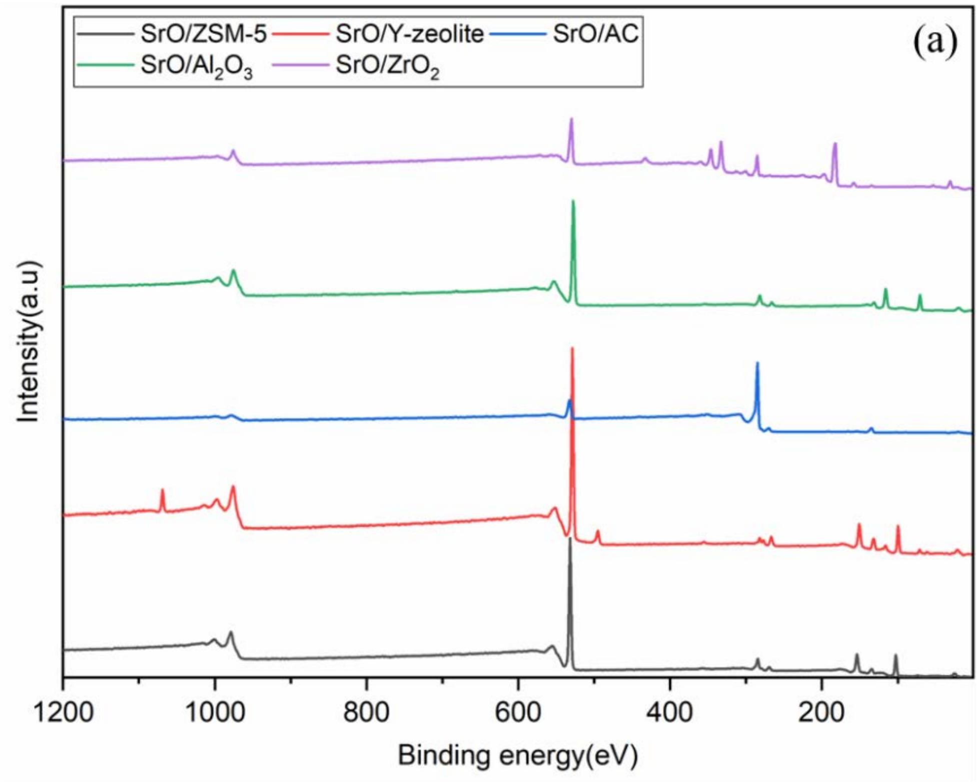

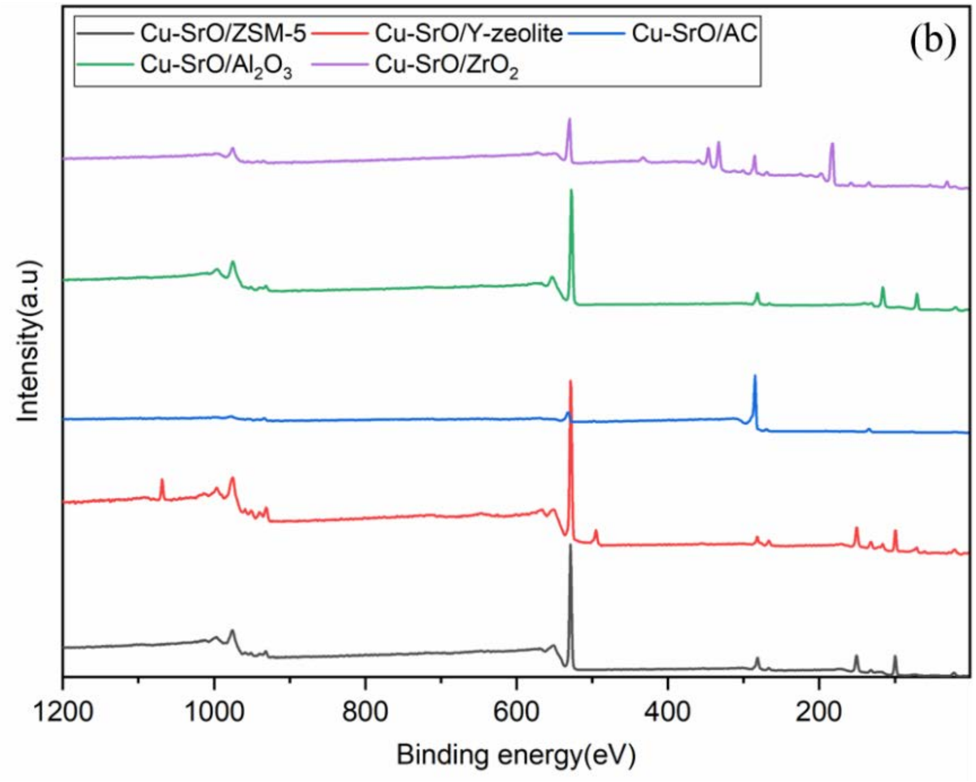

Figure A.23. X-ray photoelectron spectra of various catalyst supports (ZSM-5, Y-zeolite, AC (activated carbon), Al_2O_3, and ZrO_2): (a) mono-metallic catalysts; (b) bimetallic catalysts.

Table A.1. Kinetic parameters Coasts-Redfern equation based on TGA/DTG curves for IB, PW, IB+PW and catalytic co-pyrolysis of IB and PW mixture.

Sample Name	Reaction model	Slope	Y-Intercept	Activation Energy, KJ/mol	Pre-exponential factor, min^{-1}	R^2
Iron Bark	1	-5567	-5.15	46.28	9.40	0.897
	2	-6515	-4.07	54.17	32.60	0.918
	3	-3881	-6.78	32.27	1.29	0.933
	4	-3881	-7.47	32.27	0.65	0.933
	5	-3881	-7.47	32.27	0.65	0.933
	6	-2861	-7.17	23.79	0.64	0.925
	7	-6269	-2.33	52.12	178.71	0.965
	8	-9253	3.20	76.93	$6.6\text{x}10^4$	0.907
PW	1	-23966	22.40	199.25	$3.7\text{x}10^{13}$	0.971
	2	-26287	25.63	218.55	$1.1\text{x}10^{15}$	0.969
	3	-16092	11.69	133.79	$5.6\text{x}10^8$	0.966
	4	-16092	11.01	133.79	$2.8\text{x}10^8$	0.966
	5	-16092	10.60	133.79	$1.8\text{x}10^8$	0.966
	6	-11401	6.21	94.79	$1.6\text{x}10^6$	0.672
	7	-24014	24.87	199.65	$4.4\text{x}10^{14}$	0.927
	8	-34047	41.55	283.07	0.86	0.927
IB+PW	1	-8978	-0.41	74.64	0.86	0.987
	2	-10087	0.91	83.86	0.86	0.988
	3	-5965	-3.86	49.59	36.82	0.970
	4	-5965	-4.55	49.59	18.47	0.970
	5	-5965	-4.95	49.59	12.38	0.970
	6	-3936	-5.58	32.72	4.35	0.676
	7	-9040	1.64	75.16	$1.3\text{x}10^4$	0.919
	8	-12900	8.51	107.25	$1.8\text{x}10^7$	0.870

SrD-AT1-0.2M	1	-7295	-2.95	60.65	$1.1x10^2$	0.926
	2	-8407	-1.61	69.90	$4.9x10^2$	0.919
	3	-5171	-5.03	42.99	9.91	0.874
	4	-5171	-5.72	42.99	4.97	0.874
	5	-5171	-6.21	42.99	3.04	0.874
	6	-4134	-5.2	34.37	6.68	0.653
	7	-8396	0.74	69.80	$5.1x10^3$	0.833
	8	-12477	8.02	103.73	$1.1x10^7$	0.800
SrD-AT1-0.4M	1	-9123	0.33	75.85	$3.7x10^3$	0.952
	2	-10271	1.05	85.39	$8.5x10^3$	0.945
	3	-6146	-3.65	51.10	46.80	0.905
	4	-6146	-4.34	51.10	23.48	0.905
	5	-6146	-4.75	51.10	15.58	0.905
	6	-4286	-5.01	35.63	8.38	0.625
	7	-9462	2.24	78.67	$2.6x10^4$	0.851
	8	-13644	9.65	113.44	$6.2x10^7$	0.806
SrD-AT1-0.8M	1	-8107	-1.81	67.40	$3.8x10^2$	0.943
	2	-9215	-0.49	76.61	$1.6x10^3$	0.936
	3	-5550	-4.52	46.14	17.71	0.895
	4	-5550	-5.22	46.14	8.79	0.895
	5	-5550	-5.62	46.14	5.89	0.895
	6	-4031	-5.42	33.51	5.23	0.637
	7	-8699	1.09	72.32	$7.5x10^3$	0.846
	8	-12668	8.15	105.32	$1.3x10^7$	0.807
SrW-AT1-0.2M	1	-8115	-1.79	67.47	$3.9x10^2$	0.944
	2	-9237	-0.45	76.80	$1.7x10^3$	0.936
	3	-5603	-4.43	46.58	19.56	0.891
	4	-5603	-5.13	46.58	9.71	0.891
	5	-5603	-5.53	46.58	6.51	0.891

	6	-4202	-5.13	34.94	7.28	0.624
	7	-8874	1.39	73.78	1.0×10^4	0.837
	8	-13008	8.74	108.15	2.3×10^7	0.794
SrW-AT1-0.4M	1	-8977	-0.533	74.63	1.5×10^3	0.960
	2	-10109	0.82	84.05	6.7×10^3	0.954
	3	-6035	-3.81	50.17	39.16	0.916
	4	-6035	-4.51	50.17	19.45	0.916
	5	-6035	-4.91	50.17	13.04	0.916
	6	-4170	-5.21	34.67	6.67	0.627
	7	-9273	1.95	77.10	1.9×10^4	0.86
	8	-13354	9.18	111.03	3.7×10^7	0.813
SrW-AT1-0.8M	1	-8809	-0.79	73.24	1.1×10^3	0.954
	2	-9940	0.56	82.64	5.1×10^3	0.946
	3	-5954	-3.93	49.50	34.27	0.907
	4	-5954	-4.63	49.50	17.02	0.907
	5	-5954	-5.03	49.50	11.41	0.907
	6	-4190	-5.17	34.84	6.98	0.623
	7	-9209	1.85	76.56	1.7×10^4	0.851
	8	-13313	9.13	110.68	3.5×10^7	0.805
SrW-AT2-0.2M	1	-6804	-3.63	56.57	52.86	0.974
	2	-7791	-2.50	64.77	1.8×10^2	0.972
	3	-4606	-5.91	38.29	3.66	0.948
	4	-4606	-6.60	38.29	1.84	0.948
	5	-4606	-7.01	38.29	1.22	0.948
	6	-3168	-6.84	26.34	0.99	0.721
	7	-7184	-1.24	59.73	6.0×10^2	0.913
	8	-10403	4.55	86.49	2.8×10^5	0.881
	1	-7121	-3.25	59.20	80.90	0.905
	2	-8105	-2.14	67.38	2.7×10^2	0.904

SrW-AT2-0.4M	3	-4737	-5.78	39.38	4.29	0.872
	4	-4737	-6.47	39.38	2.15	0.872
	5	-4737	-6.88	39.38	1.43	0.872
	6	-3054.4	-7.07	25.39	0.76	0.697
	7	-7229	-1.27	60.10	5.9x10^{2}	0.859
	8	-10324	4.29	85.83	2.2x10^{5}	0.843
SrW-AT2-0.8M	1	-8325	-1.48	69.21	5.5x10^{2}	0.952
	2	-9443	-0.14	78.51	2.4x10^{3}	0.944
	3	-5683	-4.32	47.25	22.15	0.903
	4	-5683	-5.02	47.25	11.00	0.903
	5	-5683	-5.42	47.25	7.37	0.903
	6	-4106	-5.29	34.14	6.07	0.634
	7	-8883	1.38	73.85	1.0x10^{4}	0.851
	8	-12918	8.54	107.40	1.9x10^{7}	0.807
SrD-AT2-0.2M	1	-8496	-1.16	70.64	7.8x10^{2}	0.935
	2	-9669	0.34	80.39	3.0x10^{3}	0.932
	3	-5874	-4.63	48.84	16.79	0.905
	4	-5874	-4.63	48.84	16.79	0.905
	5	-5874	-4.63	48.84	16.79	0.905
	6	-4364	-4.81	36.28	10.42	0.702
	7	-9227	2.06	76.71	2.2x10^{4}	0.873
	8	-13460	9.59	111.91	5.7x10^{7}	0.843
SrD-AT2-0.4M	1	-7259	-2.94	60.35	1.1x10^{2}	0.976
	2	-8307	-1.71	69.06	4.4x10^{2}	0.973
	3	-4976	-5.31	41.37	7.21	0.947
	4	-4976	-6.01	41.37	3.58	0.947
	5	-4976	-6.41	41.37	2.40	0.947
	6	-3579	-6.14	29.76	2.26	0.707
	7	-7823	-0.18	65.04	1.9x10^{3}	0.905

	8	-11397	6.18	94.75	1.6x10^{6}	0.868
SrD-AT2-0.8M	1	-7929	-2.04	65.92	3.0x10^{2}	0.961
	2	-9011	-0.75	74.92	1.2x10^{3}	0.954
	3	-5392	-4.75	44.83	13.67	0.918
	4	-5392	-5.44	44.83	6.86	0.918
	5	-5392	-5.84	44.83	4.60	0.918
	6	-3814	-5.78	31.71	3.45	0.656
	7	-8393	0.62	69.78	4.5x10^{3}	0.871
	8	-12167	7.34	101.16	5.4x10^{5}	0.830

Table A.2. Proximate and ultimate analysis of IB.

Sample	Proximate analysis [a] (%)				Ultimate analysis (%)			
	Moisture	Volatiles	Ash	Fixed carbon	C	H	N	O[b]
IB	6.8	61.4	23.4	8.4	48.9	5.9	0.2	45.1

[a] Values on a dry weight basis; [b] Calculated by weight difference

Table A.3. Activation energy calculated by OFW and KAS method along with fitted equation and correlation coefficient for both non-catalytic and catalytic co-pyrolysis.

Feedstock / Catalyst	Conversion (α)	OFW Method			KAS Method		
		Activation Energy, E_a (kJ/mol)	Fitted linear equation	Correlation coefficient (R^2)	Activation Energy, E_a (kJ/mol)	Fitted linear equation	Correlation coefficient (R^2)
IB+WCO	0.1	162.40	$y = -20550x + 39.778$	0.9205	161.57	$y = -19434x + 25.128$	0.9119
	0.2	168.34	$y = -21301x + 38.056$	0.9975	167.03	$y = -20091x + 23.245$	0.9971
	0.3	172.28	$y = -21799x + 37.526$	0.9993	170.78	$y = -20542x + 22.638$	0.9992
	0.4	171812	$y = -21740x + 36.594$	1	170.03	$y = -20452x + 21.658$	1
	0.5	182.42	$y = -23080x + 37.717$	0.9965	180.87	$y = -21756x + 22.726$	0.9961
	0.6	197.31	$y = -24966x + 39.782$	0.9992	196.33	$y = -23615x + 24.751$	0.9991
	0.7	185.77	$y = -23506x + 37.072$	0.9998	184.022	$y = -22134x + 22.009$	0.9998
	0.8	201.26	$y = -25466x + 39.372$	1	200.13	$y = -24072x + 24.278$	1
	0.9	297.35	$y = -37625x + 55.452$	0.991	300.92	$y = -36194x + 40.307$	0.9991
	Avg	193.21			192.41		
Ni-SrO/Y-zeolite	0.1	49.78	$y = -6298.6x + 18.029$	0.9417	45.51	$y = -5473.5x + 3.9834$	0.9245
	0.2	193.23	$y = -24450x + 44.964$	0.9978	193.63	$y = -23290x + 30.238$	0.9976
	0.3	192.59	$y = -24369x + 42.443$	0.9994	192.37	$y = -23139x + 27.6$	0.9993
	0.4	181.26	$y = -22936x + 38.988$	0.9956	180.15	$y = -21668x + 24.084$	0.9951
	0.5	183.83	$y = -23261x + 38.728$	0.9930	182.61	$y = -21964x + 23.778$	0.9921
	0.6	192.43	$y = -24349x + 39.557$	0.9931	191.39	$y = -23021x + 24.561$	0.9921

	0.7	191.08	y = -24178x + 38.532	0.9871	189.74	y = -22822x + 23.493	0.9855
	0.8	272.06	y = -34425x + 52.436	0.9344	274.64	y = -33034x + 37.346	0.9291
	0.9	30.80	y = -389.73`x + 3.729	0.8697	29.20	y = -351.32x + 37.798	1
	Avg	162.15			161.44		
Cu-SrO/Y-zeolite	0.1	71.83	y = -9089.2x + 26.354	0.9602	45.51	y = -5473.5x + 3.9834	0.9245
	0.2	252.85	y = -31994x + 59.564	0.9916	193.63	y = -23290x + 30.238	0.9976
	0.3	171.58	y = -21711x + 38.401	0.9878	192.34	y = -23139x + 27.6	0.993
	0.4	165.90	y = -20992x + 35.999	0.9720	180.15	y = -21668x + 24.084	0.9951
	0.5	166.41	y = -21057x + 35.351	0.9805	182.62	y = -21964x + 23.778	0.9921
	0.6	174.71	y = -22107x + 36.15	0.9804	191.39	y = -23021x + 24.561	0.9921
	0.7	175.47	y = -22203x + 35.525	0.9868	189.74	y = -22822x + 23.493	0.9855
	0.8	176.14	y = -22287x + 34.913	0.9915	274.64	y = -33034x + 37.346	0.9291
	0.9	231.56	y = -29300x + 43.042	0.9799	255.06	y = -30679x + 31.744	0.9977
	Avg	176.27			189.45		
Zn-SrO/Y-zeolite	0.1	83.29	y = -10540x + 25.319	0.9999	41.38	y = -4936.1x + 1.2364	0.9650
	0.2	157.99	y = -19991x + 36.827	0.9999	156.43	y = -18815x + 22.073	0.9999
	0.3	174.52	y = -22083x + 38.562	0.9999	173.32	y = -20847x + 23.709	0.9999
	0.4	167.83	y = -21236x + 36.296	0.9966	165.99	y = -19966x + 21.389	0.9961
	0.5	174.76	y = -22114x + 36.98	0.966	173.08	y = -20818x + 22.032	0.9961
	0.6	173.63	y = -21970x + 36.059	0.9987	171.65	y = -20647x + 21.07	0.9985
	0.7	179.86	y = -22759x + 36.523	0.9998	177.98	y = -21408x + 21.492	0.9998

	0.8	207.93	y = -26311x + 40.946	0.9993	207.26	y = -24930x + 25.87	0.9992
	0.9	217.16	y = -27479x + 91.868	0.9981	216.23	y = -26009x + 76.668	0.9981
	Avg	170.77			164.77		
Ag-SrO/Y-zeolite	0.1	75.08	y = -9501x + 23.7	0.9999	71.42	y = -8590.5x + 9.4573	0.9999
	0.2	144.19	y = -18245x + 34.418	0.9991	142.09	y = -17091x + 19.701	0.9999
	0.3	149.07	y = -18862x + 33.66	0.9924	146.63	y = -17637x + 18.824	0.9912
	0.4	215.71	y = -27295x + 45.911	0.9545	216.37	y = -26025x + 31.004	0.9501
	0.5	157.09	y = -19877x + 33.707	0.9998	154.54	y = -18589x + 18.771	0.9997
	0.6	148.25	y = -18759x + 31.459	0.9572	145.03	y = -17444x + 16.482	0.9506
	0.7	155.63	y = -19693x + 32.329	0.9994	152.62	y = -18357x + 17.321	0.9993
	0.8	194.39	y = -24597x + 38.743	1	193.12	y = -23227x + 23.684	1
	0.9	245.52	y = -31067x + 45.211	0.9999	246.12	y = -29601x + 30.017	0.9999
	Avg	164.99			163.10		
Fe-SrO/Y-zeolite	0.1	70.97	y = -8980.2x + 23.665	0.9863	67.51	y = -8119.8x + 9.536	0.9834
	0.2	164.78	y = -20851x + 38.569	0.9998	163.65	y = -19684x + 23.831	0.9998
	0.3	167.38	y = -21179x + 37.029	0.9993	165.78	y = -19940x + 22.171	0.9992
	0.4	167.47	y = -21191x + 36.155	0.9720	165.58	y = -19916x + 21.24	0.9683
	0.5	167.90	y = -21245x + 35.507	0.9987	165.81	y = -19944x + 20.552	0.9985
	0.6	166.99	y = -21130x + 34.665	0.9997	164.63	y = -19802x + 19.669	0.9997
	0.7	172.19	y = -21788x + 35.01	0.9989	169.88	y = -20434x + 19.975	0.9988
	0.8	178.87	y = -22633x + 35.629	0.9990	176.69	y = -21253x + 20.555	0.9988

	0.9	232.31	y = -29395x + 44.055	0.9999	232.53	y = -27969x + 28.916	0.9999
	Avg	165.43			163.56		

Table A.4. Distribution of compounds in bio-oil derived from both non-catalytic and catalytic co-pyrolysis of IB and WCO with bimetallic catalysts.

IB+WCO			
R.T. (min)	Quality	Compound name	Relative peak area %
Hydrocarbons			13.35
2.345	50	1-Hexene	1.98
3.048	94	1-Heptene	0.69
3.143	50	Heptane	0.53
4.226	97	1-Octene	0.27
4.726	87	1,3-Octadiene	0.15
5.742	91	1-Nonene	0.26
7.371	95	1-Decene	0.27
8.47	90	n-Butylbenzene	0.30
8.982	96	1-Undecene	0.27
9.326	95	5-Undecene	0.25
9.519	68	Cycloheptene	0.40
10.052	83	pentyl-Benzene	0.57
11.023	87	Cyclodecene	0.42
14.042	72	1,2,3-trimethoxy-Benzene	0.89
14.722	98	Pentadecane	0.25
15	90	2,3,5-Trimethoxytoluene	0.84
15.675	64	1,13-Tetradecadiene	0.63
16.764	92	1,13-Tetradecadiene	0.33
22.494	83	5-Dodecyne	0.57
22.563	52	5,6-Bis(2,2-dimethylpropylidene)-Decane	3.49
Phenols			11.26
4.315	50	2-(1-Methylheptyl)-	0.35
5.121	94	2-Furanmethanol	0.09
8.366	95	O-Cresol	0.20
8.709	94	3-Methoxy-Phenol	0.37
8.935	97	2-Methoxy-Phenol	0.69

10.534	95	2-Methoxy-4-methylphenol	1.44
11.536	91	3-Methoxy-,2-Benzenediol	1.60
11.768	93	4-Ethyl-2-methoxy-Phenol	0.64
11.934	94	4 Methyl Catechol	0.59
12.302	90	4-Vinyl-2-methoxy-phenol	1.14
12.791	91	2,6-Dimethoxyphenol	1.46
12.867	97	2-Methoxy-4-(2-propenyl)-Phenol	0.42
15.111	59	2-Methoxy-4-propyl-phenol	0.62
20.102	94	3',5'-Dimethoxy-4'-hydroxyphenyl	0.60
24.029	80	2-Monoolein 2-Oleoylglycerol	1.05
Acids			60.68
2.502	90	Acetic acid	1.17
4.151	59	Propanoic acid	0.32
10.313	92	Octanoic Acid	0.28
15.203	52	Hexanoic acid	1.43
16.518	94	4-hydroxy-3-methoxy-Benzoic acid	0.28
21.173	99	Methyl este-13-Octadecenoic acid,	0.37
21.851	99	Oleic acid	44.11
21.958	99	Octadecanoic acid	3.96
22.089	99	9,12-Octadecadienoic acid	1.90
22.409	94	Linoleic acid	2.33
23.33	99	Oleic acid	3.86
23.524	98	Eicosanoic acid	0.64
Ketones			5.33
2.772	45	1-Hydroxy-2-Propanone	0.98
6.036	58	2(5H)-Furanone	0.35
6.299	64	2(3H)-Furanone, 5-methyl	0.70
7.934	96	2-Hydroxy-3-methyl--Cyclopenten	0.41
14.607	87	4-Hydroxy-3-methoxyacetophenone	0.37
15.532	90	2,6-Dimethyl-3-(methoxymethyl)-p-benzoquinone	2.53
Aldehydes			3.67

4.094	59	Propanal	0.41
4.814	94	2-Furancarboxaldehyde	0.84
6.889	81	5 Methyl Furfural	0.47
7.552	72	3-Methyl Hydantoin	0.84
11.114	95	2-Furancarboxaldehyde	0.37
12.386	70	2,4 Nonadienal	0.21
16.66	94	4-Hydroxy-3,5-dimethoxy-Benzaldehyde	0.53
Esters			0.22
24.22	59	Methyl oleate	0.22
others			1.41
22.61	58	4-Isocyanatocyclohexylmethane	1.11
22.764	90	Benzothieno[2,3-c]quinoline, 6-(propylthio)-	0.30
SrO/Y-zeolite			
R.T. (min)	Quality	Compound name	Peak area %
Hydrocarbons			20.91
3.303	95	1-Heptene	3.89
3.972	50	Toluene	2.57
5.54	95	p-Xylene	0.81
5.815	95	1-Nonene	0.79
5.884	53	Benzene, 1,4-dimethyl-	0.78
6.041	68	4,5-Nonadiene	0.85
6.712	53	4-Decyne	0.23
6.84	68	n-Propylbenzene	0.15
7.472	76	Benzene, 1,2,4-trimethyl	0.72
8.175	68	Benzene, 2-propenyl-	0.33
8.338	59	1H-Indene	0.25
8.988	93	1-Undecene	0.87
9.197	95	5-Undecene	1.12
9.512	64	Cycloheptene	1.02
11.02	94	Cyclodecene	0.96
11.527	50	2,4-Dodecadiene	0.37

11.566	60	Benzene, hexyl-	1.00
12.187	86	Naphthalene, 1-methyl-	0.23
12.289	78	Naphthalene, 2-methyl-	0.83
13.856	91	Naphthalene, 2,7-dimethyl-	0.22
14.715	90	1-Pentadecene	0.38
16.837	99	8-Heptadecene	1.37
22.512	50	1-Nonadecene	1.19
Phenols			13.67
8.923	76	4-Methyl-Phenol	3.80
8.938	94	Guaiacol	2.55
11.759	94	4-Ethyl-2-methoxy-phenol	0.53
12.292	97	4-Vinyl-2-methoxy-phenol	2.99
12.756	91	2,6-Dimethoxyphenol	0.49
12.855	95	Phenol, 2-methoxy-4-(2-propenyl)	0.61
14.126	95	Phenol, 2-methoxy-4-(1-propenyl)	2.69
Acids			44.92
7.27	64	Hexanoic acid	1.37
8.763	72	Heptanoic acid	3.89
10.174	98	Octanoic acid	0.97
12.925	95	Decanoic Acid	1.30
14.006	80	Dehydroacetic acid	0.75
19.836	90	Palmitic acid	4.75
21.524	99	Oleic acid	24.13
21.566	93	14-Pentadecenoic acid	1.94
21.711	81	Octadecanoic acid	1.61
21.918	99	Linoleic acid	4.22
Ketones			8.80
4.854	67	2-Cyclohepten-1-one	0.75
6.318	64	1,3-Cyclopentanedione	4.40
7.933	70	2-Cyclopenten-1-one, 2-hydroxy-3-methyl-	0.75
11.623	83	2-Methyl-1-phenylbutadiene	1.91
17.433	90	Acetosyringone	0.60

18.952	87	9-Heptadecanone	0.40
Aldehydes			3.62
4.953	81	2-Furancarboxaldehyde	2.25
7.58	91	N-Octanal	0.97
10.488	72	Heptanal	0.40
Esters			8.08
19.456	86	Hexadecanoic acid, methyl ester	2.99
24.002	59	2-Hydroxy-1-(hydroxymethyl)ethyl ester	5.09
Ni-SrO/Y-zeolite			
R.T. (min)	Quality	Compound name	Relative peak area %
Hydrocarbons			14.84
3.034	91	1-Heptene	0.73
5.738	96	1-Nonene	0.40
7.367	96	1-Decene	0.24
8.978	95	1-Undecene	0.28
9.515	76	Cyclooctene	0.55
10.052	55	4-Undecene	0.75
11.02	91	Cyclododecene	0.51
11.525	55	2,4-Dodecadiene	0.78
14.611	90	1-Methoxy-2-(1-methyl-2-propenyl)	0.78
14.72	83	Pentadecane	2.16
14.984	90	2,3,5-Trimethoxytoluene	0.36
15.661	83	1H-Indene	0.84
16.763	93	6,8-Tetradecadiene	0.37
16.842	99	8-Heptadecene	1.65
16.905	86	Ethyl 2-(p-tolyl)propanoate	1.49
22.521	72	Decane	2.96
Phenols			6.67
8.922	94	2-Methoxy-Phenol	0.64
10.516	93	2-Methoxy-4-methylphenol	0.96
12.285	91	4-Vinyl-2-methoxy-phenol	0.79

12.758	94	2,6-Dimethoxyphenol	0.76
14.124	98	2-Methoxy-4-Phenol	0.91
14.188	80	2-Methoxy-4-propyl-Phenol	0.58
17.105	93	2,6-Dimethoxy-4-allylphenol	1.66
20.062	58	2-Allyl-3-ethoxy-4-methoxyphenol	0.37
Acids			68.89
2.333	50	Acetic acid	4.47
14.008	72	Dehydroacetic acid	0.76
19.832	99	Palmitic acid	3.75
21.632	99	Oleic acid	52.23
21.775	99	Octadecanoic acid	5.22
21.943	95	Linoleic acid	1.52
24.005	72	9-Octadecenoic acid	0.94
Ketones			1.89
7.515	72	3-Methyl Hydantoin	0.38
7.91	95	2-Hydroxy-3-methyl-2-Cyclopenten-1-one	0.40
9.189	94	1,2-Dibutyl-Cyclopropane	0.38
16.979	53	5,6-Dimethoxy-1-indanone	0.73
Aldehydes			2.66
4.321	89	Hexanal	1.02
4.806	90	3-Furancarboxaldehyde	1.16
16.624	91	Syringyl aldehyde	0.47
			2.66
Esters			
21.167	99	Methyl ester	2.52
others			2.53
14.541	90	Ethyl 1,4-benzodioxin-2-carboxylate	0.47
22.576	72	4-(4-Pentylcyclohexyl) cyclohexanecarboxylate	0.44
29.405	83	Peri-Xanthenoxanthene-4,10-dione, 2,8-bis(1-methylethyl)-	1.62
		Cu/SrO/Y-zeolite	

R.T. (min)	Quality	Compound name	Peak area %
Hydrocarbons			32.97
3.005	70	1-Heptene	1.87
5.723	95	1-Nonene	2.63
9.512	50	Cycloheptene	1.36
10.053	51	(1-methyl-2-cyclopropen-1-yl)-Benzene	4.63
11.566	60	Benzene, hexyl-	0.73
12.191	85	Naphthalene, 1-methyl-	2.32
14.54	90	2-Ethyl-1,4-benzodioxin	0.69
14.608	83	Dimethyltbenzo[b]hiophene	0.88
16.84	99	8-Heptadecene	9.47
26.292	64	2,2'-Binaphthalene	7.64
29.403	53	8,9-Triphenylbenzocyc-7-methyl	0.75
Phenols			14.64
7.134	60	Phenol	1.27
7.356	58	2-Pentyl-Furan	0.70
8.35	95	2-Methylphenol	0.70
8.683	96	4-Methyl-Phenol	1.09
8.921	94	Guaiacol	1.24
11.505	76	3-Methoxy-1,2-Benzenediol	0.48
11.755	83	4-Ethyl-2-methoxy-Phenol	0.34
12.284	94	4-Vinyl-2-methoxy-phenol	1.13
12.758	95	2,6-Dimethoxyphenol	1.51
14.123	98	2-Methoxy-4-propenylphenol	1.07
14.68	80	1,6-Anhydro-D-glucose	2.00
15.911	97	2,6-Dimethoxyphenol	0.61
17.104	90	4-Allyl-2,6-dimethoxyphenol	2.51
Acids			31.15
7.289	90	Hexanoic acid	1.80
10.187	98	Octanoic acid	1.86
14.007	80	Dehydroacetic acid	1.09

19.812	99	Palmitic acid	1.98
21.552	99	Oleic acid	17.26
21.728	99	Octadecanoic acid	3.36
21.918	99	Linoleic acid	3.09
22.515	52	Hexadecyl ester of gallic acid	0.71
Ketones			8.99
8.968	76	2-Nonanone	0.42
15.496	90	2-(Methoxymethyl)-3,5-dimethyl-1,4-benzoquinone	2.54
17.433	90	Acetosyringone	0.44
4.319	96	N-Hexanal	1.58
5.898	97	n-Heptanal	0.59
6.246	53	2-Hydroxycyclopent-2-en-1-one	0.93
7.914	95	Corylone	0.63
16.905	83	Bicyclo[3.2.2]non-3-en-2-one, 5-methyl-1-(1-methylethyl)-	1.87
Aldehydes			5.48
4.803	90	2-Furancarboxaldehyde	2.70
9.194	91	Nonyl Aldehyde	1.18
16.623	94	Benzaldehyde	1.60
Esters			6.78
2.335	72	Acetic acid methyl ester	6.27
24.002	68	2-Hydroxy-1-(hydroxymethyl)ethyl ester	0.51
		Zn-SrO/Y-zeolite	
R.T. (min)	Quality	Compound name	peak area %
Hydrocarbons			25.00
3.054	95	1-Heptene	2.15
3.958	87	Toluene	0.45
4.232	95	Cyclooctane	0.47
4.341	53	5,6-dimethyl-Decane	0.41
4.733	93	Cyclooctene	0.26
5.308	86	ethyl-Benzene	0.37

5.745	96	1-Nonene	0.44
5.973	83	4,5-Nonadiene	0.58
7.372	96	1-Decene	0.29
8.472	76	Butylbenzene	0.34
8.981	97	1-Undecene	0.37
9.187	98	5-Undecene	0.40
9.323	94	3-Undecene	0.32
9.516	68	Cycloheptene	0.73
9.816	53	Toluene, p-allyl-	0.49
10.055	46	Pentylbenzene	0.88
11.021	90	Cyclododecene	0.75
11.524	70	2,4-Dodecadiene	1.11
13.333	99	1-Tetradecene	0.33
14.011	72	1,2,3-Trimethoxybenzene	0.81
14.611	68	Hexamethyl-Benzene	0.55
14.72	92	Pentadecane	1.06
14.984	83	2,3,5-Trimethoxytoluene	0.37
15.437	70	2-Propenyl-Cyclohexane	0.36
15.664	86	5-Dodecyne	1.30
16.762	91	1,13-Tetradecadiene	0.44
16.847	99	8-Heptadecene	2.44
17.38	90	6(Z),9(E)-Heptadecadiene	0.27
22.532	62	Decane	6.27
Phenols			13.26
6.885	76	5-Methylfurfural	0.69
7.146	74	Phenol	0.34
8.355	95	2-MethylPhenol	0.53
8.697	95	3-Methyl-Phenol	0.52
8.923	94	2-Methoxy-Phenol	0.48
9.971	90	3-Methyl-1H-Indene	0.49
10.514	93	2-Methoxy-4-methylphenol	1.28
12.76	94	2,6-Dimethoxyphenol	1.04

12.854	97	Phenol, 2-methoxy-4-(2-propenyl)-	0.47
12.909	53	3,4-Dimethoxyphenol	0.67
14.125	98	2-Methoxy-4-Phenol	0.89
14.547	78	2-Ethyl-1,4-benzodioxin	0.55
15.914	97	Phenol, 2,6-dimethoxy-4-(2-propenyl)-	0.59
17.107	97	2,6-Dimethoxy-4-prop-2-enylphenol	1.62
21.171	99	Methyl 13-Octadecenoate	1.82
24.008	80	2-Oleoylglycerol	1.28
Acids			53.53
10.179	60	Octanoic Acid	0.49
14.799	53	Heptanoic acid	0.84
16.907	86	2-Propionic	1.67
19.854	99	Hexadecanoic acid	4.80
21.685	94	Oleic acid	36.88
21.816	99	Oleic acid	4.58
21.98	95	Linoleic acid	2.07
23.286	91	9-Octadecenoic acid	0.71
23.481	98	Eicosanoic acid	0.43
28.59	59	Lignosulfonic acid	1.06
Ketones			3.98
6.26	64	α-Angelica lactone	0.74
7.518	50	3-MethyL Hydantoin	0.53
7.916	96	Corylone	0.53
12.286	90	2-Cyclopenten	0.82
15.501	90	2-(Methoxymethyl)-3,5-dimethyl-1,4-benzoquinone	1.34
Aldehydes			1.80
4.814	90	2-Furancarboxaldehyde	0.85
16.627	91	Benzaldehyde, 4-hydroxy-3,5-dimethoxy-	0.36
21.225	99	Methylelaidate	0.59
Esters			0.68
3.898	32	Acetic acid methyl ester	0.41

15.769	53	4-Hydroxy-3-methoxy-, ethyl ester	0.27
other			1.47
4.077	56	Hexanol-5	0.27
9.058	53	N-ethyl-N-methyl-Ethanamine	0.25
11.883	68	2-Methyl-1,3-Benzenediol	0.30
17.528	95	3-(p-Hydroxy-m-methoxyphenyl)-2-propenal	0.36
20.065	95	3-(3',5'-Dimethoxy-4'-hydroxyphenyl)--2-propenal	0.29
Fe-SrO/Y-zeolite			
R.T. (min)	Quality	Compound name	Peak area %
Hydrocarbons			29.43
3.033	81	1-Heptene	0.70
5.734	70	1-Nonene	0.49
7.363	91	1-Decene	0.37
7.466	87	1,2,4-trimethyl-Benzene	5.35
7.909	87	Cyclotene	0.70
8.466	76	Butyl-Benzene	0.36
8.976	96	1-Undecene	0.28
9.189	55	3-Undecene	0.60
9.513	72	Cycloheptene	0.51
11.018	81	Cyclododecene	0.50
11.525	70	2,4-Dodecadiene	0.41
12.183	93	1-Methyl-Naphthalene	9.30
14.008	72	1,2,3-Trimethoxy-benzene	0.83
14.403	83	1-Chloro-4-methyl-1-boraindane	0.68
14.607	90	2-Ethyl-1-benzothiophene	0.82
14.72	86	Pentadecane	2.24
14.983	90	6,8-Dimethylbenzocyclooctene	0.56
16.842	99	8-Heptadecene	1.38
22.522	50	1,2,4,5-Tetraethyl-Cyclohexane	2.94
22.576	52	9-Tricosene	0.40

Phenols			10.30
4.065	56	Hexanol-5	0.31
8.688	94	3-Methyl-phenol	0.77
8.921	94	2-Methoxy-Phenol	0.63
10.515	91	2-Methoxy-4-methylphenol	0.93
11.755	87	4-Ethyl-2-methoxy-Phenol	0.32
12.283	91	4-Vinyl-2-methoxy-phenol	0.83
12.758	93	2,6-Dimethoxyphenol	0.95
12.855	97	Cis-Isoeugenol	0.28
14.124	97	2-Methoxy-4-Propenylphenol	1.01
14.192	80	2-Methoxy-4-propyl-phenol	0.55
14.54	90	2-Ethyl-1,4-benzodioxin	0.65
15.659	90	1H-Indene, octahydro-	0.96
15.911	97	2,6-Dimethoxyphenol	0.55
17.104	97	4-Allyl-2,6-dimethoxyphenol	1.56
Acids			42.23
2.352	72	Acetic Acid	5.27
10.181	86	Octanoic Acid	1.05
12.899	91	Decanoic Acid	0.31
19.838	99	Hexadecanoic Acid	4.98
21.633	99	Oleic Acid	25.22
21.78	99	Octadecanoic Acid	4.98
22.299	98	Linoleic Acid	0.42
Ketones			3.22
6.251	64	1,3-Cyclopentanedione	0.93
6.879	87	5-Methylfurfural	0.17
7.513	64	3-Methyl-2,4-Imidazolidinedione	0.44
24.006		Bicyclo[4.3.1]decan-10-one	0.47
28.589	83	1-Methylbenzo[b]xanthene-7,10,12-trione	1.22
Aldehydes			7.52
4.312	68	Hexanal	1.64
4.803	91	2-Furancarboxaldehyde	1.43

9.064	56	4-Nonenal	0.35
12.989		2-Undecenal	0.33
16.622	94	Syringaldehyde	0.47
16.769	76	Benzene, 1-methyl-3-(2-phenylethenyl)	0.37
16.979	83	5-Diacetyl-4-Benzyl-1,4-Dihydropyridine	0.74
17.796	72	1-Butanone, 1-(2,4,6-trihydroxy-3-methylphenyl)-	0.20
20.063	91	3-(3',5'-dimethoxy-4'-hydroxyphenyl)-E-2-propenal	0.35
21.223	99	Methylelaidate	0.50
21.946	95	9,17-Octadecadienal	1.14
Esters			2.75
21.168	99	Methyl Oleate	0.97
24.402	50	9-Octadecenoic acid (Z)-, methyl ester	0.27
29.408	90	25-EpiaplysterylAcetate-1	1.51
other			3.65
15.497	90	2,5-Cyclohexadiene-1,4-dione, 2-(methoxymethyl)-3,5-dimethyl-	1.33
16.904	53	1H-2-Benzopyran-1-one, 6,8-dihydroxy-3-methyl	1.47
17.524	97	Benzene, 1,2-dimethoxy-4-(2-propenyl	0.37
23.281	95	Cyclohexane, 1,2-dimethyl-3-pentyl-4-propyl-	0.47
		Ag-SrO/Y-zeolite	
R.T. (min)	Quality	Compound name	Peak area %
Hydrocarbons			34.27
3.047	94	1-Heptene	0.81
3.952	70	Toluene	0.56
4.226	96	Cyclooctane	0.47
5.741	86	1-Nonene	0.46
5.968	68	Cyclooctene	0.54

7.37	95	1-Decene	0.34
7.916	53	3-Octyne	0.46
8.468	90	Butyl-Benzene	0.41
8.98	97	1-Undecene	0.41
9.186	98	5-Undecene	0.48
9.321	95	3-Undecene	0.41
9.515	68	Cyclooctene	0.75
10.052	46	Pentyl-Benzene	0.85
11.02	81	5-Methylcycloheptene	0.87
11.52	70	2,4-Dodecadiene	0.87
11.568	50	Hexyl-benzene	0.38
11.962	98	1-Tridecene	0.22
12.188	72	Methylnaphthalene	0.57
13.332	98	1-Tetradecene	0.22
14.012	72	1,2,3-Trimethoxy-benzene	0.90
14.406	90	1,2-Epoxy-1-vinylcyclododecene	0.51
14.72	93	Pentadecane	8.96
15.437	64	n-Nonylcyclohexane	0.51
15.662	81	Decahydro-naphthalene	1.32
15.847	98	1-Hexadecene	0.22
16.762	97	6(E),8(E)-Heptadecadiene	0.46
16.847	99	8-Heptadecene	5.66
17.741	99	6(Z),9(E)-Heptadecadiene	0.31
22.536	52	Decane	5.35
Phenols			15.79
7.143	68	Phenol	0.53
8.355	93	4-Methyl-Phenol	0.57
8.693	94	3-Methyl-Phenol	0.31
8.921	94	2-Methoxy-Phenol	0.69
10.514	94	Creosol	1.50
11.756	76	4-Ethyl-2-methoxy-Phenol	0.26
11.885	81	4 Methyl Catechol	0.29

12.286	91	4-Vinyl-2-methoxy-phenol	0.72
12.761	95	2,6-Dimethoxy-phenol	0.82
12.854	98	2-Methoxy-4-(2-propenyl)-Phenol	0.32
12.908	64	3,4-Dimethoxy-Phenol	0.43
14.125	98	2-Methoxy-4-Phenol	0.95
14.189	78	2-Methoxy-4-propyl-phenol	0.69
15.502	83	2,6-Dimethoxy-4-prop-2-enylphenol	1.51
15.914	97	2,6-Dimethoxyphenol	0.88
17.109	96	4-Allyl-2,6-dimethoxyphenol	2.07
22.322	98	Methyl-8-hexadecyn-1-ol	1.35
29.411	64	Ergosta-4,6,22-trien-3-ol	1.88
Acids			40.57
10.181	70	Octanoic Acid	0.63
14.918	50	Butanoic acid	2.69
19.854	99	Hexadecanoic acid	5.33
21.682	99	Oleic acid	23.37
21.82	99	Octadecanoic acid	5.61
21.982	98	Linoleic acid	2.47
23.482	96	Eicosanoic acid	0.47
Ketones			3.85
6.255	86	1,3-Cyclopentanedione	0.68
7.52	56	3-Methyl Hydantoin	0.91
16.983	53	1H-2-Benzopyran-1-one, 6,8-dihydroxy-3-methyl-	0.71
17.802	80	2-Pentanone, 1-(2,4,6-trihydroxyphenyl)	0.38
19.202	92	14-Methyl-8-hexadecyn-1-ol	0.40
23.288	58	2-Hydroxy-cyclopentadecanone	0.78
Aldehydes			3.36
4.071	59	Pentanal	0.29
4.808	93	2-Furancarboxaldehyde	1.04
6.884	76	5 Methyl Furfural	0.46
16.63	94	Syringaldehyde	0.48

17.53	96	3-(p-Hydroxy-m-methoxyphenyl)-2-propenal	0.47
20.066	96	3-(3',5'-Dimethoxy-4'-hydroxyphenyl)-E-2-propenal	0.62
Esters			2.16
14.545	90	2-Ethyl-1,4-benzodioxin	0.60
21.168	99	Oleic acid methyl ester	0.47
21.226	92	Methyl ester 6-Octadecenoic acid	0.26
24.008		9-Octadecenoic acid (Z)-, 2-hydroxy-1-(hydroxymethyl)ethyl ester	0.82